Distributed Meandering Resonator Add-Drop Filters

in Silicon Photonic Integrated Circuits

Design, Fabrication and Analysis

by

Suat Kurt

A Dissertation Submitted to the Graduate School of Sciences and Engineering in Partial Fulfillment of the Requirements for

the Degree of Doctor of Philosophy

in

Electrical and Electronics Engineering

KOÇ ÜNİVERSİTESİ

August 12, 2024

Distributed Meandering Resonator Add-Drop Filters

in Silicon Photonic Integrated Circuits

Design, Fabrication and Analysis

Koç University

Graduate School of Sciences and Engineering

This is to certify that I have examined this copy of a doctoral dissertation by

Suat Kurt

and have found that it is complete and satisfactory in all respects, and that any and all revisions required by the final examining committee have been made.

Committee Members:

____

Prof. Alper Kiraz (Advisor)

____

Prof. Erdem Alaca

____

Prof. Mehmet Burçin Ünlü

____

Assoc. Prof. Ahmet Öncü

____

Assist. Prof. Emir Salih Mağden

____

Prof. Ali Serpengüzel [Co-Advisor]

Date: ______

To parents, wife and daughter.

ABSTRACT

Distributed Meandering Resonator Add-Drop Filters

in Silicon Photonic Integrated Circuits

Design, Fabrication and Analysis

Suat Kurt

Doctor of Philosophy in Electrical and Electronics Engineering

August 12, 2024

Add-drop filters (ADF) based on meandering loop mirrors (MLMs) and resonators based on MLMs are designed, fabricated, and analyzed using silicon integrated photonics circuit (Si-PIC) technology for operation in the standard near-infrared (near-IR) telecommunication band. Optical waveguides, directional couplers, MLMs, meandering resonators (MRs), antisymmetric meandering resonators (AMRs), and symmetric meandering resonators (SMRs) with symmetric and antisymmetric directional couplers are utilized as a function of the directional coupler length to scan the desired near-IR telecommunication band.

A silicon on insulator (SOI) platform is used to realize strip waveguides in transverse electric (TE) mode polarized single mode configuration. The structures' design is based on numerical simulations using a photonics design kit and resulting geometry of the structures were incorporated into the photonics layout for fabrication by e-beam lithography. After the writing of the silicon strip waveguide, and before oxide deposition, the photonic structures were imaged with scanning electron microscopy (SEM) to physically characterize the fabricated devices.

Surface gratings are used to couple in and out of these photonic structures with single mode optical fibers. The excitation source for the spectral measurement of the device transmission is a tunable laser operating in the 1500 – 1580 nm wavelength range. The transmission signals in logarithmic (dB) scale are detected in the same experimental region using calibrated near-IR photodetectors. The data is acquired by a control and data acquisition computer.

The experimentally measured transmission spectra are analyzed. To make the results more reader friendly, the spectra are color coded: port number 1,2,3 are utilized as outputs and colored as green, blue, and red, respectively. The reflection and transmission intensities are

plotted in logarithmic (dB) scale. The free spectral range (FSR), quality factor (Q-factor), mode split, insertion loss (IL), extinction ratio (ER), and slope rate (SR) are deduced from experimentally measured spectra.

To understand the actual spectral response, we first analyzed the spectra. Since the input and outputs of the devices had to be connected to the grating couplers, to couple in and out from the optical fibers, the measurement responses are always modulated by the grating coupler responses.

First, we analyzed the wavelength dependence of a DC, one of the basic elements used in our designs. Then we look at the MLM spectral response, which incorporates a directional coupler. After developing the understanding of directional coupler and the MLM, we moved to the analysis of the spectral responses of more complex structures with ADF, MLM, DC-MR, DC-SMR, DC-RMR, SC-MR, and DC-AMR.

The general response of a tunable mirror is observed for the MLMs. DC-MR shows the behavior of a Fabry-Pérot resonator with power distributed according to the coupling constants. DC-RMR shows the behavior of RE-MZI. SC-MRs show the typical Fabry-Pérot response. The DC-AMRs show the typical spectra like the coupled resonator induced transparency (CRIT), the analogue of the electromagnetically induced transparency (EIT) spectral responses. Whereas the DC-SMRs show the mode split Fano resonance spectral responses.

The figures of merits (FOMs) are given as the best result achieved for each design. The devices themselves have almost no insertion loss and the loss mechanism almost directly comes from the surface grating couplers -in and out- for all structures. SC-MR has an FSR of 1.6 nm with a best Q-factor of 19000, has an extinction ratio of 23 dB and a slope rate of 163 dB/nm. SC-MR has an FSR of 1.1 nm with a best Q-factor of 12000, has an extinction ratio of 30 dB and a slope rate of 307 dB/nm. DC-SMR has an FSR of 2.05 nm with a best Q-factor of 10000, a mode split of 1.1 nm, has an extinction ratio of 27 dB and a slope rate of 450 dB/nm. DC-AMR has an FSR of 1.83 nm with a best Q-factor of 40000, a mode split of 0.1 nm, has an extinction ratio of 33 dB and a slope rate of 872 dB/nm. DC-RMR has an FSR of 3.6 nm with a best Q-factor of 8000, a mode split of 1.1 nm, has an extinction ratio of 29 dB and a slope rate of 183 dB/nm.

In all of our designs we introduced a subsection of a waveguide with a specific length, if the round-trip optical path length is increased by increasing the length of the subsection, these devices can even be used for dense wavelength division multiplexing (DWDM) applications, which should have a spacing of 0.2 nm at 1550 nm. These results show that proposed devices, ADF-MLM, ADF resonators are good candidates for WDM applications, but still further modifications are required to be used as novel integrated photonic elements for optical communication, computation, and sensing.

ÖZETÇE

Silisyum Tümleşik Fotonik Devrelerde

Dağıtılmış Kıvrımlı Çınlaç Ekleme-Düşürme Süzgeçleri

Tasarım, Üretim ile İnceleme

Suat Kurt

Elektrik ve Elektronik Mühendisliği, Doktora

12 Ağustos 2024

Kıvrımlı döngü aynalarına (MLM'ler) dayalı ekleme-bırakma filtreleri (ADF) ve MLM'lere dayalı çınlaçlar, standart yakın kızılötesi (yakın-IR) telekomünikasyon bandında çalışmak üzere silikon bütünleşik fotonik devre (Si-PIC) teknolojisi kullanılarak tasarlanmış, üretilmiş ve incelenmiştir. Optik dalga kılavuzları, yönlü bağlaştırıcılar, MLM'ler, kıvrımlı çınlaçlar (MR'ler), asimetrik kıvrımlı çınlaçlar (AMR'ler) ve simetrik ve asimetrik yönlü bağlaştırıcılara sahip simetrik kıvrımlı çınlaçlar (SMR'ler), istenen yakın-IR telekomünikasyon bandını taramak için yönlü bağlaştırıcı uzunluğunun bir fonksiyonu olarak incelenmiştir.

Enine elektrik (TE) kutuplanmış tek kipli şerit dalga kılavuzlarını üretmek için silikon üzeri yalıtkan (SOI) yapılar kullanılmıştır. Yapıların tasarımı, fotonik tasarım yazılımı kullanılarak yapılan sayısal incelemelere dayanmaktadır ve yapıların ortaya çıkan geometrisi, elektron-ışın yazım yöntemi ile üretilmiştir. Silisyum fotonik yapıların üretiminden sonra, bu yapıları incelemek için taramalı elektron mikroskobu (SEM) ile görüntüleme yapılmıştır.

Yüzey ızgaraları, bu fotonik yapıları tek kipli optik fiberlerle bağlaştırmak için kullanılır. Cihaz iletiminin izgesel ölçümü için kullanılan ışık kaynağı, 1500-1580 nm dalga boyu aralığında çalışan ayarlanabilir bir lazerdir. Logaritmik (dB) ölçekteki iletim sinyalleri, yakın kızılötesi bandda çalışan ışık algılayıcılar kullanılarak ölçülür. Veriler, yönetim ve veri toplama bilgisayarı tarafından toplanır.

Deneysel olarak ölçülen iletim izgeleri incelenir. Sonuçları daha okunabilir hale getirmek için izgeler renk kodlu olarak verilmektedir: 1,2,3 numaralı kapılar çıktı olarak kullanılır ve sırasıyla yeşil, mavi ve kırmızı olarak renklendirilir. Yansıma ve iletim yoğunlukları logaritmik (dB) ölçekte çizilir. Serbest izgesel aralık (FSR), nitelik katsayısı (Q faktörü), kip bölünmesi, bağlaştırma kaybı (IL), sönüm oranı (ER) ve eğim oranı (SR) deneysel olarak

ölçülen izgelerden türetilmiştir.

İzgesel tepkiyi anlamak için önce sonuç izgeleri incelenmiş, bu izgelerin hepsinde yapıların giriş ve çıkışlarının optik fiberlere girip çıkmak için yüzey ızgaralarına bağlanması gerektiğinden, ölçümlerin yüzey ızgaraları tarafından kiplendiği görülmüştür.

Öncelikle tasarımlarımızda kullanılan temel unsurlardan biri olan yönlü bağlaştırıcıların dalga boyu bağımlılığını incelenmiş, daha sonra yönlü bir bağlaştırıcı içeren MLM izgesi incelenmiştir. Yönlü bağlaştırıcı ve MLM yapılarının incelenmesinden sonra ekleme bırakma süzgeçli (ADF), MLM, DC-MR, DC-SMR, DC-RMR, SC-MR ve DC-AMR gibi daha karmaşık yapıların izgesel sonuçları değerlendirilmiştir.

MLM'ler için ayarlanabilir bir aynanın genel tepkisi gözlemlenmiş, DC-MR yapısında ise, bağlaştırıcı katsayılarına göre dağıtılan güce sahip bir Fabry-Pérot çınlacı davranışı görülmüştür. DC-RMR, çınlama ile güçlendirilmiş Mach-Zehnder girişimölçeri davranışını gösterirken, SC-MR'lerde olağan Fabry-Pérot davranışı gözlemlenmiştir. DC-AMR'ler, elektromanyetik irkitilmiş saydamlık (EIT) izgesel tepkilerinin benzeri olan bağlaşmış çınlaç irkitilmiş saydamlık (CRIT) gibi olağan izgeleri göstermiştir. DC-SMR'ler ise kip bölünmüş Fano çınlaç izgesel davranışını göstermiştir.

Başarım ölçütleri her tasarım için elde edilen en iyi sonuç olarak verilmiştir. Yapıların kendisi neredeyse hiç ekleme kaybına sahip değildir ve oluşan kayıp neredeyse doğrudan, tüm yapılar için, yüzey ızgara bağdaştırıcılarından -içe veya dışa doğru- gelir. SC-MR, 19000'lik en iyi Q-katsayısı ile 1.6 nm'lik bir FSR'ye, 23 dB'lik bir sönüm oranına ve 163 dB/nm'lik bir eğim oranına sahiptir. SC-MR, 12000'lik en iyi Q-katsayısıyla, 1.1 nm'lik bir FSR'ye, 30 dB'lik bir sönüm oranına ve 307 dB/nm'lik bir eğim oranına sahiptir. DC-SMR, 10000'lik en iyi Q-katsayısıyla, 2.05 nm'lik bir FSR'ye, 1.1 nm'lik bir kip bölünmesine, 27 dB'lik bir sönüm oranına ve 450 dB/nm'lik bir eğim oranına sahiptir. DC-AMR, 40000'lik en iyi Q-katsayısı, 0.1 nm'lik kip bölünmesi, 33 dB'lik sönüm oranı ve 872 dB/nm'lik eğim oranı ile 1.83 nm'lik bir FSR'ye sahiptir. DC-RMR, 8000'lik en iyi Q-katsayısı, 1.1 nm'lik kip bölünmesi, 29 dB'lik sönüm oranı ve 183 dB/nm'lik eğim oranı ile 3.6 nm'lik bir FSR'ye sahiptir.

Tüm tasarımlarımızda, bağdaştırıcılar arasına belirli uzunlukta bir dalga kılavuzu eklenmiştir; bu dalga kılavuzunun uzunluğu artırılarak gidiş-dönüş optik yol uzunluğu artırılırsa, bu cihazlar 1550 nm'de 0.2 nm'lik bir FSR’ye sahip olması gereken yoğun dalga boyu bölmeli çoğullama (DWDM) uygulamaları için bile kullanılabilir. Bu sonuçlar önerilen cihazların, ADF-MLM, ADF çınlaçların WDM uygulamaları için iyi adaylar olduğunu göstermektedir, ancak optik iletişim, hesaplama ve algılama alanında yeni tümleşik fotonik bileşen olarak kullanılabilmeleri için bu yapılar daha fazla değişikliğe ihtiyaç duymaktadır.

ACKNOWLEDGMENTS

I would like to express my gratitude to my supervisor, Prof. Dr. Ali Serpengüzel for giving me the chance to work with him, in his research group at Koç University Microphotonics Research Laboratory (KUMRL) and for his constant guidance, understanding, patience during my PhD study in Koç University. I would also like to thank my committee members Prof. Dr. Alper Kiraz, Prof. Dr. Erdem Alaca, and Asst. Prof. Dr. Emir Salih Mağden, for their reading of my thesis, and their constructive comments. I would like to thank my external committee members Prof. Dr. Mehmet Burçin Ünlü and Assoc. Prof. Dr. Ahmet Öncü for reviewing my thesis.

I would like to thank my research group friend, Syed Sultan Shah Bukhari for his help in brainstorming sessions and moral boosting. I would like to thank Ömer Yaman for his help in scientific discussion and giving me motivation. I would like to thank our laboratory alumni for their help during my PhD.

I would also like to acknowledge Prof. Dr. Lukas Chrostowski and Iman Taghavi of University of British Columbia and, Cameron Horvath at Applied Nanotools Inc. for their efforts in the education, training, manufacturing, and measurement of the designed photonic integrated structures.

I would also like to thank the Society of Photo-optical Instrumentation Engineers (SPIE) and Scientific and Technological Research Council of Turkey (TÜBİTAK) for all the financial support.

TABLE OF CONTENTS

LIST OF TABLES

LIST OF FIGURES

ABBREVIATIONS

ADF	Add drop filter
AMR	Antisymmetric Meandering Resonator
C	Coupling constant
CMOS	Complementary metal oxide semiconductor
CMR	Coupled meandering resonator
CSCR	Coupled self-coupled resonator
DC	Double Coupled
ER	Extinction Ratio
FSR	Free Spectral Range
IL	Insertion Loss
LC	Coupling Length
MLM	Meandering loop mirror
MR	Meandering resonator
MR-ADF	Meandering resonator add drop filter
MZI	Mach-Zehnder Interferometer
Q-factor	Quality factor
RMR	Reverse Meandering Resonator
SC	Single Coupled
SCR	Self-coupled Resonator
SEM	Scanning electron microscope
SMR	Symmetric Meandering Resonator
Si-PIC	Silicon photonic integrated circuit
SR	Slope Rate
SWG	Sub-wavelength grating
TE	Transverse electric
TM	Transverse magnetic
WDM	Wavelength division multiplexing

Chapter 1

INTRODUCTION

Communication systems have an important place in the development of the world and different systems are being developed to meet these communication needs [1]. In modern systems, photonics is a key enabler of high-speed data transmission, which can be divided into unguided (free space) photonics and guided photonics. Unguided photonics include applications of light manipulation without using a guiding media other than free space, this includes applications such as Lidar [2] and Li-Fi [3]. Guided waves on the other hand, confines the light into a media other than free space or air, these confinement technologies include optical fibers [4] and integrated photonics [5,6].

1.1. Fiber Optics

Along with today's wireless communication systems [7], fiber optic communication systems are among the most effective for carrying fast, and high-capacity data [8]. Since the invention of the first fiber optic cable [5], demand in the communications industry has significantly increased. This breakthrough revolutionized communications technology, followed by the development of the first lasers, fiber optic cables, and erbium-doped fiber lasers [9]. Optical communication has since become one of the backbones of modern communication technology due to its ability to offer high-speed data transmitting and receiving especially for long distances [10,11].

Today, in addition to communication, fiber optic cables find applications in high-power lasers for industrial production [12,13], medicine [14], and sensing [15]. Furthermore, fiber optic cables are laid even under the oceans, creating a vast global network of optical fibers [16], which has enabled the development of long-distance communication systems.

In summary, optical fibers have revolutionized the communications industry, especially for high data rate communications, and beyond communication, optical fibers have a wide range of applications in numerous fields.

1.2. Fiber Optics and Integrated Photonics

Fiber optic cables are typically used in long-distance communication due to their capabilities such as low power loss, handling high power, transmitting data at high speeds, and all optical amplification [17]. These features allow the signal to travel over long distances without significant loss. On the other hand, due to sidewall roughness and sensitivity to fabrication errors, which are intrinsic challenges at the nanoscale, photonic integrated circuits (PICs) experience higher propagation losses [18] compared to fiber optic cables [19]. As a result, PICs are less suitable for long-distance data transmission, which makes fiber optics the preferred solution for long distance applications.

Nevertheless, PICs offer certain advantages. These include compatibility with the existing CMOS manufacturing processes, low production costs, high confinement of light, robustness for monolithic and mass production, as well as properties such as high refractive index contrast and small bending radius [20,21,22,23]. These characteristics make PICs attractive for use in optical systems.

Due to these benefits, PICs are preferred in applications where short-distance, high-speed data processing and signal transmission are required [24,25,26], rather than long-distance communication. They are particularly prominent in data centers, high-performance computing systems, and various communication infrastructures, where CMOS-compatible PICs solutions are favored [27,28].

1.3. Integrated Photonics

Photonics today is pervasive across individual and corporate use, and it is rapidly advancing [29,30,31,32] after the first introduction of PICs in 1985 [33] and the first implementation of SOI process in 1992 [34,35]. The receivers and transmitters used in these data centers are only one of the components that require high speed due to today's data processing demand in data centers, and PICs emerge as the solution here [36]. Today's high data rates demand with applications such as AI, cloud computing, streaming are one of the biggest reasons for the rapid development of silicon PICs, which is a rapidly maturing technology due to their compatibility with the existing CMOS infrastructure. Alongside with these properties, PIC technology has applications in the fields of communication [37], switching [38], photonic processing [39,40,41], lasers [42], and sensing [43].

1.4. Silicon Based Integrated Photonics

Although silicon is not a direct band-gap material, resulting in very low emission efficiency [44], its compatibility with the existing CMOS technology, suitability for mass production, and low-cost fabrication have made silicon photonics the most widely used SOI (Silicon-On-Insulator) platform [45] since their first introduction by Soref [46]. One of the main reasons for the rapid development of silicon photonics is that these devices can be produced using existing complementary metal oxide semiconductor (CMOS) technology [47,48], a crucial advantage as the industry was already facing high demand when this new technology emerged as a solution, particularly for the heat issues in data centers [49].

The heat problem in data centers is primarily caused by the data lines between processors and memory units [50], and silicon photonics addresses this by offering a low loss alternative [51]. Silicon photonic devices are especially useful in data centers, where cooling mechanisms are essential for managing heat dissipation [52]. This thermal issue arises from the intrinsic properties of electrons, which, when they collide, generate heat—something that Si-PIC interconnects can help mitigate. Silicon photonics has applications in fields such as sensing, communication, and computation [53,54,55] due to its low cost, low power consumption, and compactness [56,57,58].

Especially in the era of big data and AI applications, the demand for high-speed data transfer is increasing tremendously [59]. As a result, several High-Performance Computing (HPC) and data center companies are already implementing silicon photonic-based interconnects. The main reason behind this shift is that, compared to their electronic counterparts, silicon interconnects offer a significantly lower cost—less than $1/Gbps—while providing high-density integration and wavelength division multiplexing (WDM) capabilities. Furthermore, YOLE anticipates that silicon interconnects will outperform both electronic and fiber interconnects in several fields [60].

In summary, silicon photonics is a promising candidate for addressing the increasing demand for higher quality, speed, and data rates in communications, owing to its unique qualities that other technologies cannot match.

Silicon photonics integration can be categorized into several key functional blocks, such as lasers, modulators, photonic signaling, photonic processing, and photodetection. Photonic signaling, in turn, can be further classified into communication, interconnects, wavelength conversion, and related processes. Additionally, photonic processing encompasses operations such as optical filtering, switching, multiplexing, and demultiplexing [61, 62].

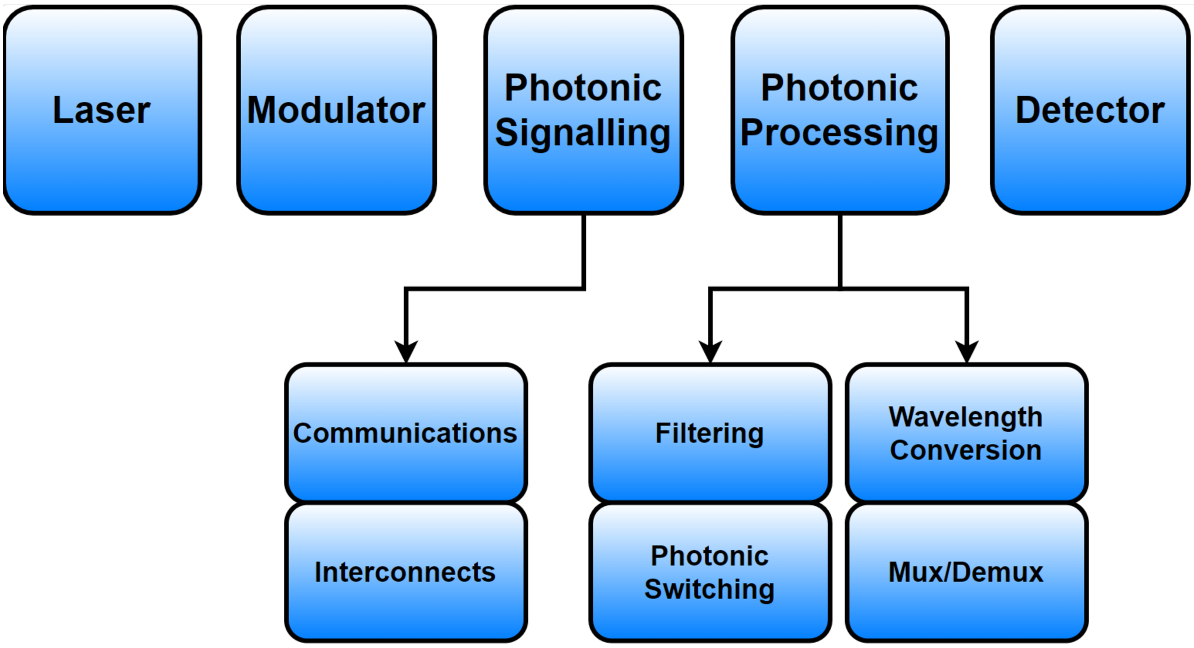

Figure-1.4-1: Main modules and applications of silicon photonics integration [61].

In a silicon-integrated platform, the process begins with the generation of light using a light source, typically a laser. This can be achieved by incorporating III-V materials onto silicon through methods such as heterogeneous integration, epitaxial growth [63,64,65]. Once the light is generated, it must be coupled into a bus waveguide via optical interconnects [66]. The transmitted light can then be modulated, and, to increase data capacity, multiple wavelengths can be combined using wavelength division multiplexing (WDM) to carry more information through the silicon-on-insulator (SOI) waveguide. Finally, the modulated data is transferred to an optical waveguide using structures such as surface grating couplers [67] or inverse tapered SOI waveguides [68]. One of the critical components for photonic processing in this integration scheme is WDM, which allows efficient use of multiple wavelengths to enhance bandwidth and communication efficiency.

Silicon photonics SOI platforms can utilize different types of waveguides such as ridge, strip waveguides or sub-wavelength gratings and slit waveguides.

Silicon photonics is widely utilized previously in applications such as modulators [69], high-speed transceivers as shipping products by Intel [70]. Silicon photonics devices with their high bandwidth capabilities, can also be utilized as wavelength division multiplexers (WDMs) [71,72,73,74,75].

Figure-1.4-2 below shows the illustration of the ridge and strip SOI waveguides, which is a commonly used structure for WDMs.

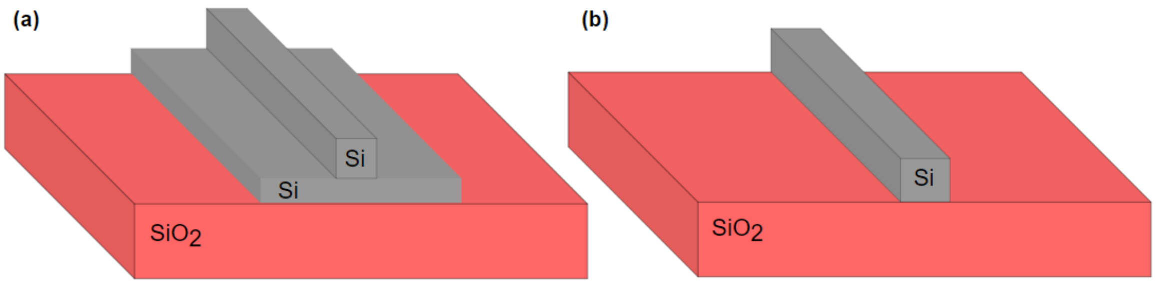

Figure-1.4-2: Representation of SOI waveguides, (a) ridge waveguide, (b) strip waveguide.

One of the most widely used structure in SOI platforms is the ring resonators due to their easy fabrication process [76]. Combination of different photonic integrated structures can reduce the size weight and power consumption of the devices [77]. Meandering resonators with their monolithic fabrication process and better footprint compared to the ring resonators are introduced before [78,79,80]. After the theoretical introduction, several different designs are also fabricated and analyzed around the world by different research groups [81]. Our proposed meandering resonators' measurement results were analyzed previously by our research group. In the scope of the thesis, we used these proposed MLM resonators and combined them to design more complex structures as add-drop filters, get them fabricated and analyzed the measurement result with several performance parameters which will be shown in the following chapters.

1.5. III-V Based Integrated Photonics

Photonic Integrated Circuits (PICs) are gaining increasing attention from the researchers due to their ability to provide high bandwidth at a low cost per Gbps, along with their potential for large-scale integration capabilities [82]. Silicon has emerged as the dominant platform for PICs, largely due to its compatibility with mature CMOS manufacturing technologies [83], however, despite these advantages, silicon-based platforms face a critical limitation in producing efficient on-chip light sources, especially when compared to other silicon-on-insulator (SOI) devices such as modulators, detectors, and multiplexers [84,85,86,87]. The underlying issue stems from silicon's intrinsic emission inefficiency, which arises from its indirect bandgap structure, making it difficult to generate light efficiently [88]. This limitation represents the primary bottleneck to achieving fully integrated optical systems on a silicon-based platform [89,90].

To address this challenge, a suitable on-chip laser must possess several key characteristics:

it must lase within the optical communication bands, specifically at 1310 nm or 1550 nm, for direct integration with optical fiber systems; it must deliver sufficient output power; and it must do so with a low cost per bit, all while being manufacturable using existing CMOS processes [91]. Integration of III-V materials into silicon is one of the promising solutions, as these materials have direct bandgaps that allow for more efficient light emission [92]. In this context, III-V doped silicon lasers have previously been reported [93,94,95,96]. Despite this progress, the most significant challenge remains the integration of III-V elements into the silicon platform.

In addition to material integration challenges, ongoing efforts in the field are focused on improving the efficiency, reliability, and cost-effectiveness of such systems, as well as addressing issues related to coupling light into and out of optical fibers. Although these challenges persist, advancements in hybrid integration techniques and material systems continue to drive rapid progress in integrated photonics, bringing the vision of fully integrated photonic systems closer to realization [97].

1.6. Silicon Nitride Based Integrated Photonics

Silicon Nitride (Si_3N_4) has emerged as a critical platform in silicon photonics, known for its compatibility with standard CMOS fabrication processes [98]. The Si_3N_4 platform offers a unique combination of low attenuation, broad transmission range, and minimal propagation loss, positioning it as a superior alternative in specific photonic applications [99]. Due to its refractive index of 1.98 (dependent on the silicon content) compared to 1.45 for SiO_2 at 1550 nm, Si_3N_4-based photonic circuits requires wider bend radii than conventional silicon photonics. However, with its ability to provide exceptionally low propagation losses, with values ranging from 0.3 dB/m to 1.0 dB/cm over a wavelength range of 400 nm to 2350 nm, making it suitable for applications from the visible to mid-IR spectrum.

Compared to InP and SOI platforms, Si_3N_4 not only offers a broader wavelength range but also delivers reduced propagation losses while maintaining moderate bending radii. It also has properties such as ultra-low nonlinear absorption loss, low thermo-optic coefficients, and enhanced dispersion engineering capabilities [100,101,102]. These features enable the platform to excel in applications requiring ultra-low loss waveguides, especially in nonlinear photonics, highly reliable microwave photonic systems, and ultra-wideband integrated photonic systems [103,104,105]. Additionally, Si_3N_4 plays a pivotal role in the development of advanced photonic devices such as waveguides, modulators, detectors, and lasers [106,107]. Si_3N_4 has also enabled the realization of on-chip optical frequency comb generators [108,109], an essential component in optical communications and precision measurements.

Due to these attributes, silicon nitride platforms continue to expand their influence across a broad range of high-performance photonic applications, particularly in areas that demand both high bandwidth and low loss [110]. Its flexibility, coupled with the capability to operate over a wide spectral range, ensures that Si_3N_4 remains a cornerstone in the field of integrated photonics, making it a preferred material in next-generation photonic devices and systems.

1.7. This Work

Add-drop filters (ADF) based on meandering loop mirrors (MLMs) and resonators based on MLMs are designed, fabricated, and analyzed using silicon integrated photonics circuit (Si-PIC) technology for operation in the telecommunication band. An SOI platform is used to realize strip waveguides in transverse electric (TE) mode polarized single mode configuration. The geometry of the structures was incorporated into the photonics layout for fabrication by e-beam lithography. After the writing of the silicon strip waveguide, and before oxide deposition, the photonic structures were imaged with scanning electron microscopy (SEM) to physically characterize the fabricated devices.

Surface gratings are used to couple in and out of these photonic structures with single mode optical fibers. The excitation source for the spectral measurement of the device transmission is a tunable laser operating in the 1500 – 1580 nm wavelength range. The transmission signals in logarithmic (dB) scale are detected in the same experimental region using calibrated near-IR photodetectors. The data is acquired by a control and data acquisition computer.

The experimentally measured transmission spectra are analyzed and the free spectral range (FSR), quality factor (Q-factor), mode split, insertion loss (IL), extinction ratio (ER), and slope rate (SR) are deduced from experimentally measured spectra. First, we analyzed the wavelength dependence of a DC, one of the basic elements used in our designs. Then we look at the MLM spectral response, which incorporates a directional coupler. After developing the understanding of directional couplers and the MLM, we moved to the analysis of the spectral responses of more complex structures with ADF, MLM, DC-MR, DC-SMR, DC-RMR, SC-MR, and DC-AMR.

As a result, ADF-MLM and ADF resonators show promise as a novel integrated photonics platform for Si-PIC elements for optical communication, computation, and sensing.

Chapter 2

Design, Fabrication and Characterization

2.1. Design

We used LUMERICAL MODE, FDTD and INTERCONECT and KLayout software to design the waveguides. Waveguide structure size is 500 nm width and 220 nm height as shown in Figure 2.1-1. The main building block for our fabricated structures is the MLM add-drop filter (ADF) and the main part that results to resonance is the IC or the CC couplers that we used in our designs. Figure 2.1-2 shows the structure of the IC couplers with a bending radius of 5 µm, and Figure 2.1-3 shows the CC coupler illustration with bend radius of 5 µm, in the illustrations L_c=15 µm is chosen and it can be changed to get the desired coupling constant for the structure. These couplers in SOI platform can be utilized for applications of wavelength division multiplexing (WDM). MLM add-drop filter, and the representation of the designed structures are shown in the following chapters.

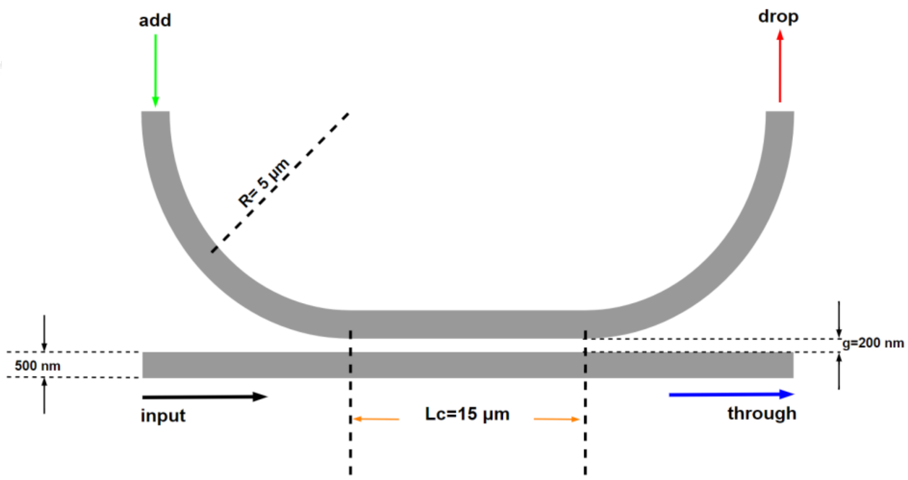

Figure 2.1-1: The illustration of the IC coupler used in photonic integrated circuits (PICs). The IC coupler utilizes a silicon-on-insulator (SOI) strip waveguide with dimensions of 500 nm in width and 220 nm in height, the bending radius is 5 µm, the gap between the waveguides in the coupling point is g=200 nm.

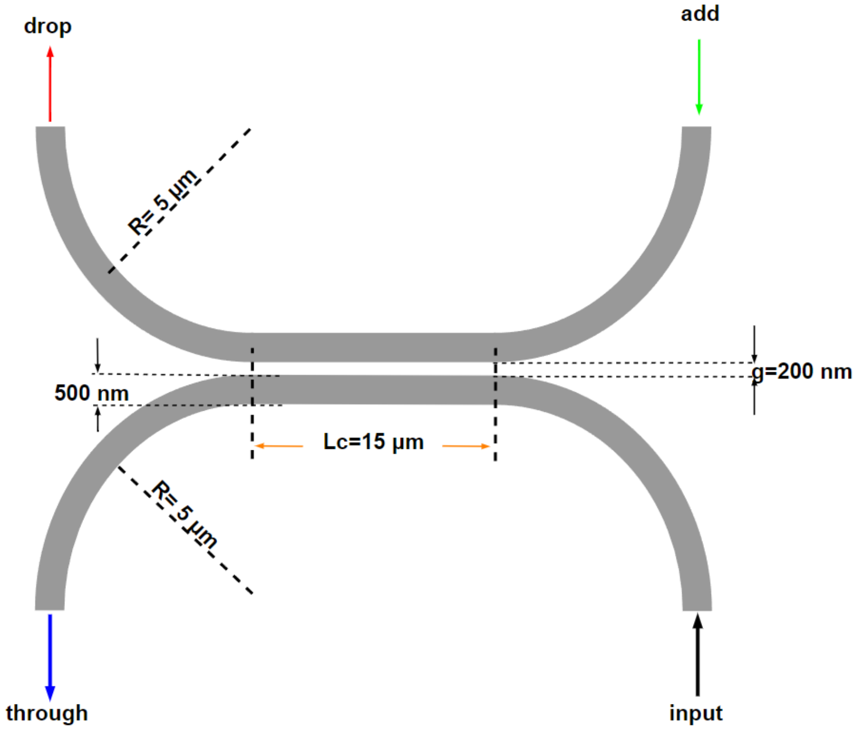

Figure 2.1-2: The representation of the CC coupler used in photonic integrated circuits (PICs). The CC coupler utilizes a silicon-on-insulator (SOI) strip waveguide with dimensions of 500 nm in width and 220 nm in height, the bending radius is 5 µm, the gap between the waveguides in the coupling point is g=200 nm.

In the following section the coupling constant analysis for the couplers is given, when the coupling length LC changes it also changes the coupling constant which specifies where the reflection and transmission will make a peak. As you can see from the figures below, the reflection and transmission 50-50 coupling point for the IC coupler is L_c=17 µm.

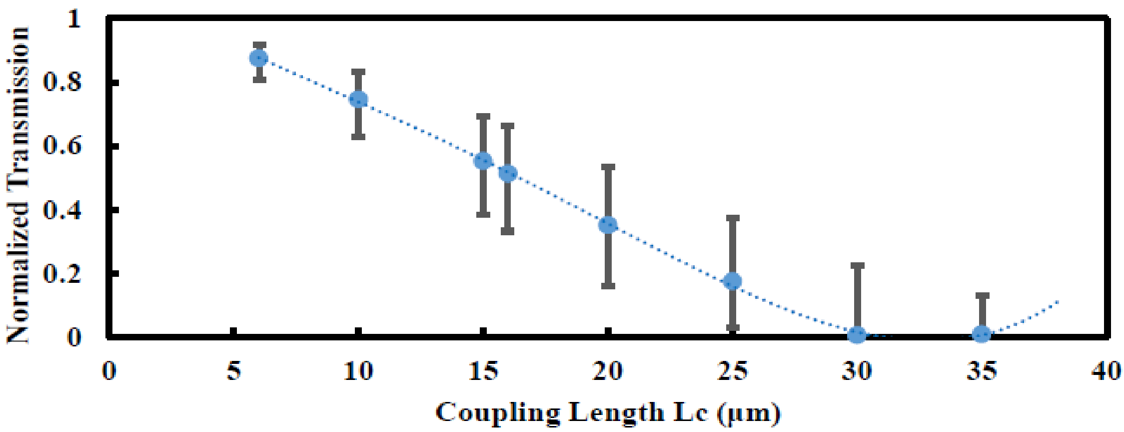

Figure 2.1-3: Coupling constant C vs. coupling length LC for IC directional couplers, through port

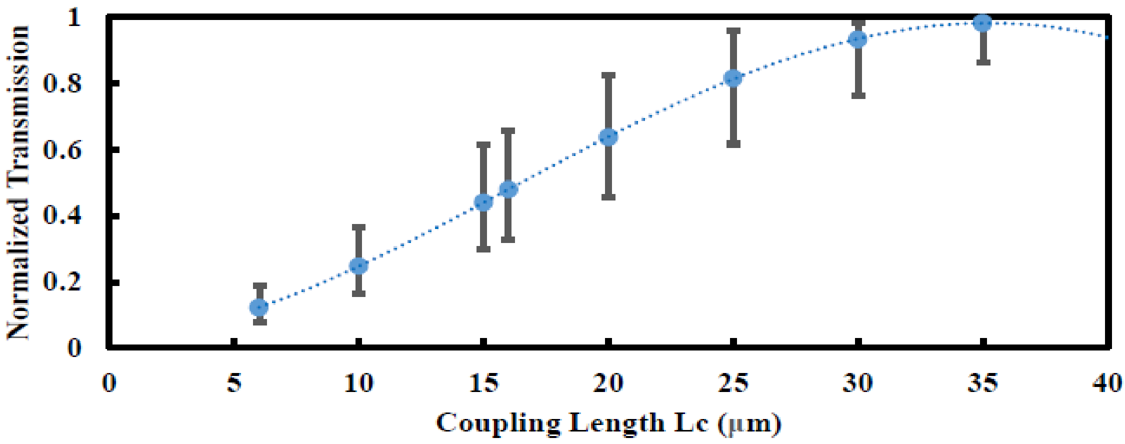

Figure 2.1-4: Coupling constant C vs. coupling length LC for IC directional couplers, drop port

Table 2.1-1 shows the directional coupler and IC coupler coupling constants with respect to the coupling length Lc.

Table 2.1-1: Coupling constant C vs. coupling length LC for the DC and IC type directional coupler

Coupling length Lc (μm)	Directional coupler (DC) coupling constant	Directional coupler (IC) coupling constant
00	0.006	0.01
15	0.40	0.44
16	0.41	0.48
17	0.45	0.52
18	0.49	0.56
19	0.53	0.60
20	0.58	0.64

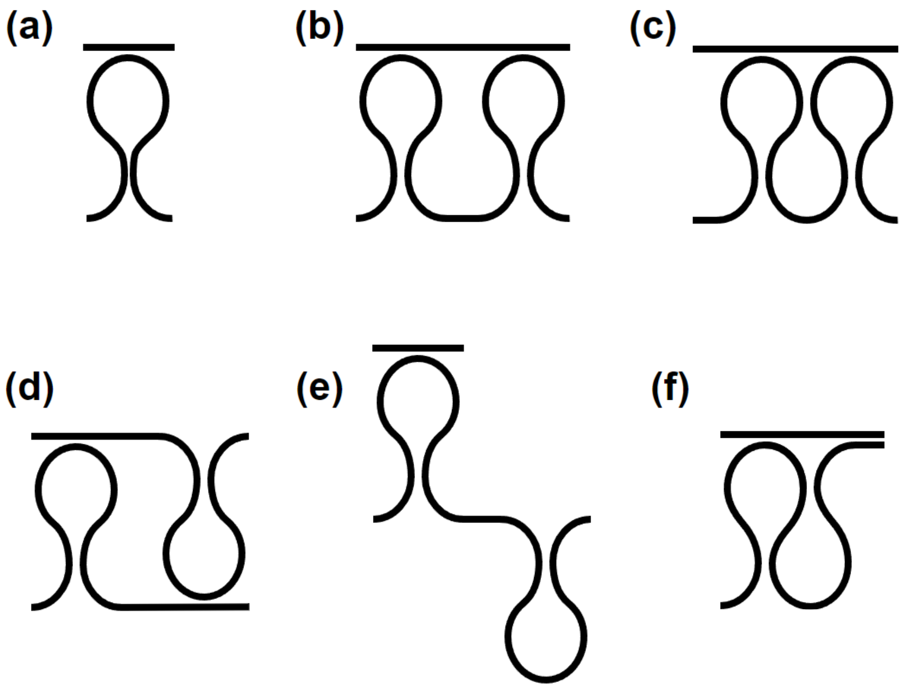

Figure 2.1-5: The illustration of the designed and fabricated SOI waveguide structures a) MLM Add-Drop Filter, b) Double Coupled MR, c) Double Coupled SMR, d) Double Coupled Rev-MR, e) SC Add-Drop MR, f) DC AMR.

The first device proposed here is an MLM (meandering loop mirror) add drop filter (ADF) which utilizes meandering loop mirrors (MLMs). These MLM structures, gives the device compactness and monolithographic fabrication property [79]. Add-drop MLM filter can be used in communication applications such as wavelength division multiplexing, all optical switches, and biomedical sensing [29]. The proposed structures show Fano lineshapes and Lorentzian peaks according to the device design parameters such as the coupling length (L_c) which results in a coupling coefficient and the round-trip path length which specifies the Free Spectral Range (FSR) of the structure.

The structures show Lorentzian and Fano lineshapes with Rabi splitting, electromagnetically induced transparency (EIT) like peaks and coupled resonator induced transparency (CRIT) spectral behaviors.

2.2. Fabrication

Applied Nanotools manufactured the structures using the NanoSOI multi-project wafer (MPW) process. This process utilizes 100 KeV electron beam lithography on silicon-on-insulator (SOI) wafers with a diameter of 200 mm. The resulting structures have a cross-section of 220 nm in height, consisting of silicon on a silicon oxide (SiO2) buffer layer, which is 2 μm thick, serving as the base material. [111,112].

The process steps are given as following:

Step 1: Predicing the 200 mm wafer into 25 mm x 25 mm dimensions square substrates by inscribing a line on the backside so that the separation into smaller chips is easier after the completion of fabrication.

Step 2: Wafer cleaning for 15 minutes using of piranha, 3 to 1 ratio H2SO4 to hydrogen peroxide H2O2, solution.

Step 3: Isopropyl alcohol (IPA) or water rinse.

Step 4: Spin coating the wafer by electron-beam lithography hydrogen silsesquioxane (HSQ) resist.

Step 5: The wafer is heated to evaporate the solvent in the resist.

Step 6: Raith EBPG 5000+ high performance, high precision, 100 keV, electron-beam lithography tool [100] was used to pattern the structures using a raster scan. The dosage for the exposure is corrected for proximity effects of the design, which result from the electrons, that backscatter due to exposure of nearby features. Efficient patterning and minimal beam drift are obtained by optimizing the shape writing order.

Step 7: Development of the wafer is done by tetramethylammonium sulfate solution (TMAH), and the structures are optically inspected for residues or defects.

Step 8: Wafer is mounted on a 4-inch handling wafer.

Step 9: Anisotropic inductively coupled plasma - reactive ion etching (ICP-RIE) process is performed using chlorine, after qualification of the etch rate.

Step 10: Removal of the resist is done using 10 to 1 ratio buffer oxide wet etch.

Step 11: Inspection of the structures and verification of patterning and etch quality is done using a scanning electron microscope (SEM).

Step 12: Plasma enhanced chemical vapor deposition (PECVD) process is done to deposit a 2.2 μm silicon oxide (SiO2) cladding using tetraethyl orthosilicate (TEOS) at 300 °C.

Step 13: Verification of cladding thickness, structure layer, and buffer oxide is done using reflectometry measurements.

2.3. Characterization

In this section the properties such as the size and dimensions, the figures of merits (FOMs), representations and the experimental measurement setups of the of the utilized designs will be addressed.

Surface Grating Coupler

Applied Nanotools (ANT) replaces these GCs with their own propriety GCs before fabrication. Figure 2.3-1 shows the representation of the de-embedded structure, and the experimental transmission spectra of two fabricated GCs connected by a 110 µm waveguide with two 5 µm bends for a TE_{00} mode is shown in Figure 2.3-2. There is an insertion loss of -32.6 dB at 1515 nm, and an insertion loss of -21.7 dB at 1550 nm in this experimental transmission spectrum, which is averaged over 10 measured spectra, and smoothed.

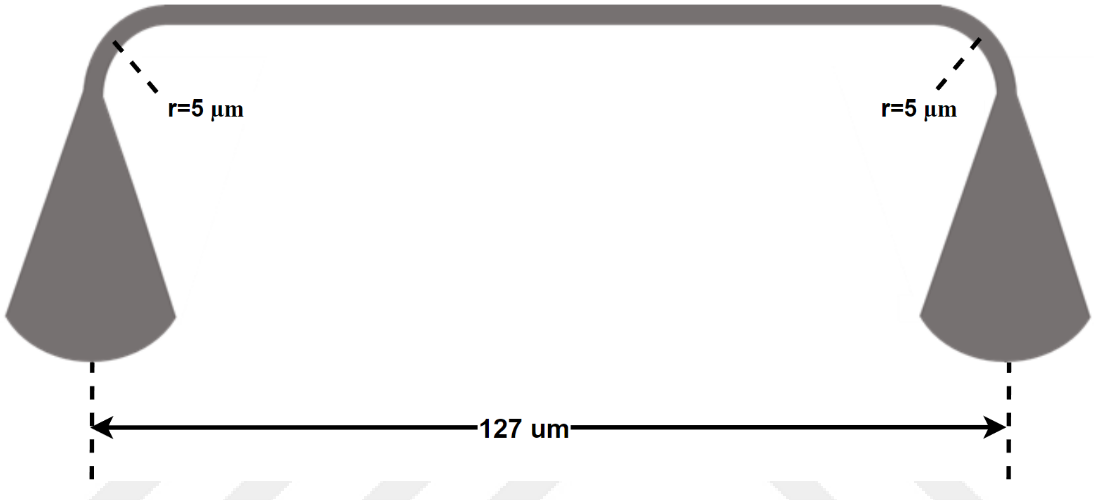

Figure 2.3-1: Two GCs spaced at 127 µm connected with 110 µm waveguide with 5 µm bends.

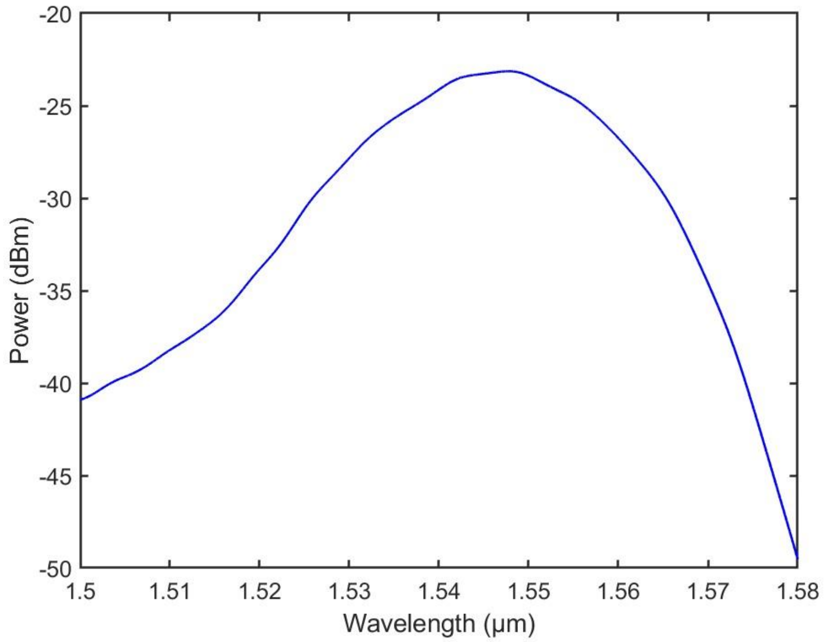

Figure 2.3-2: Experimental transmission spectrum of a two GCs connected by a 110 μm waveguide with two 5 μm bends for a TE_{00} mode shows an insertion loss of -23.6 dB at 1550 nm.

Figures of Merits

The definitions of the figures of merits for the analyzed devices such as free spectral range, Q-factor, extinction ratio (ER), Slope rate (SR) is given in the following section.

Q-factor

The Q-factor is a measure that quantifies the balance between the energy stored in a resonating or an oscillating system and the energy it loses or dissipates. Mathematically, it reflects how efficiently an oscillatory system maintains its oscillations by relating the system's total energy to its energy losses over time.

Q factor is defined as the central wavelength of a peak, divided by the 3 dB point which the intensity halves from both left and right sides which is shown below for a Fabry-Pérot etalon.

$$Q = \frac{\nu_m}{\delta_\nu}$$

Here m represents the mode number, which ν_m means the frequency of the mth mode, δ_ν is known as the linewidth, which is half of the maxima, or the 3 dB point from the both sides of the central peak.

Q-factor in the wavelength domain can also be represented as which is $\lambda_{center}/\delta_\lambda$ in wavelength domain, this approximation is valid for values of high Q-factor, which at the same time requires the 3 dB difference [Full width at half maxima (FWHM)] of the peak to be narrow. Figure 2.3-3 below shows the representation of the Q-factor for a Fabry-Pérot etalon.

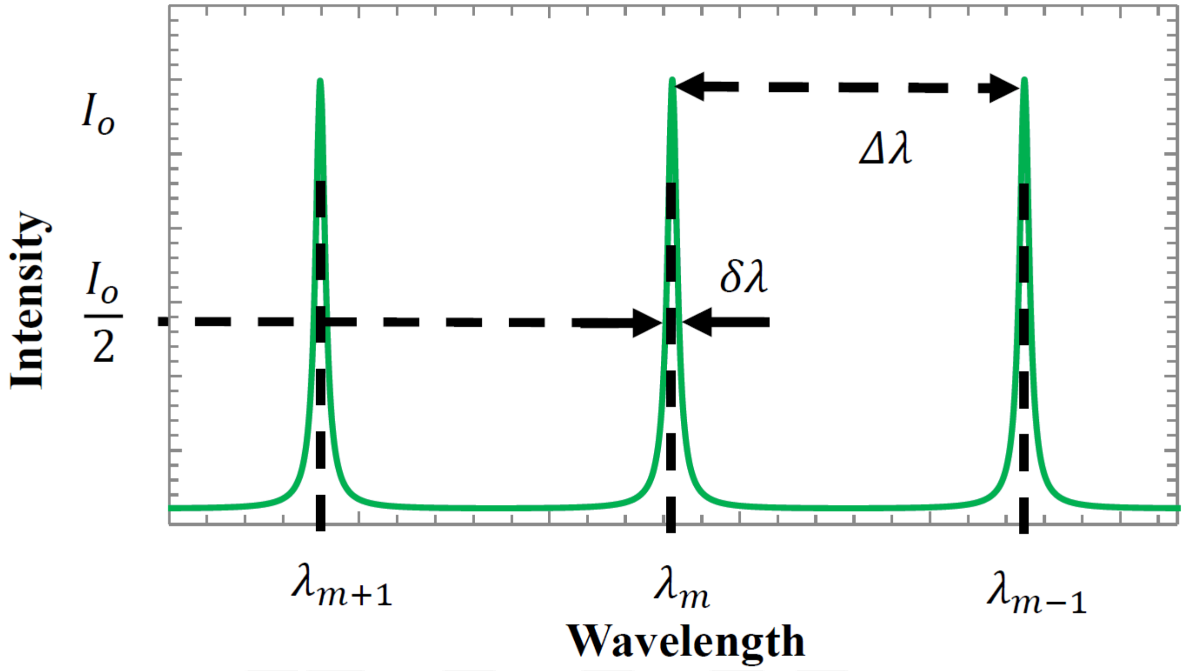

Figure 2.3-3: Representation of the Q-factor for a Fabry-Pérot etalon.

Free Spectral Range (FSR)

Free Spectral Range is defined as the frequency or wavelength difference between the mth and m+1th peaks of the same mode.

FSR is calculated as the following,

$$\mathrm{FSR} = \Delta\nu = \frac{c}{RTPL} = \frac{1}{T_R}$$

$$\mathrm{RTPL} = nL$$

In here c is the speed of light in vacuum, Δν is the frequency difference of two consecutive modes, RTPL is the round-trip path length, L is the total length of the resonator and nL gives the RTPL in the resonator itself, and T_R is the round-trip time.

FSR can also be calculated for high Q-factors as following,

$$\mathrm{FSR} = \Delta\lambda = \frac{\lambda^2}{RTPL} = \frac{\lambda^2}{cT_R}$$

Figure 2.3-4 shows the illustration of the FSR for a Fabry-Pérot etalon.

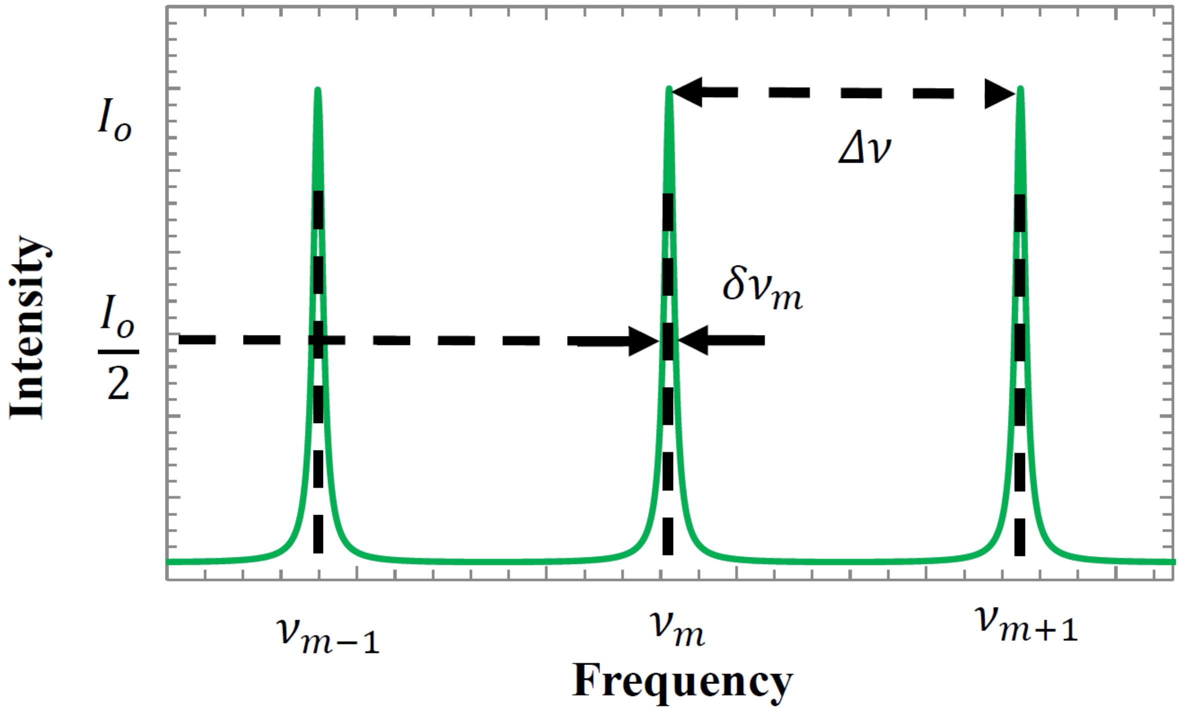

Figure 2.3-4: Representation of the free spectral range (FSR) with respect to frequency.

Mode Split

Mode split is the frequency/wavelength difference between two split/distinct modes with the same mode number. In optical resonator mod split occurs due to the coupling perturbations in the cavity often caused from coupling points inside the cavity itself or coupling with the other elements, backscattering, and defects. This phenomenon occurs when there is more than one optical round-trip path length in the cavity, such as clockwise and counterclockwise modes in the cavity may follow different paths and creates peaks with different FSR and thus with different central wavelength/frequency. Mode splitting is commonly observed in whispering gallery modes which modes with different path lengths can occur, and micro resonators. Figure 2.3-5 shows the representation for mode split in a cavity with two split modes.

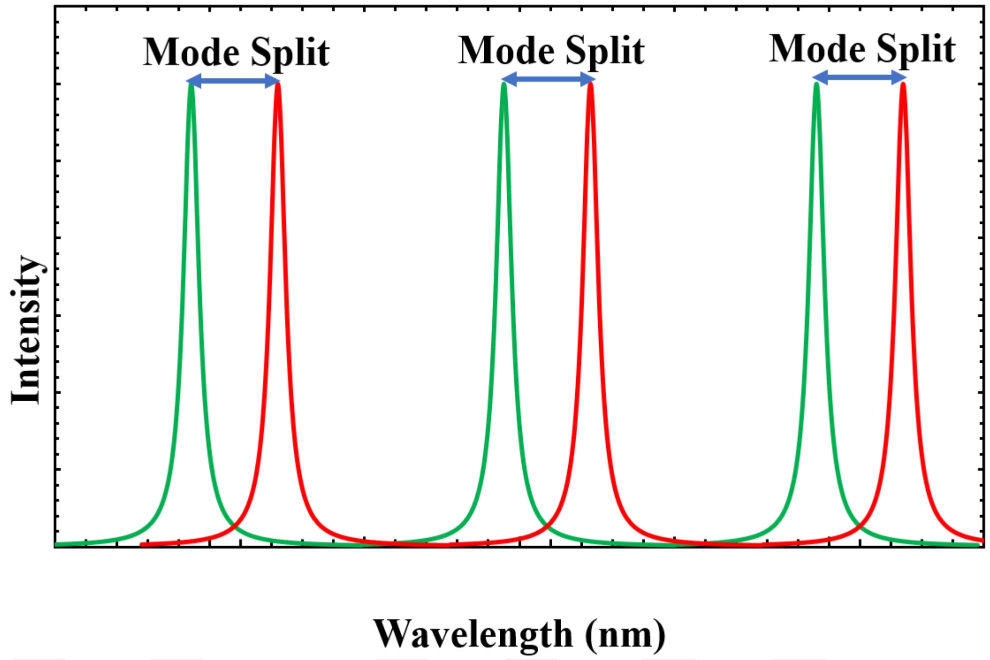

Figure 2.3-5: The representation of mode split in a resonator with two cavity modes.

Extinction Ratio

Extinction ratio is defined as the difference level between high (1) and low (0) levels of a system.

$$ER = \frac{I_{high}}{I_{low}}$$

Figure 2.3-6 shows the representation of the extinction ratio for a Fabry-Pérot Etalon.

Slope Rate

The slope rate is defined as the amount of change for a peak or dip per frequency/or wavelength unit change in resonators. Figure 2.3-6 shows the representation of the slope rate for a Fabry-Pérot Etalon.

Insertion Loss

Insertion loss is defined as the experienced loss when coupling from one system to another. Figure 2.3-6 shows the illustration of IL for a Fabry-Pérot Etalon.

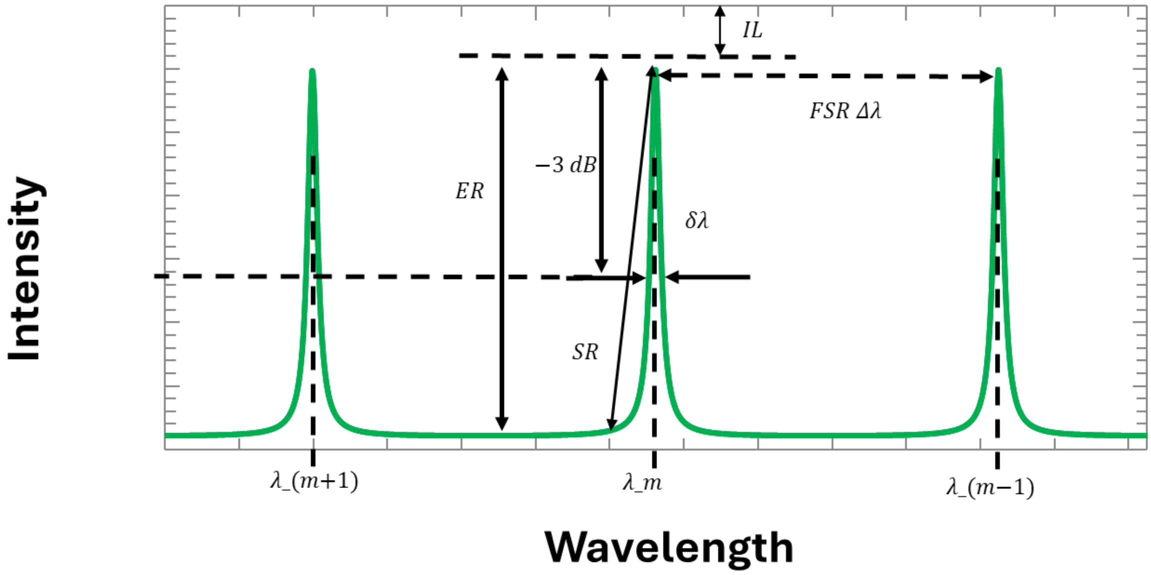

Figure 2.3-6: Representation of figures of merits (FOMs), ER (Extinction Ratio), slope rate (SR), Q-factor, free spectral range (FSR), insertion loss (IL), and their illustrations for a Fabry-Pérot resonator.

2.4. Measurement Setup

Experimental measurement spectra are achieved with an automated setup in the University of British Columbia, the light is injected with an Agilent tunable laser from 1480 nm to 1580 nm. Experimental transmission spectra are acquired by a custom-built automated setup [113], which is controlled by a Python automated control open-sourced software [114]. Inputs and outputs are obtained by a polarization maintaining four fiber ribbon arrays [115], containing optical fibers placed 127 μm apart. Input is provided at the second fiber in the array, by an Agilent 81600B tunable laser source, swept between 1500 to 1580 nm with 10 pm steps. The optical structures on the silicon photonic integrated chip (Si-PIC) have four grating couplers 127 μm apart to match the spacing of the fiber ribbon array. The fibers are polished with an 8° angle to match the surface grating couplers. The outputs are obtained at fibers 1, 3, and 4 in the fiber ribbon array connected to Agilent 81635A detectors to detect the output light. Figure 2.4-1 shows the schematic of the experimental setup which the measurements are taken. Extension on the right side of Figure 2.4-1 shows the magnified schematic of the Si-PIC interface for one structure the, with the four grating couplers and the corresponding input and output fibers angled at 8°. A typical distance between the fiber ribbon array and the PIC is 5 μm to 50 μm. The device under test is changed for all of the structures and the measurements are repeated.

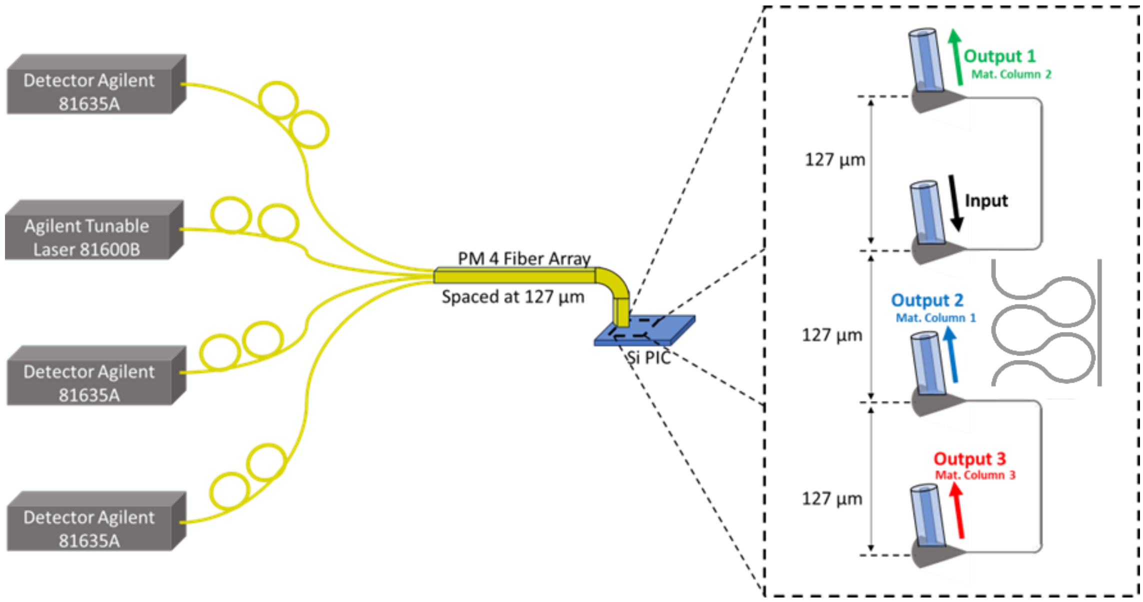

Figure 2.4-1:Schematic of the experimental setup used to take the measurements. The structures are designed to have 4 grating couplers spaced at 127 µm, with the fibers at 8° angle to couple light in or out of the structures. Input is given by an Agilent tunable laser 81600B scanned from 1500 nm to 1580 nm connected to the 2nd fiber, and the outputs are taken from first, third, and fourth fiber of the ribbon array connected to Agilent 81635A detectors. (Diagram with permission from Syed Sultan Shah Bukhari)

Figure 2.4-2 shows the experimental measurement setup with addressing and the KLayout schematics of the proposed MLM structure with a magnified image of the device on the right side. The mentioned measurement procedure is repeated for SC-MR, DC-MR, DC-SMR, DC-AMR, DC-RMR.

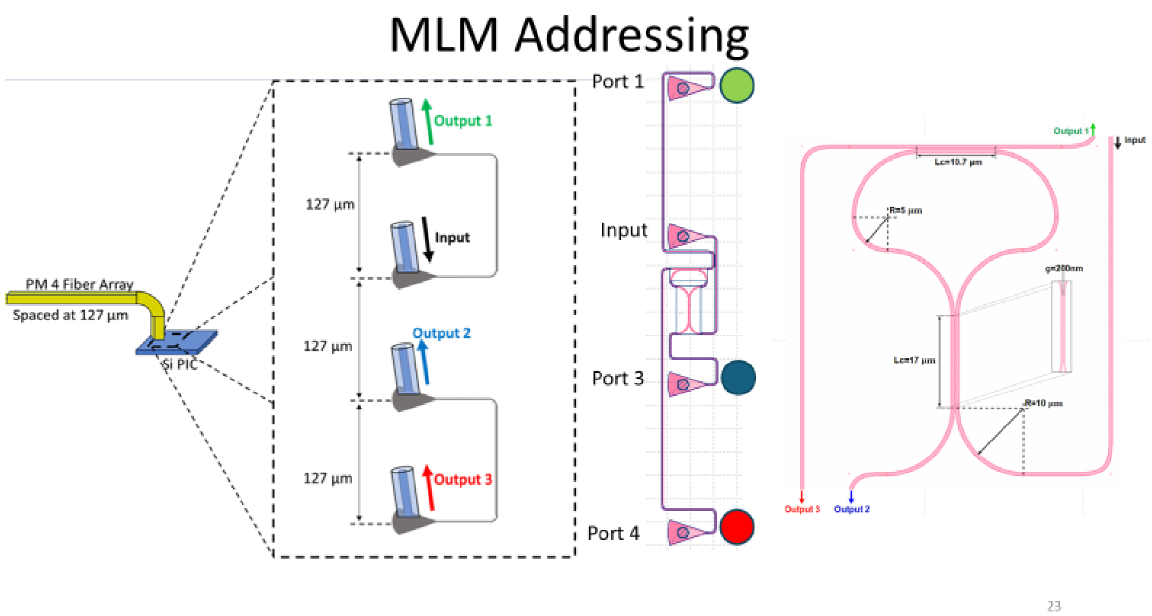

Figure 2.4-2: The experimental measurement setup with addressing of MLM, the same procedure is repeated for the other proposed structures.

Chapter 3

MEASUREMENTS AND ANALYSIS

3.1. Single Coupled MLM

The Meandering Loop Mirror (MLM) add-drop filter serves as the fundamental component of the other resonators. The MLM's architecture includes coupling points essential for generating resonances. All other structures are composed of two or more MLM add-drop filters and can be enhanced with more MLMs. Despite its integral role in configurations such as Double-MR, Reversed MR, Single Coupled MR, SMR, and AMR, the MLM add-drop filter alone cannot establish a resonant path. Figure 3.1-1 depicts the MLM add-drop filter's schematic and the Figure 3.1-2 shows its corresponding SEM image. Figure 3.1-3 shows the illustration of clockwise (CW) and counterclockwise (CCW) paths in MLM ADF. The output port numbering is given as the following, ports are numbered as 1,2,3,4 and a prefix is added if the port is used as an output port. For example, the input is always the port 2 and it is not numbered in the figures/text and mentioned only as input. On the other hand, output 1 means the first (upper most) grating coupler which is utilized as an output port, and the same is valid for output 3 and output 4. Figure 3.1-4 shows the KLayout design of the MLM ADF with the corresponding coupling dimensions and bend radii with their corresponding positions. The input and output ports of MLM ADF is shown in the same diagram with input in black, while output 1,2 and 3 is shown in green, blue, and red, respectively. The IC coupler has a coupling length of $Lc_{1=}$10.7 μm and the CC coupler has a coupling length of $Lc_{2=}$17 μm (specific to chosen design). The waveguides have a bending radius of 5 μm while the couplers' bending radius is 10 μm, the gap between the bus waveguides in the couplers is shown as g=200 nm. The coupler bending radius of 10 μm, the waveguide bending radius of 5 μm and the gap between the coupler waveguides g=200 nm is constant in all designs. In the figures of MLM response spectra the grating coupler response and the back reflections are visible. Figure 3.1-5 to Figure 3.1-14 shows the spectral response of the MLM, first figures of the MLM with the same coupling length shows the spectral range from 1500 nm to 1580 nm and the second figures of the same MLM shows the range from 1510 nm to 1520 nm.

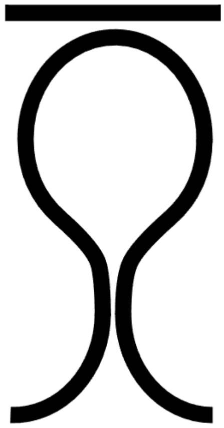

Figure 3.1-1: MLM add drop filter representation.

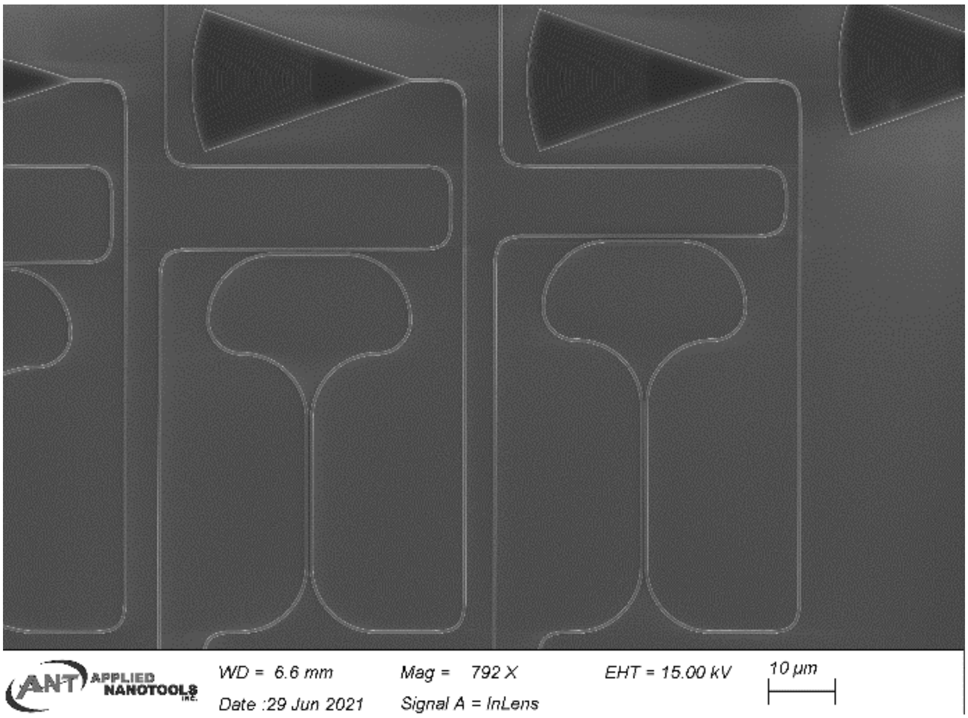

Figure 3.1-2: The SEM image of the fabricated MLM add-drop filter

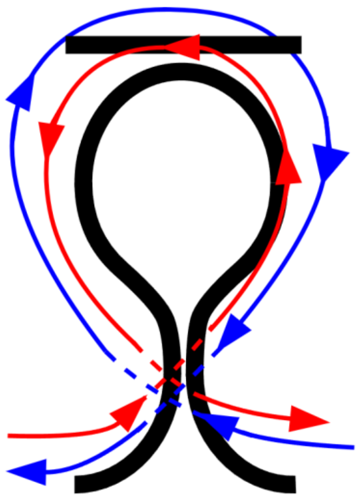

Figure 3.1-3: Representation of clockwise and counterclockwise paths in MLM add-drop filter in blue, and red, respectively.

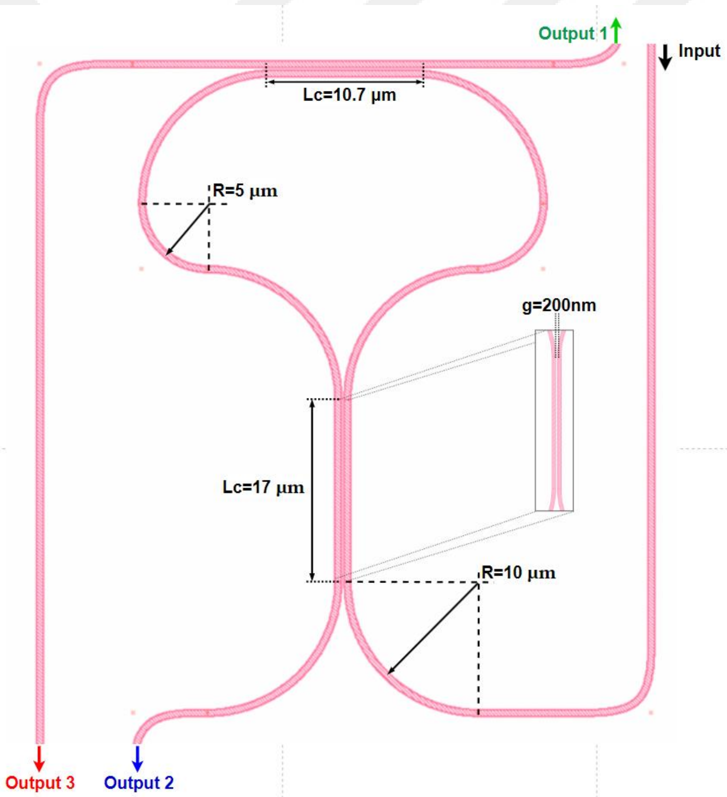

Figure 3.1-4: Representation of MLM ADF with input in black, output 1,2 and 3 is shown in green, blue, and red, respectively. The IC coupler has a coupling length of Lc_{1}=10.7 µm and the CC coupler has Lc_{2}=17 µm (specific to chosen design), waveguides have a bending radius of 5 µm while the couplers' bending radius is 10 µm, the gap between the bus waveguides in the couplers is g=200 nm.

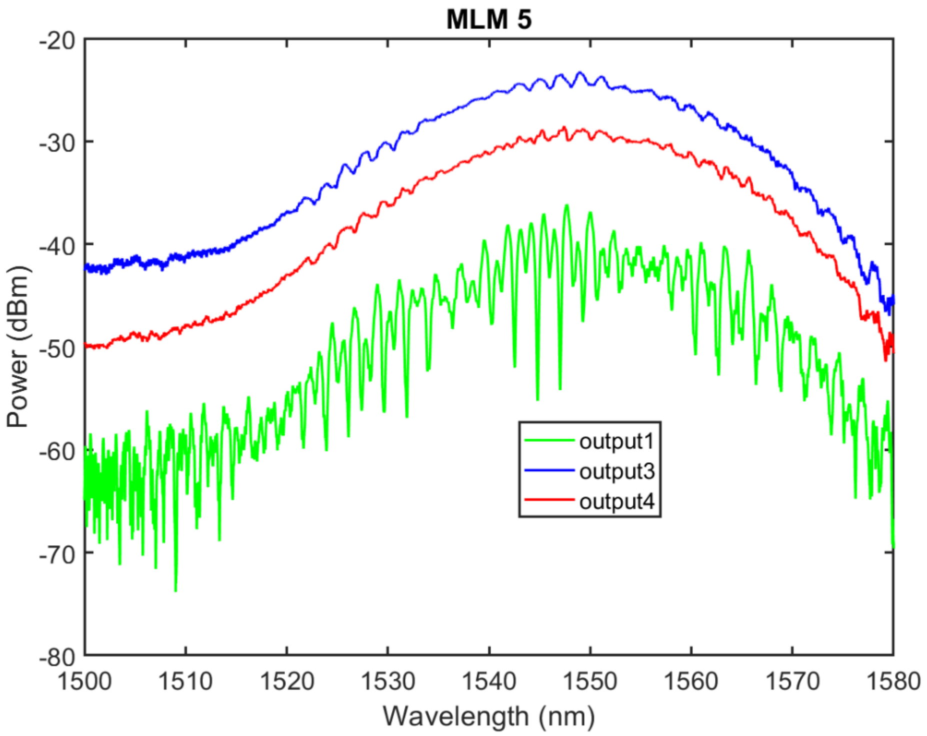

Figure 3.1-5: The experimentally measured spectra of MLM from 1500 nm to 1580 nm with Lc_1=10.7 µm and Lc_2=5 µm. The output ports 1, 3 and 4 are shown in green, blue, and red, respectively.

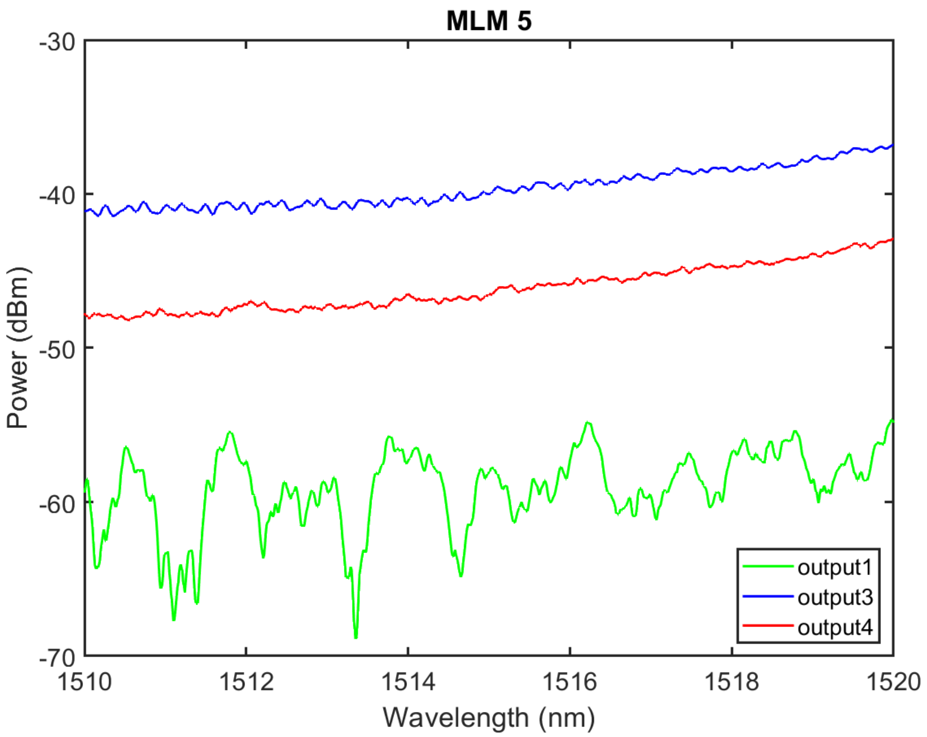

Figure 3.1-6: The experimentally measured spectra of MLM from 1510 nm to 1520 nm with Lc_1=10.7 µm and Lc_2=5 µm. The output ports 1, 3 and 4 are shown in green, blue, and red, respectively.

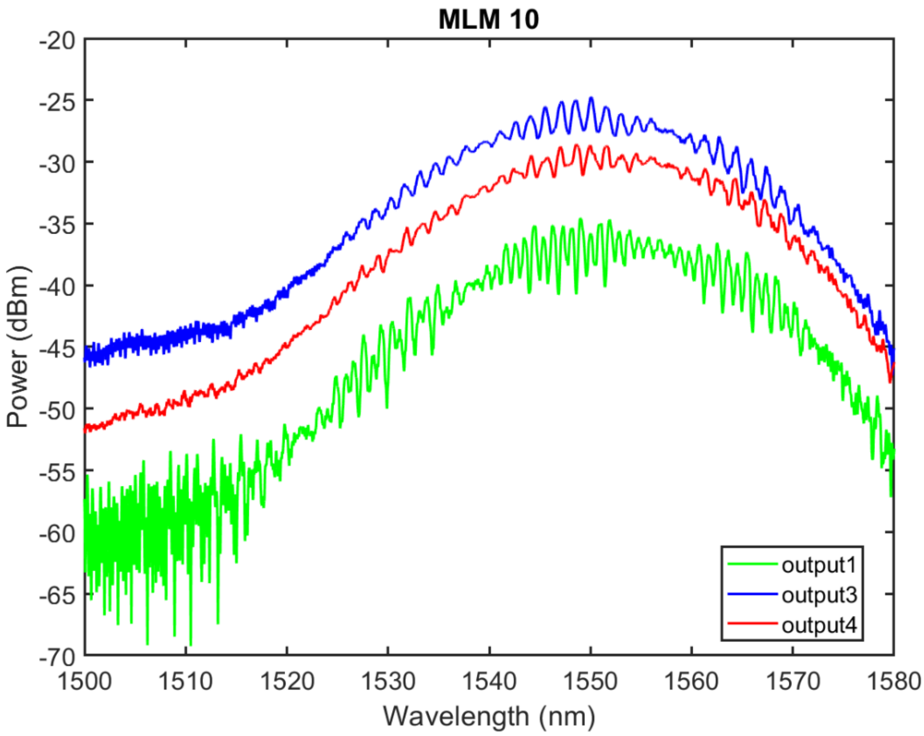

Figure 3.1-7: The experimentally measured spectra of MLM from 1500 nm to 1580 nm with Lc_1=10.7 µm and Lc_2=10 µm. The output ports 1, 3 and 4 are shown in green, blue, and red, respectively.

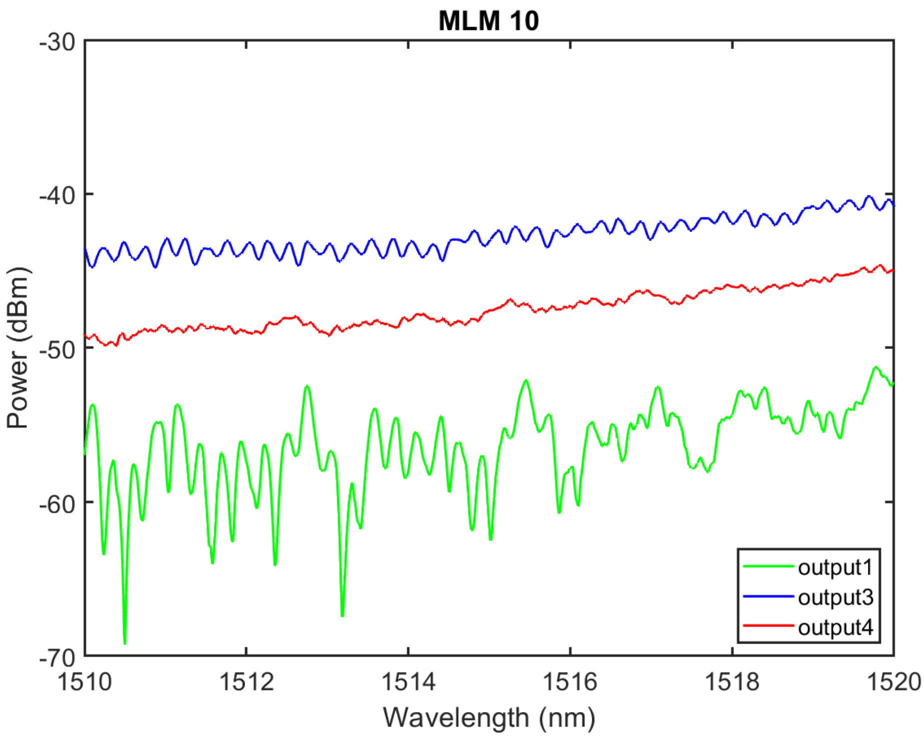

Figure 3.1-8: The experimentally measured spectra of MLM from 1510 nm to 1520 nm with Lc_1=10.7 µm and Lc_2=10 µm. The output ports 1, 3 and 4 are shown in green, blue, and red, respectively.

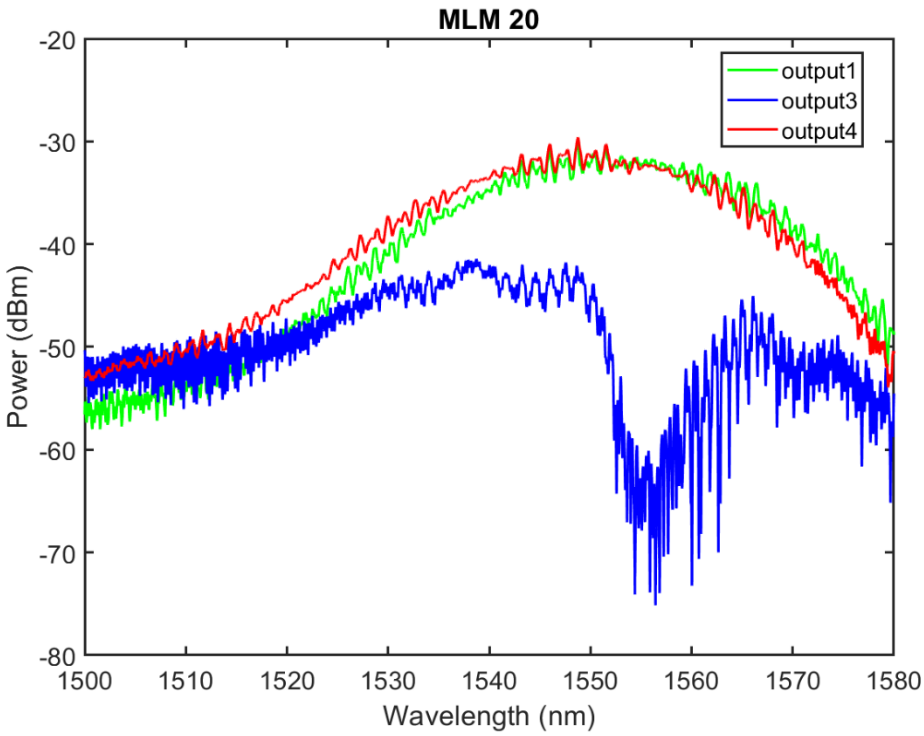

Figure 3.1-9: The experimentally measured spectra of MLM from 1500 nm to 1580 nm with Lc_1=10.7 µm and Lc_2=20 µm. The output ports 1, 3 and 4 are shown in green, blue, and red, respectively.

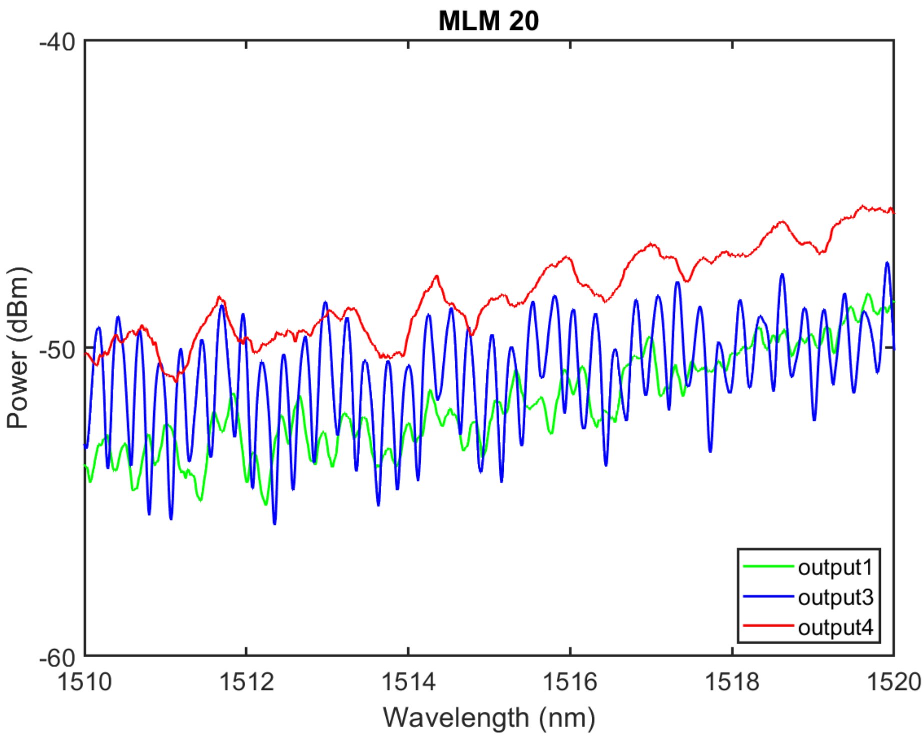

Figure 3.1-10: The experimentally measured spectra of MLM from 1510 nm to 1520 nm with Lc_1=10.7 µm and Lc_2=20 µm. The output ports 1, 3 and 4 are shown in green, blue, and red, respectively.

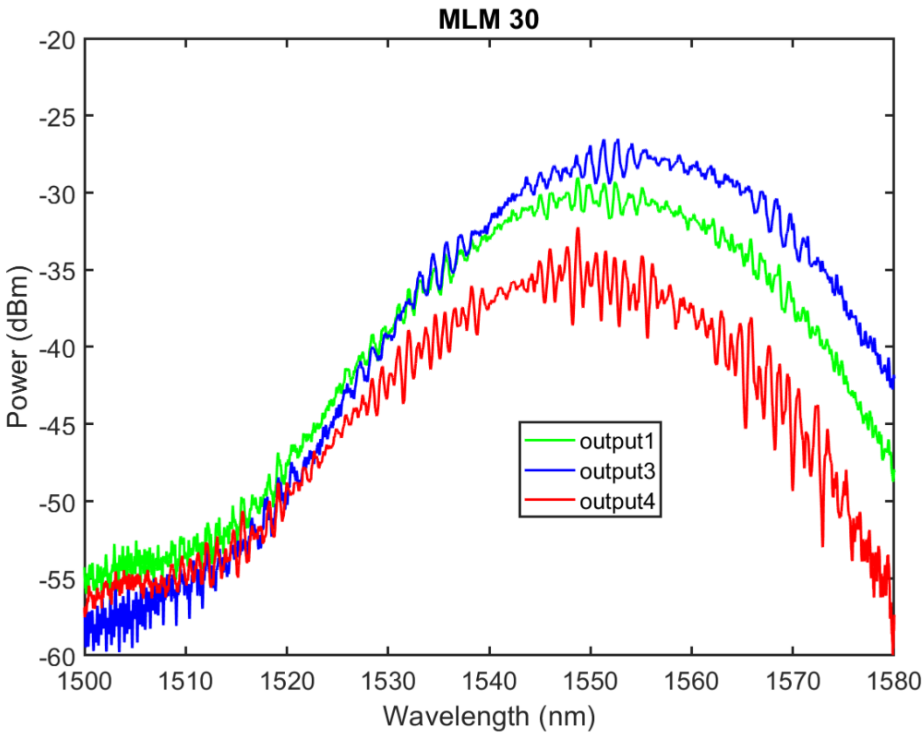

Figure 3.1-11 The experimentally measured spectra of MLM from 1500 nm to 1580 nm with Lc_1=10.7 µm and Lc_2=30 µm. The output ports 1, 3 and 4 are shown in green, blue, and red, respectively.

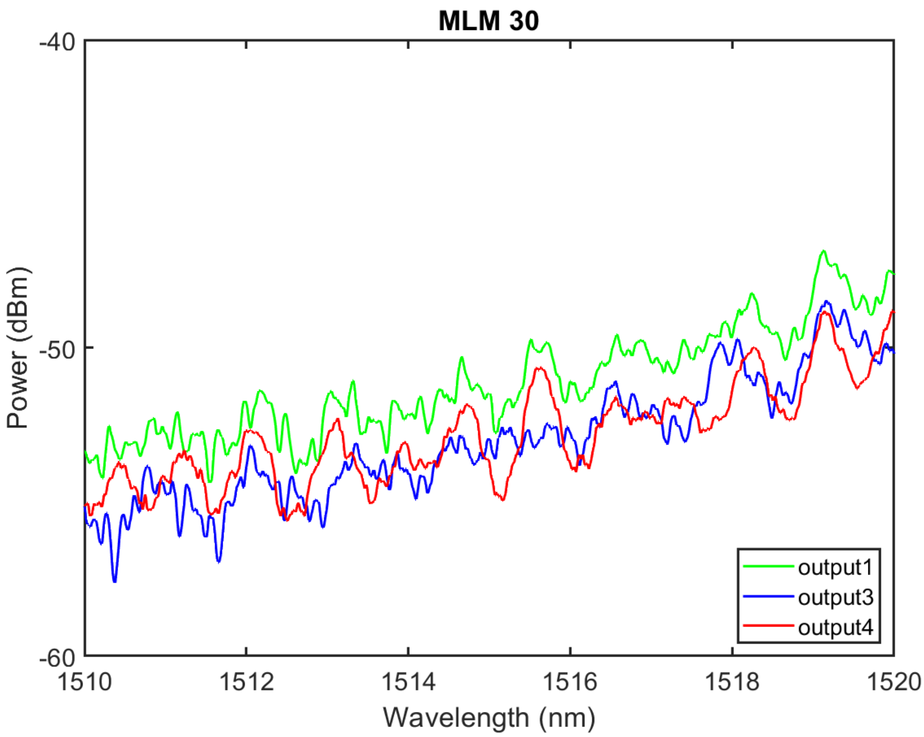

Figure 3.1-12: The experimentally measured spectra of MLM from 1510 nm to 1520 nm with Lc_1=10.7 µm and Lc_2=30 µm. The output ports 1, 3 and 4 are shown in green, blue, and red, respectively.

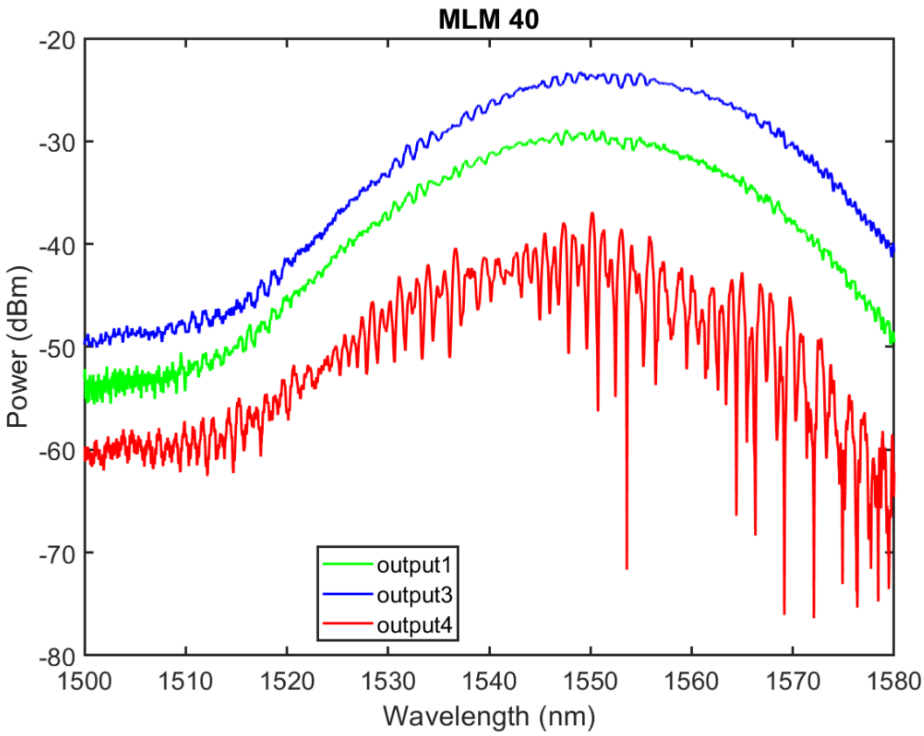

Figure 3.1-13: The experimentally measured spectra of MLM from 1500 nm to 1580 nm with Lc_1=10.7 µm and Lc_2=40 µm. The output ports 1, 3 and 4 are shown in green, blue, and red, respectively.

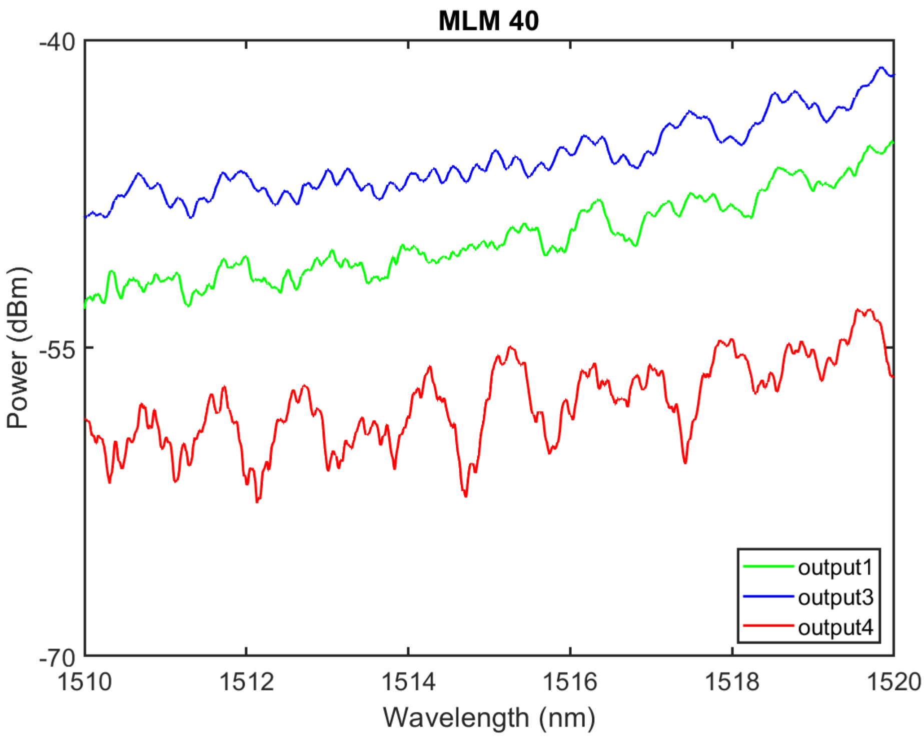

Figure 3.1-14: The experimentally measured spectra of MLM from 1510 nm to 1520 nm with Lc_1=10.7 µm and Lc_2=5 µm. The output ports 1, 3 and 4 are shown in green, blue, and red, respectively.

3.2. Single Coupled MR ADF

The single coupled MR (SC-MR) add-drop filter (ADF) is fabricated to see the effect of the second meandering resonator in the optical path by adding one more coupling point coming from the second MLM which is reversed to increase the layout efficiency due to the size limitations. The coupling length L_c of the (SC-MR) IC coupler is 10.7 µm and the IC coupler length is kept constant in all designs of SC-MR ADF and the FSR of the resonator can be calculated with $FSR = \frac{\lambda^2}{n_g L}$. Figure 3.2-1 shows the representation of SC-MR ADF and Figure 3.2-2 shows the SEM image of the SC-MR ADF. Figure 3.2-3 shows the KLayout design of the SC-MR ADF given with the corresponding coupling dimensions and bend radii with the positions of the input and output ports, Single Coupled MR with input shown in black, output 1,2 and 3 is shown in green, blue, and red, respectively. The IC coupler has a coupling length of Lc_{1}=10.7 µm and the CC coupler has a coupling length of Lc_{2}=17 µm (specific to chosen design), waveguides have a bending radius of 5 µm while the couplers' bending radius is 10 µm, the gap between the bus waveguides in the couplers is g=200 nm. The coupler bending radius of 10 µm, the waveguide bending radius of 5 µm and the gap between the coupler waveguides g=200 nm is constant in all designs.

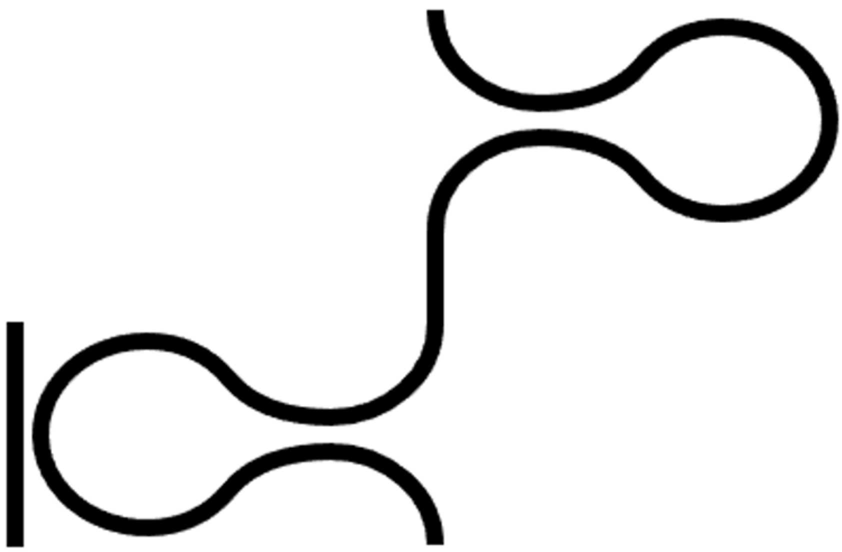

Figure 3.2-1: Representation of SC-MR ADF.

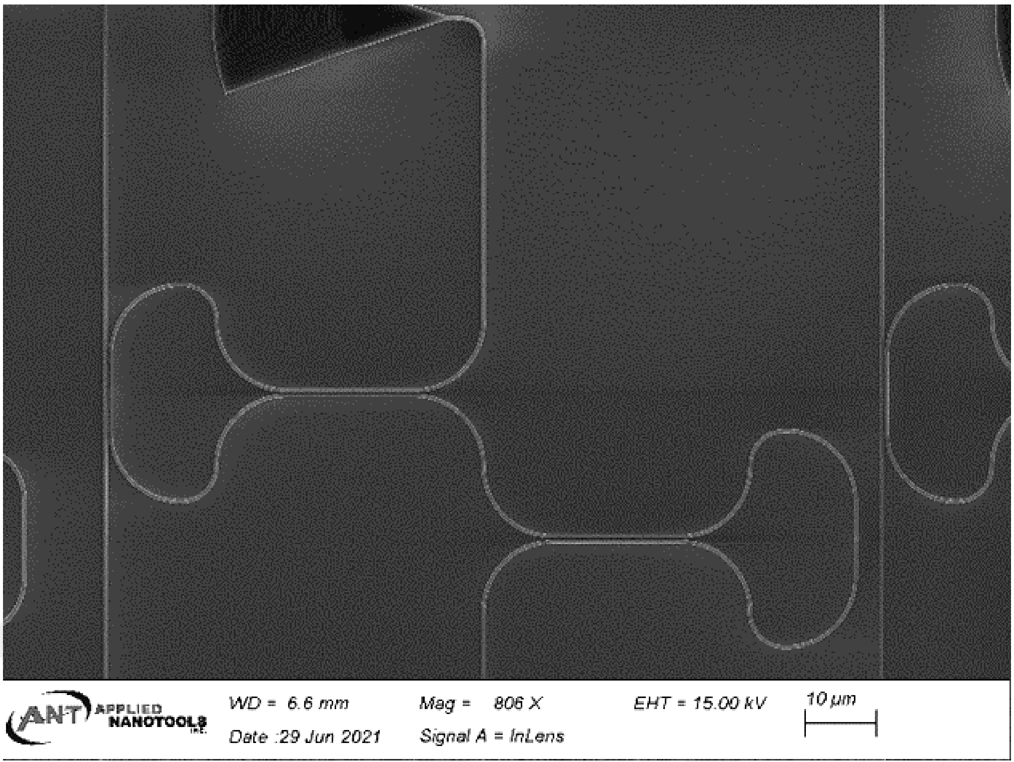

Figure 3.2-2: SEM image of the fabricated Single Coupled MR add-drop filter

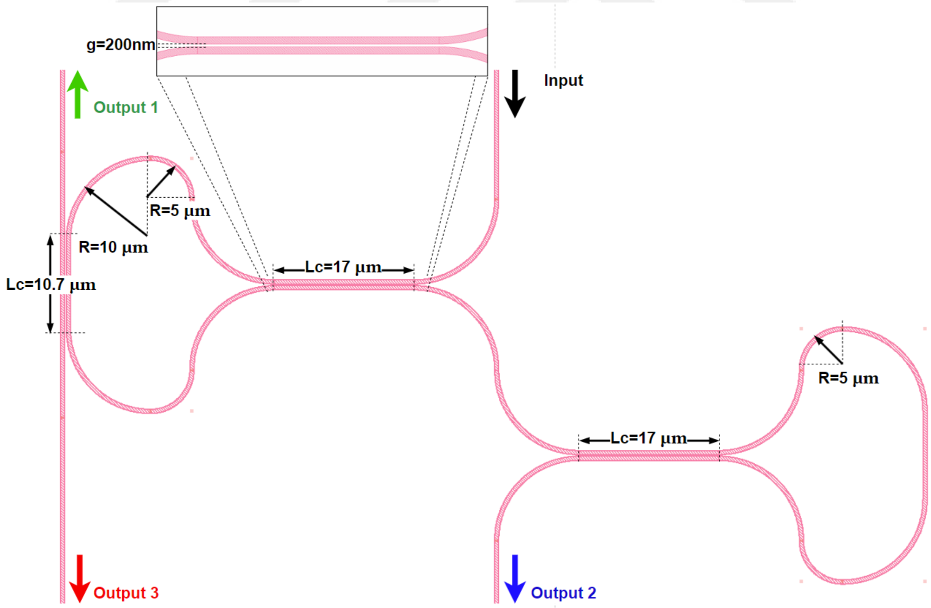

Figure 3.2-3 Representation of Single Coupled MR with output input in black, output 1,2 and 3 is shown in green, blue, and red, respectively. The IC coupler has a coupling length of Lc_{1}=10.7 µm and the CC coupler has Lc_{2}=17 µm (specific to chosen design), waveguides have a bending radius of 5 µm while the couplers' bending radius is 10 µm, the gap between the bus waveguides in the couplers is g=200 nm.

SC-MR ADF with Lc_2=17 µm

Figure 3.2-4 shows the experimentally measured spectra of SC-MR ADF from 1500 nm to 1580 nm with Lc_1=10.7 µm and Lc_2=17 µm. The output ports 1, 3 and 4 are shown in green, blue, and red, respectively. Figure 3.2-5 shows the experimentally measured SC-MR ADF spectra from 1510 nm to 1520 nm with Lc_1=10.7 µm and Lc_2=17 µm. The output ports 1, 3 and 4 are shown in green, blue, and red, respectively. The FSR of the spectra is 1.78 nm. Figure 3.2-6 shows the experimentally measured SC-MR ADF spectra of output 1 from 1516 nm to 1520 nm with Lc_1=10.7 µm and Lc_2=17 µm. The spectra have IL=17 dB, FSR=1.78 nm, the spectra show weak inverse Lorentzian lineshapes, hence the ER, SR and Q-factor calculation is not made for the output 1. Figure 3.2-7 shows the experimentally measured SC-MR ADF spectra of the output 3 from 1516 nm to 1520 nm with Lc_1=10.7 µm and Lc_2=17 µm. The spectra have Lorentzian lineshapes with IL=11 dB, FSR= 1.78 nm, best Q-factor of $9\cdot10^3$, ER=12 dB and SR=38 dB/nm. Figure 3.2-8 shows the experimentally measured SC-MR ADF spectra of the output 4 from 1516 nm to 1520 nm with coupling lengths of Lc_1=10.7 µm and Lc_2=17 µm. The spectra have IL=11 dB, FSR=1.78 nm, ER=5.6 dB, SR= 23 dB/nm.

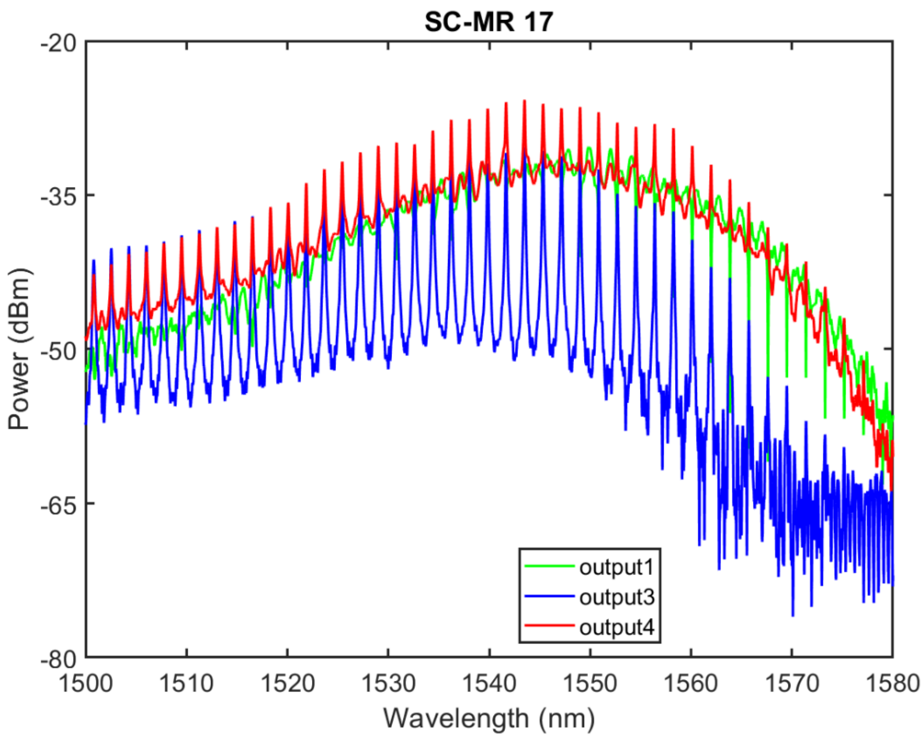

Figure 3.2-4: The experimentally measured SC-MR spectra from 1500 nm to 1580 nm with coupling lengths of Lc_1=10.7 µm and Lc_2=17 µm. The output ports 1, 3 and 4 are shown in green, blue, and red, respectively.

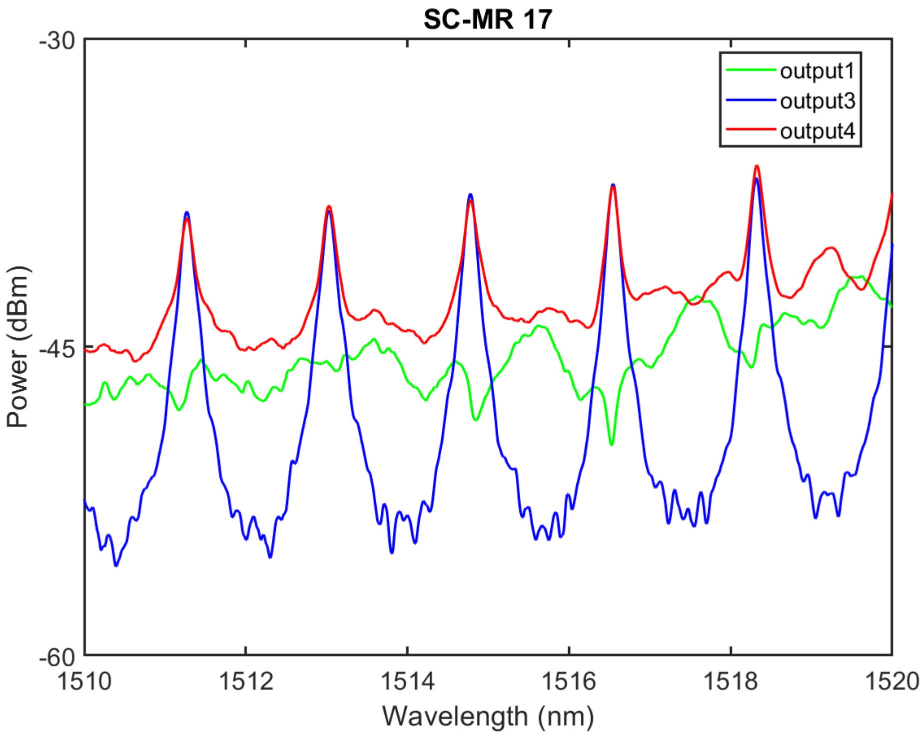

Figure 3.2-5 The experimentally measured SC-MR spectra from 1510 nm to 1520 nm with coupling lengths of Lc_1=10.7 µm and Lc_2=17 µm. The output ports 1, 3 and 4 are shown in green, blue, and red, respectively. The FSR of the spectra is 1.78 nm.

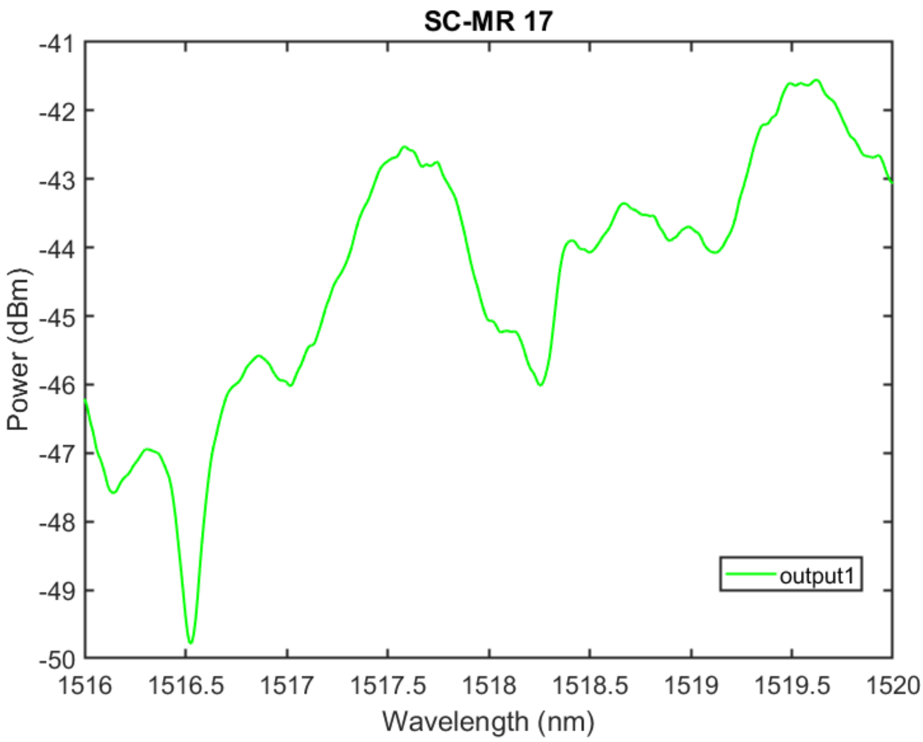

Figure 3.2-6 The experimentally measured SC-MR ADF spectra of output 1 from 1516 nm to 1520 nm with Lc_1=10.7 µm and Lc_2=17 µm. The spectra have IL=17 dB, FSR=1.78 nm.

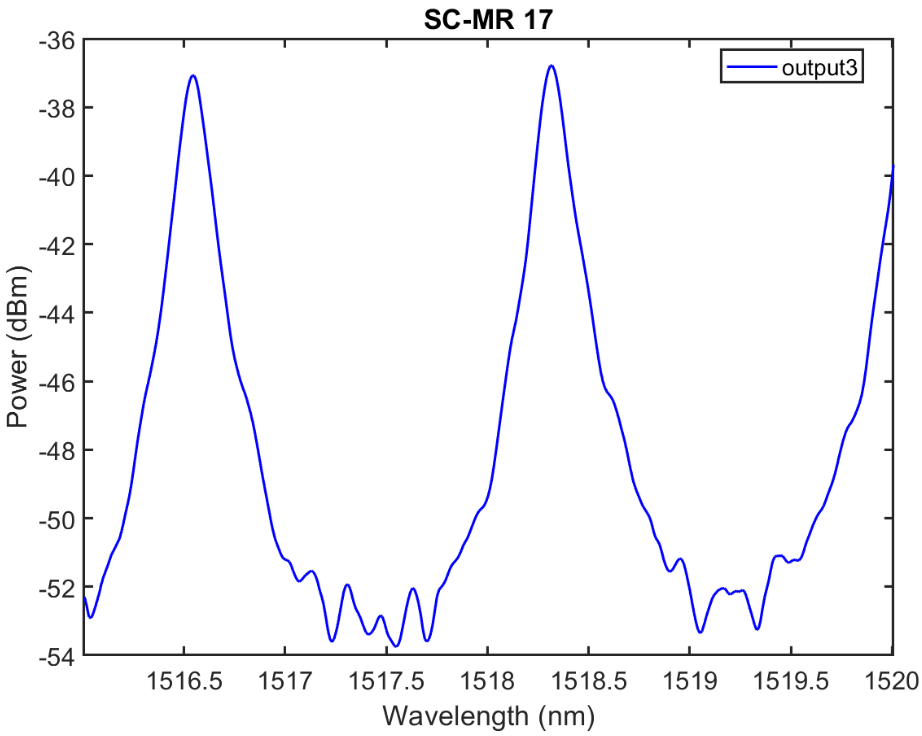

Figure 3.2-7: The experimentally measured SC-MR ADF spectra of the output 3 from 1516 nm to 1520 nm with Lc_1=10.7 μm and Lc_2=17 μm. The spectra have IL=11 dB, FSR= 1.78 nm, best Q-factor of 9·103, ER=12 dB and SR=38 dB/nm.

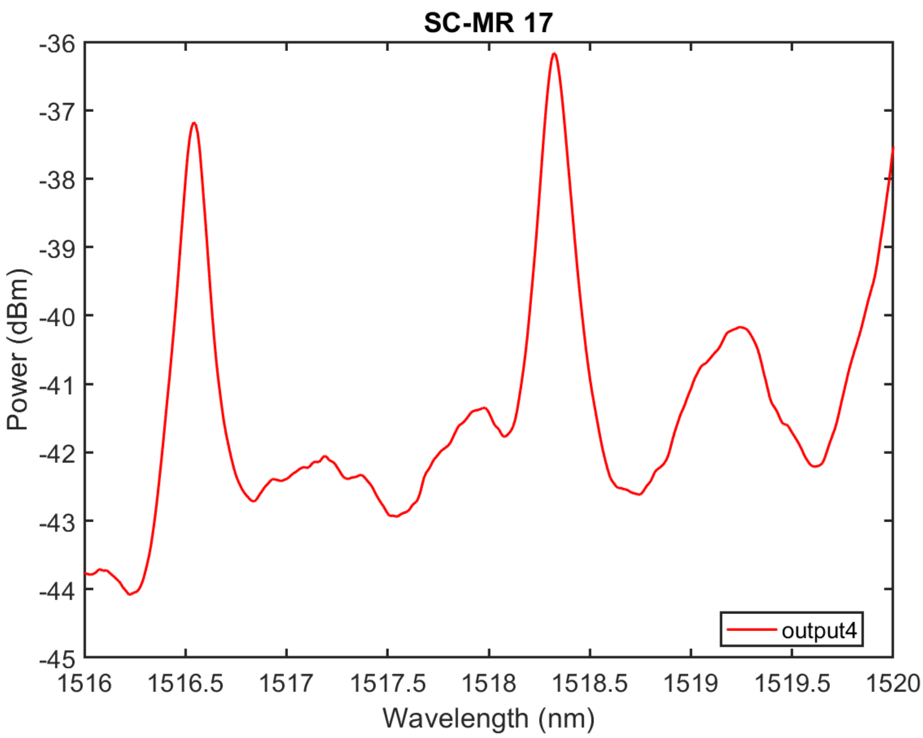

Figure 3.2-8: The experimentally measured SC-MR ADF spectra of the output 4 from 1516 nm to 1520 nm with coupling lengths of Lc_1=10.7 μm and Lc_2=17 μm. The spectra have IL=11 dB, FSR=1.78 nm, ER=5.6 dB, SR= 23 dB/nm

SC-MR ADF with Lc_2=18 µm

Figure 3.2-9 shows the experimentally measured spectra of SC-MR ADF from 1500 nm to 1580 nm with Lc_1=10.7 µm and Lc_2=18 µm. The output ports 1, 3 and 4 are shown in green, blue, and red, respectively. Figure 3.2-10 shows the experimentally measured SC-MR ADF spectra from 1510 nm to 1520 nm with Lc_1=10.7 µm and Lc_2=18 µm. The output ports 1, 3 and 4 are shown in green, blue, and red, respectively. The FSR of the spectra is 1.75 nm. Figure 3.2-11 shows the experimentally measured SC-MR ADF spectra of output 1 from 1516 nm to 1520 nm with Lc_1=10.7 µm and Lc_2=18 µm. The spectra have IL=11 dB, FSR=1.75 nm, ER=4.2 dB, SR=18 dB/nm, the spectra show weak inverse Lorentzian lineshapes, hence the Q-factor calculation is not made for the output 1. Figure 3.2-12 shows the experimentally measured SC-MR ADF spectra of the output 3 from 1516 nm to 1520 nm with Lc_1=10.7 µm and Lc_2=18 µm. The spectra have IL=6 dB, FSR= 1.75 nm, best Q-factor of $1.08 \cdot 10^4$, ER=15 dB and SR=36 dB/nm. Figure 3.2-13 shows the experimentally measured SC-MR ADF spectra of the output 4 from 1516 nm to 1520 nm with coupling lengths of Lc_1=10.7 µm and Lc_2=18 µm. The spectra have IL=9 dB, FSR=1.75 nm, ER=7.8 dB, SR= 17 dB/nm.

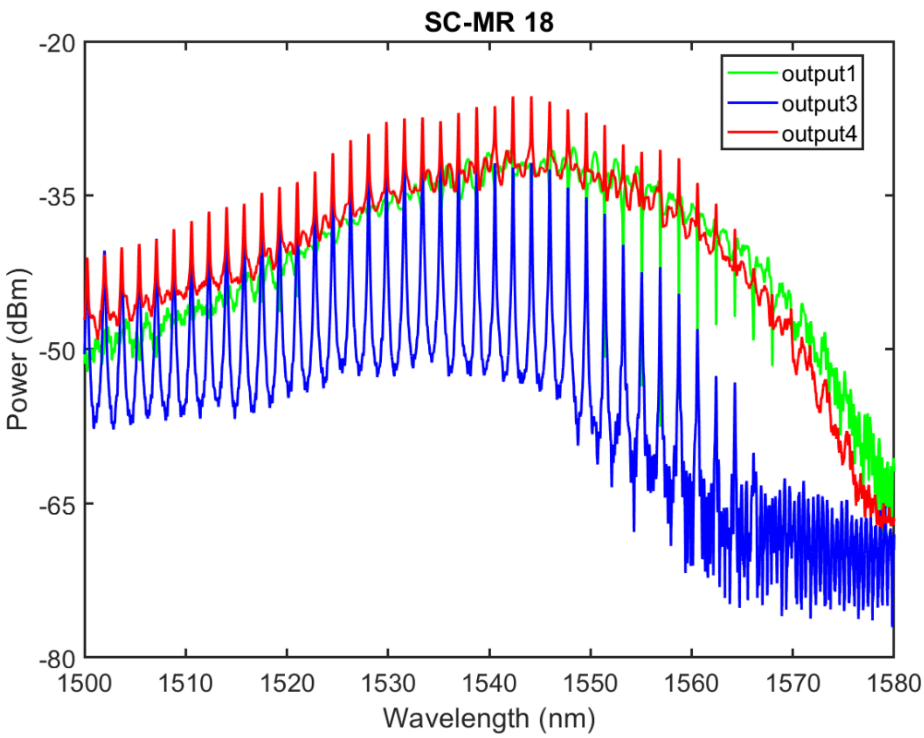

Figure 3.2-9: The resonant spectra for SC-MR structure Lc_1=10.7 µm and Lc_2=18 µm. The output ports 1, 3 and 4 are shown in green, blue, and red, respectively.

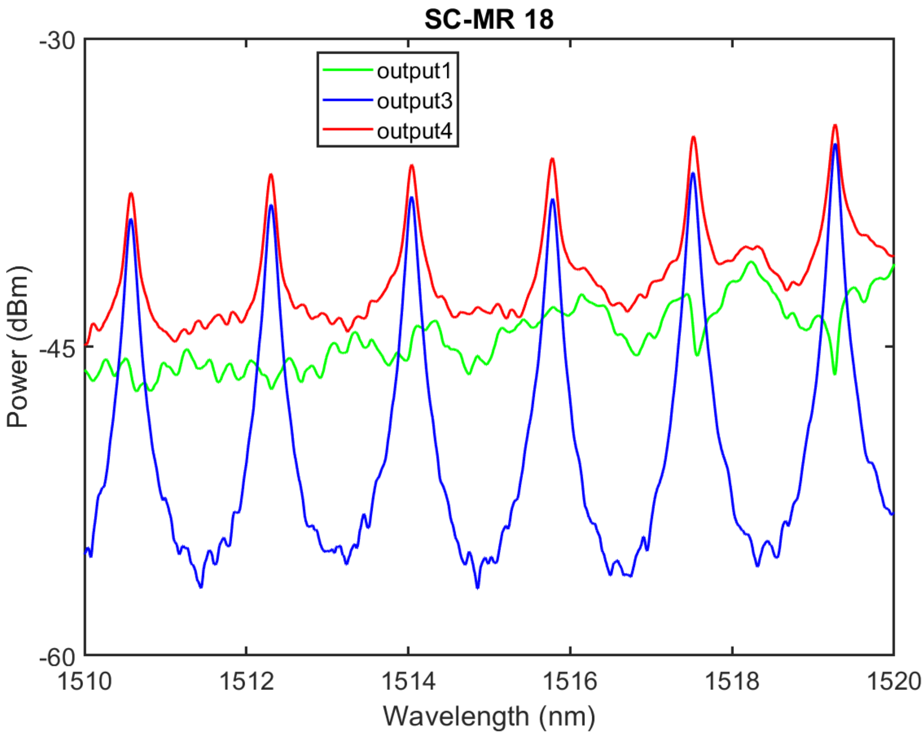

Figure 3.2-10: The experimentally measured SC-MR ADF spectra from 1510 nm to 1520 nm with Lc_1=10.7 µm and Lc_2=18 µm. The output ports 1, 3 and 4 are shown in green, blue, and red, respectively. The FSR of the spectra is 1.75 nm.

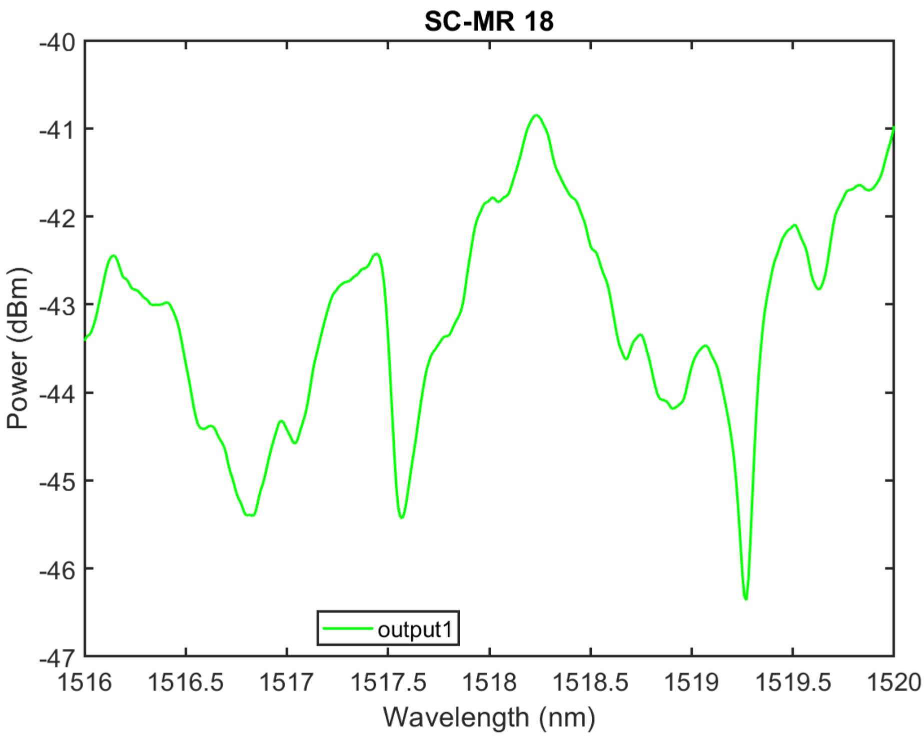

Figure 3.2-11: The experimentally measured SC-MR ADF spectra of output 1 from 1516 nm to 1520 nm with Lc_1=10.7 µm and Lc_2=18 µm. The spectra have IL=11 dB, FSR = 1.75 nm, ER = 4.2 dB, SR = 18 dB/nm.

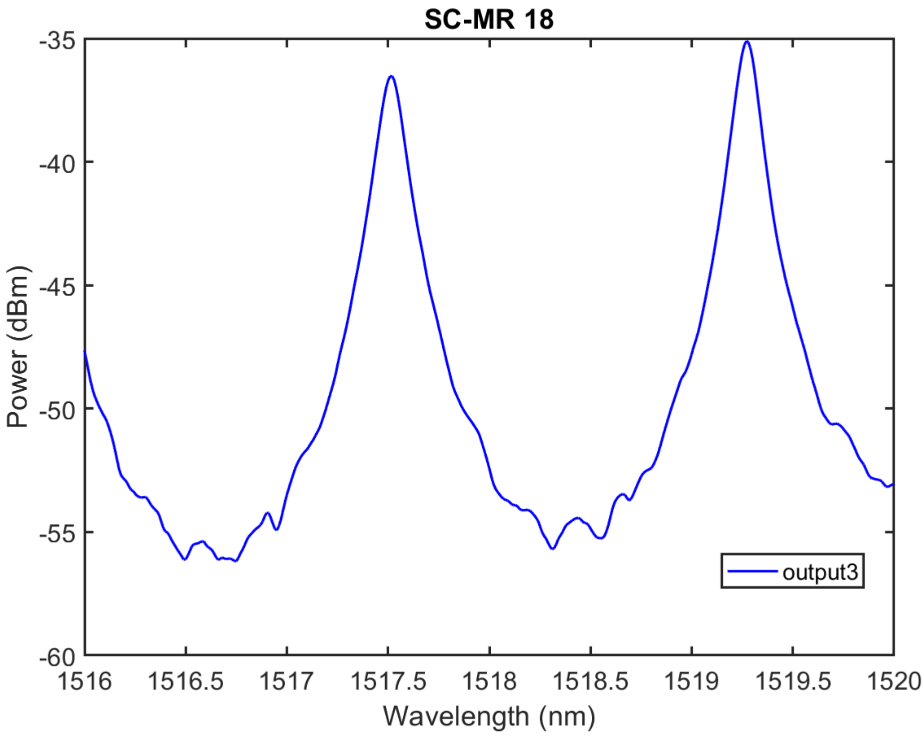

Figure 3.2-12: The experimentally measured SC-MR ADF spectra of the output 3 from 1516 nm to 1520 nm with Lc_1 = 10.7 μm and Lc_2 = 18 μm. The spectra have IL = 11 dB, FSR = 1.75 nm, best Q-factor of $1.08 \cdot 10^4$, ER = 15 dB, SR= 36 dB/nm.

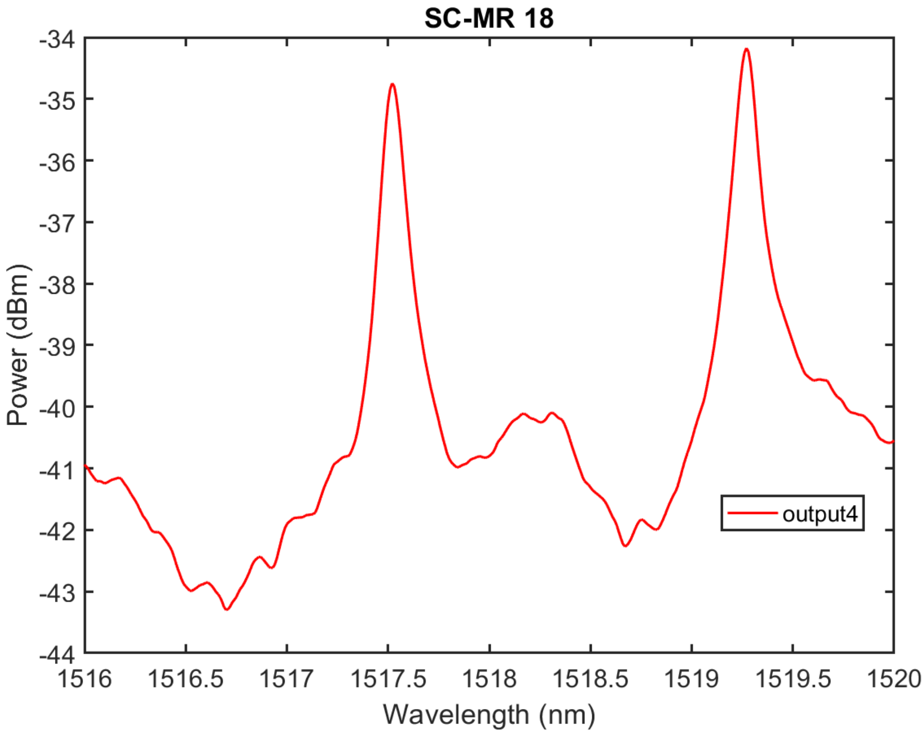

Figure 3.2-13: The experimentally measured SC-MR ADF spectra of the output 4 from 1516 nm to 1520 nm with coupling lengths of Lc_1=10.7 μm and Lc_2=18 μm. The spectra have IL=9 dB, FSR=1.75 nm, ER=7.8 dB, SR= 17 dB/nm

SC-MR ADF with Lc_2=19 µm

Figure 3.2-14 shows the experimentally measured spectra of SC-MR ADF from 1500 nm to 1580 nm with Lc_1=10.7 µm and Lc_2=18 µm. The output ports 1, 3 and 4 are shown in green, blue, and red, respectively. Figure 3.2-15 shows the experimentally measured SC-MR ADF spectra from 1510 nm to 1520 nm with Lc_1=10.7 µm and Lc_2=19 µm. The output ports 1, 3 and 4 are shown in green, blue, and red, respectively. The FSR of the spectra is 1.74 nm. Figure 3.2-16 shows the experimentally measured SC-MR ADF spectra of output 1 from 1516 nm to 1520 nm with Lc_1=10.7 µm and Lc_2=19 µm. The spectra have IL=13 dB, FSR=1.74 nm, ER=3 dB, SR=17 dB/nm, the spectra show weak inverse Lorentzian lineshapes, hence the Q-factor calculation is not made for the output 1. Figure 3.2-17 shows the experimentally measured SC-MR ADF spectra of the output 3 from 1516 nm to 1520 nm with Lc_1=10.7 µm and Lc_2=19 µm. The spectra have Lorentzian lineshapes with IL=19 dB, FSR= 1.74 nm, best Q-factor of $1.27 \cdot 10^4$, ER=20 dB and SR=45 dB/nm. Figure 3.2-18 shows the experimentally measured SC-MR ADF spectra of the output 4 from 1516 nm to 1520 nm with coupling lengths of Lc_1=10.7 µm and Lc_2=19 µm. The spectra have IL=9 dB, FSR=1.74 nm, ER=8 dB, SR= 22 dB/nm.

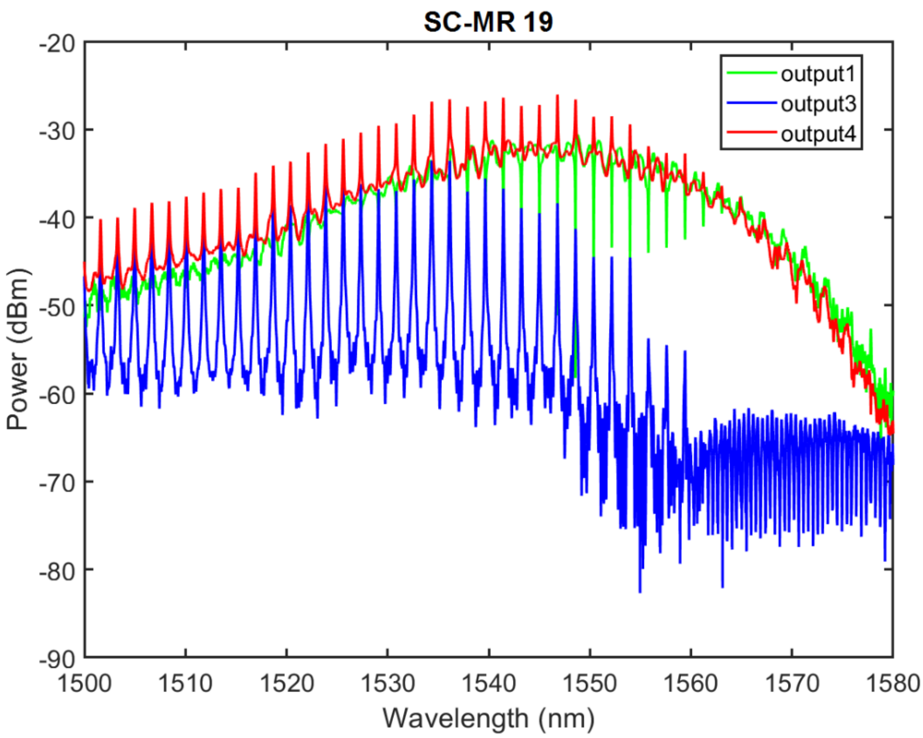

Figure 3.2-14: shows the experimentally measured spectra of SC-MR ADF from 1500 nm to 1580 nm with Lc_1=10.7 µm and Lc_2=18 µm. The output ports 1, 3 and 4 are shown in green, blue, and red, respectively.

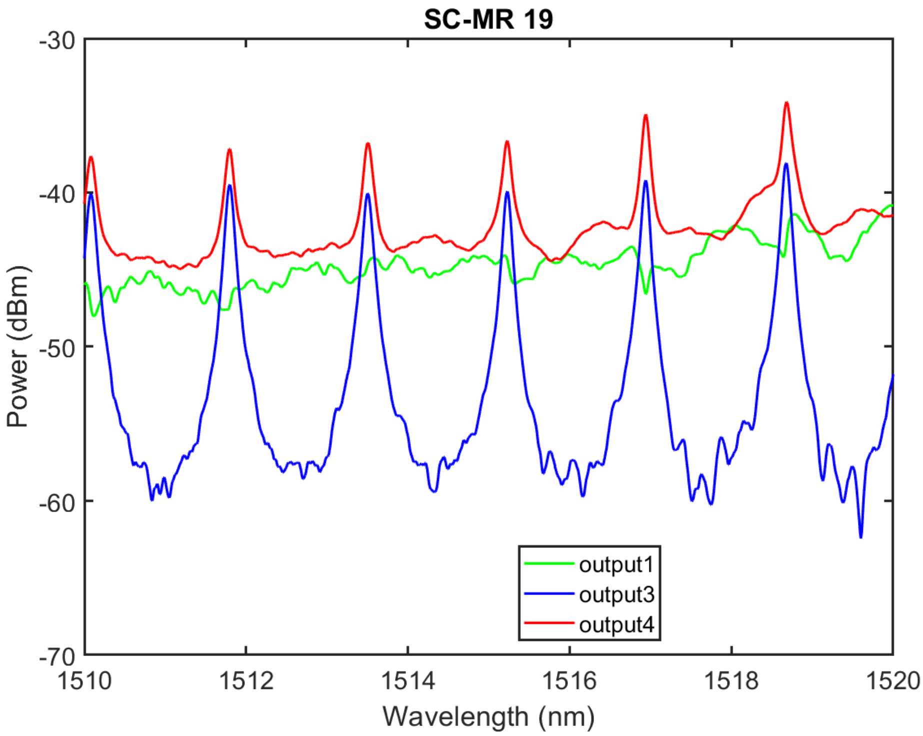

Figure 3.2-15: The experimentally measured SC-MR ADF spectra from 1510 nm to 1520 nm with Lc_1=10.7 μm and Lc_2=19 μm. The output ports 1, 3 and 4 are shown in green, blue, and red, respectively. The FSR of the spectra is 1.74 nm.

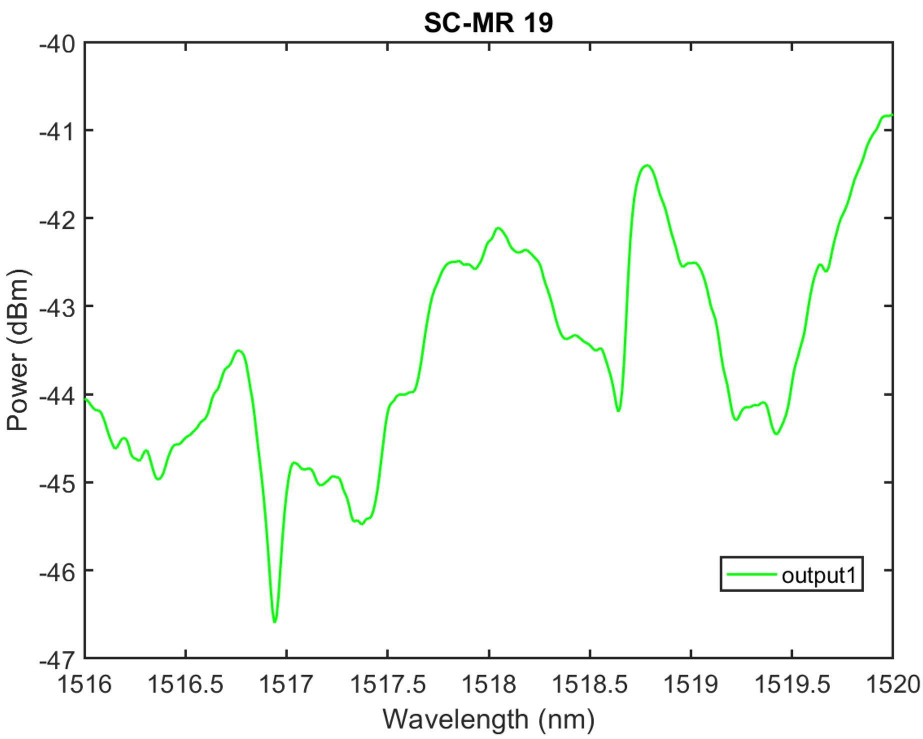

Figure 3.2-16: The experimentally measured SC-MR ADF spectra of output 1 from 1516 nm to 1520 nm with Lc_1=10.7 μm and Lc_2=19 μm. The spectra have IL=13 dB, FSR=1.74 nm, ER=3 dB, SR=17 dB/nm

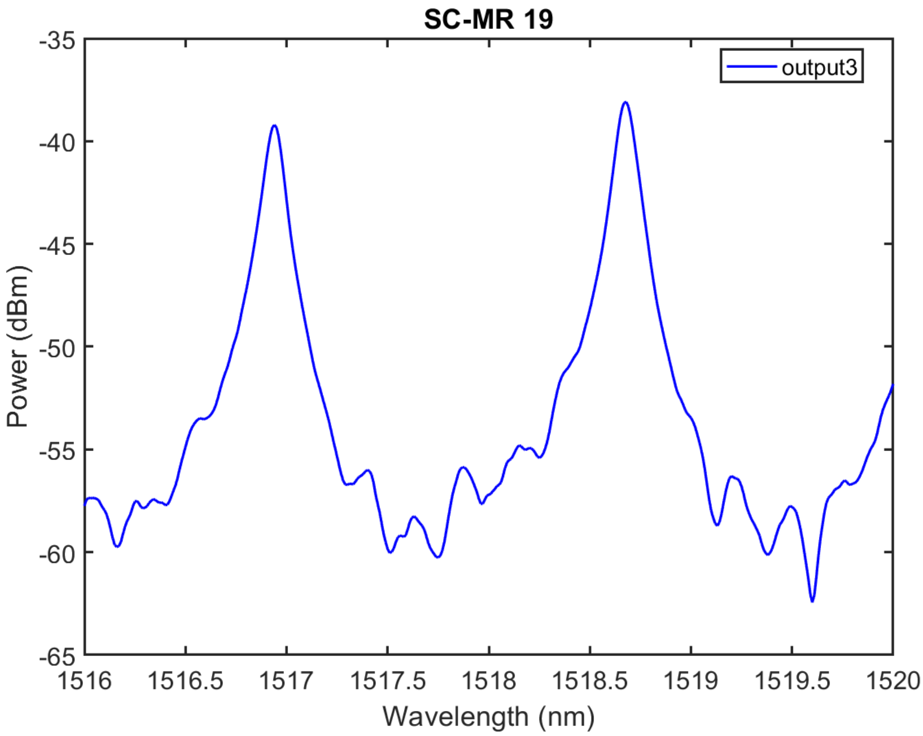

Figure 3.2-17: The experimentally measured SC-MR ADF spectra of the output 3 from 1516 nm to 1520 nm with Lc_1=10.7 µm and Lc_2=19 µm. The spectra have Lorentzian lineshapes with IL=19 dB, FSR= 1.74 nm, best Q-factor of $1.27 \cdot 10^4$, ER=20 dB and SR=45 dB/nm.

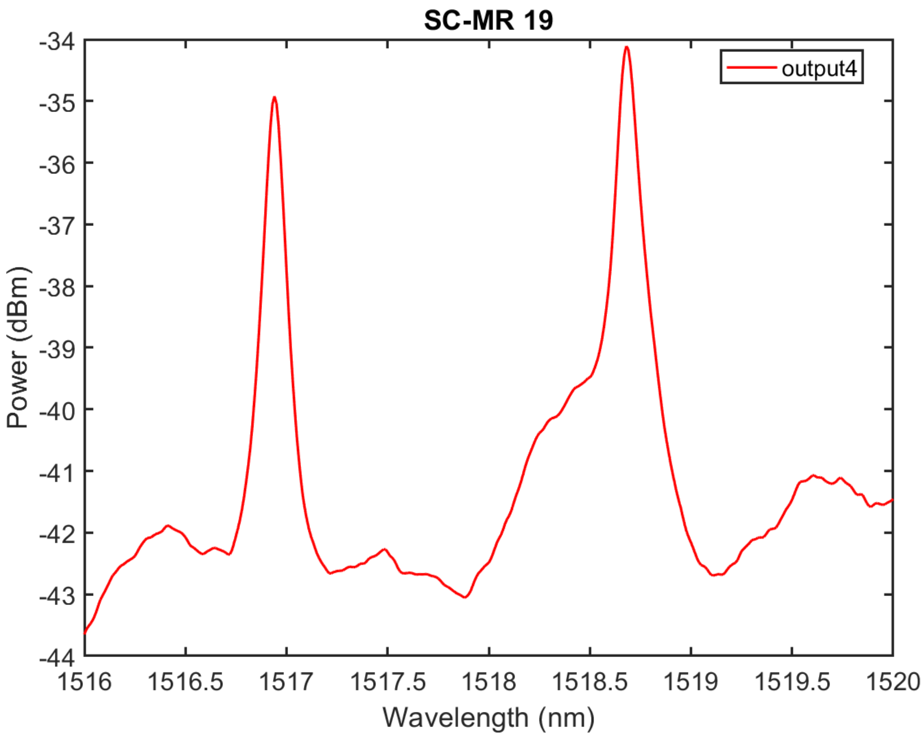

Figure 3.2-18: The experimentally measured SC-MR ADF spectra of the output 4 from 1516 nm to 1520 nm with coupling lengths of Lc_1=10.7 µm and Lc_2=19 µm. The spectra have IL=9 dB, FSR=1.74 nm, ER=8 dB, SR= 22 dB/nm.

SC-MR ADF with Lc_2=20 µm

Figure 3.2-19 shows the experimentally measured spectra of SC-MR ADF from 1500 nm to 1580 nm with Lc_1=10.7 µm and Lc_2=20 µm. The output ports 1, 3 and 4 are shown in green, blue, and red, respectively. Figure 3.2-20 shows the experimentally measured SC-MR ADF spectra from 1510 nm to 1520 nm with Lc_1=10.7 µm and Lc_2=20 µm. The output ports 1, 3 and 4 are shown in green, blue, and red, respectively. The FSR of the spectra is 1.7 nm. Figure 3.2-21 shows the experimentally measured SC-MR ADF spectra of output 1 from 1516 nm to 1520 nm with Lc_1=10.7 µm and Lc_2=20 µm. The spectra have IL=21 dB, FSR=1.7 nm, ER=2.9 dB, SR=26 dB/nm, the spectra show weak inverse Lorentzian lineshapes, hence the Q-factor calculation is not made for the output 1. Figure 3.2-22 shows the experimentally measured SC-MR ADF spectra of the output 3 from 1516 nm to 1520 nm with Lc_1=10.7 µm and Lc_2=20 µm. The spectra have IL=17 dB, FSR= 1.7 nm, best Q-factor of $1.7 \cdot 10^4$, ER=20 dB and SR=49 dB/nm. Figure 3.2-23 shows the experimentally measured SC-MR ADF spectra of the output 4 from 1516 nm to 1520 nm with coupling lengths of Lc_1=10.7 µm and Lc_2=20 µm. The spectra have IL=10 dB, FSR=1.7 nm, ER=8 dB, SR= 37 dB/nm.

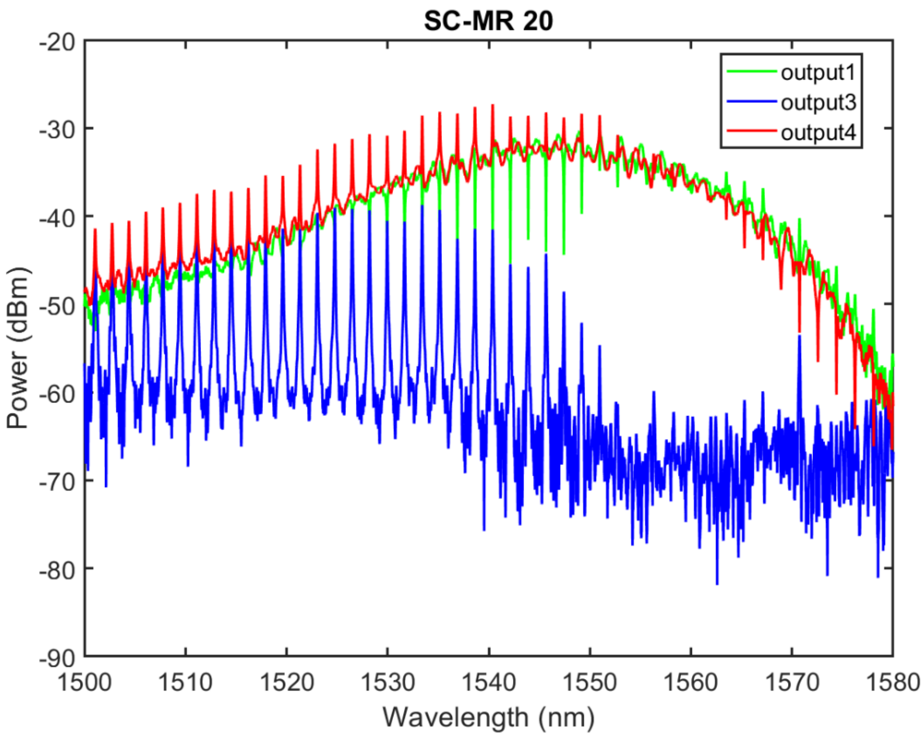

Figure 3.2-19: The experimentally measured spectra of SC-MR ADF from 1500 nm to 1580 nm with Lc_1=10.7 µm and Lc_2=20 µm. The output ports 1, 3 and 4 are shown in green, blue, and red, respectively.

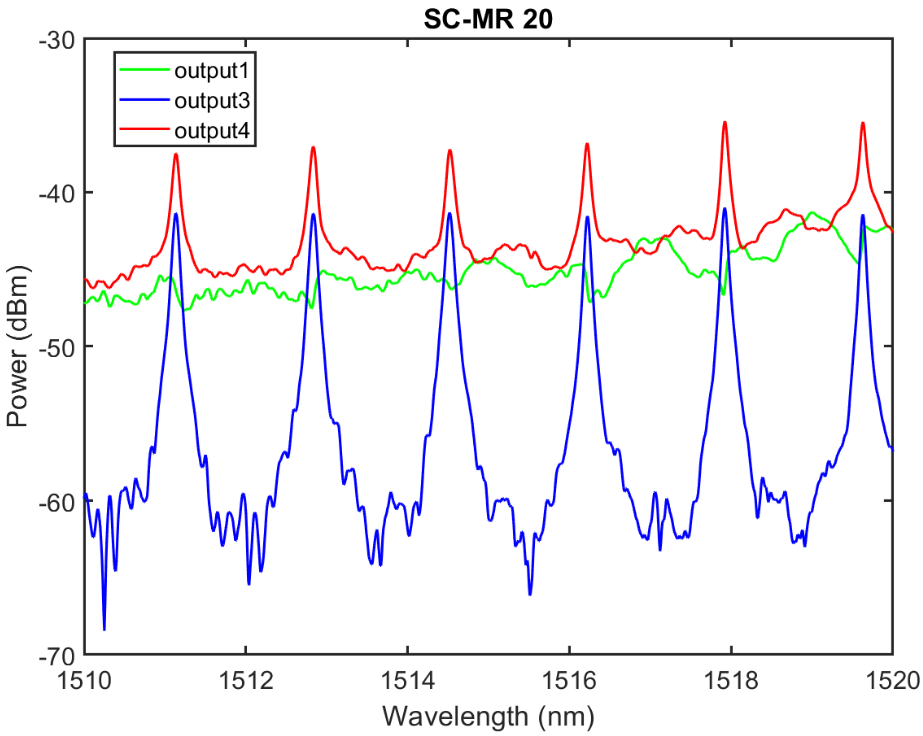

Figure 3.2-20: The experimentally measured SC-MR ADF spectra from 1510 nm to 1520 nm with Lc_1=10.7 µm and Lc_2=20 µm. The output ports 1, 3 and 4 are shown in green, blue, and red, respectively. The FSR of the spectra is 1.7 nm.

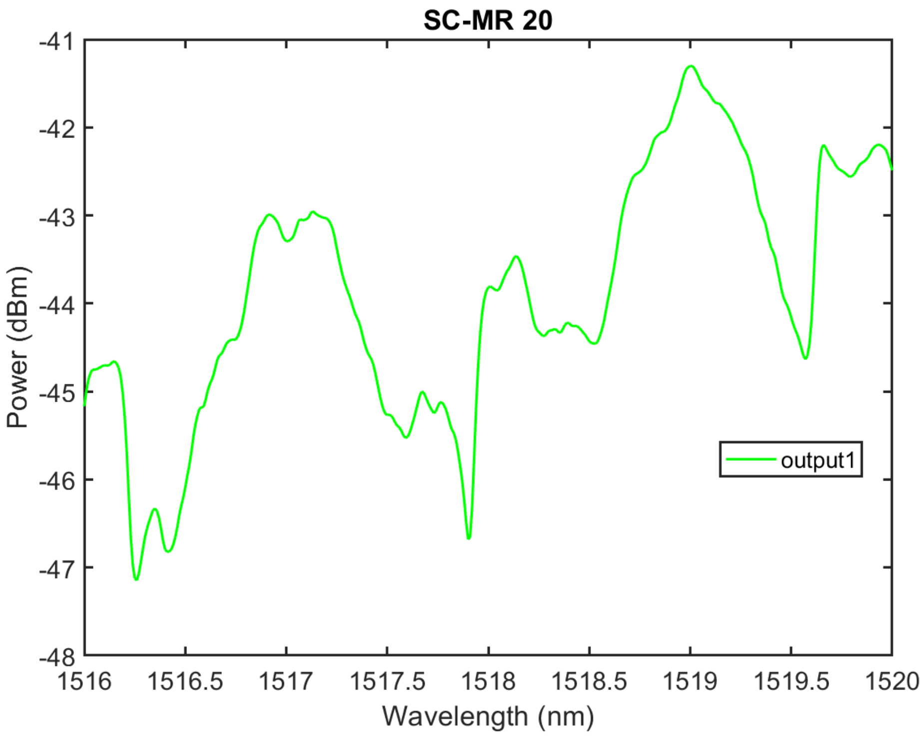

Figure 3.2-21: the experimentally measured SC-MR ADF spectra of output 1 from 1516 nm to 1520 nm with Lc_1=10.7 µm and Lc_2=20 µm. The spectra have IL=21 dB, FSR=1.7 nm, ER=2.9 dB, SR=26 dB/nm.

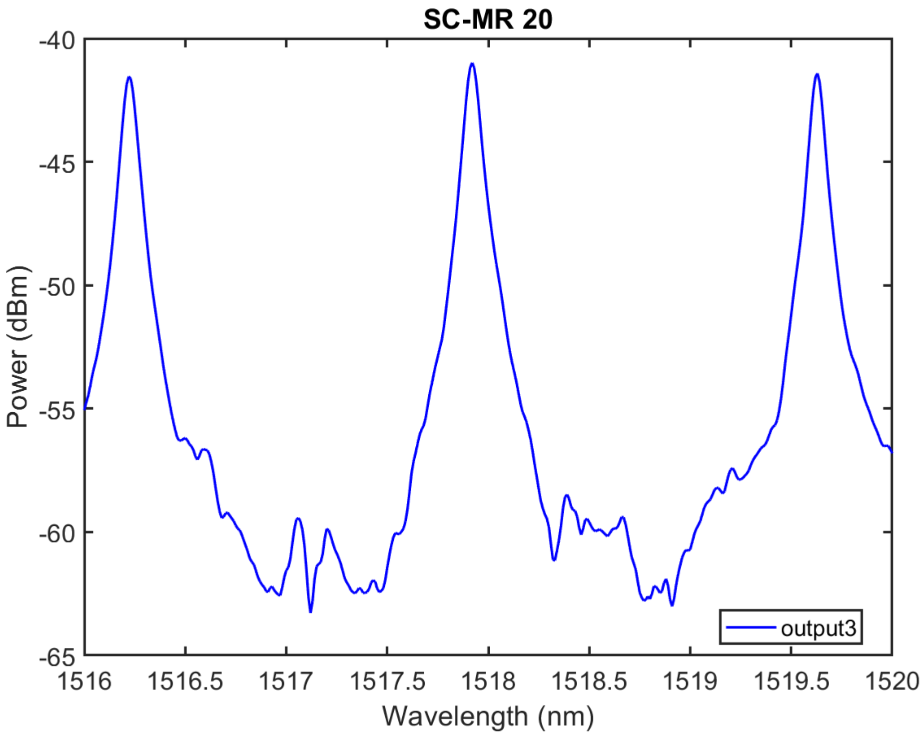

Figure 3.2-22: The experimentally measured SC-MR ADF spectra of the output 3 from 1516 nm to 1520 nm with Lc_1=10.7 µm and Lc_2=20 µm. The spectra have IL=17 dB, FSR= 1.7 nm, best Q-factor of $1.7 \cdot 10^4$, ER=20 dB and SR=49 dB/nm.

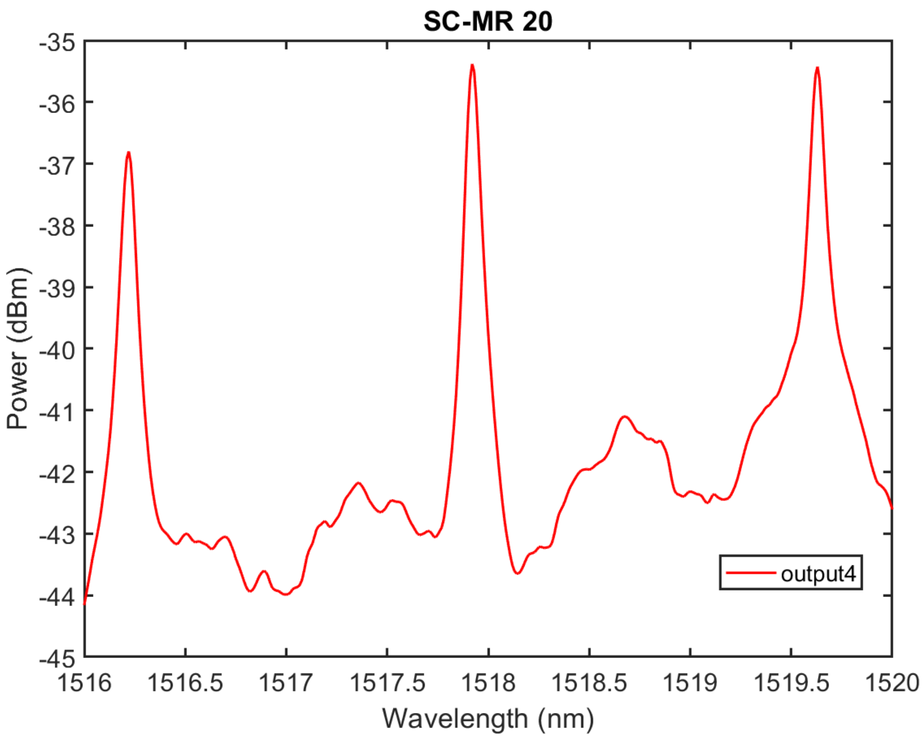

Figure 3.2-23: The experimentally measured SC-MR ADF spectra of the output 4 from 1516 nm to 1520 nm with coupling lengths of Lc_1=10.7 µm and Lc_2=20 µm. The spectra have IL=10 dB, FSR=1.7 nm, ER=8 dB, SR= 37 dB/nm.

SC-MR ADF with Lc_2=21 µm

Figure 3.2-24 shows the experimentally measured spectra of SC-MR ADF from 1500 nm to 1580 nm with Lc_1=10.7 µm and Lc_2=21 µm. The output ports 1, 3 and 4 are shown in green, blue, and red, respectively. Figure 3.2-25 shows the experimentally measured SC-MR ADF spectra from 1510 nm to 1520 nm with Lc_1=10.7 µm and Lc_2=21 µm. The output ports 1, 3 and 4 are shown in green, blue, and red, respectively. The FSR of the spectra is 1.68 nm. Figure 3.2-26 shows the experimentally measured SC-MR ADF spectra of output 1 from 1516 nm to 1520 nm with Lc_1=10.7 µm and Lc_2=21 µm. The spectra have IL=19 dB, FSR=1.68 nm, best eff-Q=$3 \cdot 10^4$, ER=6.37 dB, SR=63.64 dB/nm. Figure 3.2-27 shows the experimentally measured SC-MR ADF spectra of the output 3 from 1516 nm to 1520 nm with Lc_1=10.7 µm and Lc_2=21 µm. The spectra have IL=25 dB, FSR= 1.68 nm, best Q-factor of $1.89 \cdot 10^4$, ER=27 dB and SR=79 dB/nm. Figure 3.2-28 shows the experimentally measured SC-MR ADF spectra of the output 4 from 1516 nm to 1520 nm with coupling lengths of Lc_1=10.7 µm and Lc_2=21 µm. The spectra have IL=11 dB, FSR=1.68 nm, ER=6.5 dB, SR= 32 dB/nm.

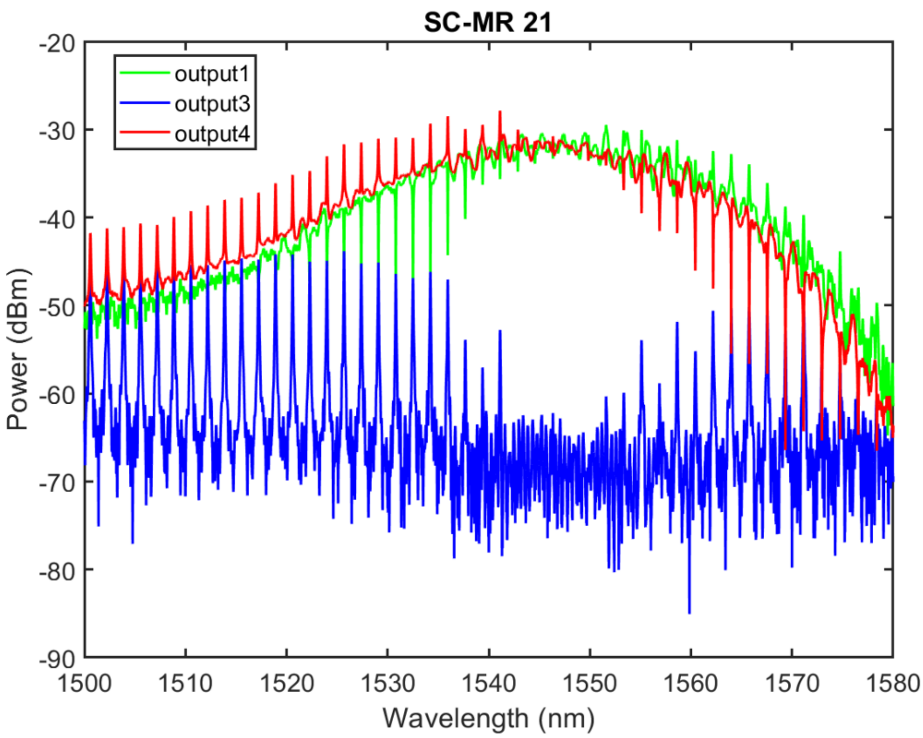

Figure 3.2-24: The experimentally measured spectra of SC-MR ADF from 1500 nm to 1580 nm with Lc_1=10.7 µm and Lc_2=21 µm. The output ports 1, 3 and 4 are shown in green, blue, and red, respectively.

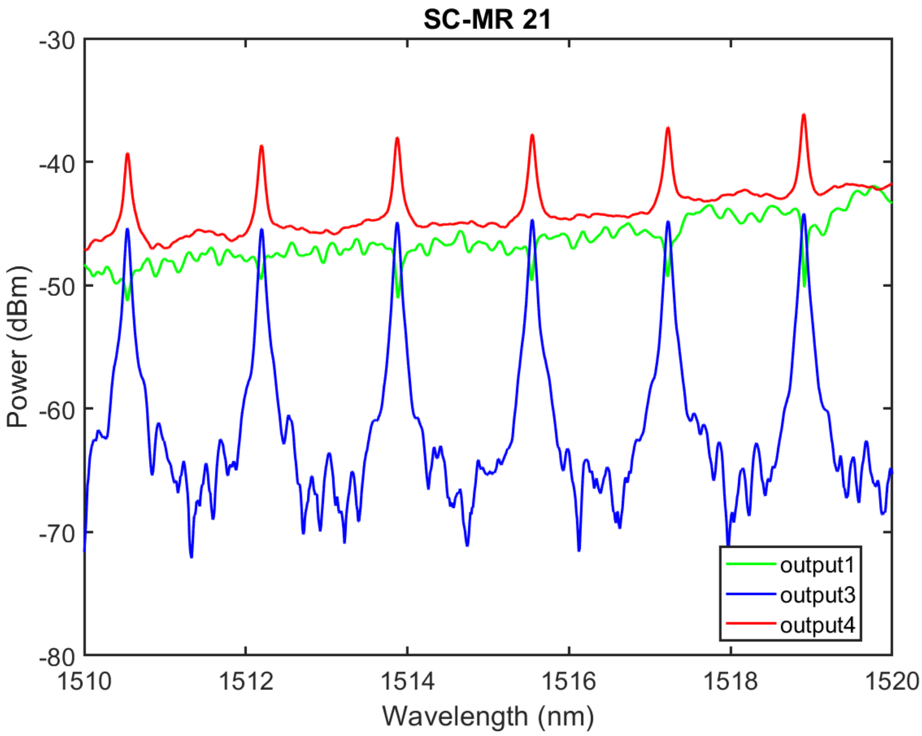

Figure 3.2-25: The experimentally measured SC-MR ADF spectra from 1510 nm to 1520 nm with Lc_1=10.7 µm and Lc_2=21 µm. The output ports 1, 3 and 4 are shown in green, blue, and red, respectively. The FSR of the spectra is 1.68 nm.

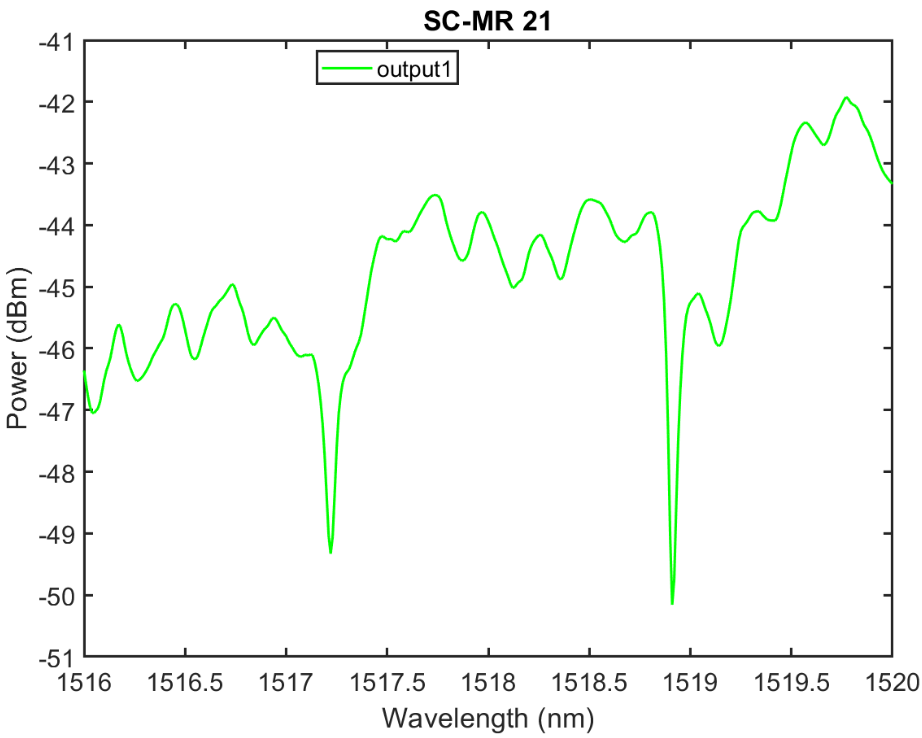

Figure 3.2-26: The experimentally measured SC-MR ADF spectra of output 1 from 1516 nm to 1520 nm with Lc_1=10.7 µm and Lc_2=21 µm. The spectra have IL=19 dB, FSR=1.68 nm, best eff-Q=$3\cdot10^4$, ER=6.37 dB, SR=63.64 dB/nm.

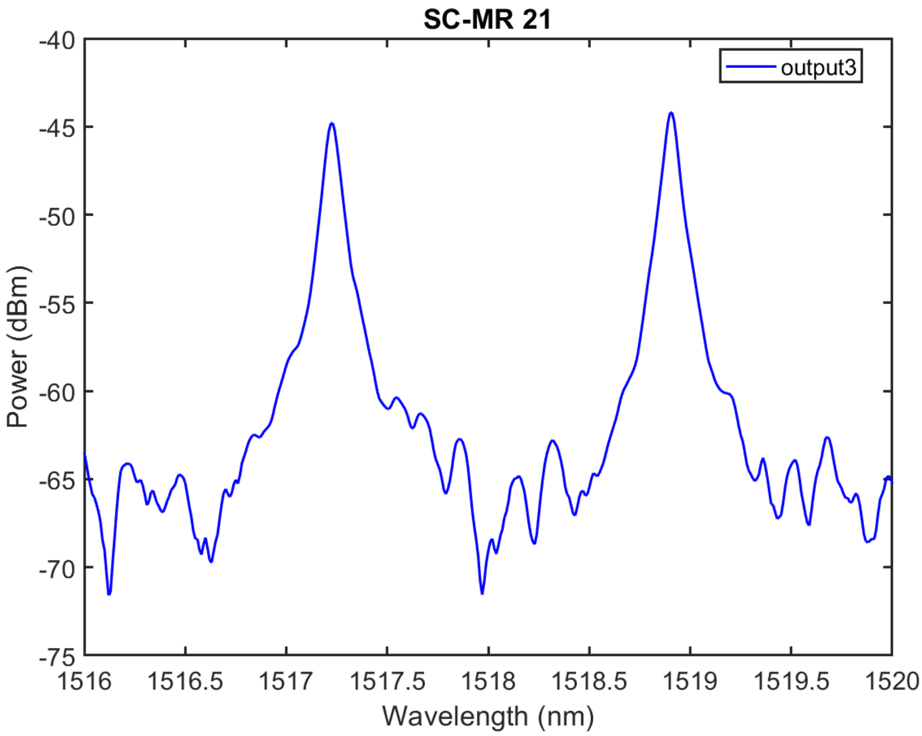

Figure 3.2-27: The experimentally measured SC-MR ADF spectra of the output 3 from 1516 nm to 1520 nm with Lc_1=10.7 µm and Lc_2=21 µm. The spectra have IL=25 dB, FSR= 1.68 nm, best Q-factor of $1.89 \cdot 10^4$, ER=27 dB and SR=79 dB/nm.

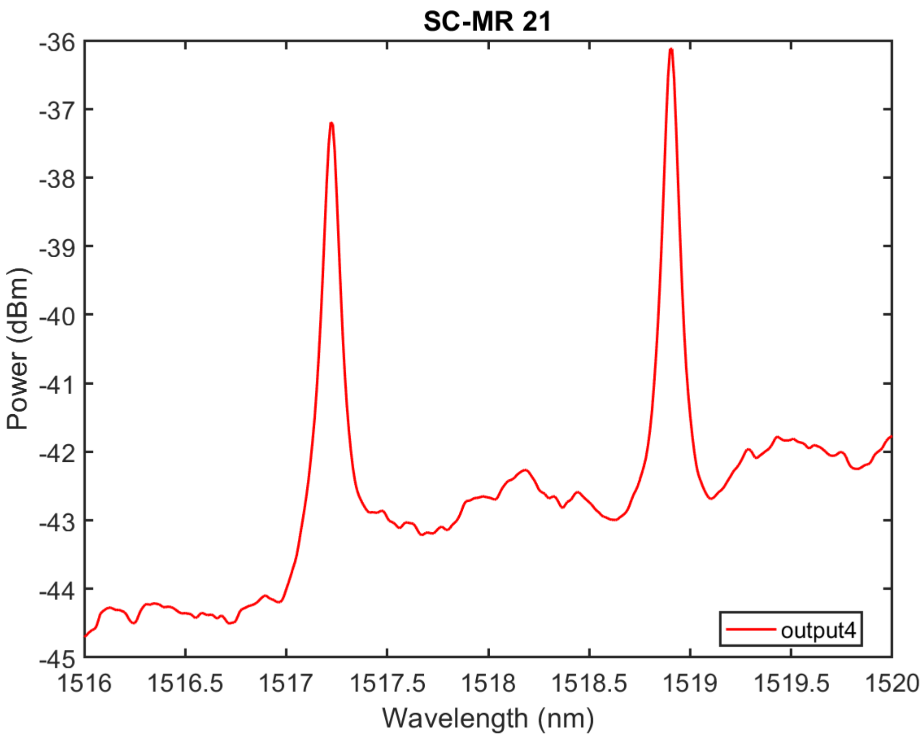

Figure 3.2-28: The experimentally measured SC-MR ADF spectra of the output 4 from 1516 nm to 1520 nm with coupling lengths of Lc_1=10.7 µm and Lc_2=21 µm. The spectra have IL=11 dB, FSR=1.68 nm, ER=6.5 dB, SR= 32 dB/nm.

SC-MR ADF with Lc_2=23 µm

Figure 3.2-29 shows the experimentally measured spectra of SC-MR ADF from 1500 nm to 1580 nm with Lc_1=10.7 µm and Lc_2=23 µm. The output ports 1, 3 and 4 are shown in green, blue, and red, respectively. Figure 3.2-30 shows the experimentally measured SC-MR ADF spectra from 1510 nm to 1520 nm with Lc_1=10.7 µm and Lc_2=23 µm. The output ports 1, 3 and 4 are shown in green, blue, and red, respectively. The FSR of the spectra is 1.65 nm. Figure 3.2-31 shows the experimentally measured SC-MR ADF spectra of output 1 from 1516 nm to 1520 nm with Lc_1=10.7 µm and Lc_2=23 µm. The spectra have IL=17 dB, FSR=1.65 nm, best eff-Q=$7.6\cdot10^3$, ER=12 dB, SR=151 dB/nm. Figure 3.2-32 shows the experimentally measured SC-MR ADF spectra of the output 3 from 1516 nm to 1520 nm with Lc_1=10.7 µm and Lc_2=23 µm. The spectra have IL=20 dB, FSR= 1.65 nm, best Q-factor of $2.5\cdot10^4$, ER=13 dB and SR=163 dB/nm. Figure 3.2-33 shows the experimentally measured SC-MR ADF spectra of the output 4 from 1516 nm to 1520 nm with coupling lengths of Lc_1=10.7 µm and Lc_2=23 µm. The spectra have IL=12 dB, FSR=1.65 nm, best Q-factor of $1.2\cdot10^{4,}$ ER=6.2 dB, SR= 13.5 dB/nm.

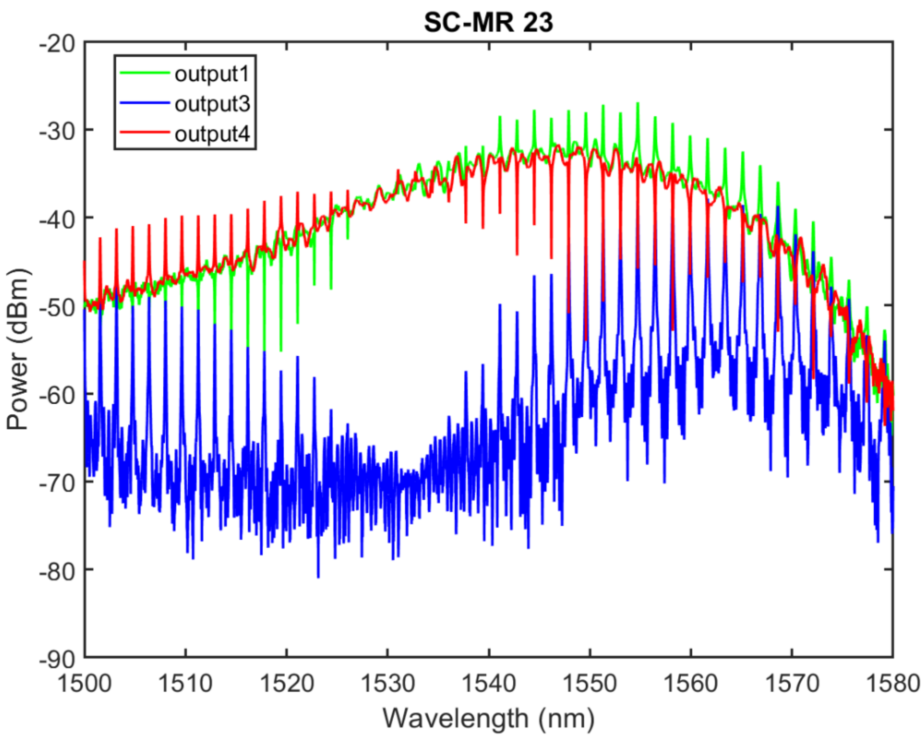

Figure 3.2-29: The experimentally measured spectra of SC-MR ADF from 1500 nm to 1580 nm with Lc_1=10.7 µm and Lc_2=23 µm

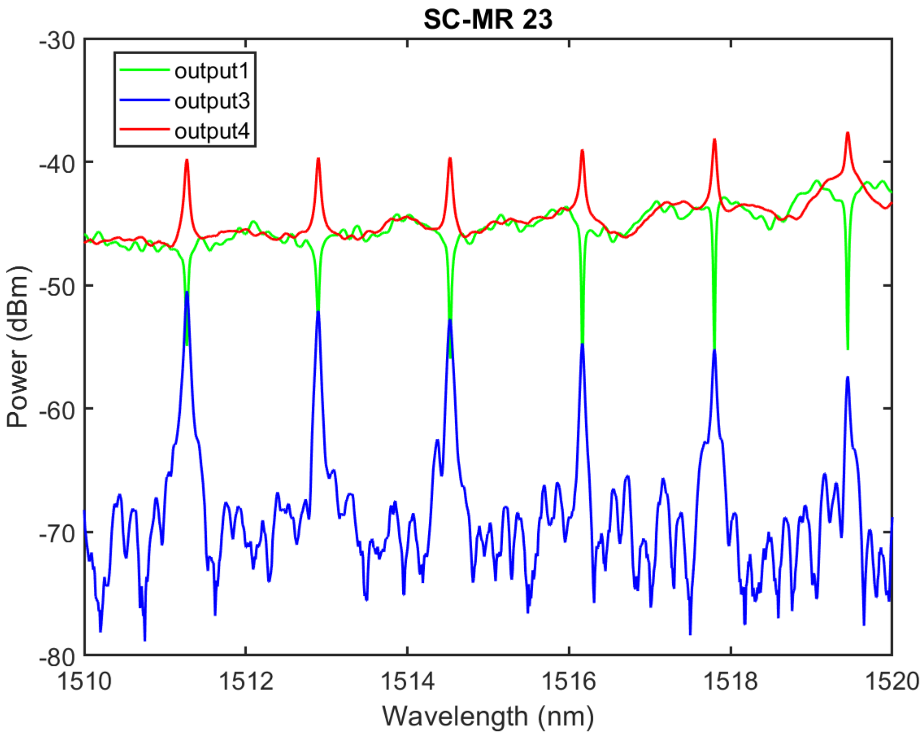

Figure 3.2-30: The experimentally measured SC-MR ADF spectra from 1510 nm to 1520 nm with Lc_1=10.7 µm and Lc_2=23 µm. The output ports 1, 3 and 4 are shown in green, blue, and red, respectively. The FSR of the spectra is 1.65 nm.

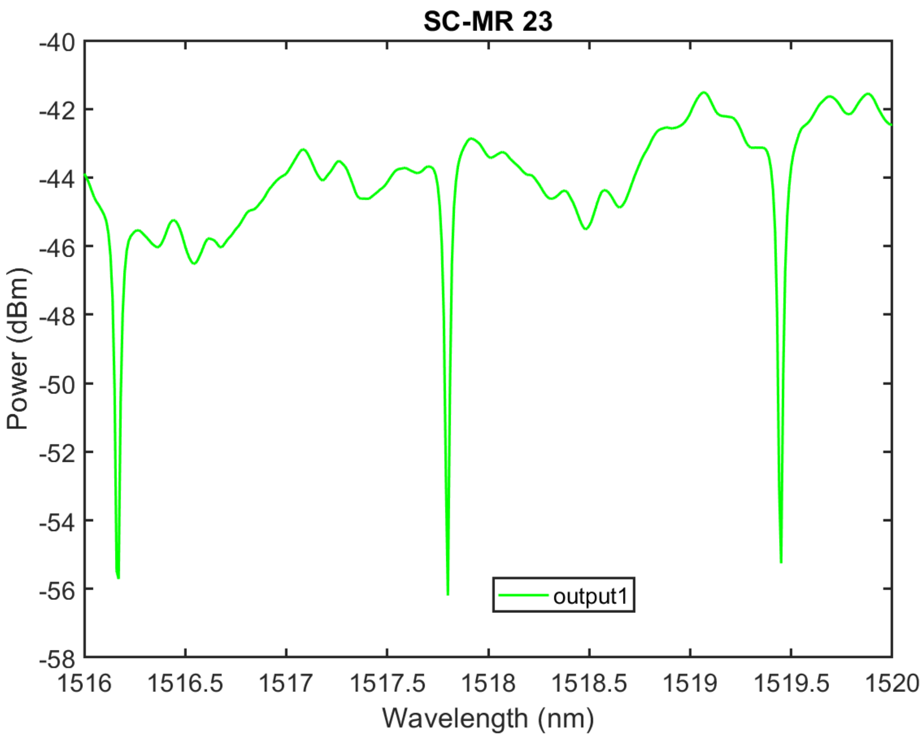

Figure 3.2-31: The experimentally measured SC-MR ADF spectra of output 1 from 1516 nm to 1520 nm with Lc_1=10.7 µm and Lc_2=23 µm. The spectra have IL=30 dB, FSR=1.65 nm, best eff-Q=$7.6 \cdot 10^3$, ER=12 dB, SR=151 dB/nm.

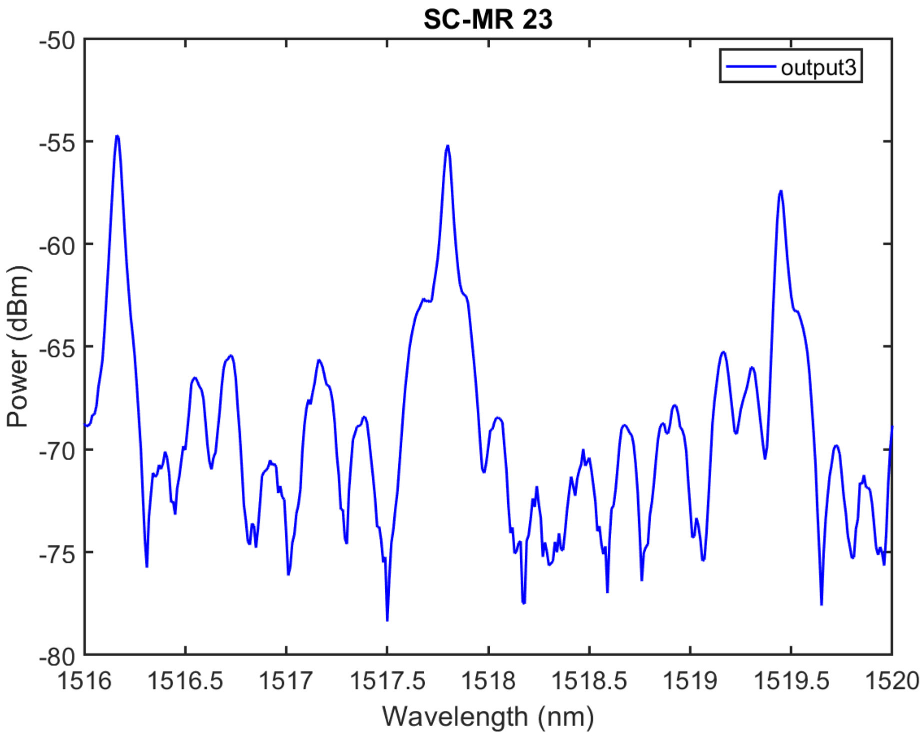

Figure 3.2-32: The experimentally measured SC-MR ADF spectra of the output 3 from 1516 nm to 1520 nm with Lc_1=10.7 µm and Lc_2=23 µm. The spectra have IL=32 dB, FSR= 1.65 nm, best Q-factor of $2.5 \cdot 10^4$, ER=13 dB and SR=163 dB/nm.

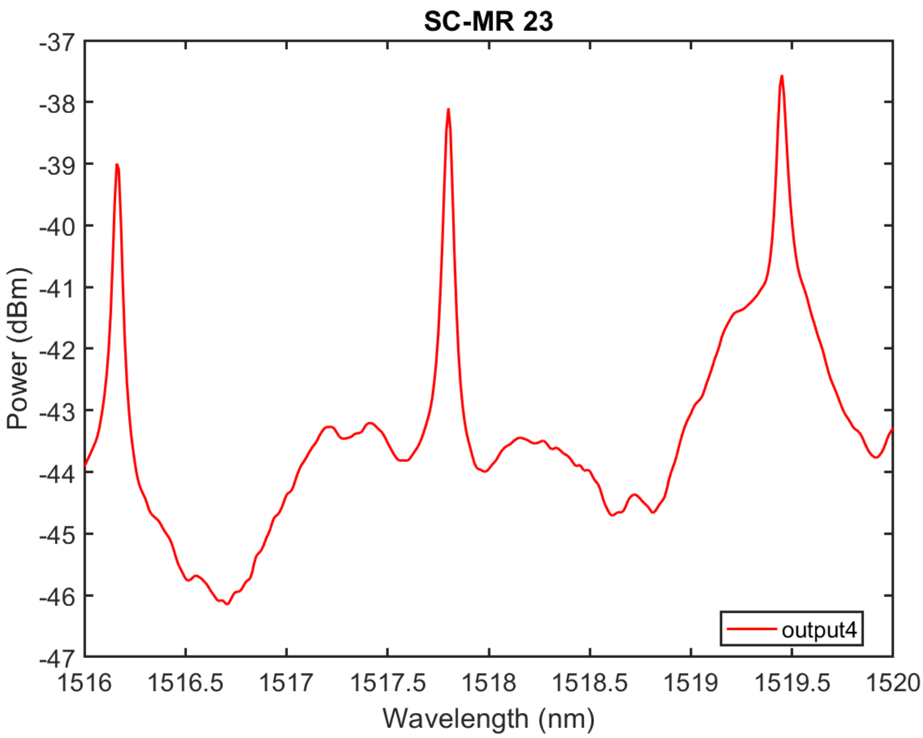

Figure 3.2-33: The experimentally measured SC-MR ADF spectra of the output 4 from 1516 nm to 1520 nm with coupling lengths of Lc_1=10.7 µm and Lc_2=23 µm. The spectra have IL=11 dB, FSR=1.65 nm, best Q-factor of $1.2 \cdot 10^{4,}$ ER=6.2 dB, SR= 13.5 dB/nm.

3.3. Double Coupled MR ADF

Double Coupled Meandering Resonator (DC-MR) filter consists of two MLM add-drop filter (ADF) connected to each other with a distance between. There are two resonant optical paths in DC-MR and the structure shows Fano and Lorentzian lineshapes. The coupling length of Lc_2 is changed to investigate the effect of coupling constant in the structure design. The distance of the optical path determines the FSR of the structure. The DC-MR spectra show Lorentzian peaks with power distributed to each port according to the coupling constants which is specified by the coupling length. Figure 3.3-1 shows the representation of the DC-MR ADF. Figure 3.3-2 shows the SEM image of DC-MR ADF. MR add-drop filter spectrum shows Fano, Lorentzian and inverse Lorentzian lineshapes with a Q- factor figure of merit on the order of 10^4, and the FSR changes from 1.12 nm to 1.54 nm dependent on the round-trip path length, at 1510 nm. Figure 3.3-3 shows the KLayout design of the DC-MR ADF given with the corresponding coupling dimensions and bend radii with the positions of the input and output ports, DC-MR with input shown in black, output 1, 2 and 3 is shown in green, blue, and red, respectively. The IC coupler has a coupling length of $Lc_{1=}$10.7 µm and the CC coupler has a coupling length of $Lc_{2=}$17 µm (specific to chosen design), waveguides have a bending radius of 5 µm while the couplers' bending radius is 10 µm, the gap between the bus waveguides in the couplers is g=200 nm. The coupler bending radius of 10 µm, the waveguide bending radius of 5 µm and the gap between the coupler waveguides g=200 nm is constant in all designs.

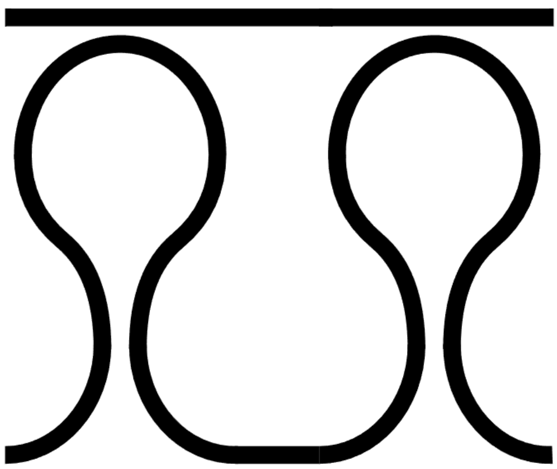

Figure 3.3-1: MR add drop filter representation.

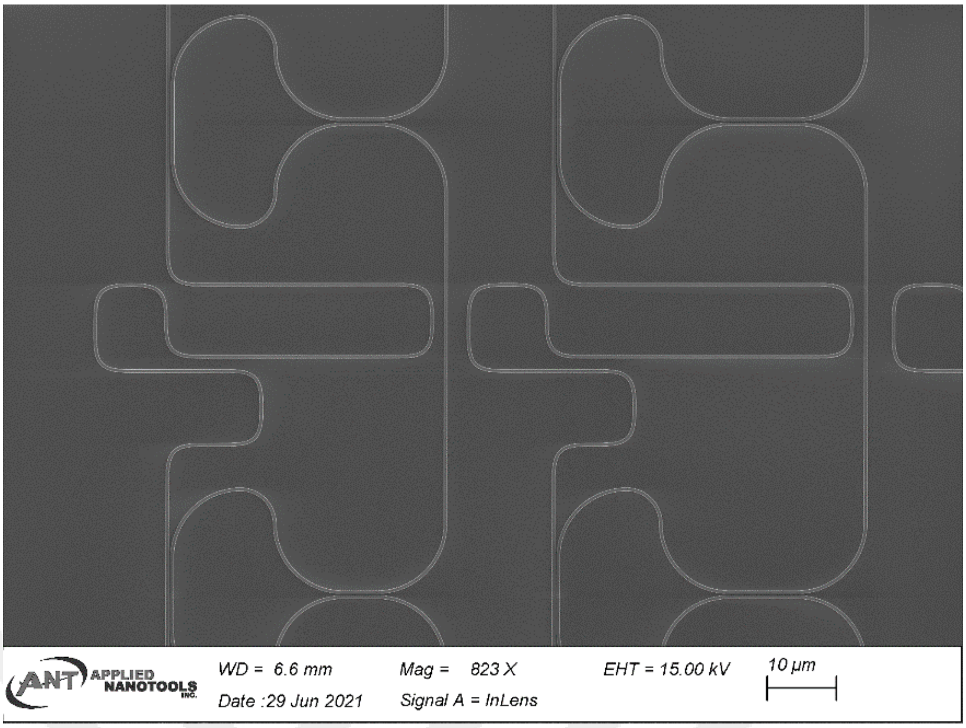

Figure 3.3-2: The SEM image of DC-MR ADF.

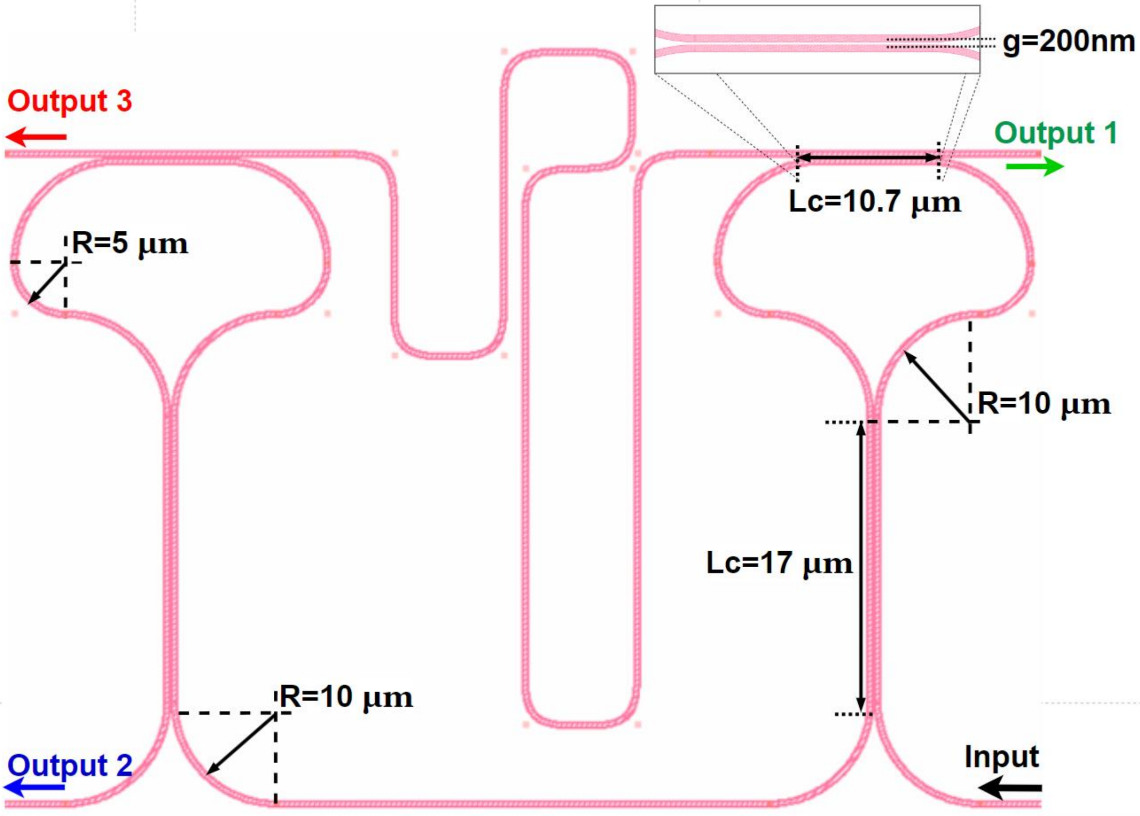

Figure 3.3-3: Representation of DC-MR with output input in black, output 1,2 and 3 is shown in green, blue, and red, respectively. The IC coupler has a coupling length of $L_{c=}$10.7 µm and the CC coupler has $L_{c=}$17 µm (specific to chosen design), waveguides have a bending radius of 5 µm while the couplers' bending radius is 10 µm, the gap between the bus waveguides in the couplers is g=200 nm.

MR-ADF with Lc_2=16 µm

Figure 3.3-4 shows the experimentally measured spectra of DC-AMR ADF from 1500 nm to 1580 nm with Lc_1=10.7 µm and Lc_2=16 µm. The output ports 1, 3 and 4 are shown in green, blue, and red, respectively. Figure 3.3-5 shows the experimentally measured DC-MR ADF spectra from 1510 nm to 1520 nm with Lc_1=10.7 µm and Lc_2=16 µm. The output ports 1, 3 and 4 are shown in green, blue, and red, respectively. The FSR of the spectra is 1.38 nm. Figure 3.3-6 shows the experimentally measured DC-MR ADF spectra of output 1 from 1516 nm to 1520 nm with Lc_1=10.7 µm and Lc_2=16 µm. The spectra have IL=20 dB, FSR=1.38 nm, best Q-factor=$6.1\cdot10^3$, ER=7 dB, SR=54.76 dB/nm. Figure 3.3-7 shows the experimentally measured DC-MR ADF spectra of the output 3 from 1516 nm to 1520 nm with Lc_1=10.7 µm and Lc_2=16 µm. The spectra have IL=18 dB, FSR=1.38 nm, best Q-factor of $6\cdot10^3$, ER=13.7 dB and SR=31 dB/nm. Figure 3.3-8 shows the experimentally measured DC-MR ADF spectra of the output 4 from 1516 nm to 1520 nm with coupling lengths of Lc_1=10.7 µm and Lc_2=16 µm. The spectra have IL=14 dB, FSR=1.38 nm, ER=5.8 dB, SR= 12 dB/nm.

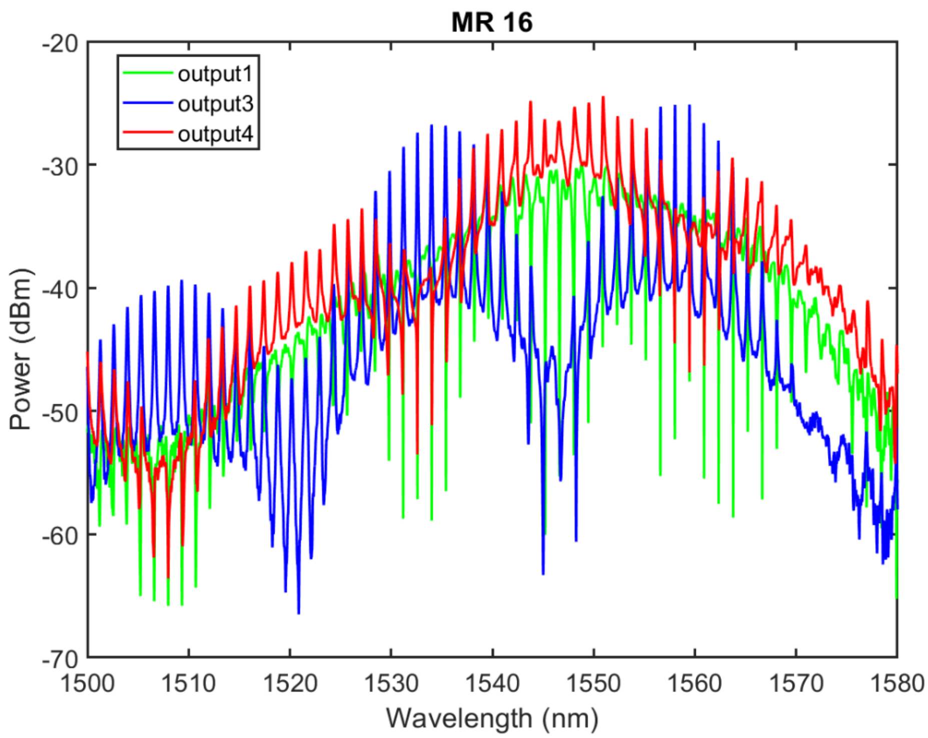

Figure 3.3-4: The experimentally measured graph of DC-MR ADF from 1500 nm to 1580 nm with Lc_1=10.7 µm and Lc_2=16 µm. The outputs 1,2 and 3 are shown in green, blue, and red, respectively.

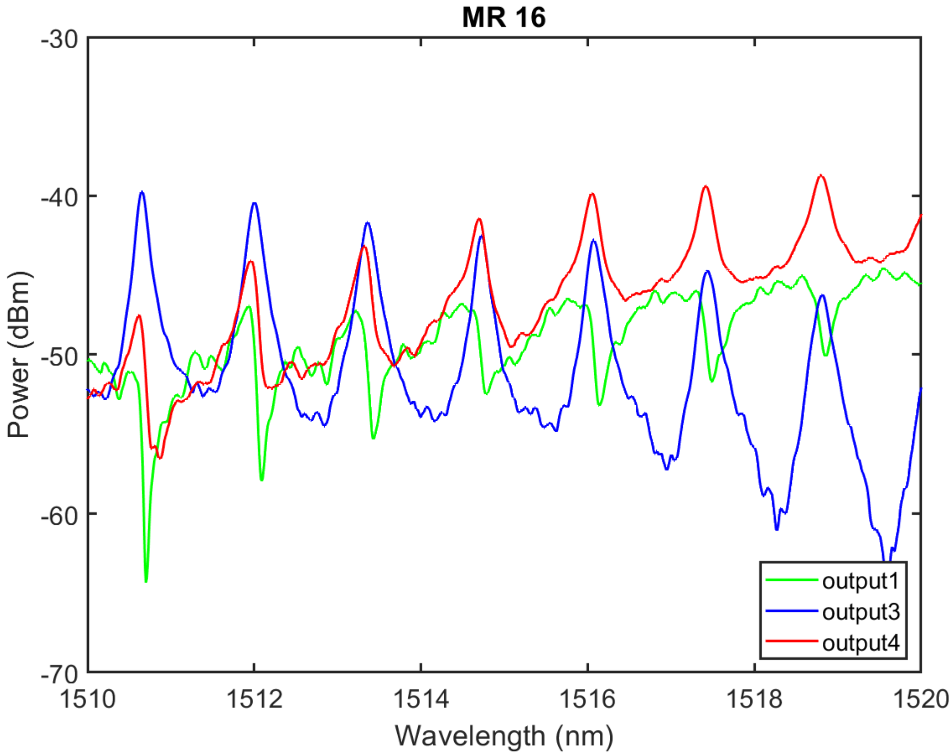

Figure 3.3-5: The experimentally measured DC-MR ADF spectra from 1510 nm to 1520 nm with Lc_1=10.7 µm and Lc_2=16 µm. The output ports 1, 3 and 4 are shown in green, blue, and red, respectively. The FSR of the spectra is 1.38 nm.

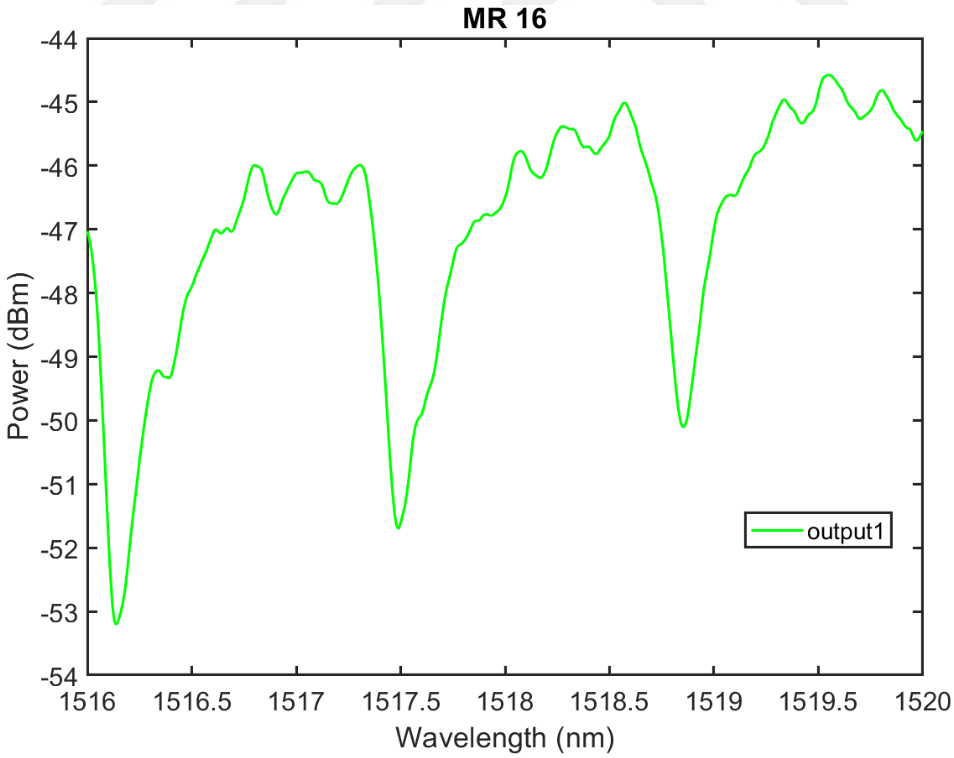

Figure 3.3-6: The experimentally measured DC-MR ADF spectra of output 1 from 1516 nm to 1520 nm with Lc_1=10.7 µm and Lc_2=16 µm. The spectra have IL=20 dB, FSR=1.38 nm, best Q-factor=6.1·103, ER=7 dB, SR=54.76 dB/nm.

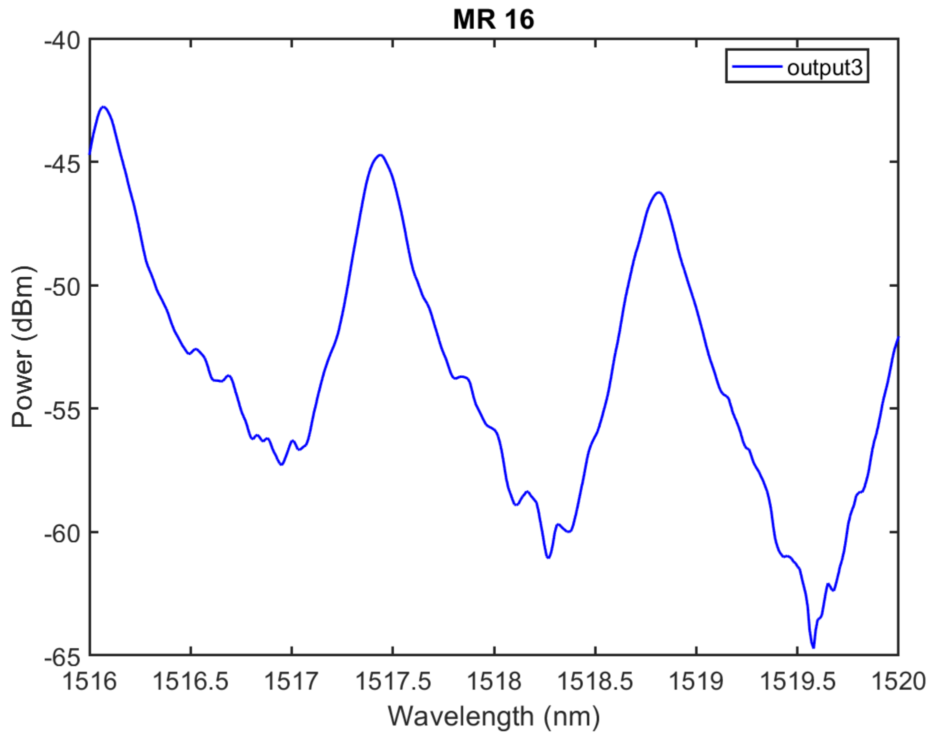

Figure 3.3-7: The experimentally measured DC-MR ADF spectra of the output 3 from 1516 nm to 1520 nm with Lc_1=10.7 µm and Lc_2=16 µm. The spectra have IL=18 dB, FSR=1.38 nm, best Q-factor of $6 \cdot 10^3$, ER=13.7 dB and SR=31 dB/nm.

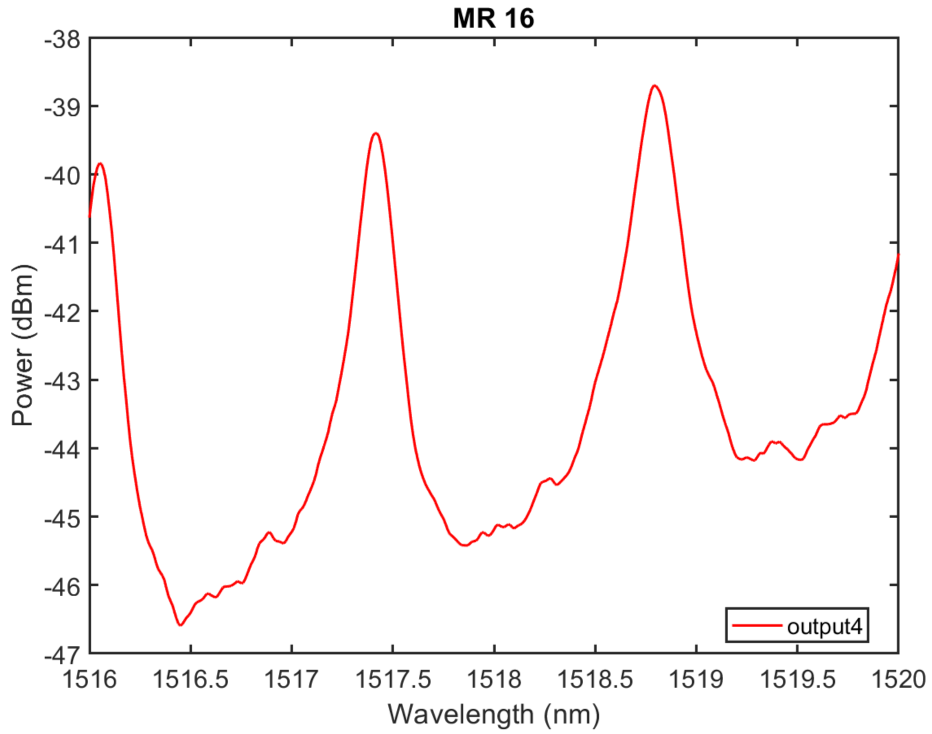

Figure 3.3-8: The experimentally measured DC-MR ADF spectra of the output 4 from 1516 nm to 1520 nm with coupling lengths of Lc_1=10.7 µm and Lc_2=16 µm. The spectra have IL=14 dB, FSR=1.38 nm, ER=5.8 dB, SR= 12 dB/nm.

MR-ADF with Lc_2=17 µm

Figure 3.3-9 shows the experimentally measured spectra of DC-MR ADF from 1500 nm to 1580 nm with Lc_1=10.7 µm and Lc_2=17 µm. The output ports 1, 3 and 4 are shown in green, blue, and red, respectively. Figure 3.3-10 shows the experimentally measured DC-MR ADF spectra from 1510 nm to 1520 nm with Lc_1=10.7 µm and Lc_2=17 µm. The output ports 1, 3 and 4 are shown in green, blue, and red, respectively. The FSR of the spectra is 1.35 nm. Figure 3.3-11 shows the experimentally measured DC-MR ADF spectra of output 1 from 1516 nm to 1520 nm with Lc_1=10.7 µm and Lc_2=17 µm. The spectra have IL=20 dB, FSR=1.35 nm, best eff-Q=$2.1 \cdot 10^4$, ER=15 dB, SR=92 dB/nm. Figure 3.3-12 shows the experimentally measured DC-MR ADF spectra of the output 3 from 1516 nm to 1520 nm with Lc_1=10.7 µm and Lc_2=17 µm. The spectra have Lorentzian lineshapes with IL=12 dB, FSR=1.35 nm, best Q-factor of $1.1 \cdot 10^3$, ER=12 dB and SR=36 dB/nm. Figure 3.3-13 shows the experimentally measured DC-MR ADF spectra of the output 4 from 1516 nm to 1520 nm with coupling lengths of Lc_1=10.7 µm and Lc_2=17 µm. The spectra have IL=16 dB, FSR=1.35 nm, ER=4.1 dB, SR= 51 dB/nm.

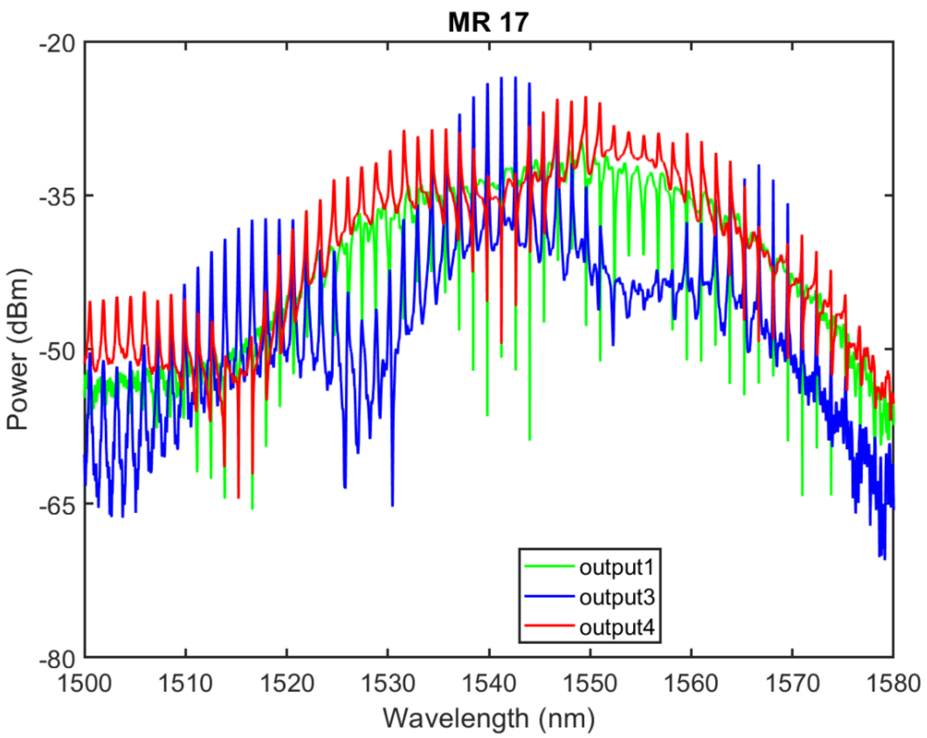

Figure 3.3-9: The experimentally measured spectra of DC-MR ADF from 1500 nm to 1580 nm with Lc_1=10.7 µm and Lc_2=17 µm. The output ports 1, 3 and 4 are shown in green, blue, and red, respectively.

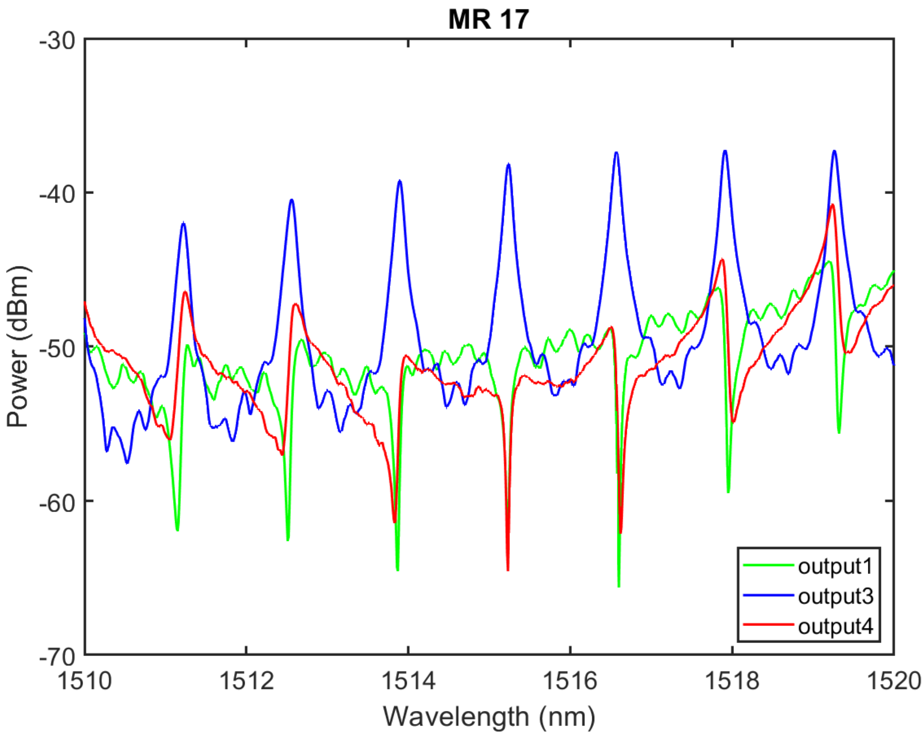

Figure 3.3-10: the experimentally measured DC-MR ADF spectra from 1510 nm to 1520 nm with Lc_1=10.7 µm and Lc_2=17 µm. The output ports 1, 3 and 4 are shown in green, blue, and red, respectively. The FSR of the spectra is 1.35 nm.

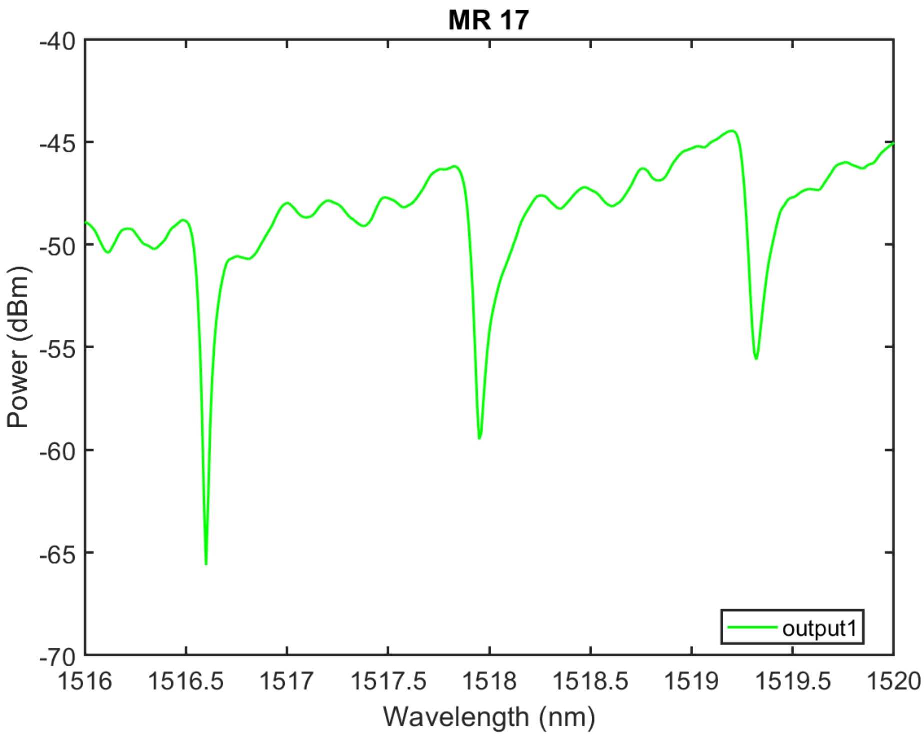

Figure 3.3-11: The experimentally measured DC-MR ADF spectra of output 1 from 1516 nm to 1520 nm with Lc_1=10.7 µm and Lc_2=17 µm. The spectra have IL=20 dB, FSR=1.35 nm, best eff-Q=$2.1\cdot10^4$, ER=15 dB, SR=92 dB/nm.

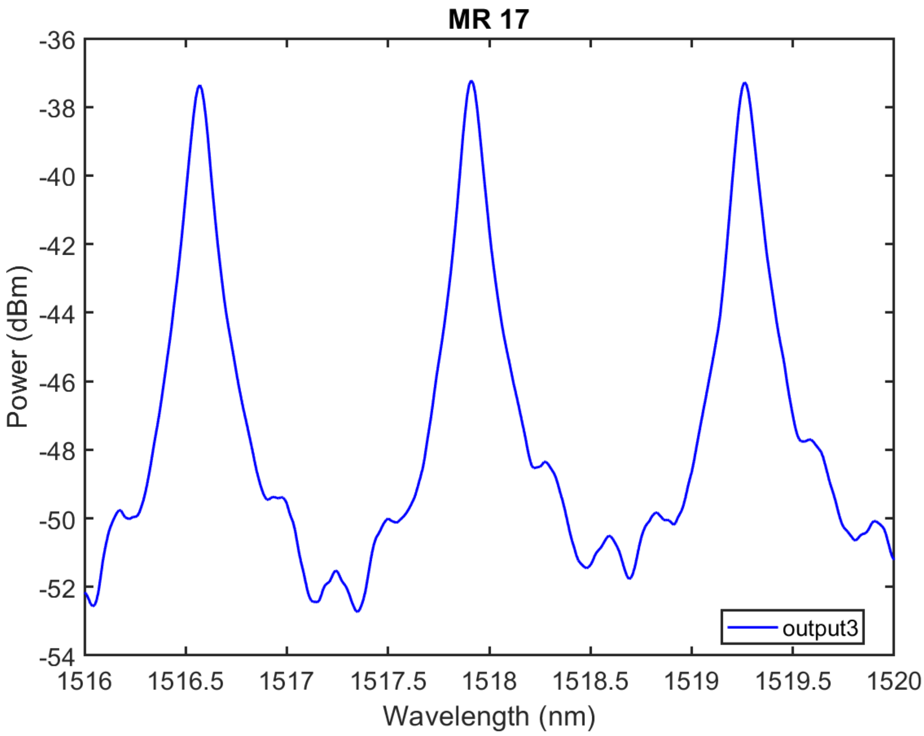

Figure 3.3-12: The experimentally measured DC-MR ADF spectra of output 1 from 1516 nm to 1520 nm with Lc_1=10.7 µm and Lc_2=17 µm. The spectra have IL=12 dB, FSR=1.35 nm, best eff-Q=$2.1 \cdot 10^4$, ER=11 dB, SR=92 dB/nm.

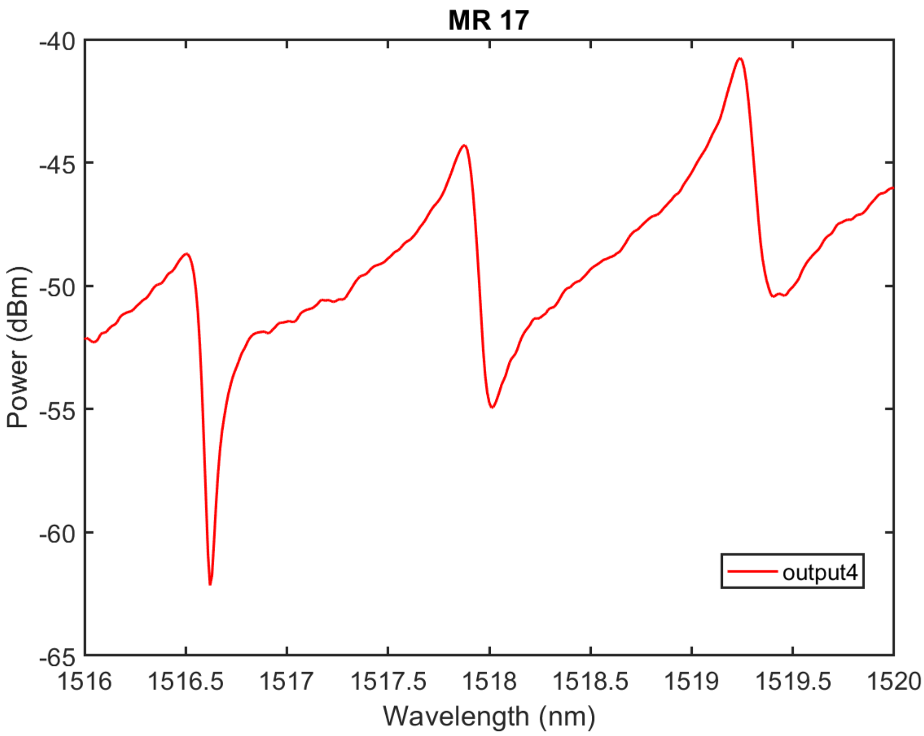

Figure 3.3-13: The experimentally measured DC-MR ADF spectra of the output 4 from 1516 nm to 1520 nm with coupling lengths of Lc_1=10.7 µm and Lc_2=17 µm. The spectra have IL=16 dB, FSR=1.35 nm, ER=4.1 dB, SR= 51 dB/nm.

MR-ADF with Lc_2=18 μm

Figure 3.3-14 shows the experimentally measured spectra of DC-MR ADF from 1500 nm to 1580 nm with Lc_1=10.7 μm and Lc_2=18 μm. The output ports 1, 3 and 4 are shown in green, blue, and red, respectively. Figure 3.3-15 shows the experimentally measured SC-MR ADF spectra from 1510 nm to 1520 nm with Lc_1=10.7 μm and Lc_2=18 μm. The output ports 1, 3 and 4 are shown in green, blue, and red, respectively. The FSR of the spectra is 1.33 nm. Figure 3.3-16 shows the experimentally measured DC-MR ADF spectra of output 1 from 1516 nm to 1520 nm with Lc_1=10.7 μm and Lc_2=18 μm. The spectra have IL=17 dB, FSR=1.33 nm, best eff-Q=$1.3\cdot10^4$, ER=26 dB, SR=242 dB/nm. Figure 3.3-17 shows the experimentally measured DC-MR ADF spectra of the output 3 from 1516 nm to 1520 nm with Lc_1=10.7 μm and Lc_2=18 μm. The spectra have IL=17 dB, FSR= 1.33 nm, best Q-factor of $7.2\cdot10^3$, ER=20 dB and SR=79 dB/nm. Figure 3.3-18 shows the experimentally measured DC-MR ADF spectra of the output 4 from 1516 nm to 1520 nm with coupling lengths of Lc_1=10.7 μm and Lc_2=18 μm. The spectra have IL=15 dB, FSR=1.34 nm, best Q factor of $6.9\cdot10^3$, ER=6.5 dB, SR= 100 dB/nm.

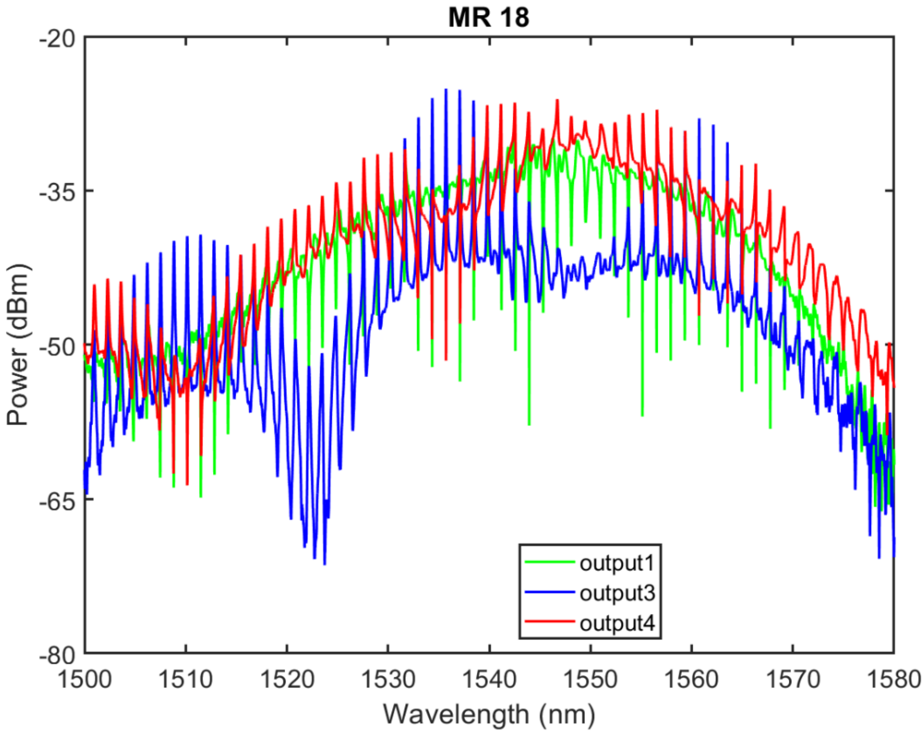

Figure 3.3-14: the experimentally measured spectra of DC-MR ADF from 1500 nm to 1580 nm with Lc_1=10.7 μm and Lc_2=18 μm. The output ports 1, 3 and 4 are shown in green, blue, and red, respectively.

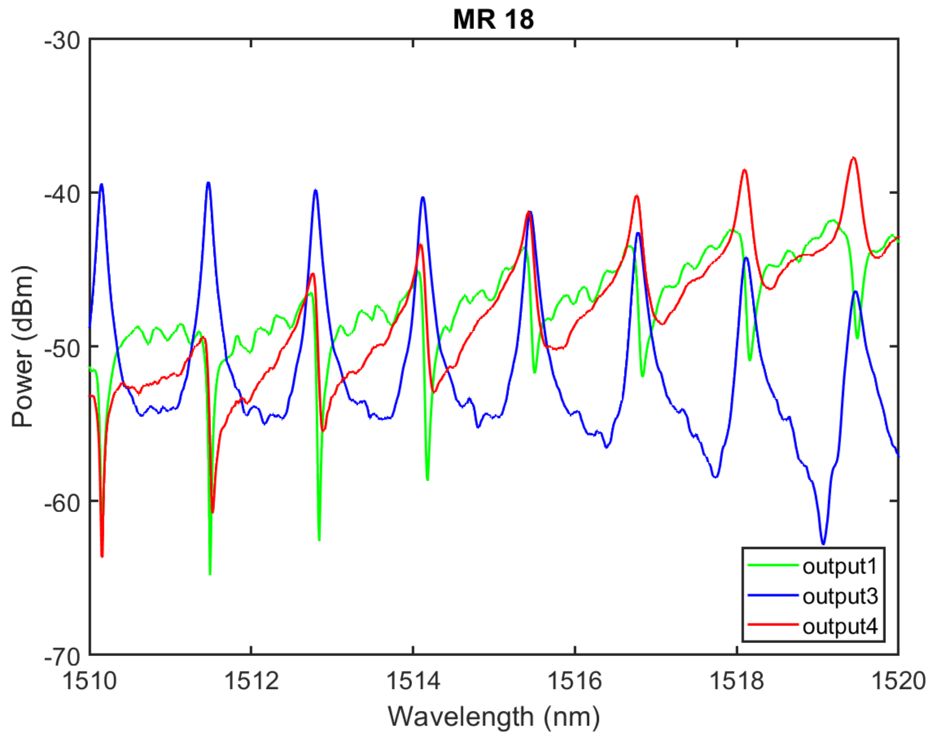

Figure 3.3-15: The experimentally measured SC-MR ADF spectra from 1510 nm to 1520 nm with Lc_1=10.7 µm and Lc_2=18 µm. The output ports 1, 3 and 4 are shown in green, blue, and red, respectively. The FSR of the spectra is 1.33 nm.

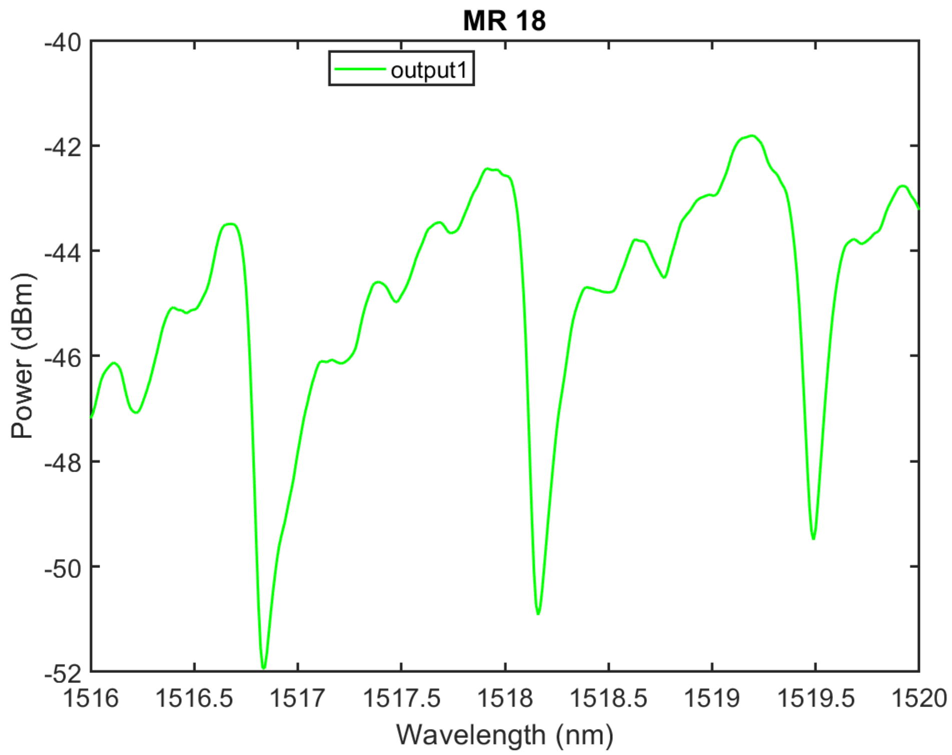

Figure 3.3-16: The experimentally measured DC-MR ADF spectra of output 1 from 1516 nm to 1520 nm with Lc_1=10.7 µm and Lc_2=18 µm. The spectra have IL=17 dB, FSR=1.32 nm, best eff-Q=$2.16\cdot10^4$, ER=8.8 dB, SR=62 dB/nm.

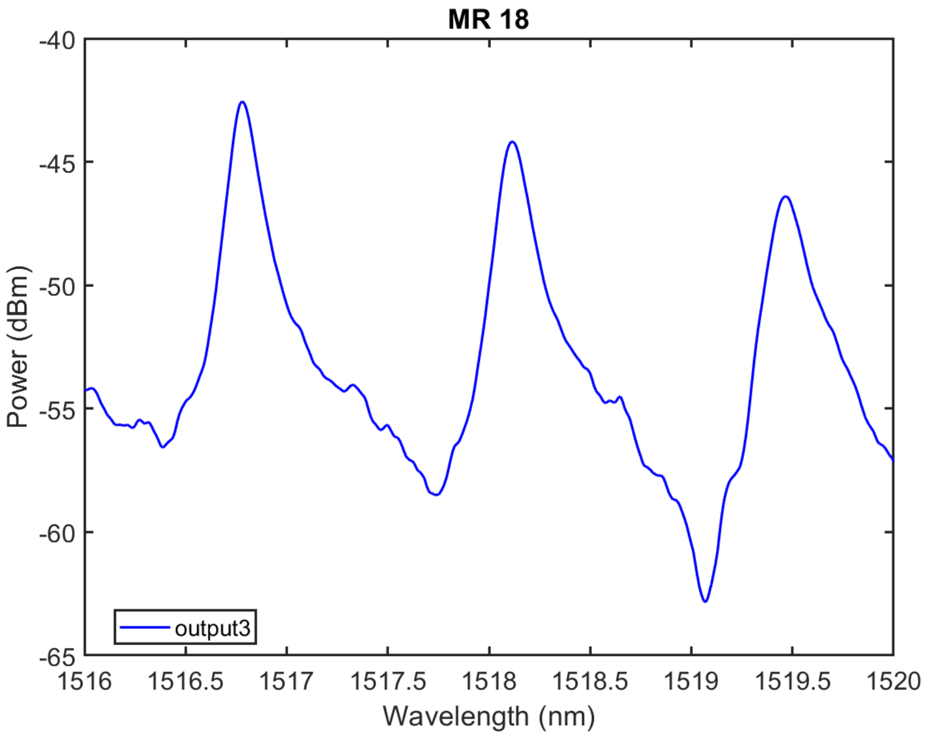

Figure 3.3-17: The experimentally measured DC-MR ADF spectra of the output 3 from 1516 nm to 1520 nm with Lc_1=10.7 μm and Lc_2=18 μm. The spectra have IL=17 dB, FSR= 1.33 nm, best Q-factor of $7.2 \cdot 10^3$, ER=20 dB and SR=79 dB/nm.

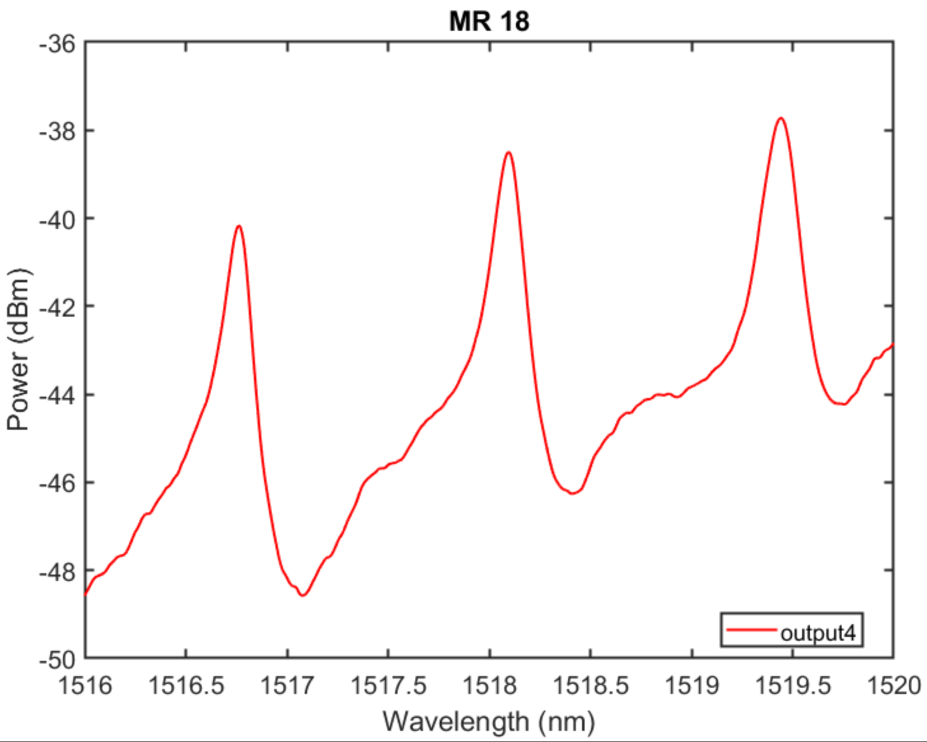

Figure 3.3-18: The experimentally measured DC-MR ADF spectra of the output 4 from 1516 nm to 1520 nm with coupling lengths of Lc_1=10.7 μm and Lc_2=18 μm. The spectra have IL=15 dB, FSR=1.34 nm, best Q factor of $6.9 \cdot 10^3$, ER=6.5 dB, SR= 100 dB/nm.

MR-ADF with Lc_2=19 µm

Figure 3.3-19 shows the experimentally measured spectra of DC-MR ADF from 1500 nm to 1580 nm with Lc_1=10.7 µm and Lc_2=19 µm. The output ports 1, 3 and 4 are shown in green, blue, and red, respectively. Figure 3.3-20 shows the experimentally measured DC-MR ADF spectra from 1510 nm to 1520 nm with Lc_1=10.7 µm and Lc_2=19 µm. The output ports 1, 3 and 4 are shown in green, blue, and red, respectively. The FSR of the spectra is 1.33 nm. Figure 3.3-21 shows the experimentally measured DC-MR ADF spectra of output 1 from 1516 nm to 1520 nm with Lc_1=10.7 µm and Lc_2=19 µm. The spectra have IL=18 dB, FSR=1.32 nm, best eff-Q=$1.2\cdot10^4$, ER=8.8 dB, SR=42 dB/nm. Figure 3.3-22 shows the experimentally measured DC-MR ADF spectra of the output 3 from 1516 nm to 1520 nm with Lc_1=10.7 µm and Lc_2=19 µm. The spectra have IL=20 dB, FSR= 1.33 nm, best Q-factor of $9\cdot10^3$, ER=16 dB and SR=64 dB/nm. Figure 3.3-23 shows the experimentally measured DC-MR ADF spectra of the output 4 from 1516 nm to 1520 nm with coupling lengths of Lc_1=10.7 µm and Lc_2=19 µm. The spectra have IL=13 dB, FSR=1.34 nm, best Q factor of $7.2\cdot10^3$, ER=6.6 dB, SR= 31 dB/nm.

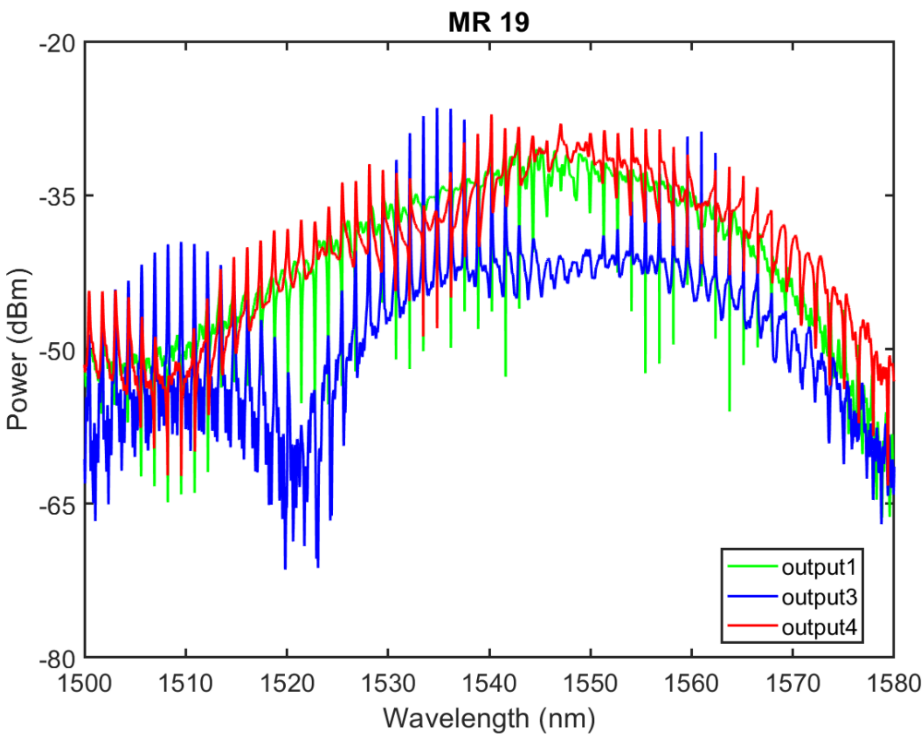

Figure 3.3-19: The experimentally measured spectra of DC-MR ADF from 1500 nm to 1580 nm with Lc_1=10.7 µm and Lc_2=19 µm. The output ports 1, 3 and 4 are shown in green, blue, and red, respectively.

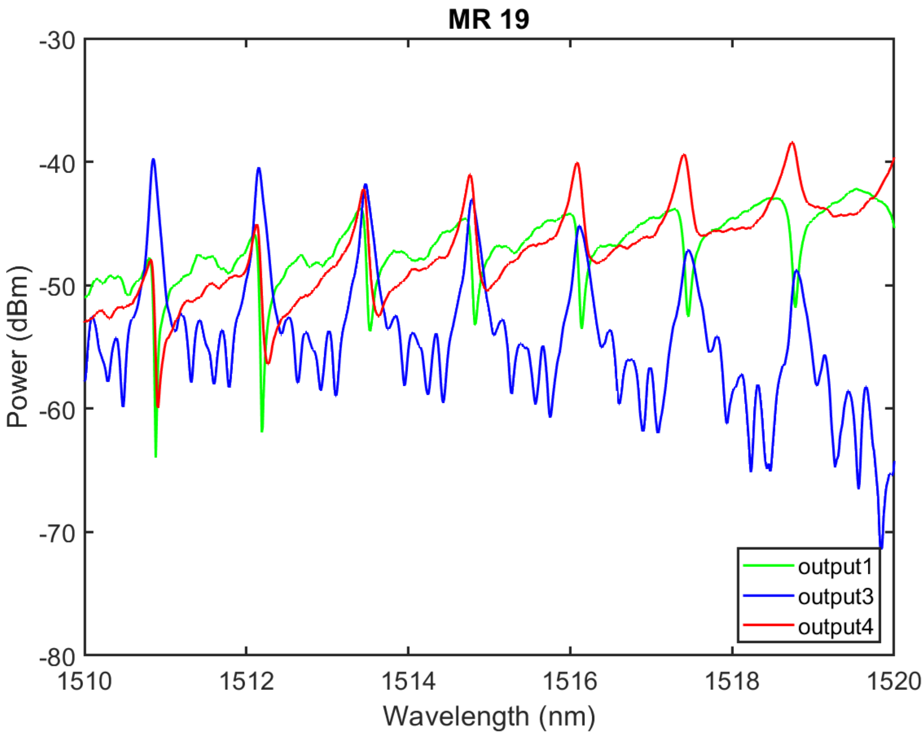

Figure 3.3-20: The experimentally measured DC-MR ADF spectra from 1510 nm to 1520 nm with Lc_1=10.7 µm and Lc_2=19 µm. The output ports 1, 3 and 4 are shown in green, blue, and red, respectively. The FSR of the spectra is 1.33 nm.

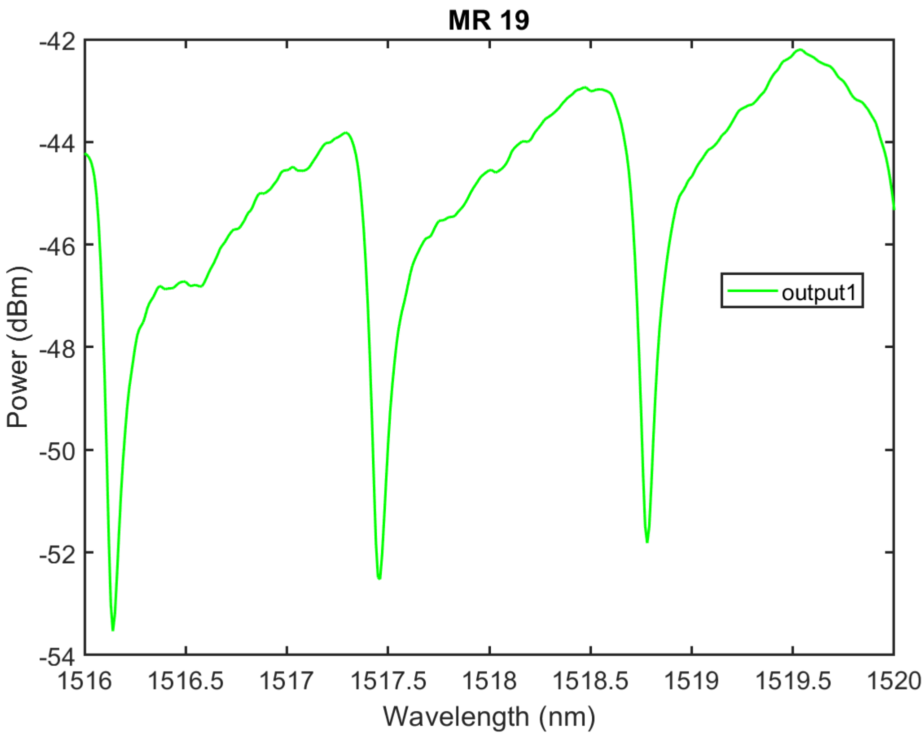

Figure 3.3-21: The experimentally measured DC-MR ADF spectra of output 1 from 1516 nm to 1520 nm with Lc_1=10.7 µm and Lc_2=19 µm. The spectra have IL=18 dB, FSR=1.32 nm, best eff-Q=$1.2 \cdot 10^4$, ER=8.8 dB, SR=42 dB/nm.

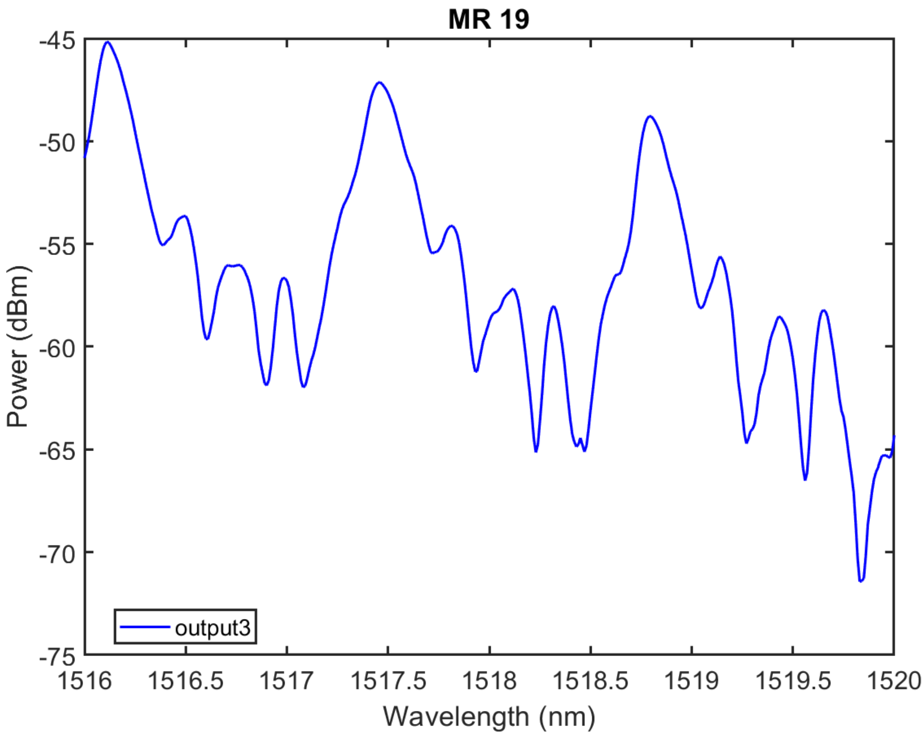

Figure 3.3-22: The experimentally measured DC-MR ADF spectra of the output 3 from 1516 nm to 1520 nm with Lc_1=10.7 μm and Lc_2=19 μm. The spectra have IL=20 dB, FSR= 1.33 nm, best Q-factor of $9 \cdot 10^3$, ER=16 dB and SR=64 dB/nm.

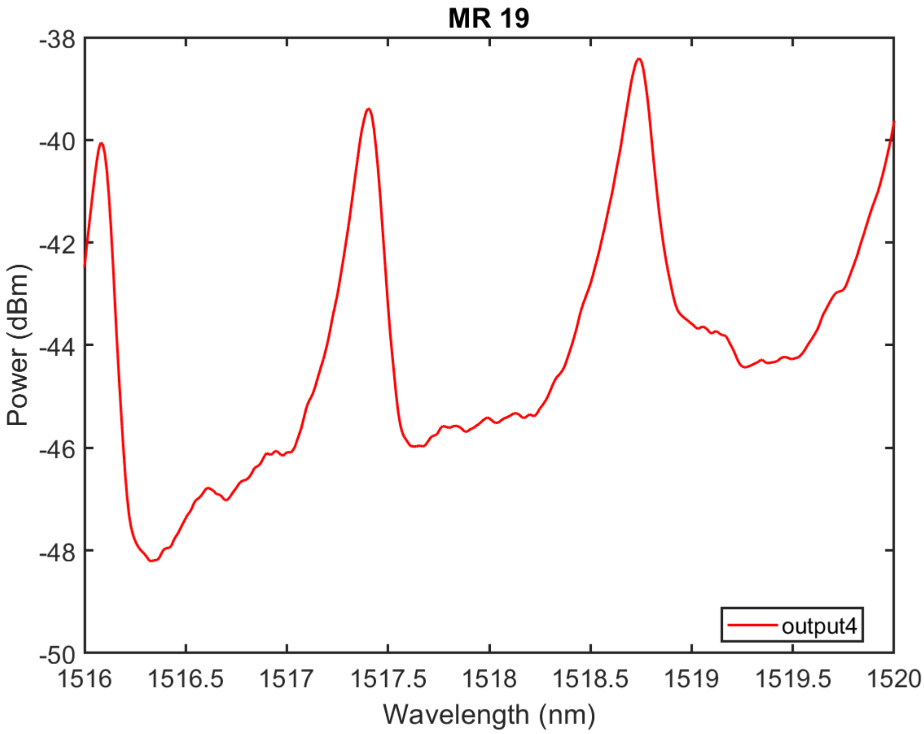

Figure 3.3-23: The experimentally measured DC-MR ADF spectra of the output 4 from 1516 nm to 1520 nm with coupling lengths of Lc_1=10.7 μm and Lc_2=19 μm. The spectra have IL=13 dB, FSR=1.34 nm, best Q factor of $7.2 \cdot 10^3$, ER=6.6 dB, SR= 31 dB/nm.

MR-ADF with Lc_2=20 µm

Figure 3.3-24 shows the experimentally measured spectra of DC-MR ADF from 1500 nm to 1580 nm with Lc_1=10.7 µm and Lc_2=20 µm. The output ports 1, 3 and 4 are shown in green, blue, and red, respectively. Figure 3.3-25 shows the experimentally measured DC-MR ADF spectra from 1510 nm to 1520 nm with Lc_1=10.7 µm and Lc_2=20 µm. The output ports 1, 3 and 4 are shown in green, blue, and red, respectively. The FSR of the spectra is 1.32 nm. Figure 3.3-26 shows the experimentally measured DC-MR ADF spectra of output 1 from 1516 nm to 1520 nm with Lc_1=10.7 µm and Lc_2=20 µm. The spectra have IL=11 dB, FSR=1.32 nm, best eff-Q=$2.2\cdot10^4$, ER=8.7 dB, SR=62 dB/nm. Figure 3.3-27 shows the experimentally measured DC-MR ADF spectra of the output 3 from 1516 nm to 1520 nm with Lc_1=10.7 µm and Lc_2=20 µm. The spectra have IL=11 dB, FSR= 1.32 nm, best Q-factor of $1\cdot10^4$, ER=17 dB and SR=39 dB/nm. Figure 3.3-28 shows the experimentally measured DC-MR ADF spectra of the output 4 from 1516 nm to 1520 nm with coupling lengths of Lc_1=10.7 µm and Lc_2=20 µm. The spectra have IL=15 dB, FSR=1.32 nm, best Q-factor of $7.2\cdot10^3$, ER=6.5 dB, SR= 30 dB/nm.

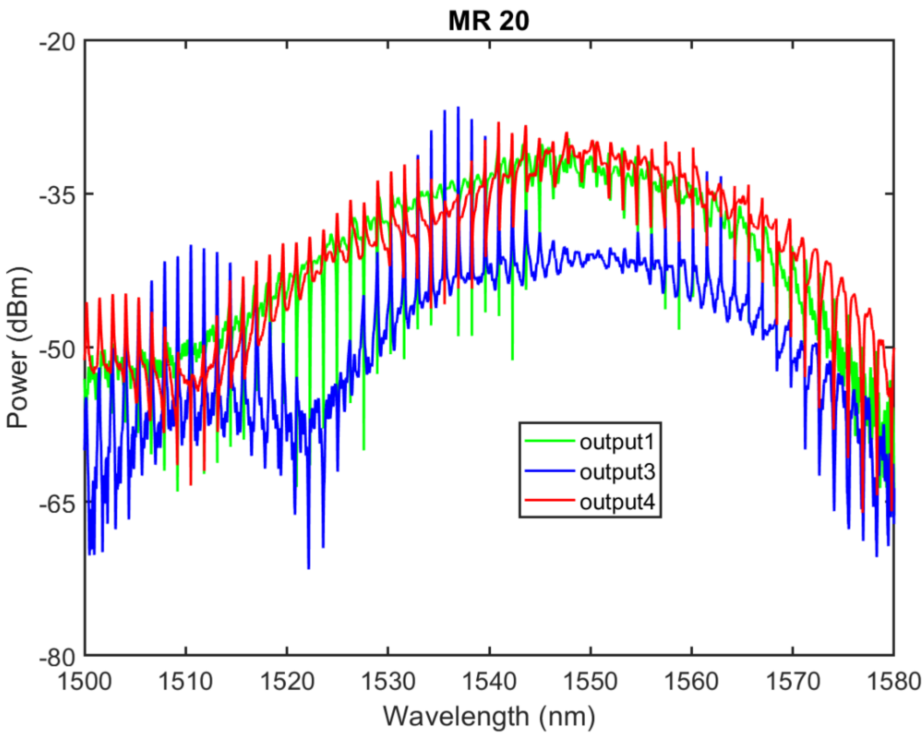

Figure 3.3-24: The experimentally measured spectra of DC-MR ADF from 1500 nm to 1580 nm with Lc_1=10.7 µm and Lc_2=20 µm. The output ports 1, 3 and 4 are shown in green, blue, and red, respectively.

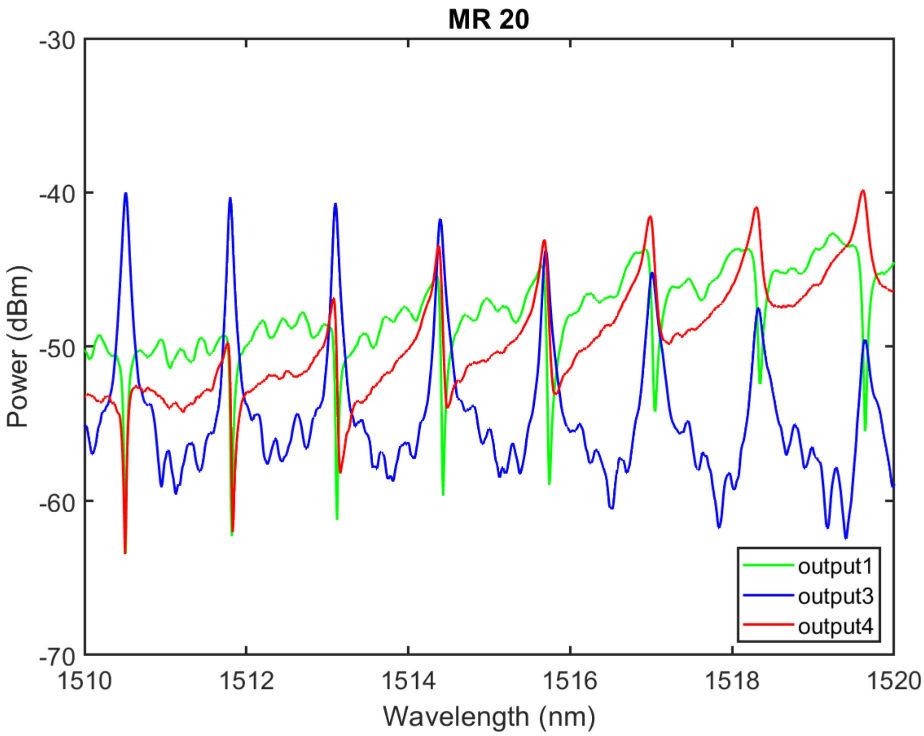

Figure 3.3-25: The experimentally measured DC-MR ADF spectra from 1510 nm to 1520 nm with Lc_1=10.7 μm and Lc_2=20 μm. The output ports 1, 3 and 4 are shown in green, blue, and red, respectively. The FSR of the spectra is 1.32 nm.

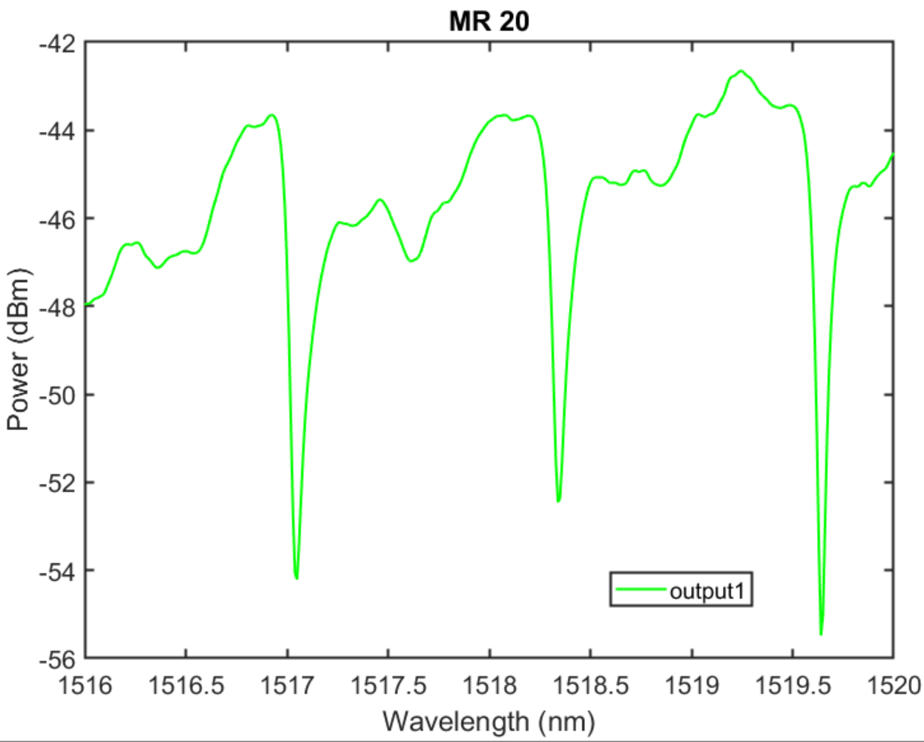

Figure 3.3-26: The experimentally measured DC-MR ADF spectra of output 1 from 1516 nm to 1520 nm with Lc_1=10.7 μm and Lc_2=20 μm. The spectra have IL=11 dB, FSR=1.32 nm, best eff-Q=$2.2\cdot10^4$, ER=8.7 dB, SR=62 dB/nm.

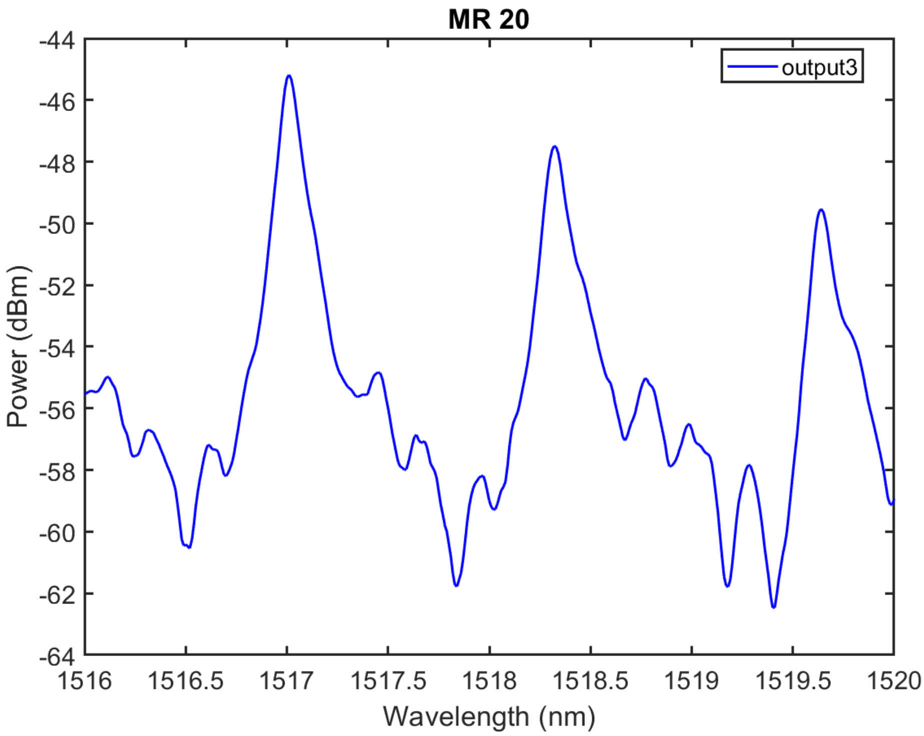

Figure 3.3-27: The experimentally measured DC-MR ADF spectra of the output 3 from 1516 nm to 1520 nm with Lc_1=10.7 µm and Lc_2=20 µm. The spectra have IL=11 dB, FSR= 1.32 nm, best Q-factor of $1\cdot10^4$, ER=17 dB and SR=39 dB/nm.

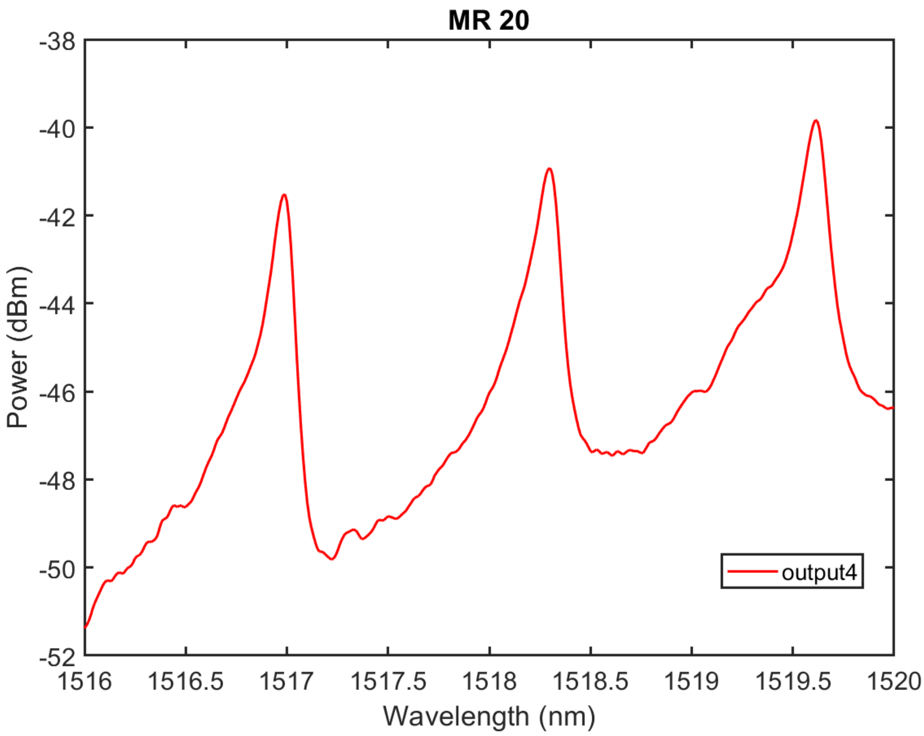

Figure 3.3-28: The experimentally measured DC-MR ADF spectra of the output 4 from 1516 nm to 1520 nm with coupling lengths of Lc_1=10.7 µm and Lc_2=20 µm. The spectra have IL=15 dB, FSR=1.32 nm, best Q-factor of $7.2\cdot10^3$, ER=6.5 dB, SR= 30 dB/nm.

3.4. Double Coupled SMR ADF

The double coupled SMR (DC-SMR) add-drop filter (ADF) is fabricated to see the effect of the second meandering resonator in the optical path by adding one more coupling point coming from the second MLM which is reversed to increase the layout efficiency due to the size limitations. The coupling length L_c of the (DC-SMR) IC coupler is 10.7 μm and the IC coupler length is kept constant in all designs of DC-SMR ADF. The FSR can be calculated with the formula $FSR = \frac{\lambda^2}{n_g L}$. Figure 3.4-1 shows the representation of DC-SMR ADF and Figure 3.4-2 shows the SEM image of DC-SMR ADF. Figure 3.4-3 shows the KLayout design of the DC-SMR with the corresponding coupling dimensions and bend radii with the positions of the input and output ports, which the ports are numbered as 1,2,3,4 and a prefix is added if the port is used as output. For example, the input is always the port 2 and it is not numbered, and mentioned only as input while the output 1, meaning the first (upper most) grating coupler) which is utilized as an output port. The coupler bending radius of 10 μm and the waveguide bending radius of 5 μm and the gap between the coupler waveguides g=200 nm is constant in all designs.

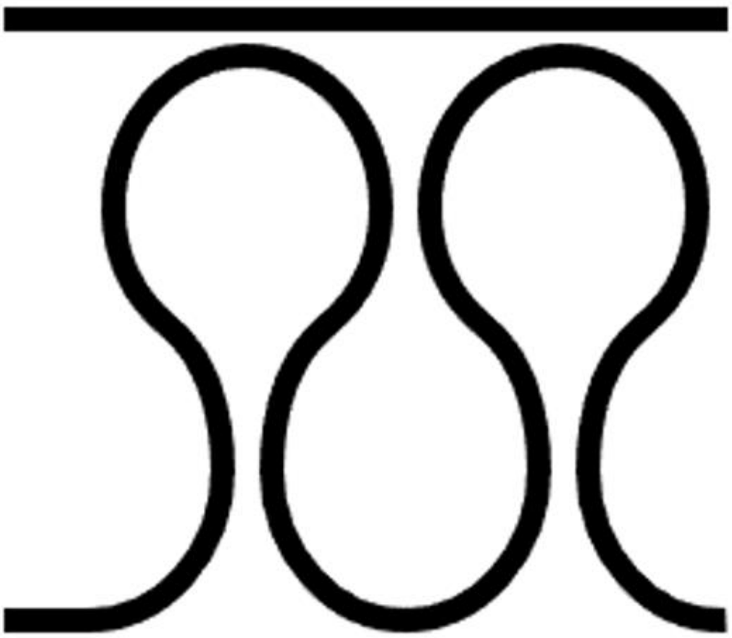

Figure 3.4-1: The representation of SMR ADF.

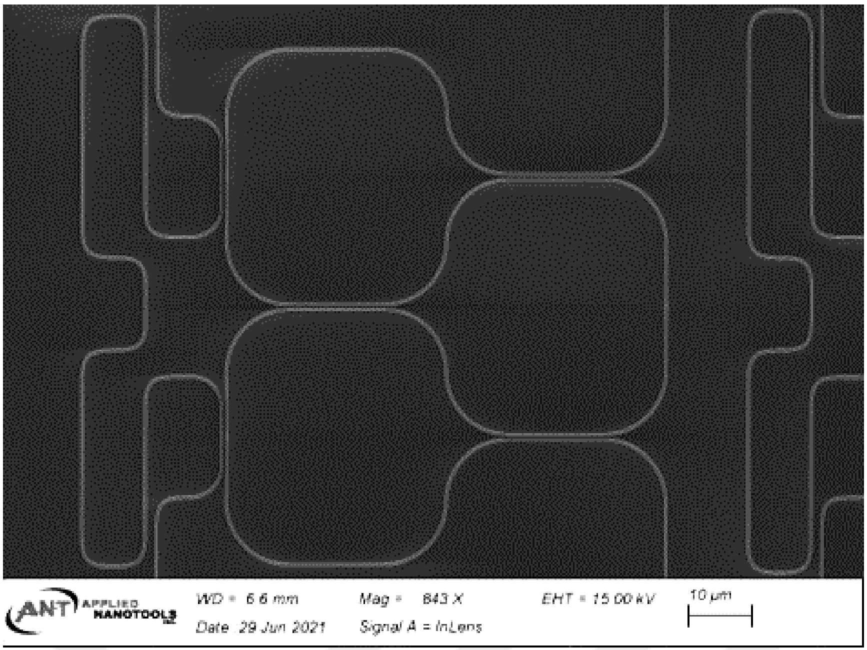

Figure 3.4-2: SEM image of the fabricated DC-SMR add-drop filter

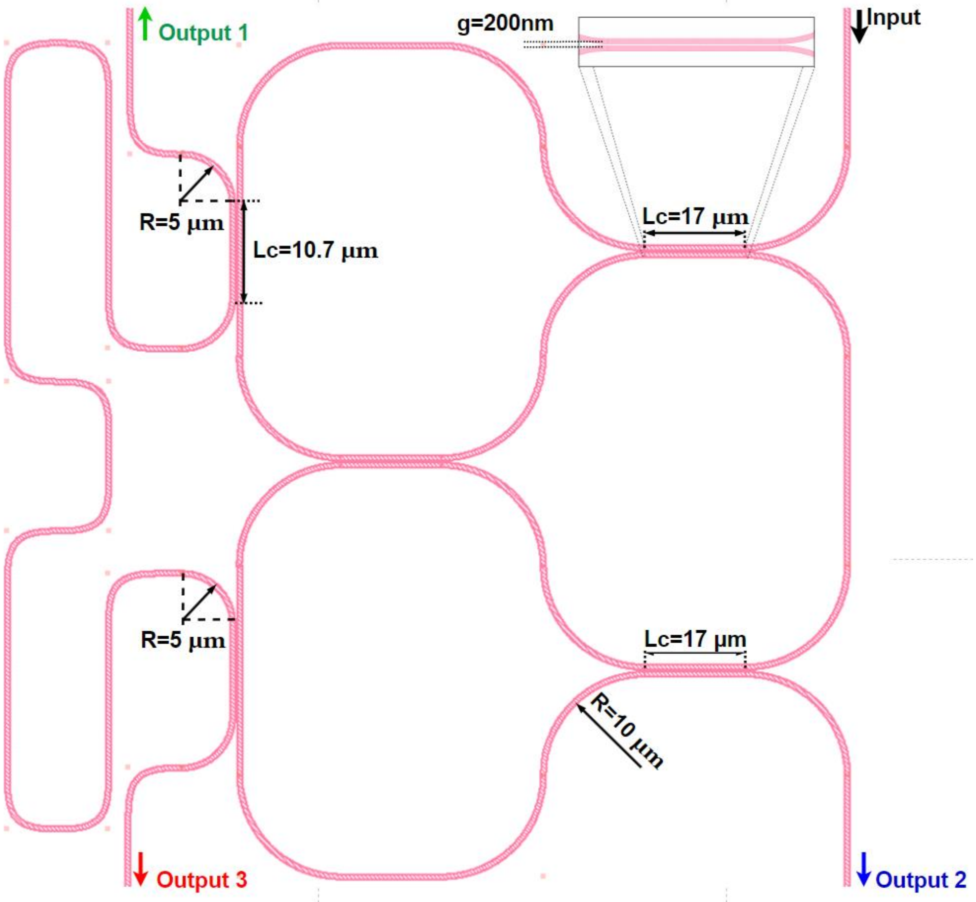

Figure 3.4-3 Representation of DC-SMR with output shown in black, output 1,2 and 3 is shown in green, blue, and red, respectively. The IC coupler has a coupling length of $L_{c=}10.7$ µm and the CC coupler has $L_{c=}17$ µm (specific to chosen design), waveguides have a bending radius of 5 µm while the couplers' bending radius is 10 µm, the gap between the bus waveguides in the couplers is g=200 nm

DC-SMR ADF with Lc_2=10 µm

Figure 3.4-4 shows the experimentally measured spectra of DC-SMR ADF from 1500 nm to 1580 nm with Lc_1=10.7 µm and Lc_2=10 µm. The output ports 1, 3 and 4 are shown in green, blue, and red, respectively. Figure 3.4-5 shows the experimentally measured DC-SMR ADF spectra from 1545 nm to 1555 nm with Lc_1=10.7 µm and Lc_2=10 µm. The output ports 1, 3 and 4 are shown in green, blue, and red, respectively. The FSR of the spectra is 2.77 nm. Figure 3.4-6 shows the experimentally measured DC-SMR ADF spectra of output 1 from 1547 nm to 1552 nm with Lc_1=10.7 µm and Lc_2=10 µm. The spectra have IL=15 dB, FSR=2.77 nm, best eff-Q=$4.4 \cdot 10^3$, ER=15.2 dB, SR=35 dB/nm. Figure 3.4-7 shows the experimentally measured DC-SMR ADF spectra of the output 3 from 1547 nm to 1552 nm with Lc_1=10.7 µm and Lc_2=10 µm. The spectra have IL=11 dB, FSR= 2.77 nm, best eff-Q=$4.4 \cdot 10^3$, ER=30 dB and SR=8 dB/nm. Figure 3.4-8 shows the experimentally measured DC-SMR ADF spectra of the output 4 from 1547 nm to 1552 nm with coupling lengths of Lc_1=10.7 µm and Lc_2=10 µm. The spectra have IL=9 dB, FSR=2.77 nm, ER=10.3 dB, SR= 14 dB/nm.

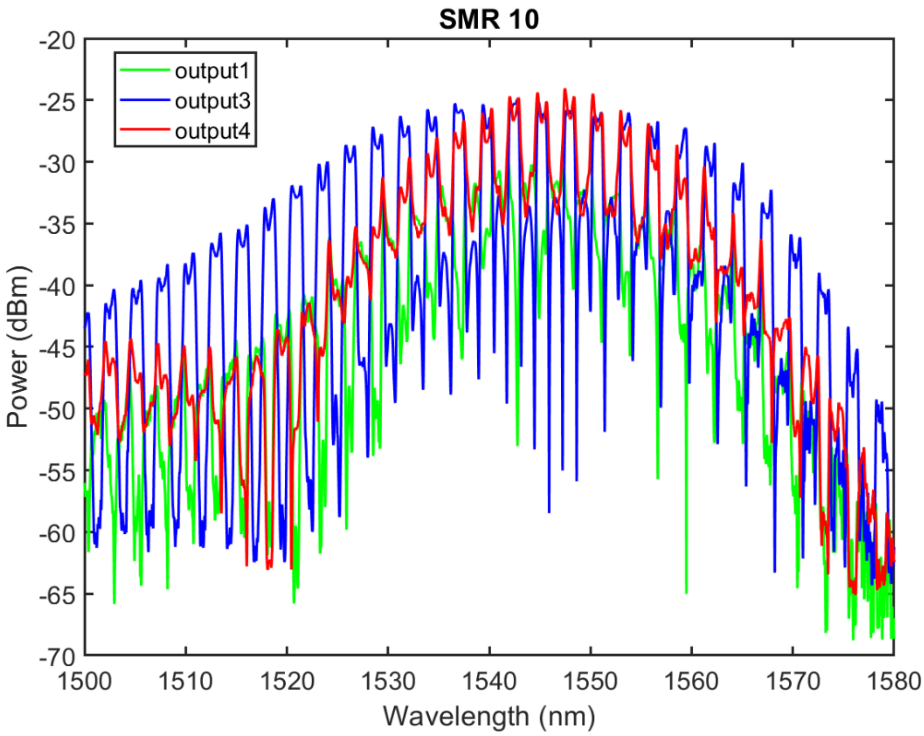

Figure 3.4-4: The experimentally measured spectra of DC-SMR ADF from 1500 nm to 1580 nm with Lc_1=10.7 µm and Lc_2=10 µm. The output ports 1, 3 and 4 are shown in green, blue, and red, respectively.

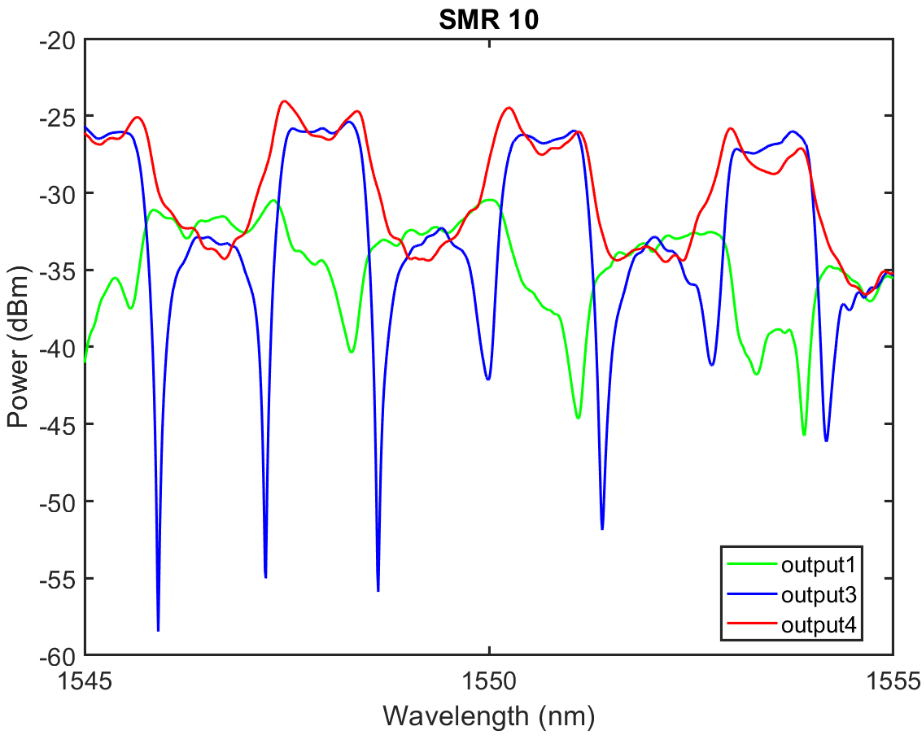

Figure 3.4-5: The experimentally measured DC-SMR ADF spectra from 1545 nm to 1555 nm with Lc_1=10.7 μm and Lc_2=10 μm. The output ports 1, 3 and 4 are shown in green, blue, and red, respectively. The FSR of the spectra is 2.77 nm.

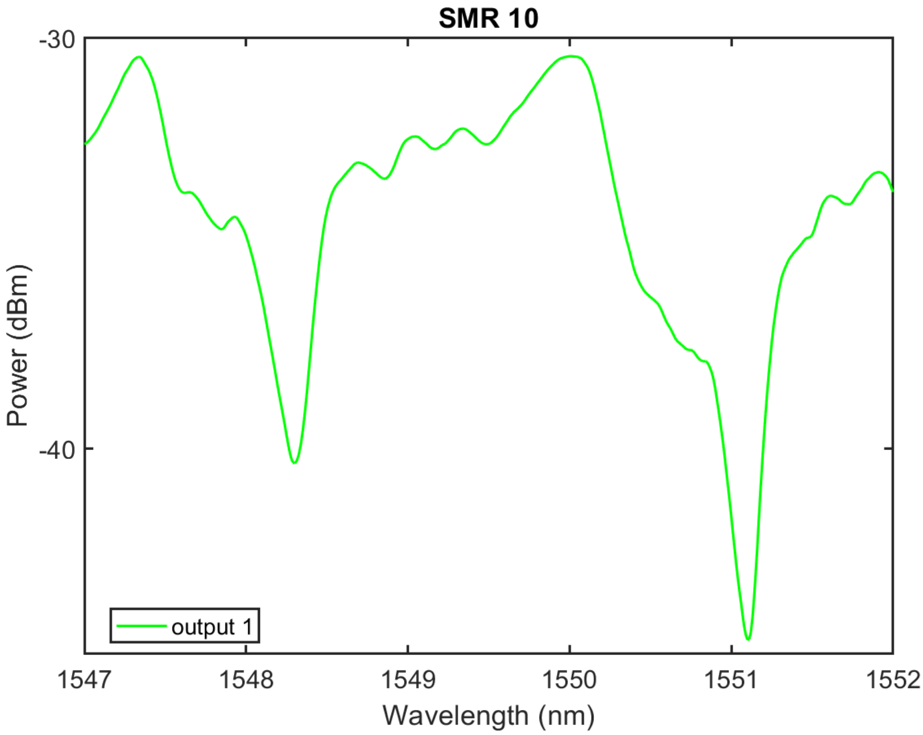

Figure 3.4-6: The experimentally measured DC-SMR ADF spectra of output 1 from 1547 nm to 1552 nm with Lc_1=10.7 μm and Lc_2=10 μm. The spectra have IL=15 dB, FSR=2.77 nm, best eff-Q=$4.4\cdot10^3$, ER=15.2 dB, SR=35 dB/nm.

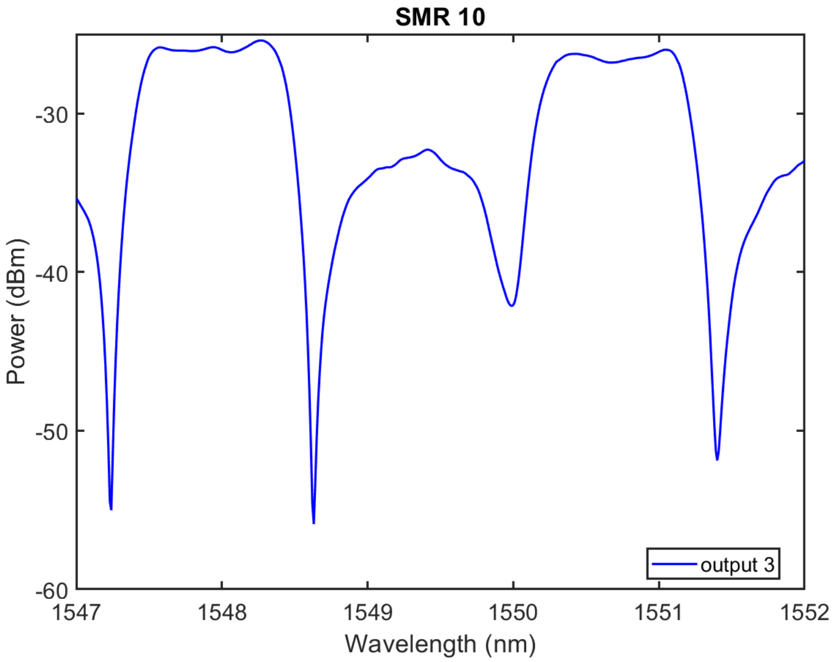

Figure 3.4-7: The experimentally measured DC-SMR ADF spectra of the output 3 from 1547 nm to 1552 nm with Lc_1=10.7 μm and Lc_2=10 μm. The spectra have IL=11 dB, FSR= 2.77 nm, best eff-Q=$4.4 \cdot 10^3$, ER=30 dB and SR=8 dB/nm.

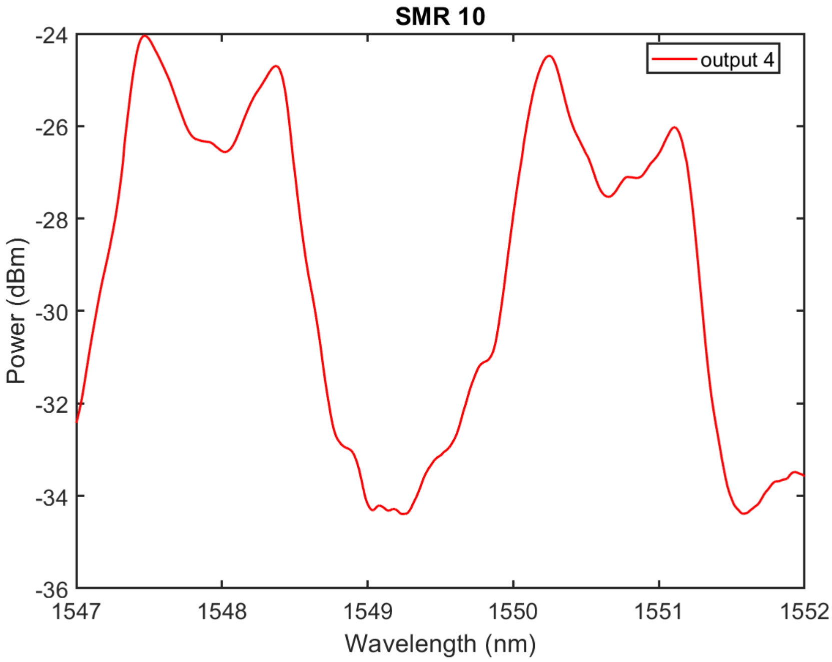

Figure 3.4-8: The experimentally measured DC-SMR ADF spectra of the output 4 from 1547 nm to 1552 nm with coupling lengths of Lc_1=10.7 μm and Lc_2=10 μm. The spectra have IL=9 dB, FSR=2.77 nm, ER=10.3 dB, SR= 14 dB/nm.

DC-SMR ADF with Lc_2=15 µm

Figure 3.4-9 shows the experimentally measured spectra of DC-SMR ADF from 1500 nm to 1580 nm with Lc_1=10.7 µm and Lc_2=15 µm. The output ports 1, 3 and 4 are shown in green, blue, and red, respectively. Figure 3.4-10 shows the experimentally measured DC-SMR ADF spectra from 1545 nm to 1555 nm with Lc_1=10.7 µm and Lc_2=15 µm. The output ports 1, 3 and 4 are shown in green, blue, and red, respectively. The FSR of the spectra is 2.51 nm. Figure 3.4-11 shows the experimentally measured DC-SMR ADF spectra of output 1 from 1547 nm to 1552 nm with Lc_1=10.7 µm and Lc_2=15 µm. The spectra have IL=2 dB, FSR=2.52 nm, best eff-Q=$8.6\cdot10^3$, ER=7.5 dB, SR=27 dB/nm. Figure 3.4-12 shows the experimentally measured DC-SMR ADF spectra of the output 3 from 1547 nm to 1552 nm with Lc_1=10.7 µm and Lc_2=15 µm. The spectra have IL=2 dB, FSR= 2.51 nm, best eff-Q=$1.1\cdot10^4$, ER=24 dB and SR=9 dB/nm. Figure 3.4-13 shows the experimentally measured DC-SMR ADF spectra of the output 4 from 1547 nm to 1552 nm with coupling lengths of Lc_1=10.7 µm and Lc_2=15 µm. The spectra have IL=1 dB, FSR=2.52 nm, best eff-Q=$6.1\cdot10^3$, ER=9.5 dB, SR= 18 dB/nm.

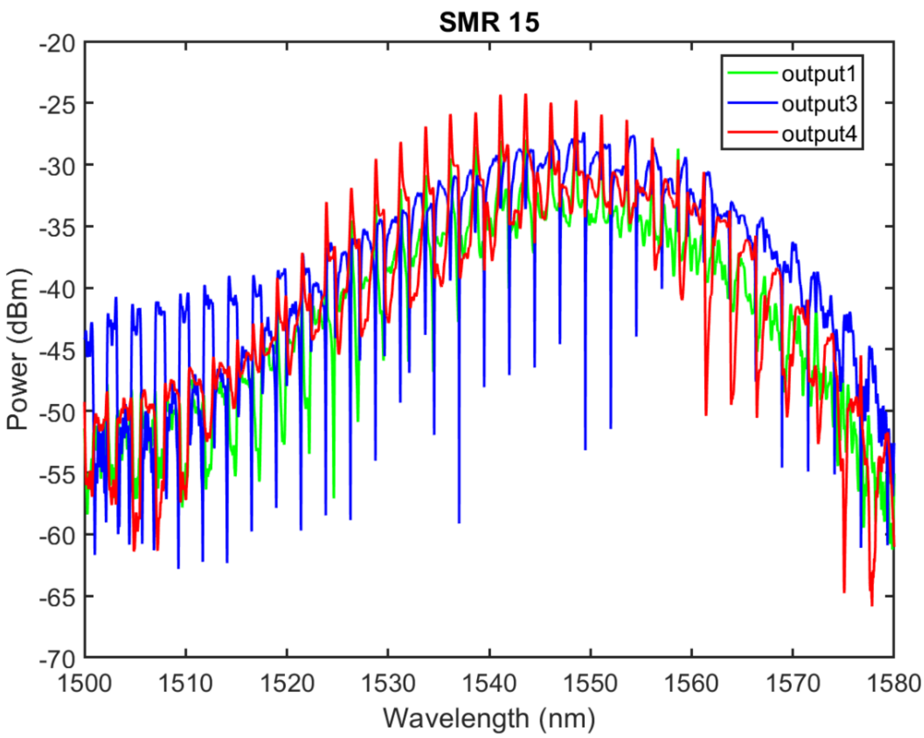

Figure 3.4-9: the experimentally measured spectra of DC-SMR ADF from 1500 nm to 1580 nm with Lc_1=10.7 µm and Lc_2=15 µm. The output ports 1, 3 and 4 are shown in green, blue, and red, respectively.

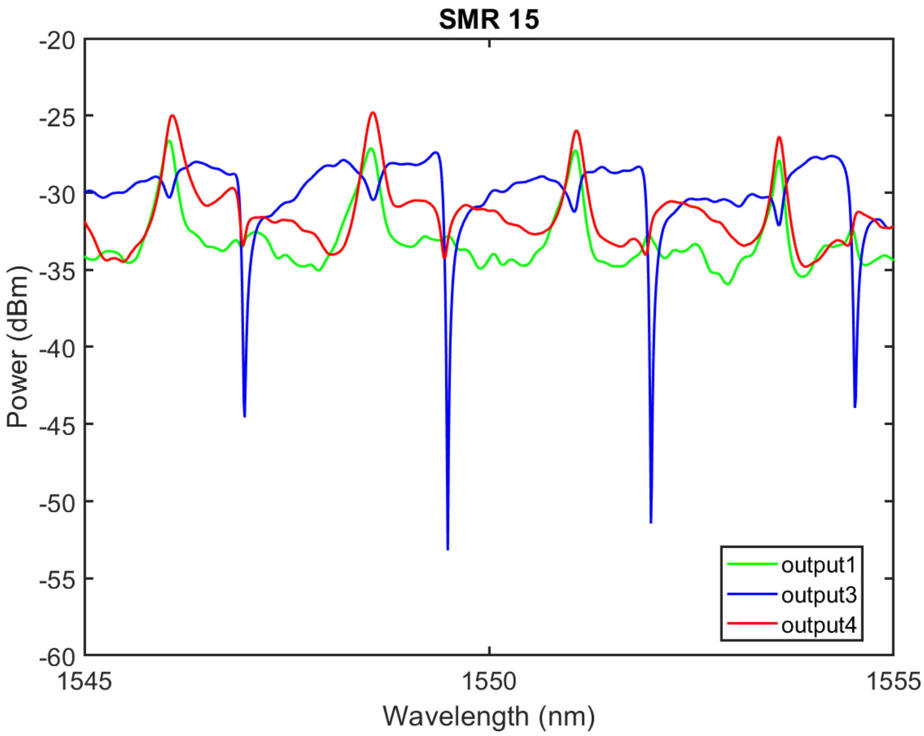

Figure 3.4-10: The experimentally measured DC-SMR ADF spectra from 1545 nm to 1555 nm with Lc_1=10.7 µm and Lc_2=15 µm. The output ports 1, 3 and 4 are shown in green, blue, and red, respectively. The FSR of the spectra is 2.51 nm.

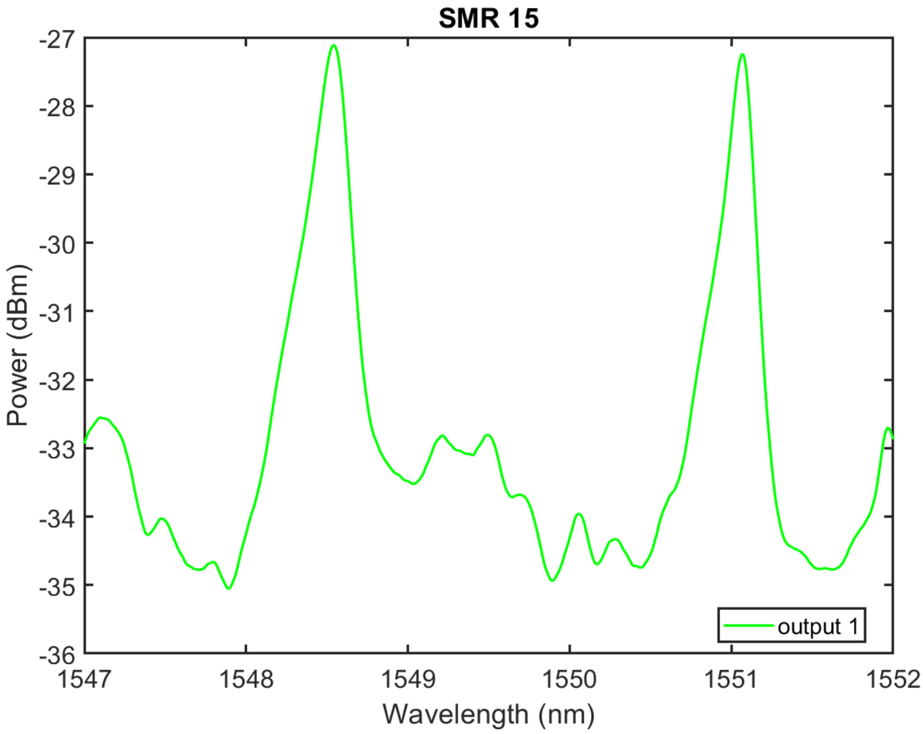

Figure 3.4-11: The experimentally measured DC-SMR ADF spectra of output 1 from 1547 nm to 1552 nm with Lc_1=10.7 µm and Lc_2=15 µm. The spectra have IL=2 dB, FSR=2.52 nm, best eff-Q=$8.6 \cdot 10^3$, ER=7.5 dB, SR=27 dB/nm.

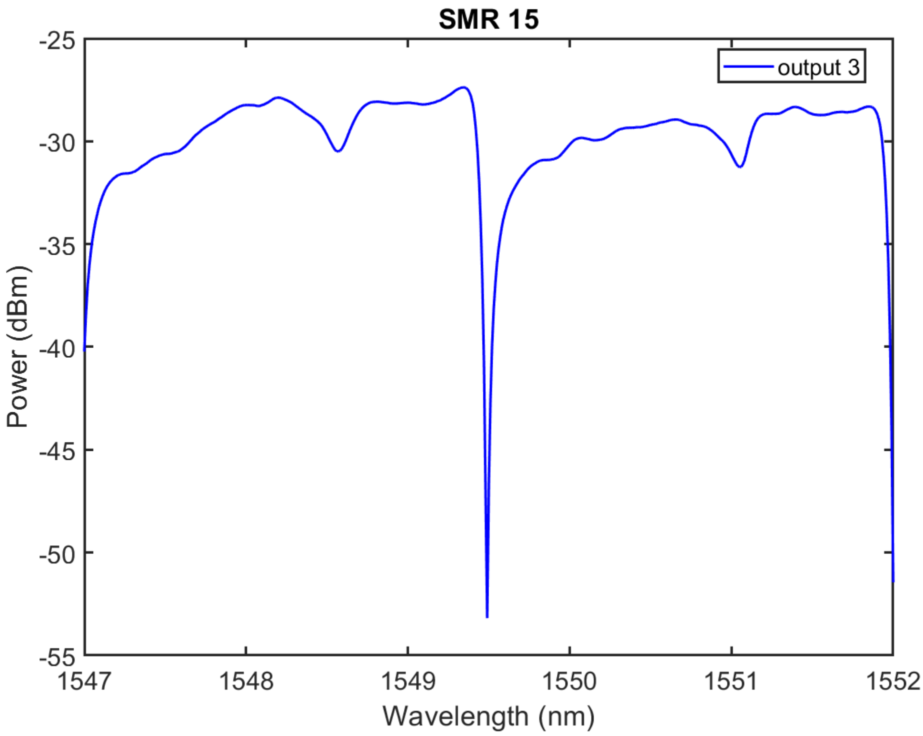

Figure 3.4-12: The experimentally measured DC-SMR ADF spectra of the output 3 from 1547 nm to 1552 nm with Lc_1=10.7 µm and Lc_2=15 µm. The spectra have IL=2 dB, FSR= 2.51 nm, best eff-Q=$1.1 \cdot 10^4$, ER=24 dB and SR=9 dB/nm.

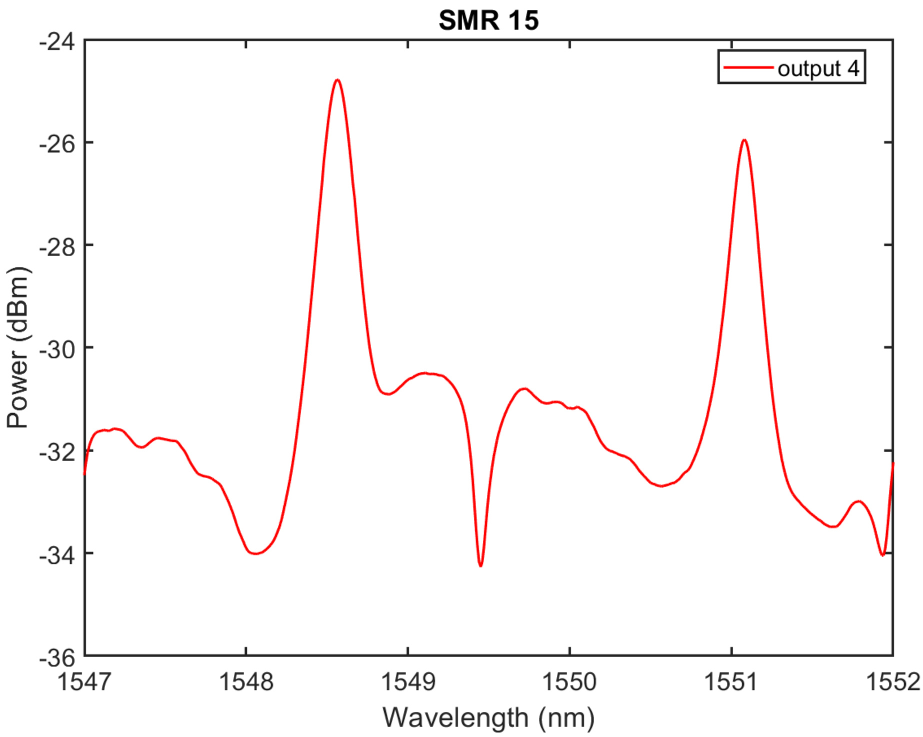

Figure 3.4-13: The experimentally measured DC-SMR ADF spectra of the output 4 from 1547 nm to 1552 nm with coupling lengths of Lc_1=10.7 µm and Lc_2=15 µm. The spectra have IL=1 dB, FSR=2.52 nm, best eff-Q=$6.1 \cdot 10^3$, ER=9.5 dB, SR= 18 dB/nm.

DC-SMR ADF with Lc_2=17 µm

Figure 3.4-14 shows the experimentally measured spectra of DC-SMR ADF from 1500 nm to 1580 nm with Lc_1=10.7 µm and Lc_2=17 µm. The output ports 1, 3 and 4 are shown in green, blue, and red, respectively. Figure 3.4-15 shows the experimentally measured DC-SMR ADF spectra from 1545 nm to 1555 nm with Lc_1=10.7 µm and Lc_2=17 µm. The output ports 1, 3 and 4 are shown in green, blue, and red, respectively. The FSR of the spectra is 2.42 nm. Figure 3.4-16 shows the experimentally measured DC-SMR ADF spectra of output 1 from 1547 nm to 1552 nm with Lc_1=10.7 µm and Lc_2=17 µm. The spectra have IL=3 dB, FSR=2.43 nm, best eff-Q=$9.1 \cdot 10^3$, ER=13 dB, SR=59 dB/nm. Figure 3.4-17 shows the experimentally measured DC-SMR ADF spectra of the output 3 from 1547 nm to 1552 nm with Lc_1=10.7 µm and Lc_2=17 µm. The spectra have IL=1 dB, FSR= 2.42 nm, best eff-Q=$3 \cdot 10^4$, ER=13.5 dB and SR=5.4 dB/nm. Figure 3.4-18 shows the experimentally measured DC-SMR ADF spectra of the output 4 from 1547 nm to 1552 nm with coupling lengths of Lc_1=10.7 µm and Lc_2=17 µm. The spectra have IL=2 dB, FSR=2.42 nm, best eff-Q=$1.1 \cdot 10^4$, ER=13 dB, SR= 110 dB/nm.

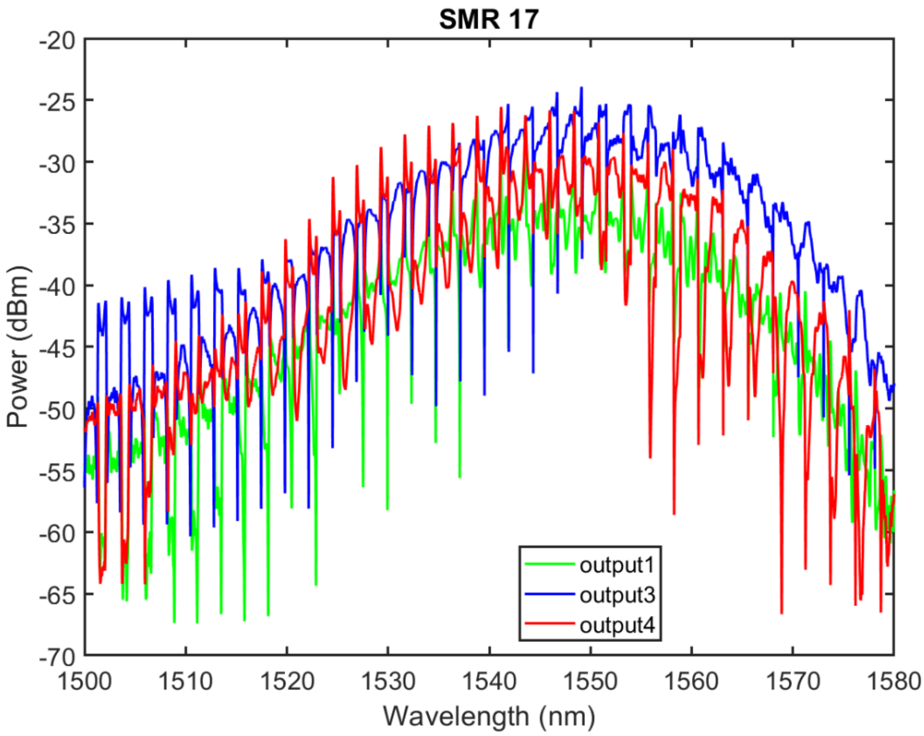

Figure 3.4-14: The experimentally measured spectra of DC-SMR ADF from 1500 nm to 1580 nm with Lc_1=10.7 µm and Lc_2=17 µm. The output ports 1, 3 and 4 are shown in green, blue, and red, respectively.

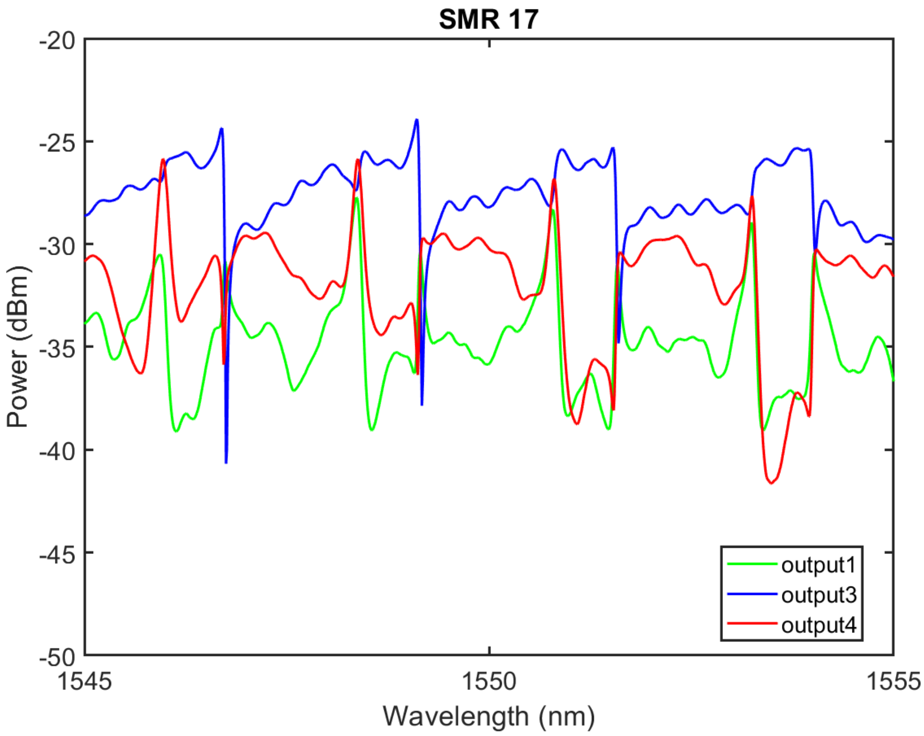

Figure 3.4-15: The experimentally measured DC-SMR ADF spectra from 1545 nm to 1555 nm with Lc_1=10.7 μm and Lc_2=17 μm. The output ports 1, 3 and 4 are shown in green, blue, and red, respectively. The FSR of the spectra is 2.42 nm.

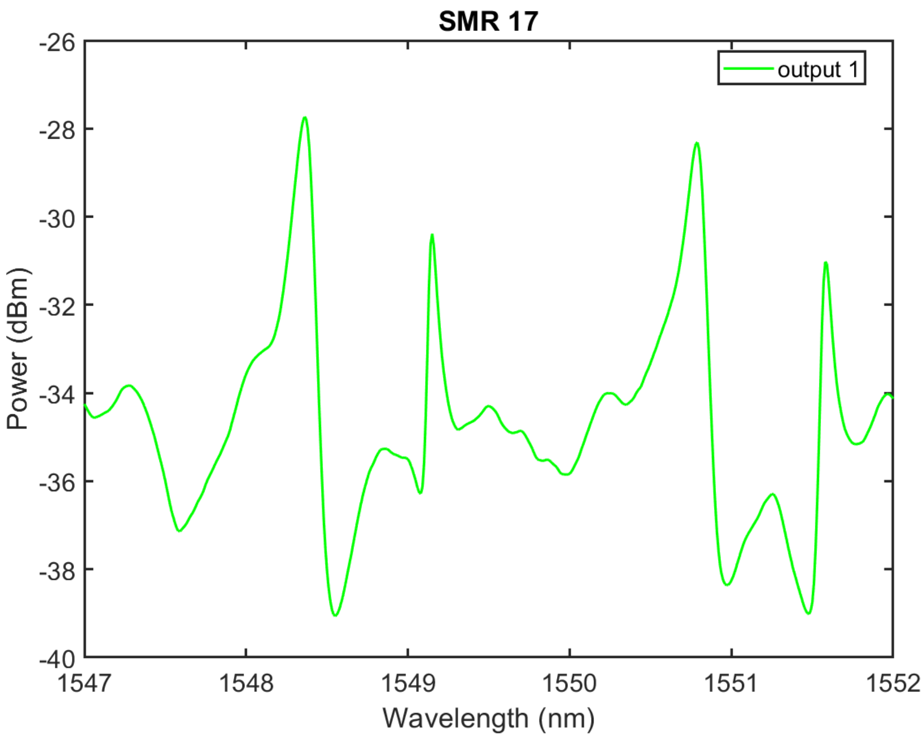

Figure 3.4-16: The experimentally measured DC-SMR ADF spectra of output 1 from 1547 nm to 1552 nm with Lc_1=10.7 μm and Lc_2=17 μm. The spectra have IL=3 dB, FSR=2.43 nm, best eff-Q=$9.1 \cdot 10^3$, ER=13 dB, SR=59 dB/nm.

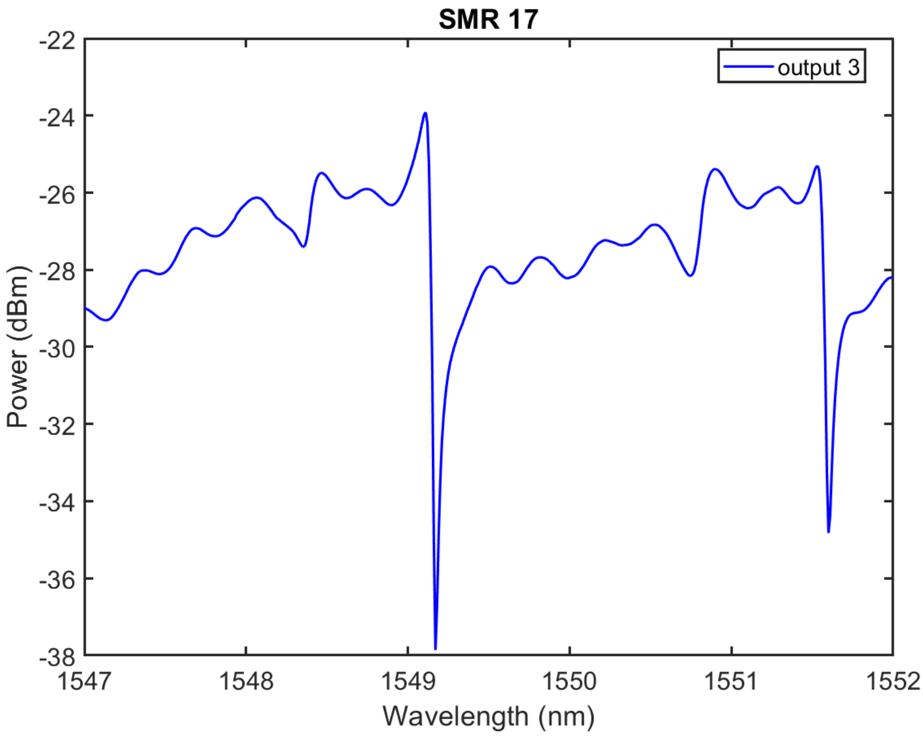

Figure 3.4-17: The experimentally measured DC-SMR ADF spectra of the output 3 from 1547 nm to 1552 nm with Lc_1=10.7 µm and Lc_2=17 µm. The spectra have IL=1 dB, FSR= 2.42 nm, best eff-Q=$3\cdot10^4$, ER=13.5 dB and SR=5.4 dB/nm.

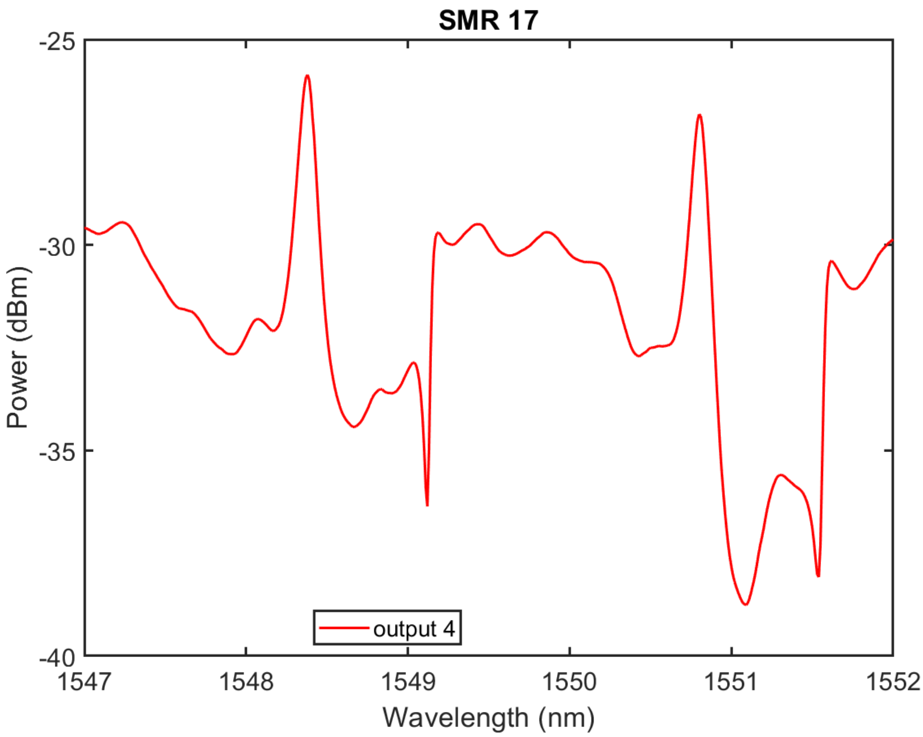

Figure 3.4-18: The experimentally measured DC-SMR ADF spectra of the output 4 from 1547 nm to 1552 nm with coupling lengths of Lc_1=10.7 µm and Lc_2=17 µm. The spectra have IL=2 dB, FSR=2.42 nm, best eff-Q=$11.1\cdot10^3$, ER=13 dB, SR= 110 dB/nm.

DC-SMR ADF with Lc_2=20 µm

Figure 3.4-19 shows the experimentally measured spectra of DC-SMR ADF from 1500 nm to 1580 nm with Lc_1=10.7 µm and Lc_2=20 µm. The output ports 1, 3 and 4 are shown in green, blue, and red, respectively. Figure 3.4-20 shows the experimentally measured DC-SMR ADF spectra from 1545 nm to 1555 nm with Lc_1=10.7 µm and Lc_2=20 µm. The output ports 1, 3 and 4 are shown in green, blue, and red, respectively. The FSR of the spectra is 2.32 nm. Figure 3.4-21 shows the experimentally measured DC-SMR ADF spectra of output 1 from 1547 nm to 1552 nm with Lc_1=10.7 µm and Lc_2=20 µm. The spectra have IL=3 dB, FSR=2.32 nm, best eff-Q=$1.03\cdot10^4$, ER=13 dB, SR=222 dB/nm. Figure 3.4-22 shows the experimentally measured DC-SMR ADF spectra of the output 3 from 1547 nm to 1552 nm with Lc_1=10.7 µm and Lc_2=20 µm. The spectra have IL=1 dB, FSR= 2.31 nm, best eff-Q=$3.87\cdot10^4$, ER=15.4 dB and SR=330 dB/nm. Figure 3.4-23 shows the experimentally measured DC-SMR ADF spectra of the output 4 from 1547 nm to 1552 nm with coupling lengths of Lc_1=10.7 µm and Lc_2=20 µm. The spectra have IL=3 dB, FSR=2.32 nm, best eff-Q=$9.1\cdot10^3$, ER=26 dB, SR= 69.6 dB/nm.

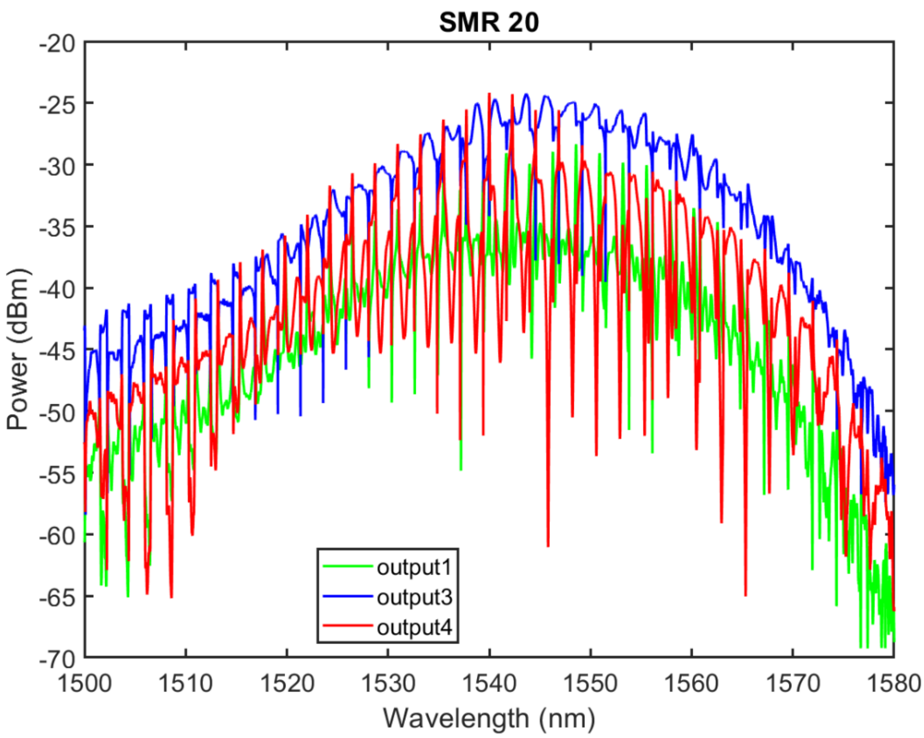

Figure 3.4-19: The experimentally measured spectra of DC-SMR ADF from 1500 nm to 1580 nm with Lc_1=10.7 µm and Lc_2=20 µm. The output ports 1, 3 and 4 are shown in green, blue, and red, respectively.

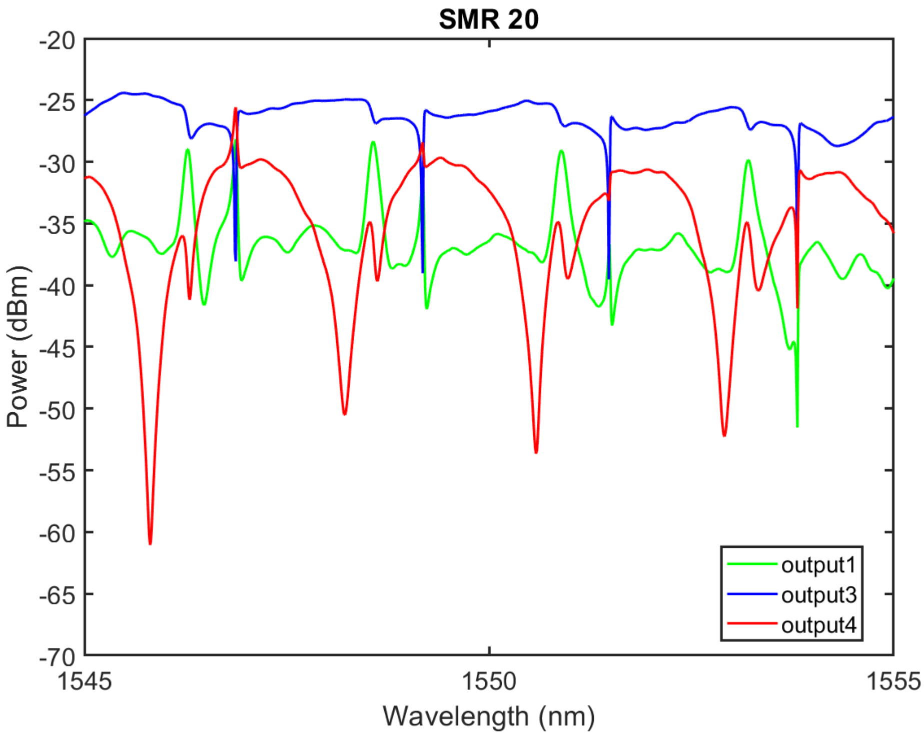

Figure 3.4-20: The experimentally measured DC-SMR ADF spectra from 1510 nm to 1520 nm with Lc_1=10.7 µm and Lc_2=20 µm. The output ports 1, 3 and 4 are shown in green, blue, and red, respectively. The FSR of the spectra is 2.32 nm.

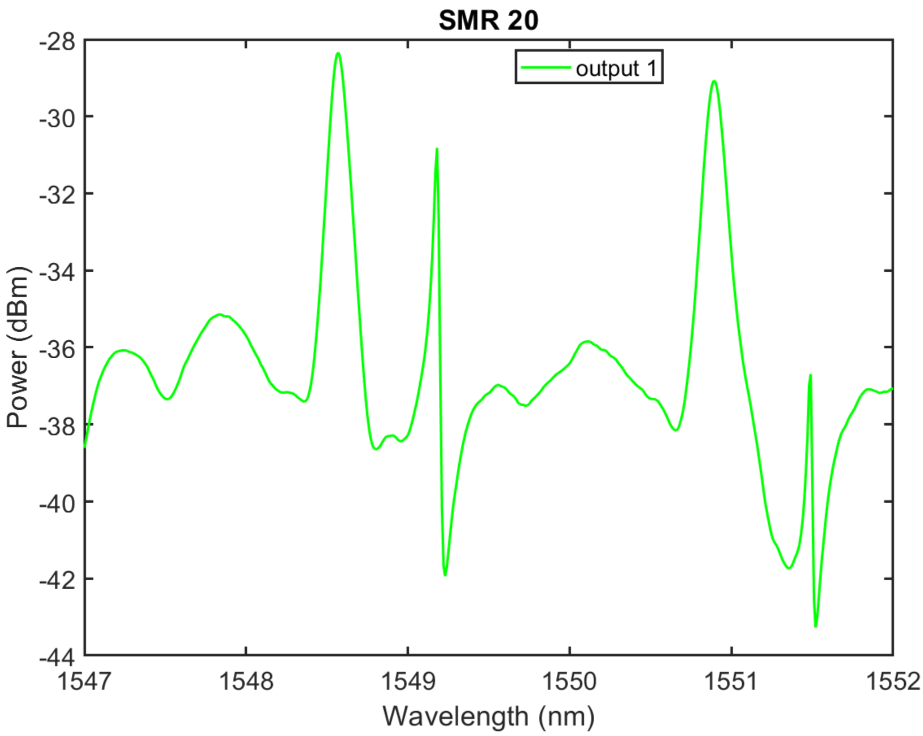

Figure 3.4-21: The experimentally measured DC-SMR ADF spectra of output 1 from 1547 nm to 1552 nm with Lc_1=10.7 µm and Lc_2=20 µm. The spectra have IL=3 dB, FSR=2.32 nm, best eff-Q=$1.03 \cdot 10^4$, ER=13 dB, SR=222 dB/nm.

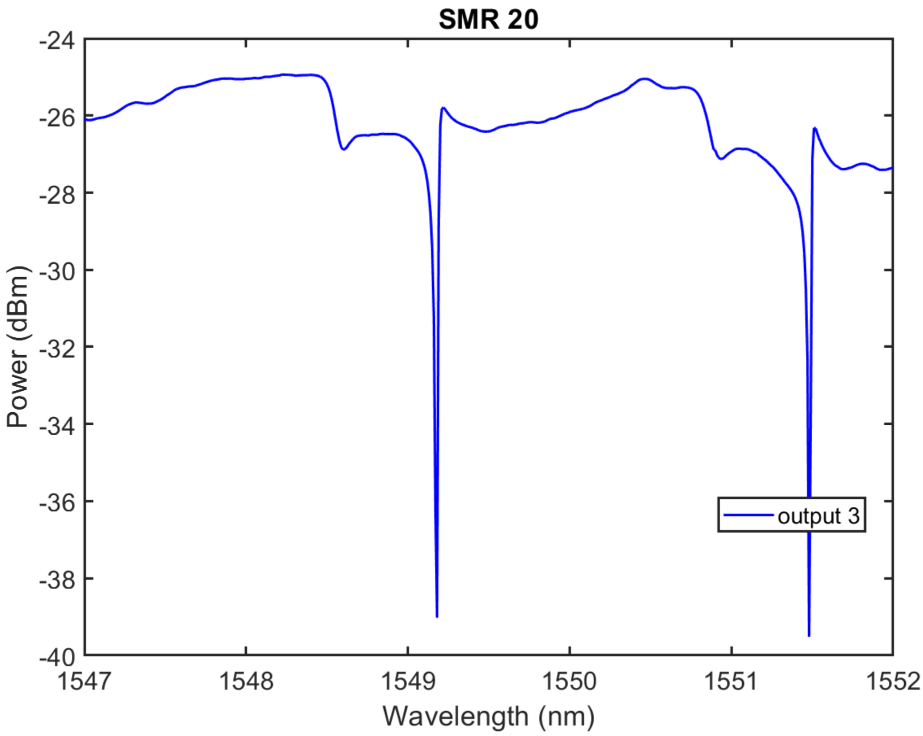

Figure 3.4-22: The experimentally measured DC-SMR ADF spectra of the output 3 from 1547 nm to 1552 nm with Lc_1=10.7 μm and Lc_2=20 μm. The spectra have IL=1 dB, FSR= 2.31 nm, best eff-Q=$3.87 \cdot 10^4$, ER=15.4 dB and SR=330 dB/nm.

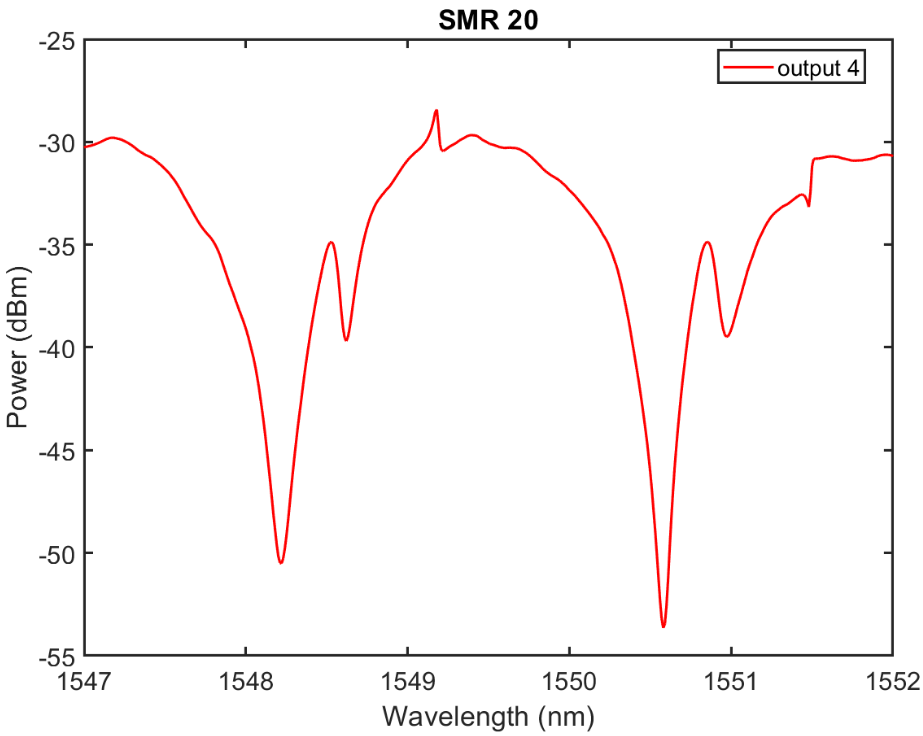

Figure 3.4-23: The experimentally measured DC-SMR ADF spectra of the output 4 from 1547 nm to 1552 nm with coupling lengths of Lc_1=10.7 μm and Lc_2=20 μm. The spectra have IL=3 dB, FSR=2.32 nm, best eff-Q=$9.1 \cdot 10^3$, ER=26 dB, SR= 69.6 dB/nm.

DC-SMR ADF with Lc_2=24 µm

Figure 3.4-24 shows the experimentally measured spectra of DC-SMR ADF from 1500 nm to 1580 nm with Lc_1=10.7 µm and Lc_2=24 µm. The output ports 1, 3 and 4 are shown in green, blue, and red, respectively. Figure 3.4-25 shows the experimentally measured DC-SMR ADF spectra from 1545 nm to 1555 nm with Lc_1=10.7 µm and Lc_2=24 µm. The output ports 1, 3 and 4 are shown in green, blue, and red, respectively. The FSR of the spectra is 2.17 nm. Figure 3.4-26 shows the experimentally measured DC-SMR ADF spectra of output 1 from 1547 nm to 1552 nm with Lc_1=10.7 µm and Lc_2=24 µm. The spectra have IL=2 dB, FSR=2.17 nm, best eff-Q=$3.8 \cdot 10^4$, ER=18.1 dB, SR=453 dB/nm. Figure 3.4-27Figure 2.1-3 shows the experimentally measured DC-SMR ADF spectra of the output 3 from 1547 nm to 1552 nm with Lc_1=10.7 µm and Lc_2=24 µm. The spectra have IL=1 dB, FSR= 2.17 nm, best eff-Q=$3.87 \cdot 10^4$, ER=15.4 dB and SR=330 dB/nm. Figure 3.4-28 shows the experimentally measured DC-SMR ADF spectra of the output 4 from 1547 nm to 1552 nm with coupling lengths of Lc_1=10.7 µm and Lc_2=24 µm. The spectra have IL=2 dB, FSR=2.17 nm, best eff-Q=$9.1 \cdot 10^3$, ER=13 dB, SR= 367 dB/nm.

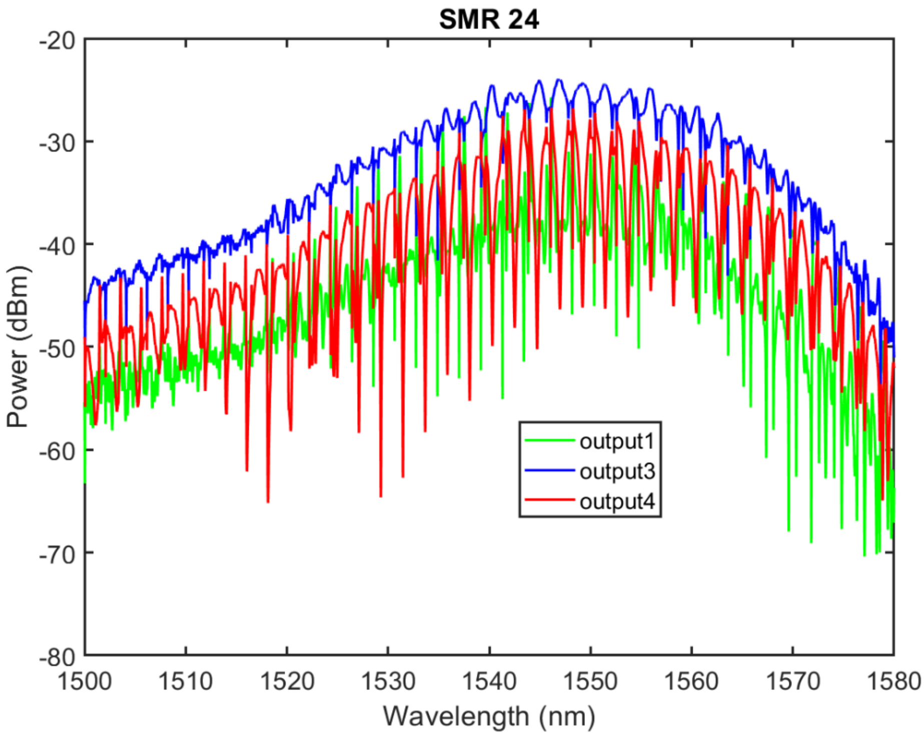

Figure 3.4-24: The experimentally measured spectra of DC-SMR ADF from 1500 nm to 1580 nm with Lc_1=10.7 µm and Lc_2=24 µm. The output ports 1, 3 and 4 are shown in green, blue, and red, respectively.

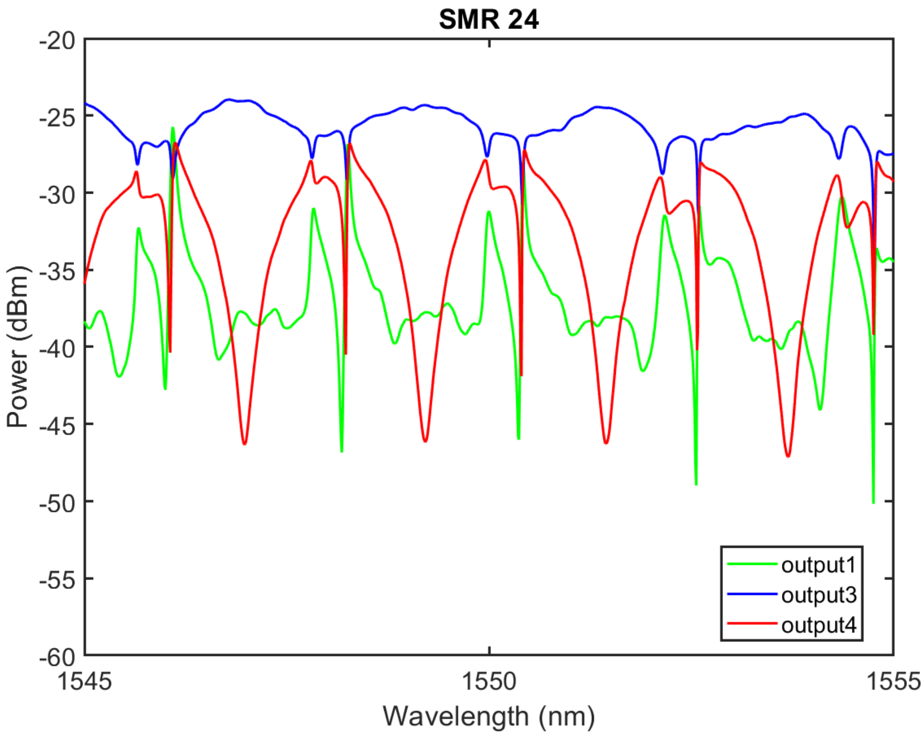

Figure 3.4-25: The experimentally measured DC-SMR ADF spectra from 1545 nm to 1555 nm with Lc_1=10.7 µm and Lc_2=24 µm. The output ports 1, 3 and 4 are shown in green, blue, and red, respectively. The FSR of the spectra is 2.17 nm.

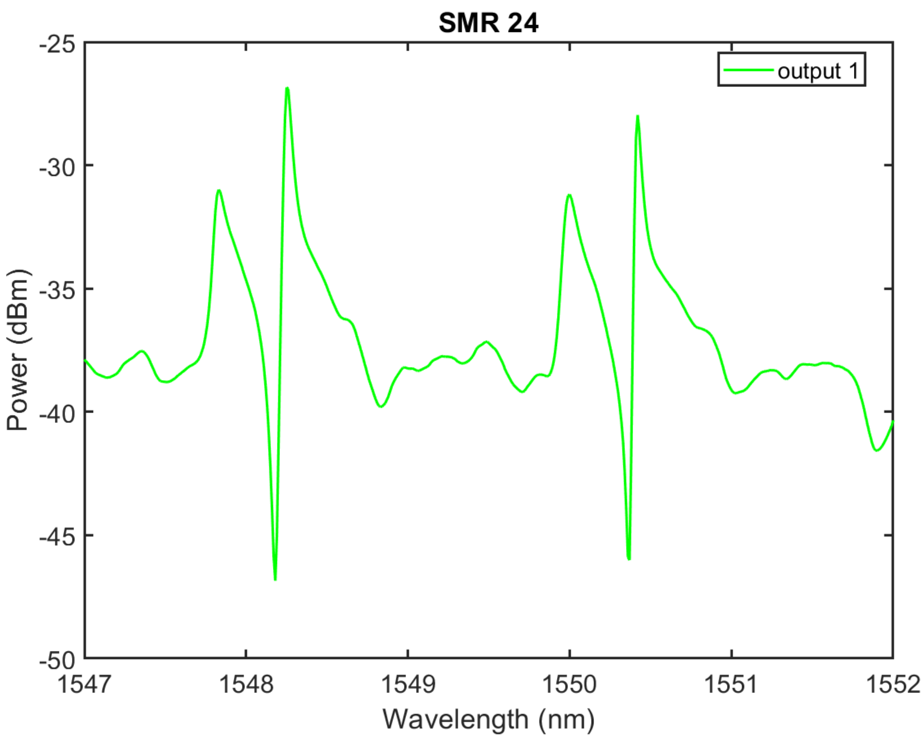

Figure 3.4-26: The experimentally measured DC-SMR ADF spectra of output 1 from 1547 nm to 1552 nm with Lc_1=10.7 µm and Lc_2=24 µm. The spectra have IL=2 dB, FSR=2.17 nm, best eff-Q=$3.8\cdot10^4$, ER=18.1 dB, SR=453 dB/nm.

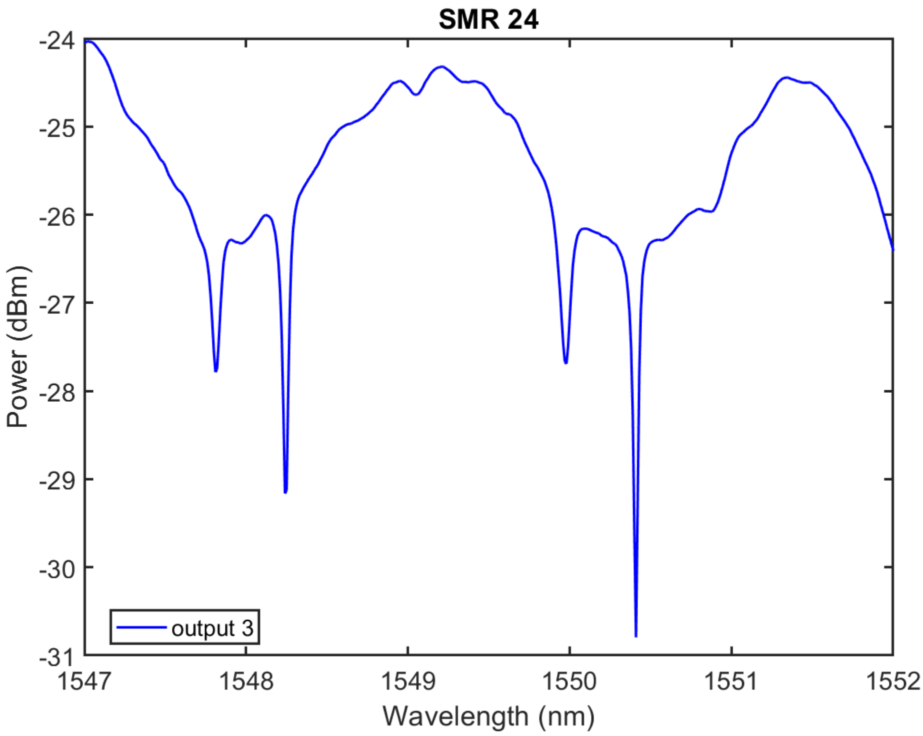

Figure 3.4-27: The experimentally measured DC-SMR ADF spectra of the output 3 from 1547 nm to 1552 nm with Lc_1=10.7 µm and Lc_2=24 µm. The spectra have IL=1 dB, FSR= 2.17 nm, best eff-Q=$3.87 \cdot 10^4$, ER=15.4 dB and SR=330 dB/nm.

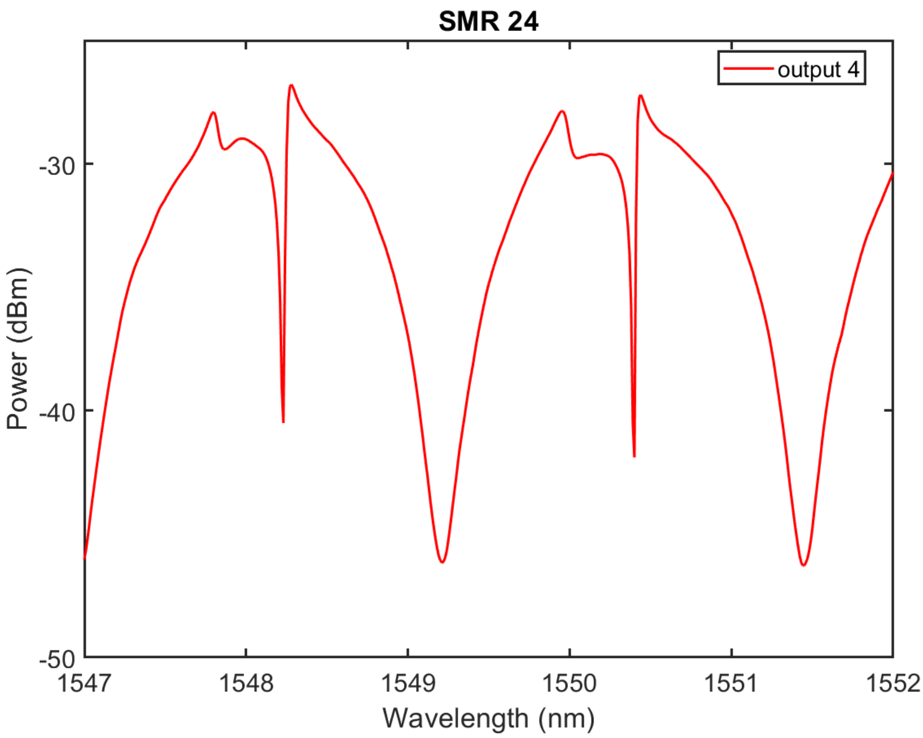

Figure 3.4-28: The experimentally measured DC-SMR ADF spectra of the output 4 from 1547 nm to 1552 nm with coupling lengths of Lc_1=10.7 µm and Lc_2=24 µm. The spectra have IL=2 dB, FSR=2.17 nm, best eff-Q=$9.1 \cdot 10^3$, ER=13 dB, SR= 367 dB/nm.

DC-SMR ADF with Lc_2=28 μm

Figure 3.4-29 shows the experimentally measured spectra of DC-SMR ADF from 1500 nm to 1580 nm with Lc_1=10.7 μm and Lc_2=28 μm. The output ports 1, 3 and 4 are shown in green, blue, and red, respectively. Figure 3.4-30 shows the experimentally measured DC-SMR ADF spectra from 1545 nm to 1555 nm with Lc_1=10.7 μm and Lc_2=28 μm. The output ports 1, 3 and 4 are shown in green, blue, and red, respectively. The FSR of the spectra is 2.06 nm. Figure 3.4-31 shows the experimentally measured DC-SMR ADF spectra of output 1 from 1547 nm to 1552 nm with Lc_1=10.7 μm and Lc_2=28 μm. The spectra have IL=3 dB, FSR=2.05 nm, best eff-Q=$1.55\cdot10^4$, ER=9 dB, SR=92.5 dB/nm. Figure 3.4-32 shows the experimentally measured DC-SMR ADF spectra of the output 3 from 1547 nm to 1552 nm with Lc_1=10.7 μm and Lc_2=28 μm. The spectra have IL=1 dB, FSR= 2.06 nm, best eff-Q=$9.7\cdot10^3$, ER=18.7 dB and SR=89 dB/nm. Figure 3.4-33 shows the experimentally measured DC-SMR ADF spectra of the output 4 from 1547 nm to 1552 nm with coupling lengths of Lc_1=10.7 μm and Lc_2=28 μm. The spectra have IL=2 dB, FSR=2.06 nm, best eff-Q=$5\cdot10^3$, ER=16.3 dB, SR= 34.6 dB/nm.

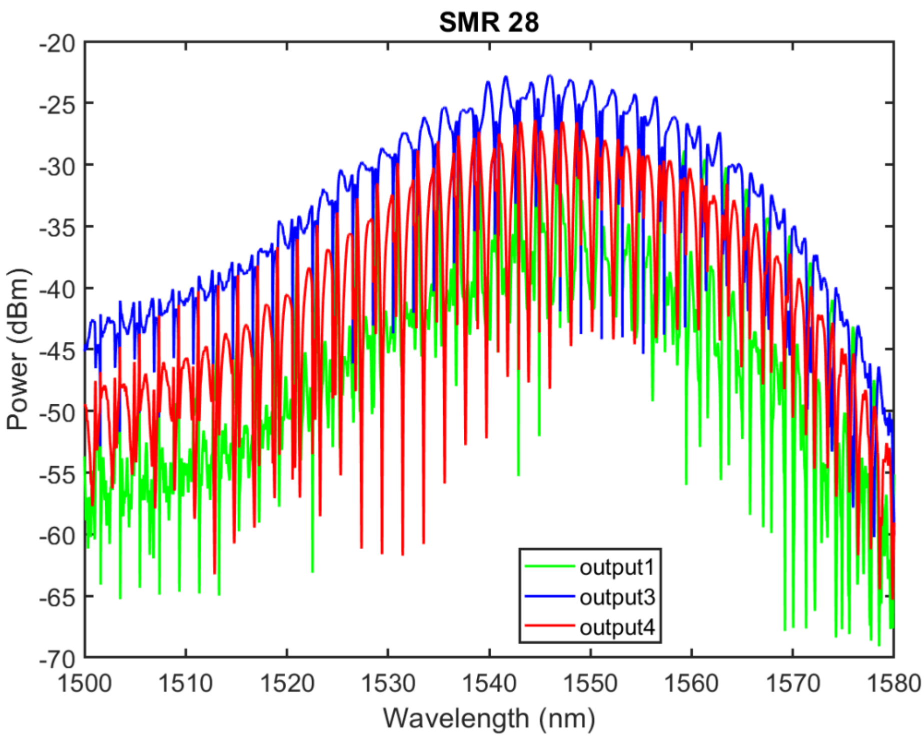

Figure 3.4-29: The experimentally measured spectra of DC-SMR ADF from 1500 nm to 1580 nm with Lc_1=10.7 μm and Lc_2=28 μm. The output ports 1, 3 and 4 are shown in green, blue, and red, respectively.

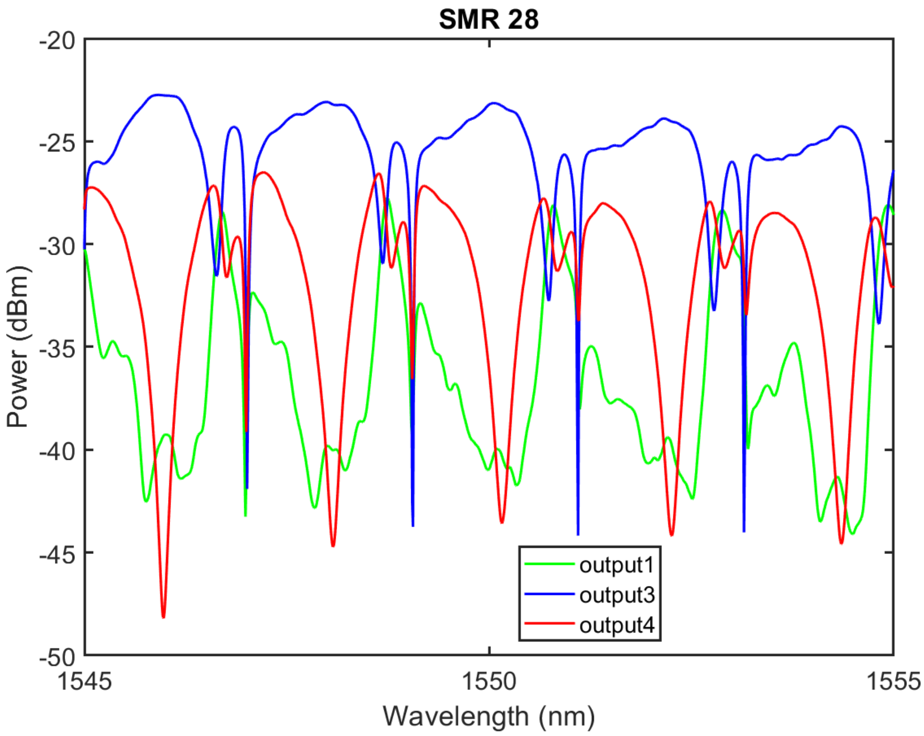

Figure 3.4-30: The experimentally measured DC-SMR ADF spectra from 1545 nm to 1555 nm with Lc_1=10.7 μm and Lc_2=28 μm. The output ports 1, 3 and 4 are shown in green, blue, and red, respectively. The FSR of the spectra is 2.06 nm.

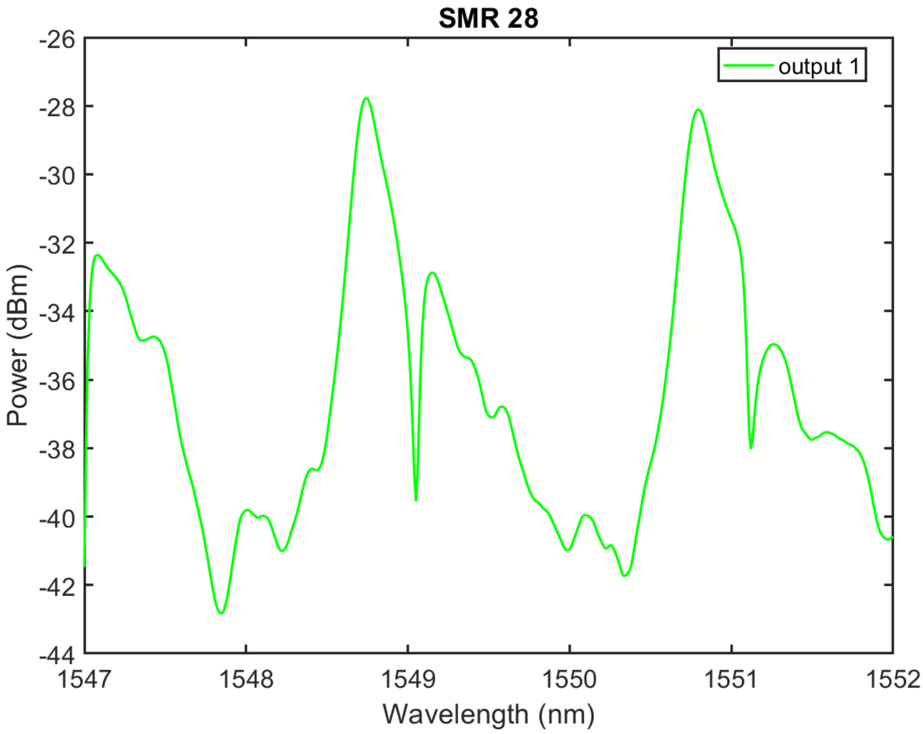

Figure 3.4-31: The experimentally measured DC-SMR ADF spectra of output 1 from 1547 nm to 1552 nm with Lc_1=10.7 μm and Lc_2=28 μm. The spectra have IL=3 dB, FSR=2.05 nm, best eff-Q=$1.55 \cdot 10^4$, ER=9 dB, SR=92.5 dB/nm.

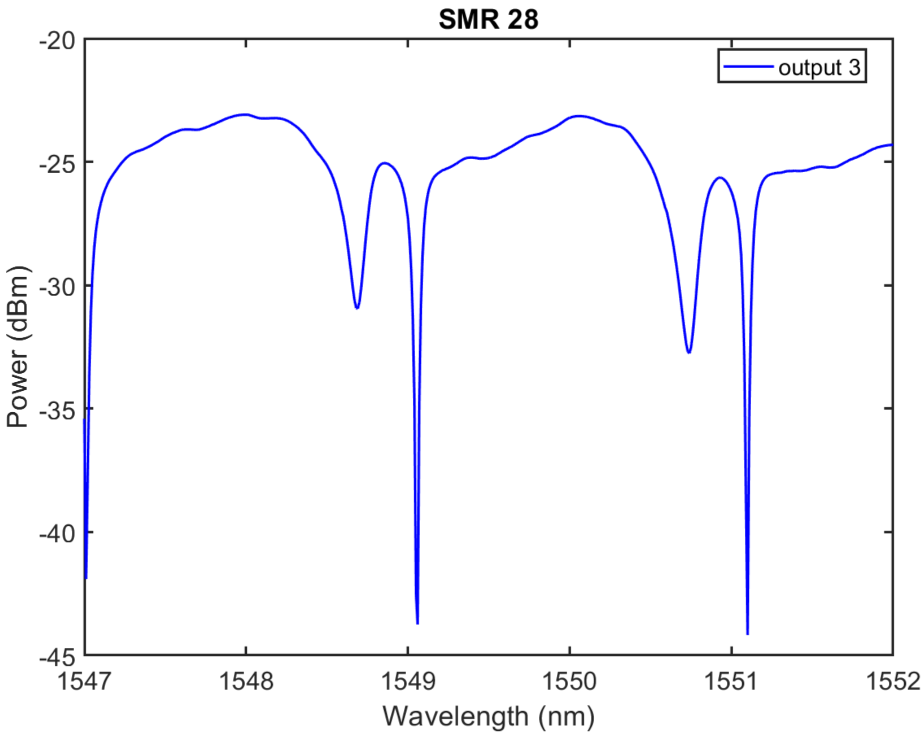

Figure 3.4-32: The experimentally measured DC-SMR ADF spectra of the output 3 from 1547 nm to 1552 nm with Lc_1=10.7 μm and Lc_2=28 μm. The spectra have IL=1 dB, FSR= 2.06 nm, best eff-Q=$9.7 \cdot 10^3$, ER=18.7 dB and SR=89 dB/nm.

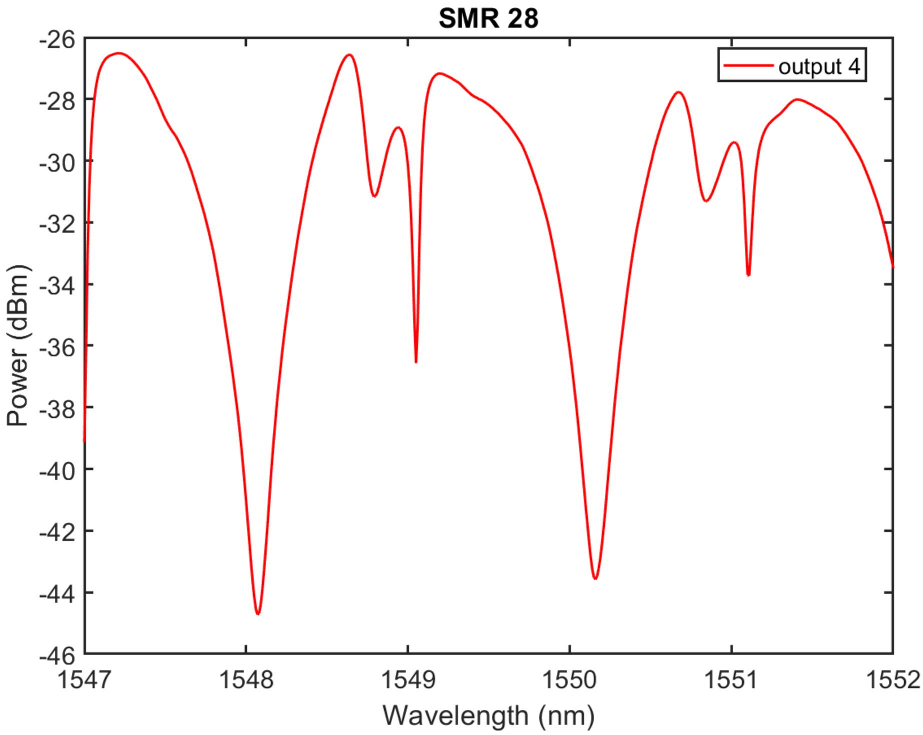

Figure 3.4-33: the experimentally measured DC-SMR ADF spectra of the output 4 from 1547 nm to 1552 nm with coupling lengths of Lc_1=10.7 μm and Lc_2=28 μm. The spectra have IL=2 dB, FSR=2.06 nm, best eff-Q=$5 \cdot 10^3$, ER=16.3 dB, SR= 34.6 dB/nm.

3.5. Double Coupled AMR

DC-AMR spectra show EIT-like Lorentzian peaks in output 3 between the relatively flat top filter response of the AMR. Fano spectral lineshapes can be observed in output 4 at the points where the output 3 shows Lorentzian spectral response. Figure 3.5-1 shows the representation of the DC-AMR ADF, Figure 3.5-2 shows the SEM image of DC-MR ADF. MR add-drop filter spectrum shows Fano, Lorentzian with EIT like peaks and coupled resonator induced transparency (CRIT) behaviors. Figure 3.5-3 shows the KLayout design of the DC-AMR ADF given with the corresponding coupling dimensions and bend radii with the positions of the input and output ports, DC-AMR with input shown in black, output 1,2 and 3 is shown in green, blue, and red, respectively. The IC coupler has a coupling length of $Lc_{1=}$10.7 µm and the CC coupler has a coupling length of $Lc_{2=}$17 µm (specific to chosen design), waveguides have a bending radius of 5 µm while the couplers' bending radius is 10 µm, the gap between the bus waveguides in the couplers is g=200 nm. The coupler bending radius of 10 µm, the waveguide bending radius of 5 µm and the gap between the coupler waveguides g=200 nm is constant in all designs.

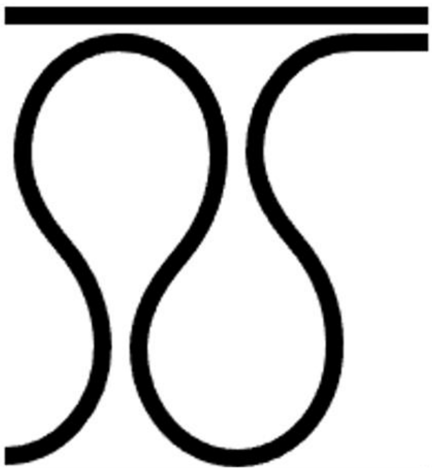

Figure 3.5-1: The representation of the DC-AMR ADF

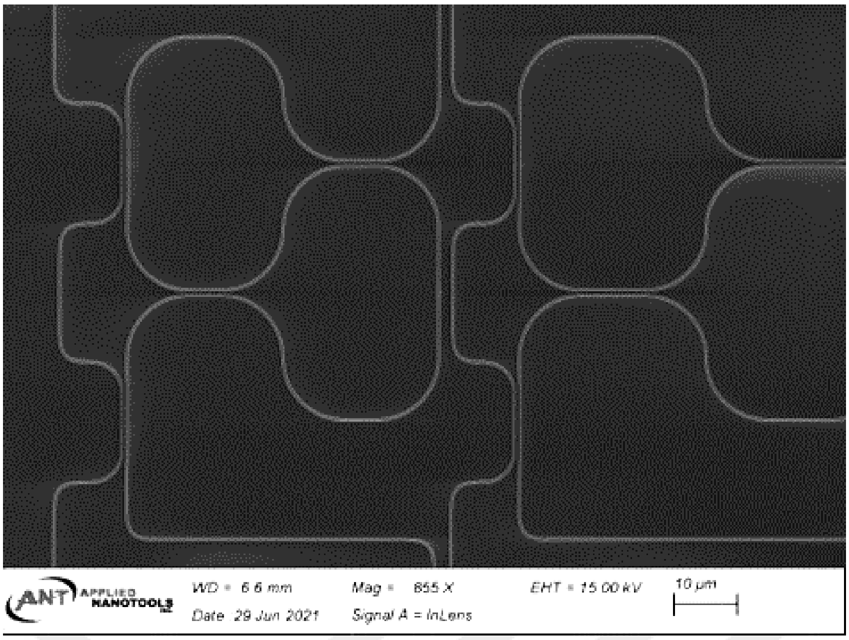

Figure 3.5-2: The SEM image of DC-MR ADF

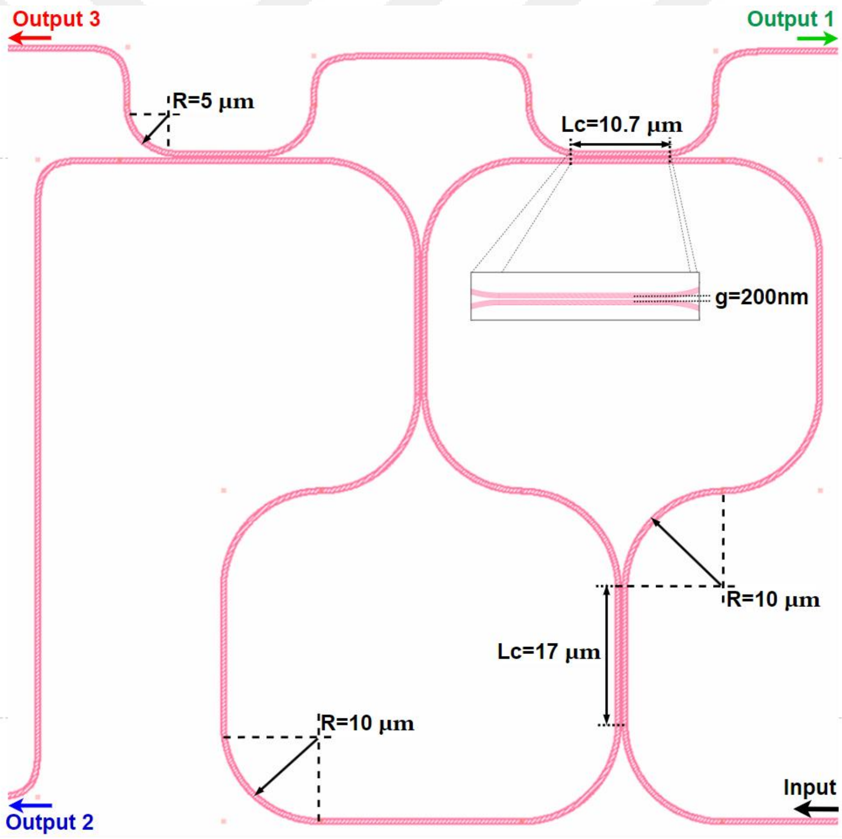

Figure 3.5-3: Representation of Double Coupled SMR with output shown in black, output 1,2 and 3 is shown in green, blue, and red, respectively. The IC coupler has a coupling length of $L_{c=}$10.7 µm and the CC coupler has $L_{c=}$17 µm (specific to chosen design), waveguides have a bending radius of 5 µm while the couplers' bending radius is 10 µm, the gap between the bus waveguides in the couplers is g=200 nm.

DC-AMR ADF with Lc_2=28 µm

Figure 3.5-4 shows the experimentally measured spectra of DC-AMR ADF from 1500 nm to 1580 nm with Lc_1=8.7 µm and Lc_2=28 µm. The output ports 1, 3 and 4 are shown in green, blue, and red, respectively. Figure 3.5-5 shows the experimentally measured DC-AMR ADF spectra from 1545 nm to 1555 nm with Lc_1=10.7 µm and Lc_2=28 µm. The output ports 1, 3 and 4 are shown in green, blue, and red, respectively. The FSR of the spectra is 2.02 nm. Figure 3.5-6 shows the experimentally measured DC-AMR ADF spectra of output 1 from 1547 nm to 1552 nm with Lc_1=10.7 µm and Lc_2=28 µm. The spectra have IL=2 dB, FSR=2.02 nm, best eff-Q=$1.5\cdot 10^4$, ER=11.8 dB, SR=29 dB/nm, split=0.25 nm. Figure 3.5-7 shows the experimentally measured DC-AMR ADF spectra of the output 3 from 1547 nm to 1552 nm with Lc_1=10.7 µm and Lc_2=28 µm. The spectra have IL=1 dB, FSR= 2.02 nm, best Q=$1.3\cdot 10^4$, ER=28 dB and SR=214 dB/nm, split=0.32 nm. Figure 3.5-8 shows the experimentally measured DC-AMR ADF spectra of the output 4 from 1547 nm to 1552 nm with coupling lengths of Lc_1=10.7 µm and Lc_2=28 µm. The spectra have IL= 2 dB, FSR=2.06 nm, best eff-Q=$5\cdot 10^3$, ER=16.3 dB, SR= 34.6 dB/nm.

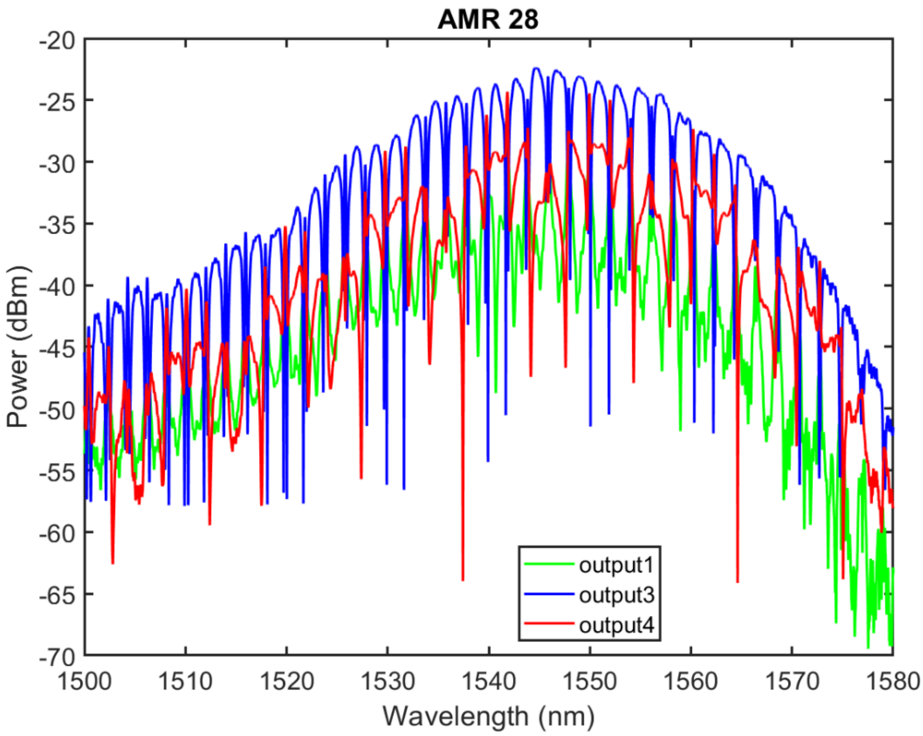

Figure 3.5-4: The experimentally measured spectra of DC-AMR ADF from 1500 nm to 1580 nm with Lc_1=8.7 µm and Lc_2=28 µm. The output ports 1, 3 and 4 are shown in green, blue, and red, respectively.

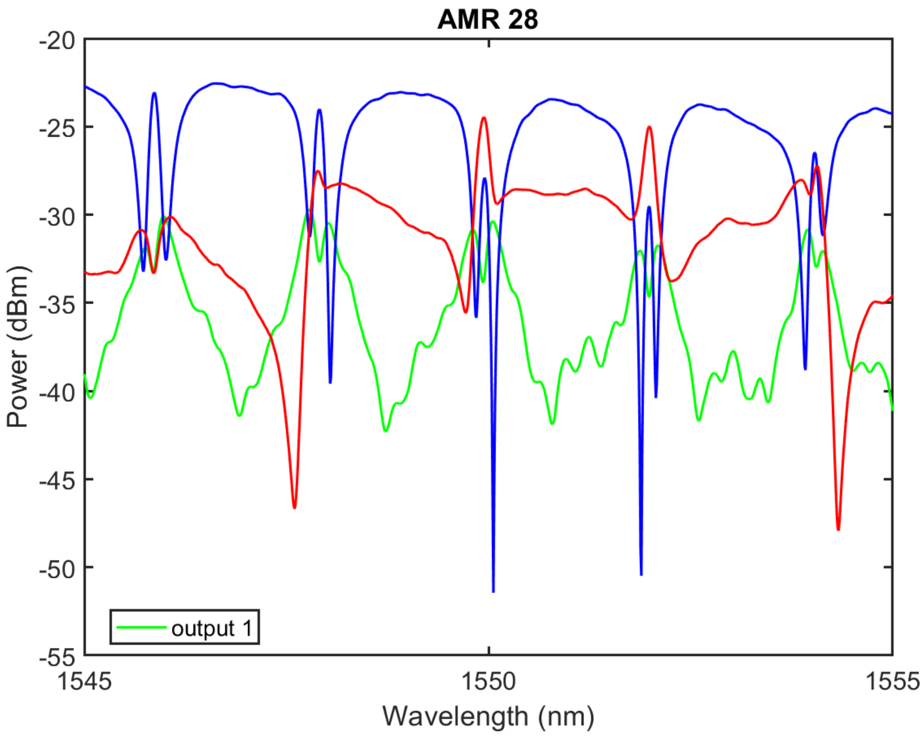

Figure 3.5-5: The experimentally measured DC-AMR ADF spectra from 1545 nm to 1555 nm with Lc_1=8.7 µm and Lc_2=28 µm. The output ports 1, 3 and 4 are shown in green, blue, and red, respectively. The FSR of the spectra is 2.02 nm.

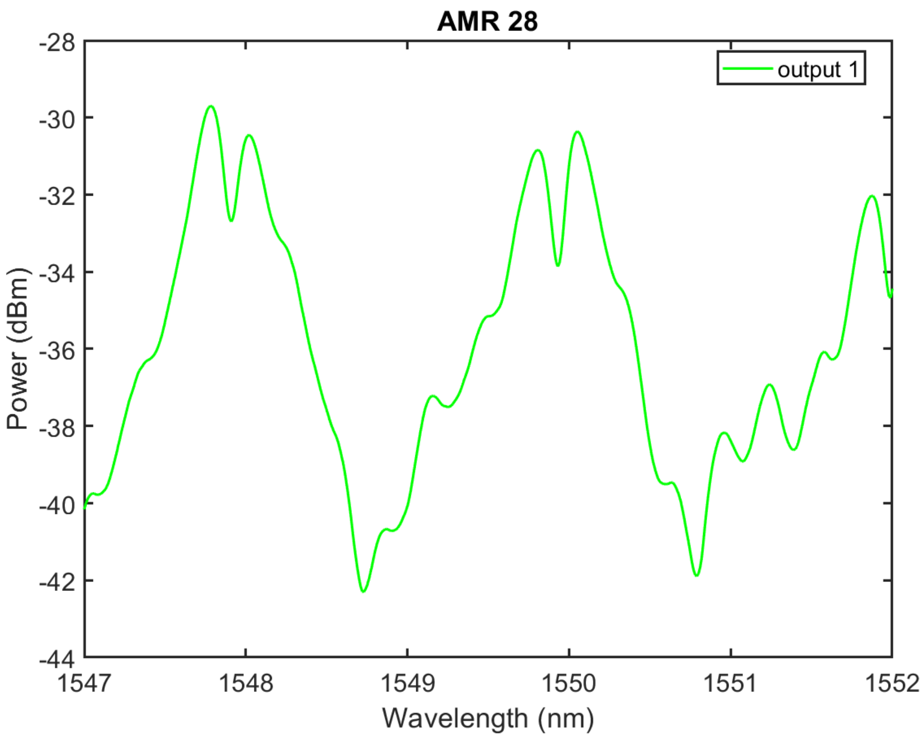

Figure 3.5-6: The experimentally measured DC-AMR ADF spectra of output 1 from 1547 nm to 1552 nm with Lc_1=8.7 µm and Lc_2=28 µm. The spectra have IL=2 dB, FSR=2.02 nm, best eff-Q=1.5·104, ER=11.8 dB, SR=29 dB/nm, split=0.25 nm

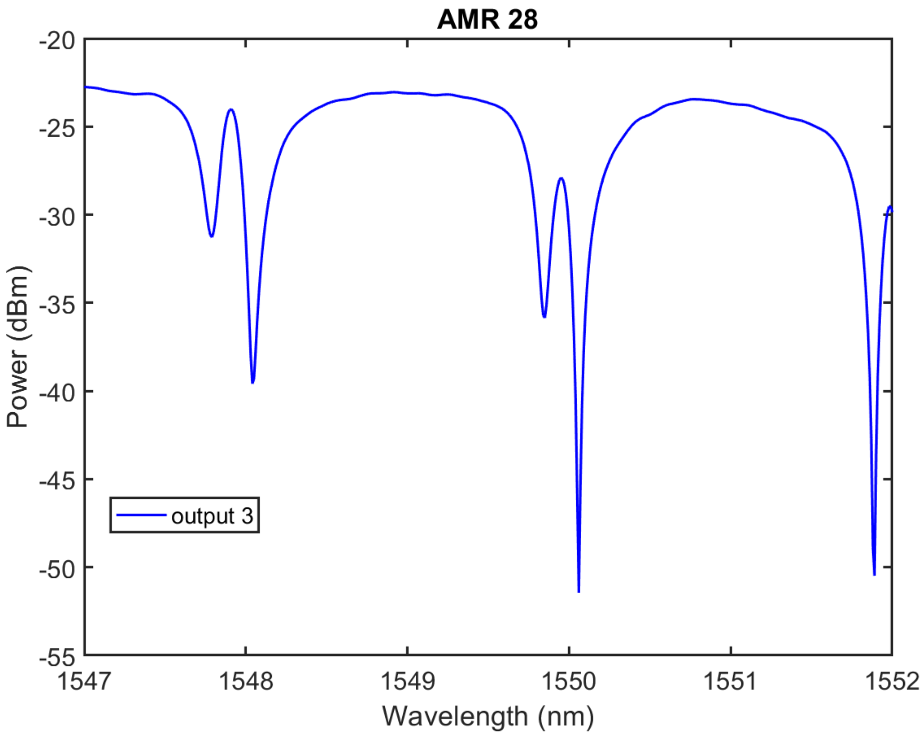

Figure 3.5-7: The experimentally measured DC-AMR ADF spectra of the output 3 from 1547 nm to 1552 nm with Lc_1=8.7 μm and Lc_2=28 μm. The spectra have IL=1 dB, FSR= 2.02 nm, best Q=1.3·104, ER=28 dB and SR=214 dB/nm, split=0.32 nm.

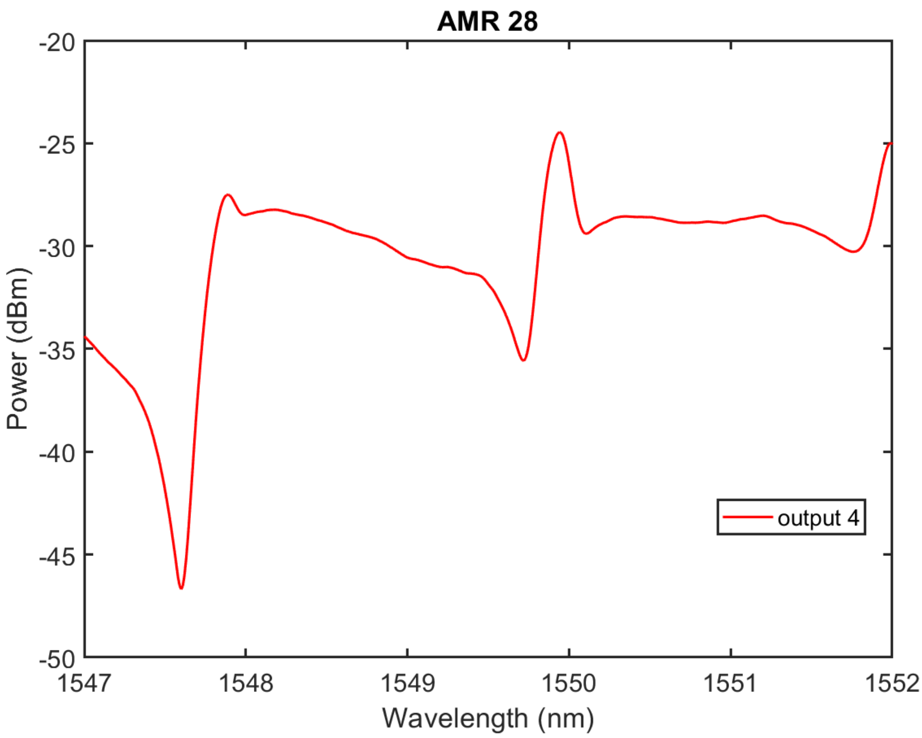

Figure 3.5-8: The experimentally measured DC-AMR ADF spectra of the output 4 from 1547 nm to 1552 nm with coupling lengths of Lc_1=8.7 μm and Lc_2=28 μm. The spectra have IL=2 dB, FSR=2.06 nm, best eff-Q=5·103, ER=16.3 dB, SR= 34.6 dB/nm.

DC-AMR ADF with Lc_2=30 µm

Figure 3.5-9 shows the experimentally measured spectra of DC-AMR ADF from 1500 nm to 1580 nm with Lc_1=8.7 µm and Lc_2=30 µm. The output ports 1, 3 and 4 are shown in green, blue, and red, respectively. Figure 3.5-10 shows the experimentally measured DC-AMR ADF spectra from 1545 nm to 1555 nm with Lc_1=8.7 µm and Lc_2=30 µm. The output ports 1, 3 and 4 are shown in green, blue, and red, respectively. The FSR of the spectra is 1.99 nm. Figure 3.5-11 shows the experimentally measured DC-AMR ADF spectra of output 1 from 1547 nm to 1552 nm with Lc_1=8.7 µm and Lc_2=30 µm. The spectra have IL=5 dB, FSR=1.99 nm, best eff-Q=$2.5\cdot10^4$, ER=12.8 dB, SR=17 dB/nm, split=0.16 nm. Figure 3.5-12 shows the experimentally measured DC-AMR ADF spectra of the output 3 from 1547 nm to 1552 nm with Lc_1=8.7 µm and Lc_2=30 µm. The spectra have IL=1 dB, FSR= 2.02 nm, best Q=$9.1\cdot10^3$, ER=22 dB and SR=229 dB/nm, split=0.38 nm. Figure 3.5-13 shows the experimentally measured DC-AMR ADF spectra of the output 4 from 1547 nm to 1552 nm with coupling lengths of Lc_1=8.7 µm and Lc_2=30 µm. The spectra have IL=2 dB, FSR=1.99 nm, best eff-Q=$8.6\cdot10^3$, ER=36 dB, SR= 113 dB/nm.

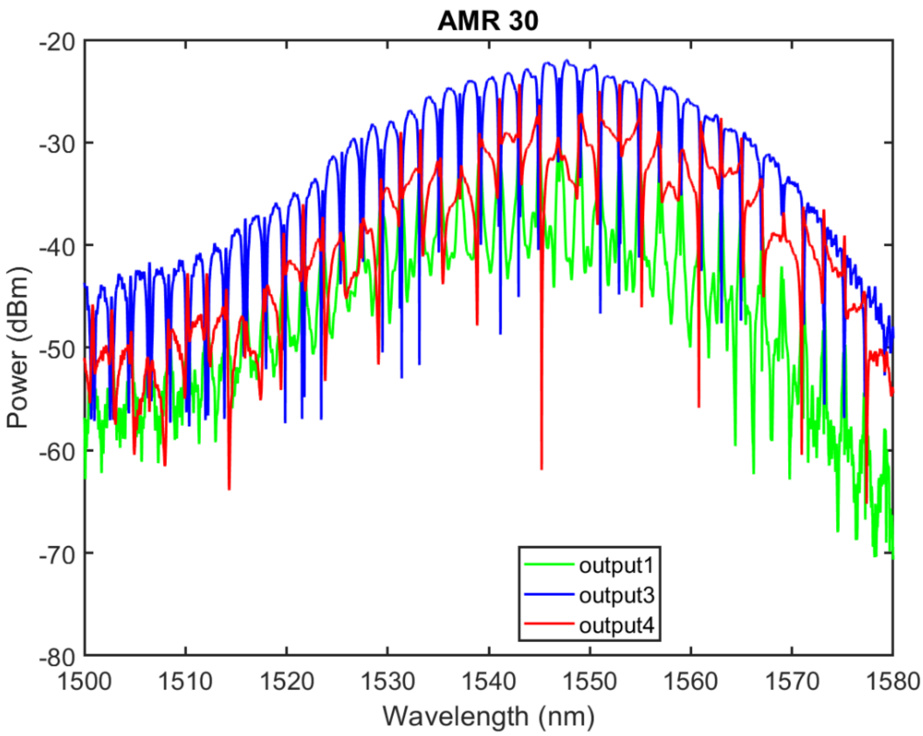

Figure 3.5-9: The experimentally measured spectra of DC-AMR ADF from 1500 nm to 1580 nm with Lc_1=8.7 µm and Lc_2=30 µm. The output ports 1, 3 and 4 are shown in green, blue, and red, respectively.

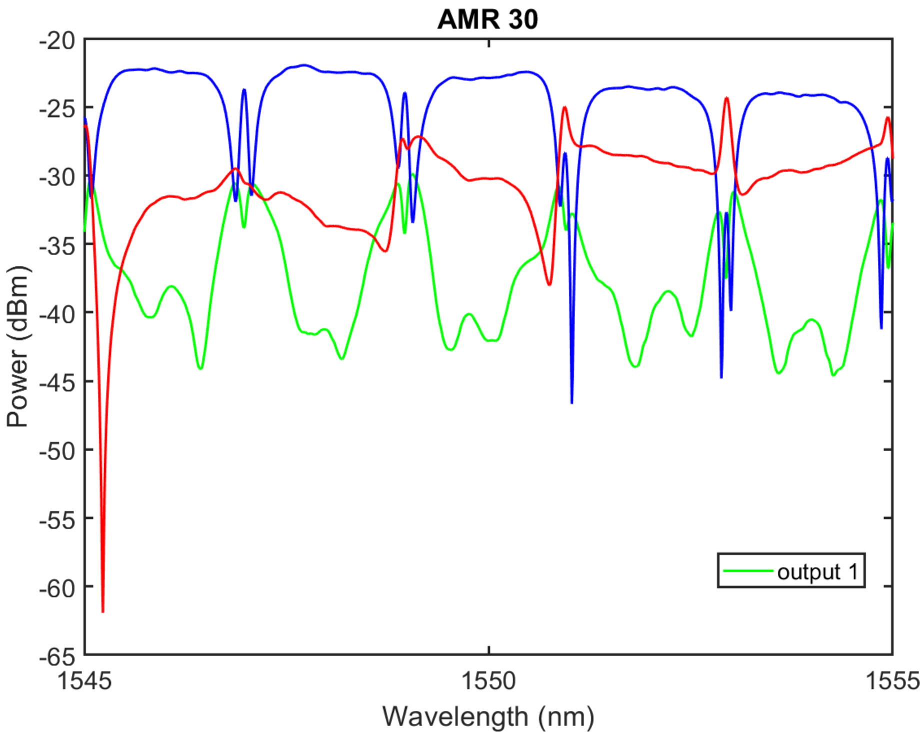

Figure 3.5-10: The experimentally measured DC-AMR ADF spectra from 1545 nm to 1555 nm with Lc_1=8.7 µm and Lc_2=30 µm. The output ports 1, 3 and 4 are shown in green, blue, and red, respectively. The FSR of the spectra is 1.99 nm.

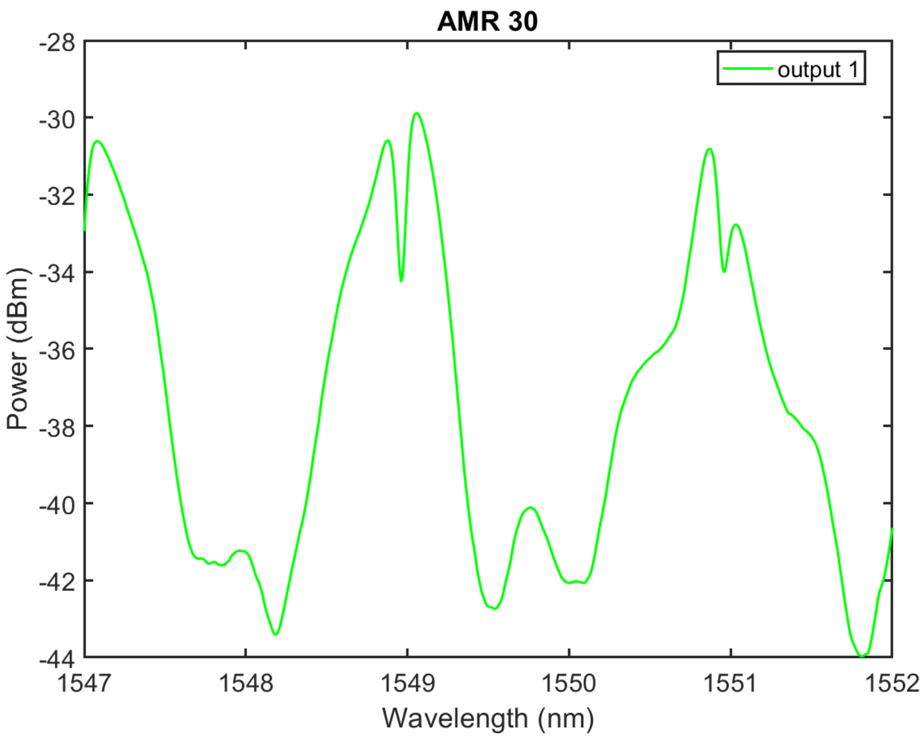

Figure 3.5-11: The experimentally measured DC-AMR ADF spectra of output 1 from 1547 nm to 1552 nm with Lc_1=8.7 µm and Lc_2=30 µm. The spectra have IL=5 dB, FSR=1.99 nm, best eff-Q=$2.5 \cdot 10^4$, ER=12.8 dB, SR=17 dB/nm, split=0.16 nm.

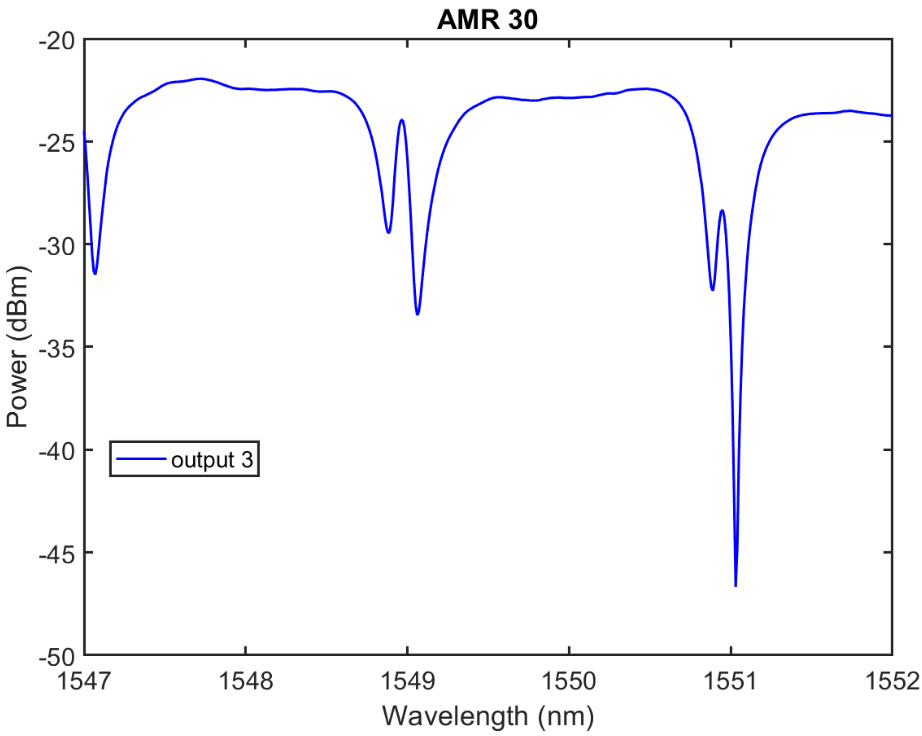

Figure 3.5-12: The experimentally measured DC-AMR ADF spectra of the output 3 from 1547 nm to 1552 nm with Lc_1=8.7 µm and Lc_2=30 µm. The spectra have IL=1 dB, FSR= 2.02 nm, best Q=$9.1 \cdot 10^3$, ER=22 dB and SR=229 dB/nm, split=0.38 nm.

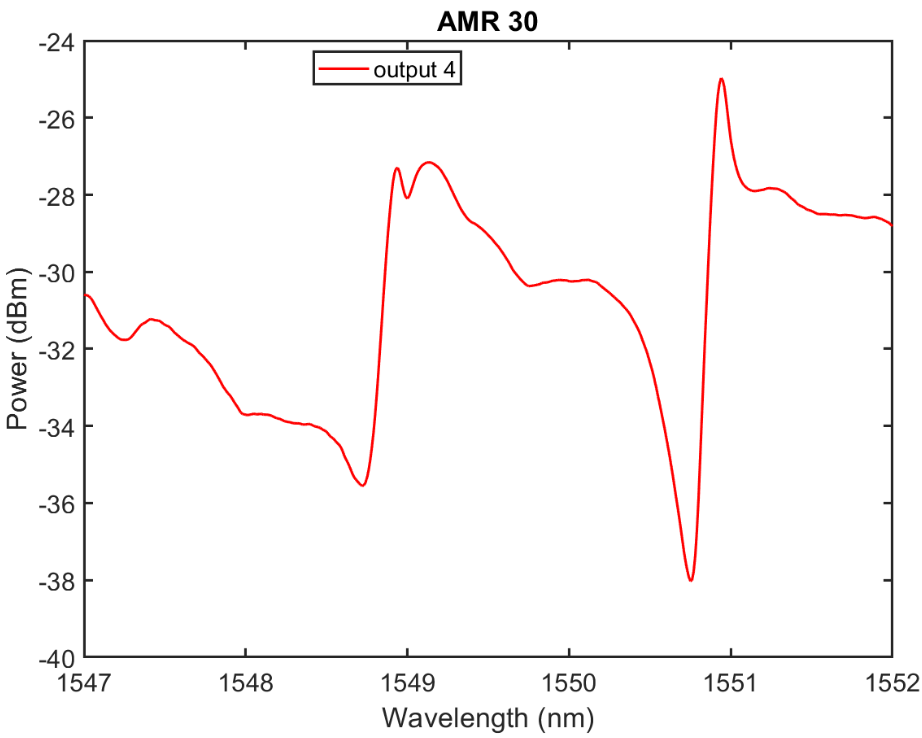

Figure 3.5-13: The experimentally measured DC-AMR ADF spectra of the output 4 from 1547 nm to 1552 nm with coupling lengths of Lc_1=8.7 µm and Lc_2=30 µm. The spectra have IL=2 dB, FSR=1.99 nm, best eff-Q=$8.6 \cdot 10^3$, ER=36 dB, SR= 113 dB/nm.

DC-AMR ADF with Lc_2=32 µm

Figure 3.5-14 shows the experimentally measured spectra of DC-AMR ADF from 1500 nm to 1580 nm with Lc_1=8.7 µm and Lc_2=32 µm. The output ports 1, 3 and 4 are shown in green, blue, and red, respectively. Figure 3.5-15 shows the experimentally measured DC-AMR ADF spectra from 1545 nm to 1555 nm with Lc_1=8.7 µm and Lc_2=32 µm. The output ports 1, 3 and 4 are shown in green, blue, and red, respectively. The FSR of the spectra is 1.94 nm. Figure 3.5-16 shows the experimentally measured DC-AMR ADF spectra of output 1 from 1547 nm to 1552 nm with Lc_1=8.7 µm and Lc_2=32 µm. The spectra have IL=5 dB, FSR=1.94 nm, best eff-Q=$3.1\cdot10^4$, ER=18.5 dB, SR=60 dB/nm, split=0.17 nm. Figure 3.5-17 shows the experimentally measured DC-AMR ADF spectra of the output 3 from 1547 nm to 1552 nm with Lc_1=8.7 µm and Lc_2=32 µm. The spectra have IL=1 dB, FSR= 1.94 nm, best Q=$1.9\cdot10^4$, ER=21 dB and SR=213 dB/nm, split=0.28 nm. Figure 3.5-18 shows the experimentally measured DC-AMR ADF spectra of the output 4 from 1547 nm to 1552 nm with coupling lengths of Lc_1=8.7 µm and Lc_2=32 µm. The spectra have IL=2 dB, FSR=1.94 nm, best eff-Q=$9.7\cdot10^3$, ER=33 dB, SR= 211 dB/nm.

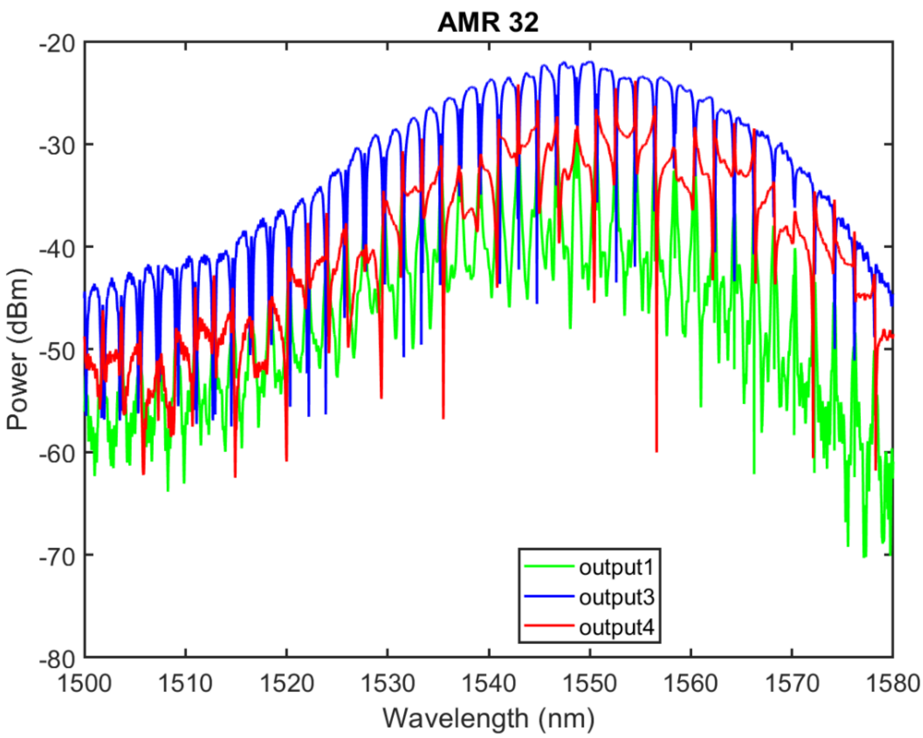

Figure 3.5-14: The experimentally measured spectra of DC-AMR ADF from 1500 nm to 1580 nm with Lc_1=8.7 µm and Lc_2=32 µm. The output ports 1, 3 and 4 are shown in green, blue, and red, respectively.

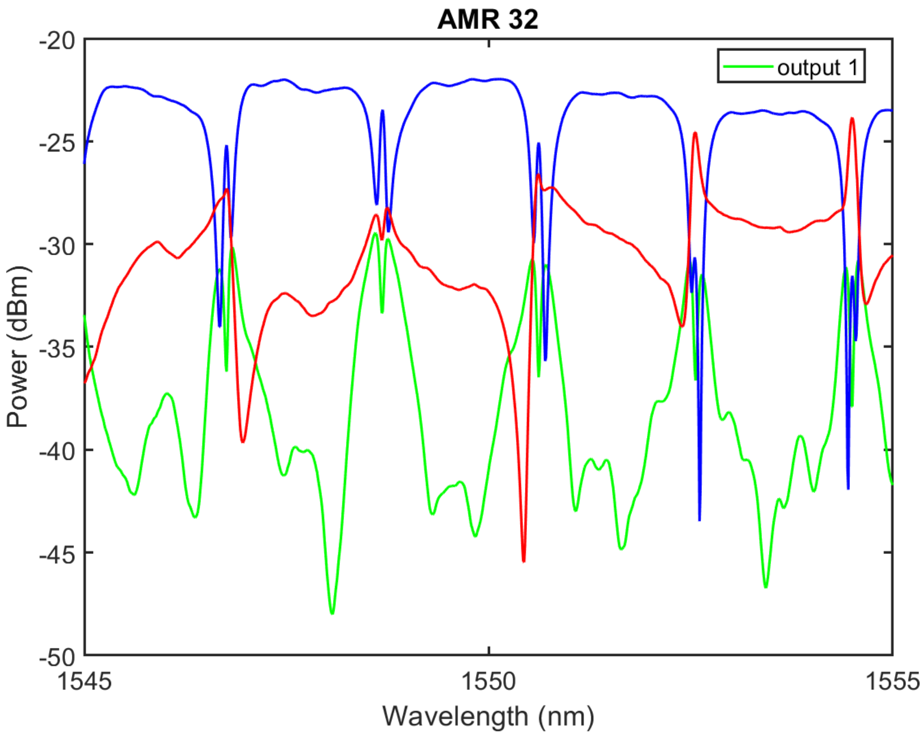

Figure 3.5-15: The experimentally measured DC-AMR ADF spectra from 1545 nm to 1555 nm with Lc_1=8.7 µm and Lc_2=32 µm. The output ports 1, 3 and 4 are shown in green, blue, and red, respectively. The FSR of the spectra is 1.94 nm

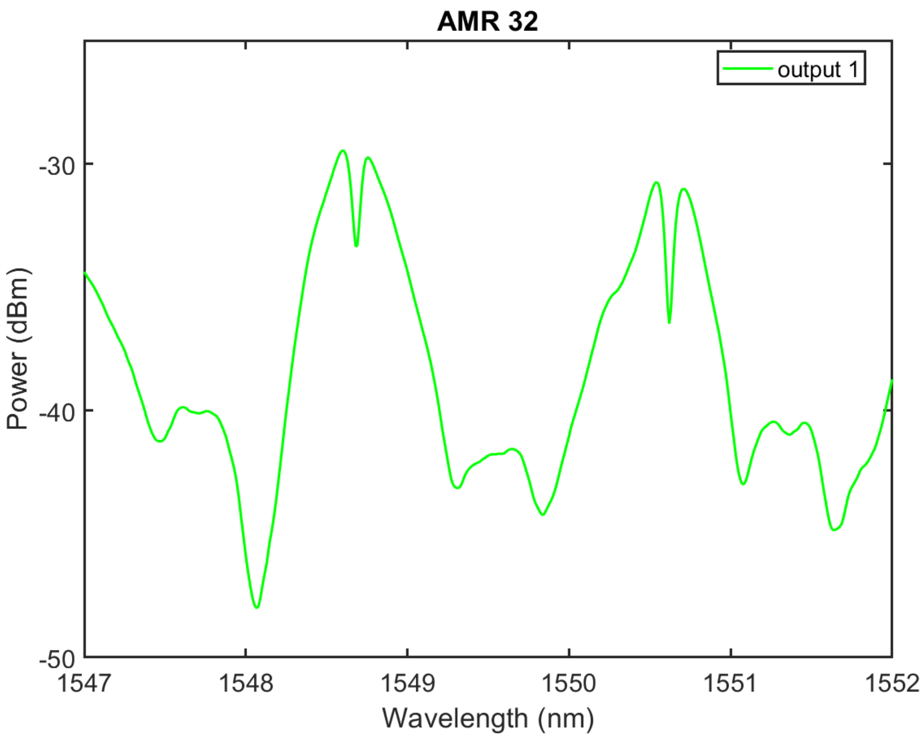

Figure 3.5-16: The experimentally measured DC-AMR ADF spectra of output 1 from 1547 nm to 1552 nm with Lc_1=8.7 µm and Lc_2=32 µm. The spectra have IL=5 dB, FSR=1.94 nm, best eff-Q=$3.1 \cdot 10^4$, ER=18.5 dB, SR=60 dB/nm, split=0.17 nm.

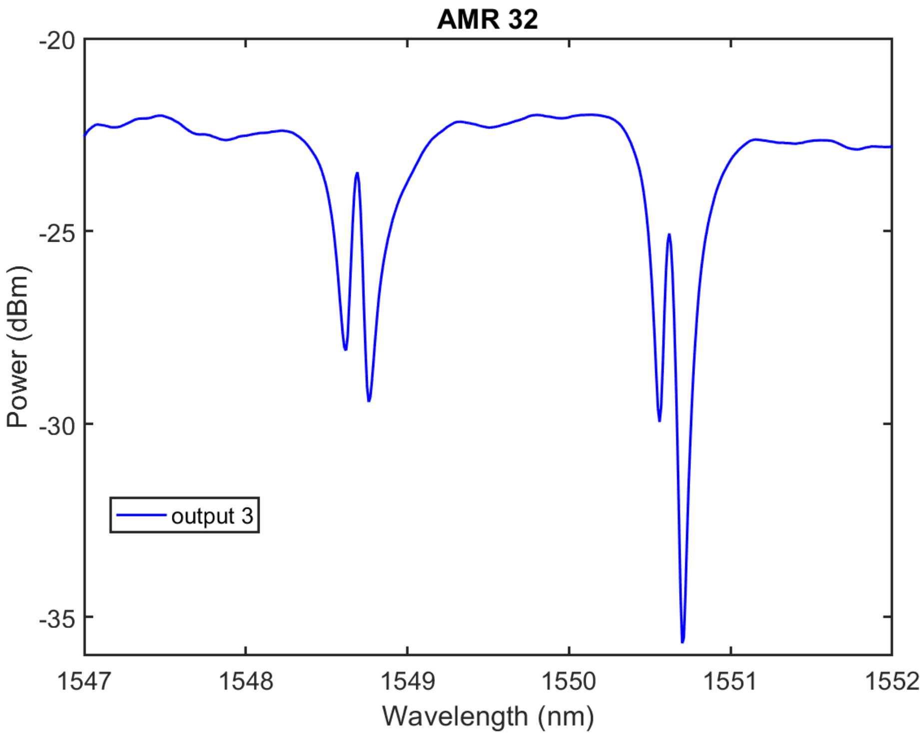

Figure 3.5-17: The experimentally measured DC-AMR ADF spectra of the output 3 from 1547 nm to 1552 nm with Lc_1=8.7 µm and Lc_2=32 µm. The spectra have IL=1 dB, FSR= 1.94 nm, best Q=$1.9\cdot 10^4$, ER=21 dB and SR=213 dB/nm, split=0.28 nm.

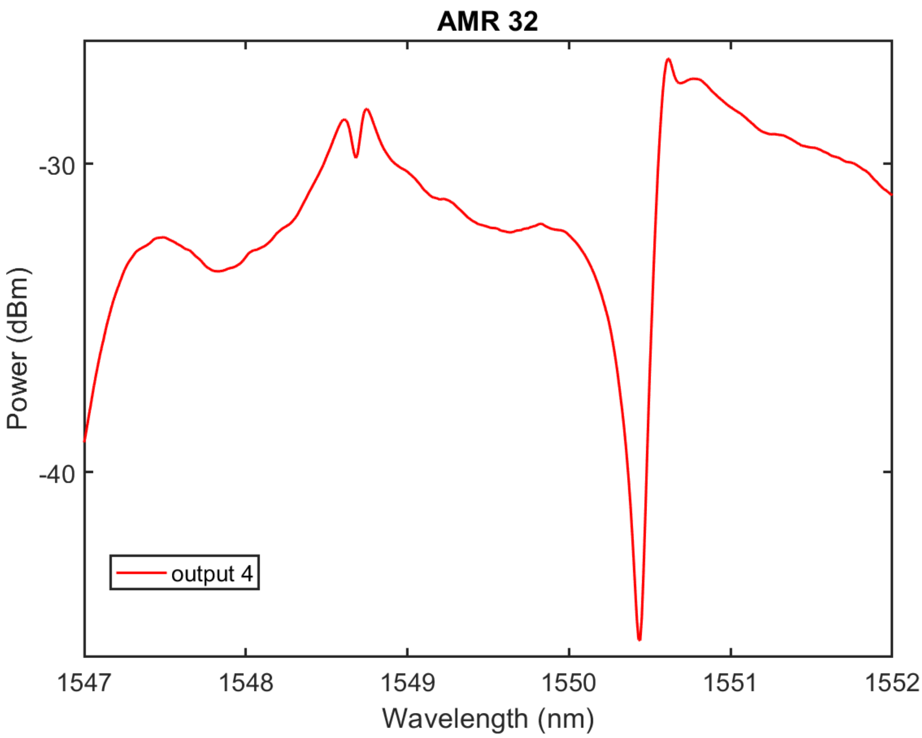

Figure 3.5-18: The experimentally measured DC-AMR ADF spectra of the output 4 from 1547 nm to 1552 nm with coupling lengths of Lc_1=8.7 µm and Lc_2=32 µm. The spectra have IL=2 dB, FSR=1.94 nm, best eff-Q=$9.7\cdot 10^3$, ER=33 dB, SR= 211 dB/nm.

DC-AMR ADF with Lc_2=34 µm

Figure 3.5-19 shows the experimentally measured spectra of DC-AMR ADF from 1500 nm to 1580 nm with Lc_1=8.7 µm and Lc_2=34 µm. The output ports 1, 3 and 4 are shown in green, blue, and red, respectively. Figure 3.5-20 shows the experimentally measured DC-AMR ADF spectra from 1545 nm to 1555 nm with Lc_1=8.7 µm and Lc_2=34 µm. The output ports 1, 3 and 4 are shown in green, blue, and red, respectively. The FSR of the spectra is 1.88 nm. Figure 3.5-21 shows the experimentally measured DC-AMR ADF spectra of output 1 from 1547 nm to 1552 nm with Lc_1=8.7 µm and Lc_2=34 µm. The spectra have IL=5 dB, FSR=1.88 nm, best eff-Q=$3.1\cdot10^4$, ER=12 dB, SR=167 dB/nm, split=0.15 nm. Figure 3.5-22 shows the experimentally measured DC-AMR ADF spectra of the output 3 from 1547 nm to 1552 nm with Lc_1=8.7 µm and Lc_2=34 µm. The spectra have IL=1 dB, FSR= 1.88 nm, best Q=$3.1\cdot10^4$, ER=16 dB and SR=253 dB/nm, split=0.2 nm. Figure 3.5-23 shows the experimentally measured DC-AMR ADF spectra of the output 4 from 1547 nm to 1552 nm with coupling lengths of Lc_1=8.7 µm and Lc_2=34 µm. The spectra have IL=2 dB, FSR=1.88 nm, best eff-Q=$9.6\cdot10^3$, ER=33 dB, SR= 211 dB/nm.

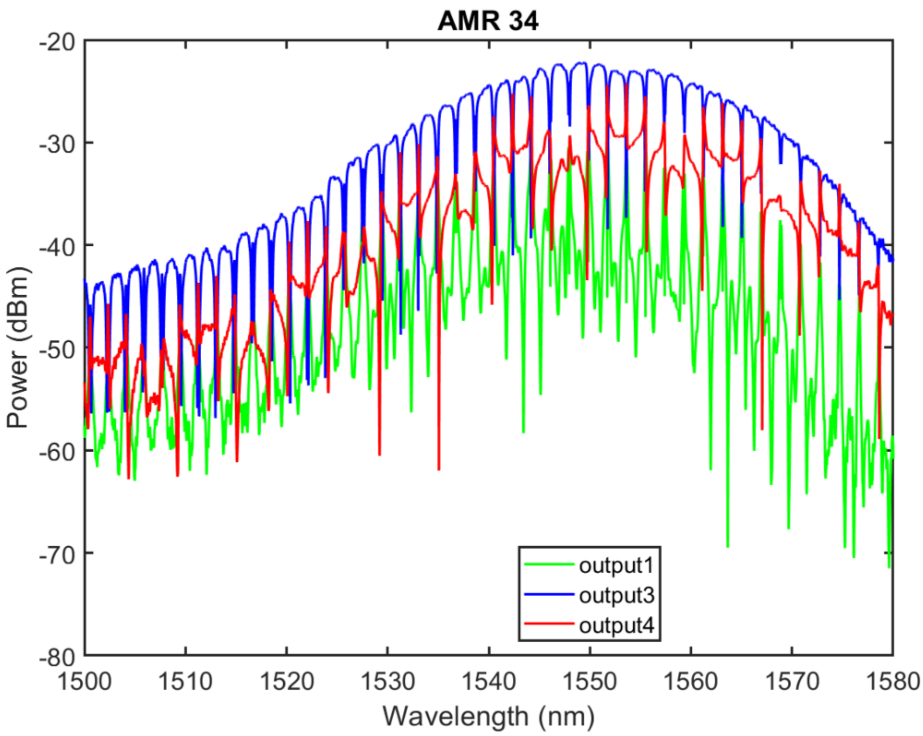

Figure 3.5-19: The experimentally measured spectra of DC-AMR ADF from 1500 nm to 1580 nm with Lc_1=8.7 µm and Lc_2=34 µm. The output ports 1, 3 and 4 are shown in green, blue, and red, respectively.

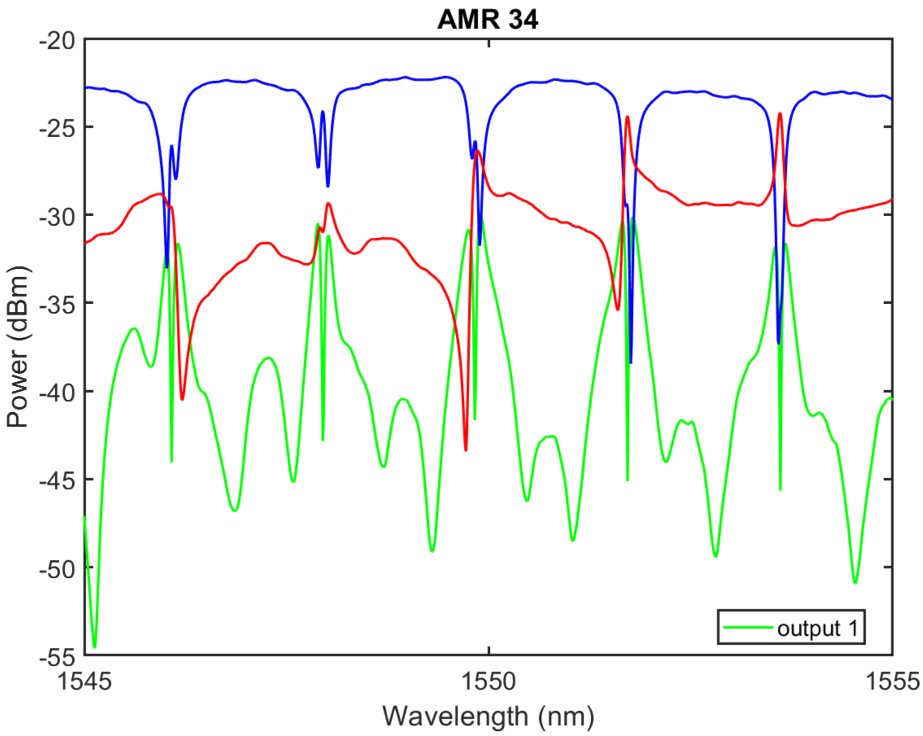

Figure 3.5-20: The experimentally measured DC-AMR ADF spectra from 1545 nm to 1555 nm with Lc_1=8.7 µm and Lc_2=34 µm. The output ports 1, 3 and 4 are shown in green, blue, and red, respectively. The FSR of the spectra is 1.88 nm.

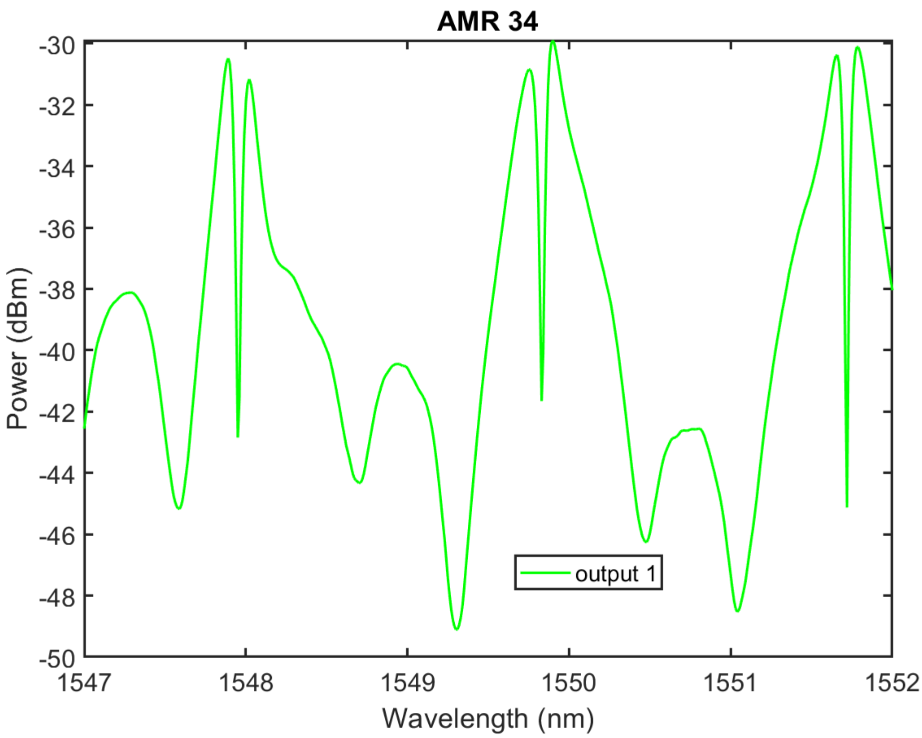

Figure 3.5-21: The experimentally measured DC-AMR ADF spectra of output 1 from 1547 nm to 1552 nm with Lc_1=8.7 µm and Lc_2=34 µm. The spectra have IL=5 dB, FSR=1.88 nm, best eff-Q=$3.1 \cdot 10^4$, ER=12 dB, SR=167 dB/nm, split=0.15 nm.

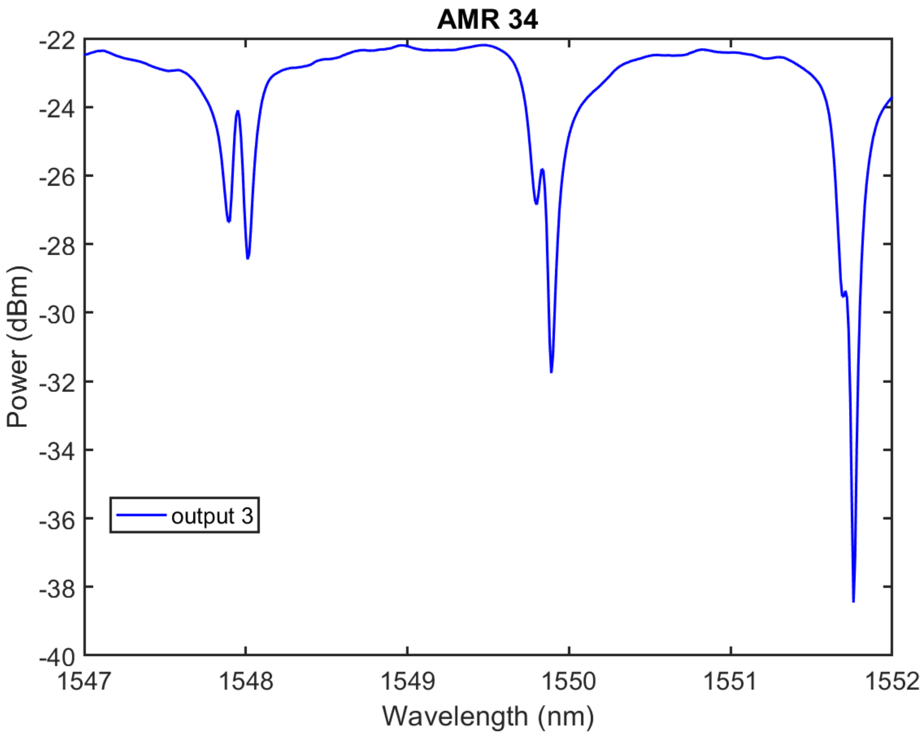

Figure 3.5-22: The experimentally measured DC-AMR ADF spectra of the output 3 from 1547 nm to 1552 nm with Lc_1=8.7 µm and Lc_2=34 µm. The spectra have IL=1 dB, FSR= 1.88 nm, best Q=$3.1 \cdot 10^4$, ER=16 dB and SR=253 dB/nm, split=0.2 nm.

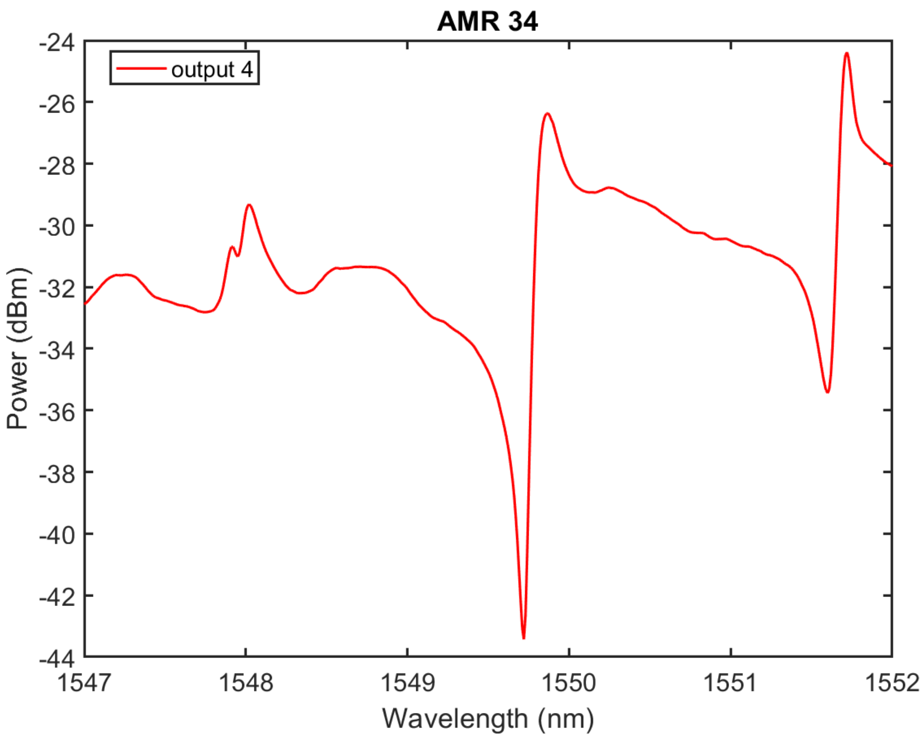

Figure 3.5-23: The experimentally measured DC-AMR ADF spectra of the output 4 from 1547 nm to 1552 nm with coupling lengths of Lc_1=8.7 µm and Lc_2=34 µm. The spectra have IL=2 dB, FSR=1.88 nm, best eff-Q=$9.6 \cdot 10^3$, ER=33 dB, SR= 211 dB/nm.

DC-AMR ADF with Lc_2=36 µm

Figure 3.5-24 shows the experimentally measured spectra of DC-AMR ADF from 1500 nm to 1580 nm with Lc_1=8.7 µm and Lc_2=36 µm. The output ports 1, 3 and 4 are shown in green, blue, and red, respectively. Figure 3.5-25 shows the experimentally measured DC-AMR ADF spectra from 1545 nm to 1555 nm with Lc_1=8.7 µm and Lc_2=36 µm. The output ports 1, 3 and 4 are shown in green, blue, and red, respectively. The FSR of the spectra is 1.83 nm. Figure 3.5-26 shows the experimentally measured DC-AMR ADF spectra of output 1 from 1547 nm to 1552 nm with Lc_1=8.7 µm and Lc_2=36 µm. The spectra have IL=5 dB, FSR=1.84 nm, best eff-Q=$3.1 \cdot 10^4$, ER=13 dB, SR=273 dB/nm, split=0.1 nm. Figure 3.5-27 shows the experimentally measured DC-AMR ADF spectra of the output 3 from 1547 nm to 1552 nm with Lc_1=8.7 µm and Lc_2=36 µm. The spectra have IL=1 dB, FSR=1.83 nm, best Q=$1.1 \cdot 10^4$, ER=10.1 dB and SR=118.6 dB/nm, split=0.18 nm. Figure 3.5-28 shows the experimentally measured DC-AMR ADF spectra of the output 4 from 1547 nm to 1552 nm with coupling lengths of Lc_1=8.7 µm and Lc_2=36 µm. The spectra have IL=2 dB, FSR=1.84 nm, best eff-Q=$1.4 \cdot 10^4$, ER=25 dB, SR= 229 dB/nm.

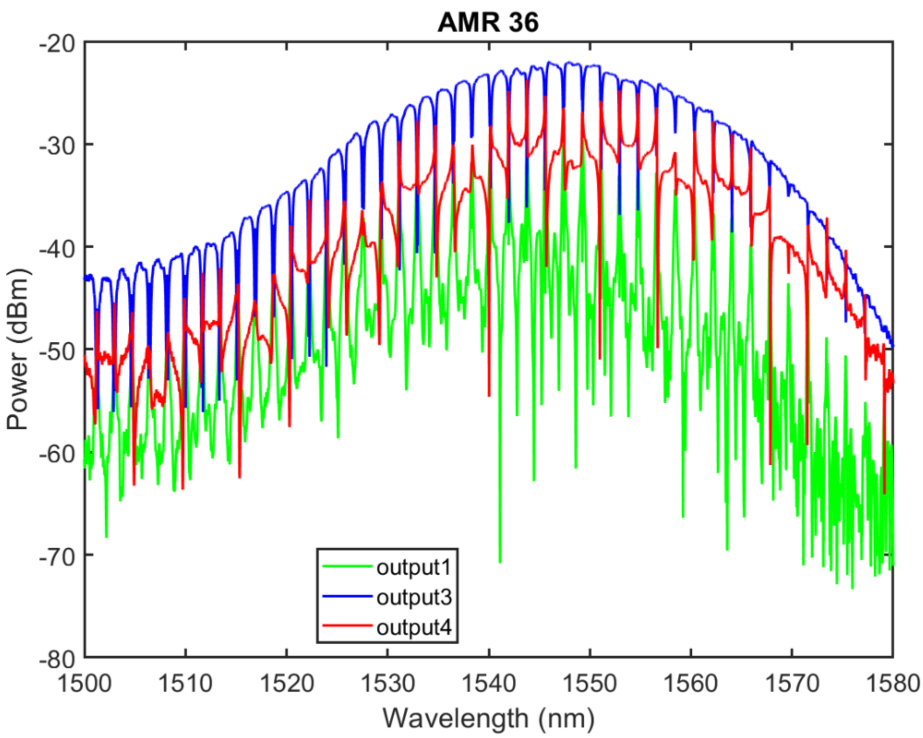

Figure 3.5-24: The experimentally measured spectra of DC-AMR ADF from 1500 nm to 1580 nm with Lc_1=8.7 µm and Lc_2=36 µm. The output ports 1, 3 and 4 are shown in green, blue, and red, respectively.

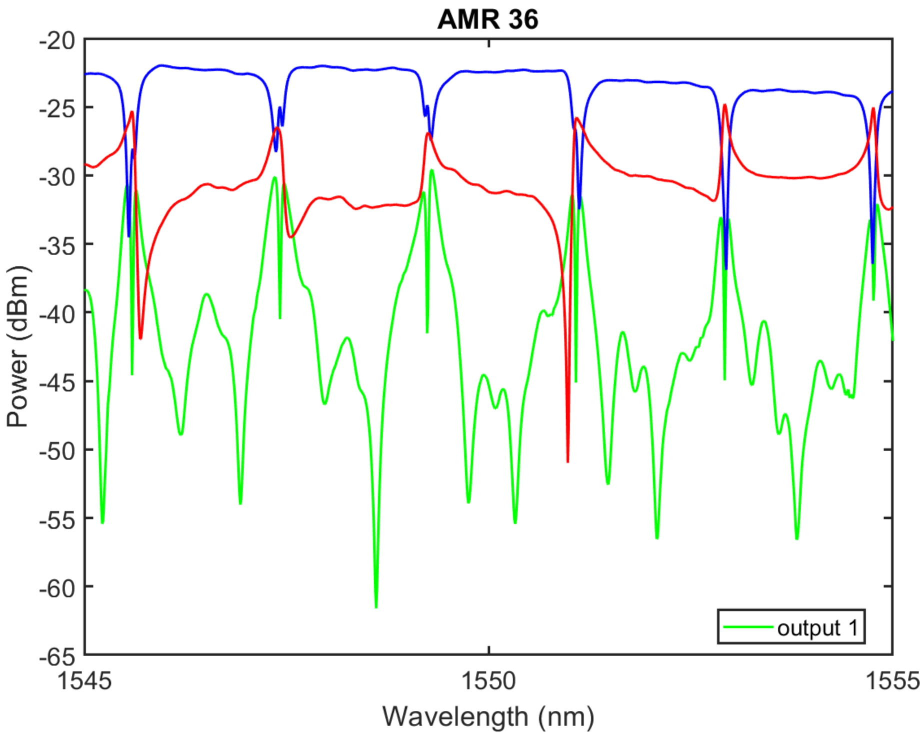

Figure 3.5-25: The experimentally measured DC-AMR ADF spectra from 1545 nm to 1555 nm with Lc_1=8.7 μm and Lc_2=36 μm. The output ports 1, 3 and 4 are shown in green, blue, and red, respectively. The FSR of the spectra is 1.83 nm.

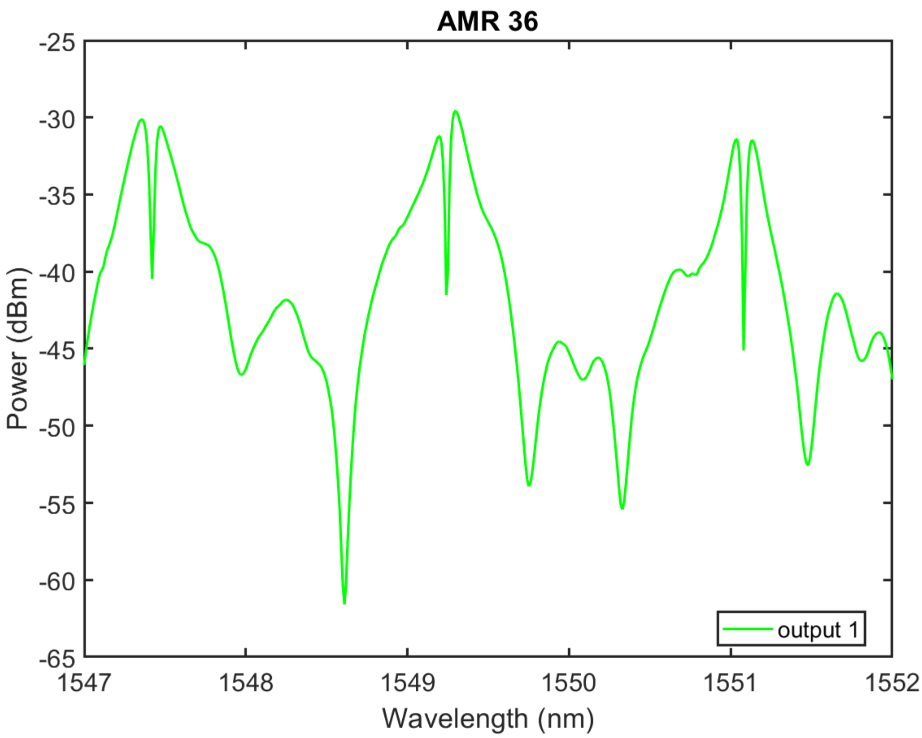

Figure 3.5-26: The experimentally measured DC-AMR ADF spectra of output 1 from 1547 nm to 1552 nm with Lc_1=8.7 μm and Lc_2=36 μm. The spectra have IL=5 dB, FSR=1.84 nm, best eff-Q=3.1·104, ER=13 dB, SR=273 dB/nm, split=0.1 nm.

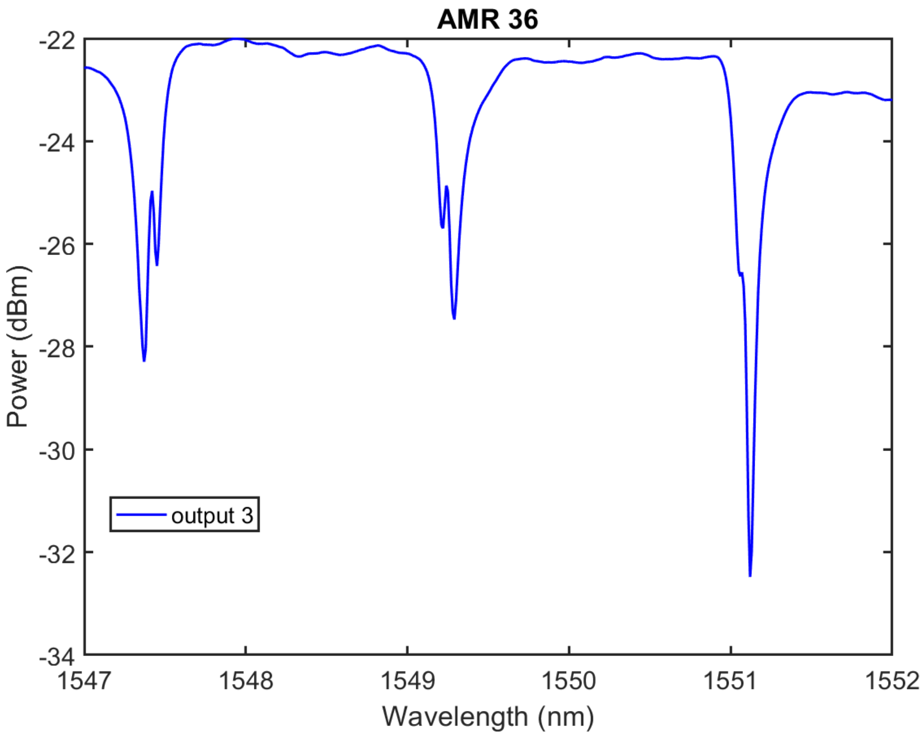

Figure 3.5-27: The experimentally measured DC-AMR ADF spectra of the output 3 from 1547 nm to 1552 nm with Lc_1=8.7 µm and Lc_2=36 µm. The spectra have IL=1 dB, FSR=1.83 nm, best Q=$1.1 \cdot 10^4$, ER=10.1 dB and SR=118.6 dB/nm, split=0.18 nm.

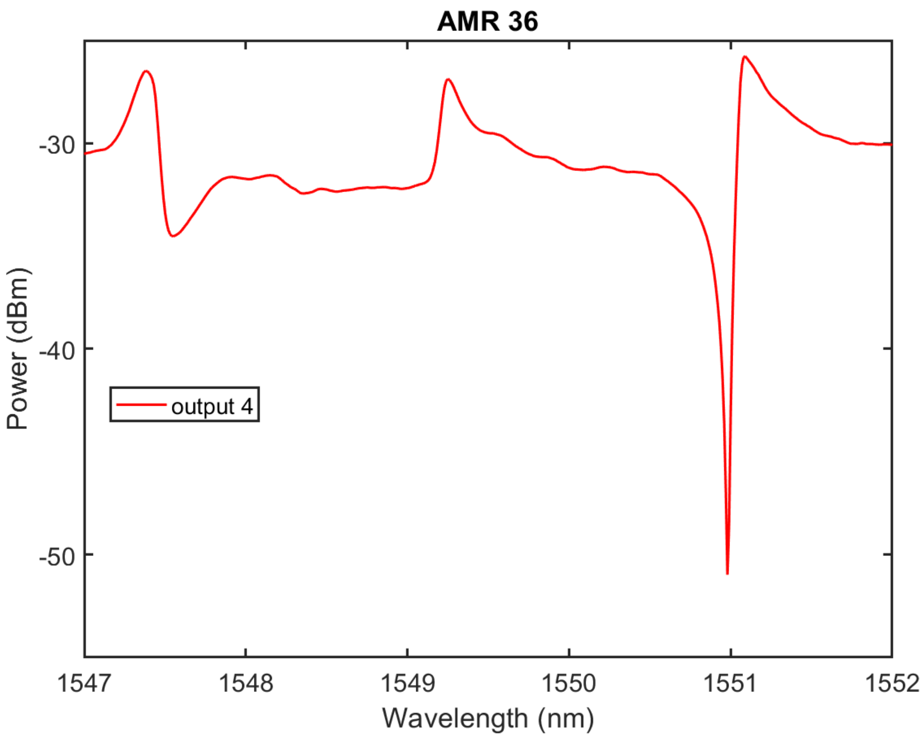

Figure 3.5-28: The experimentally measured DC-AMR ADF spectra of the output 4 from 1547 nm to 1552 nm with coupling lengths of Lc_1=8.7 µm and Lc_2=36 µm. The spectra have IL=2 dB, FSR=1.84 nm, best eff-Q=$1.4 \cdot 10^4$, ER=25 dB, SR= 229 dB/nm.

3.6. Double Coupled Reverse MR

The double coupled reverse MR is designed and fabricated to see the effect of the reversed second MLM. The reversed MLM in the design introduces a Mach-Zehnder interferometer FSR to the spectra. The coupling length L_c of the (DC-RMR) IC coupler is 10.7 μm and the IC coupler length is kept constant in all designs of SC-MR ADF and the FSR can be calculated with FSR $= \frac{\lambda^2}{n_g L}$, which the ports are numbered as 1,2,3,4 and a prefix is added if the port is used as output. The ports are named as follows, the input is always the port 2 and it is not numbered, and mentioned only as input while the output 1, 3 or 4 meaning the first (upper most), third or the fourth grating coupler which is utilized as an output port. Figure 3.6-1 shows the representation of the DC-RMR structure. Figure 3.6-2 shows the KLayout design of the DC-RMR ADF is given with the corresponding coupling dimensions and bend radii with the positions of the input and output ports. The coupler bending radius of 10 μm, the waveguide bending radius of 5 μm and the gap between the coupler waveguides g=200 nm is constant in all designs. The spectra of the DC-RMR have strong Fano and Lorentzian lineshapes with Q factors on the order of 10^4.

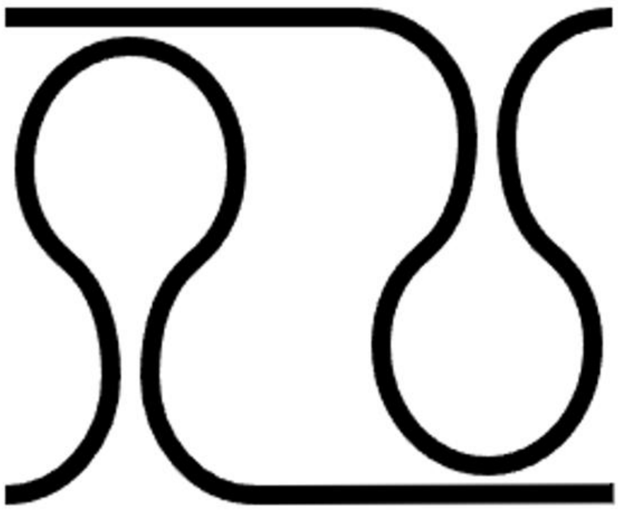

Figure 3.6-1: The representation of the DC-RMR ADF.

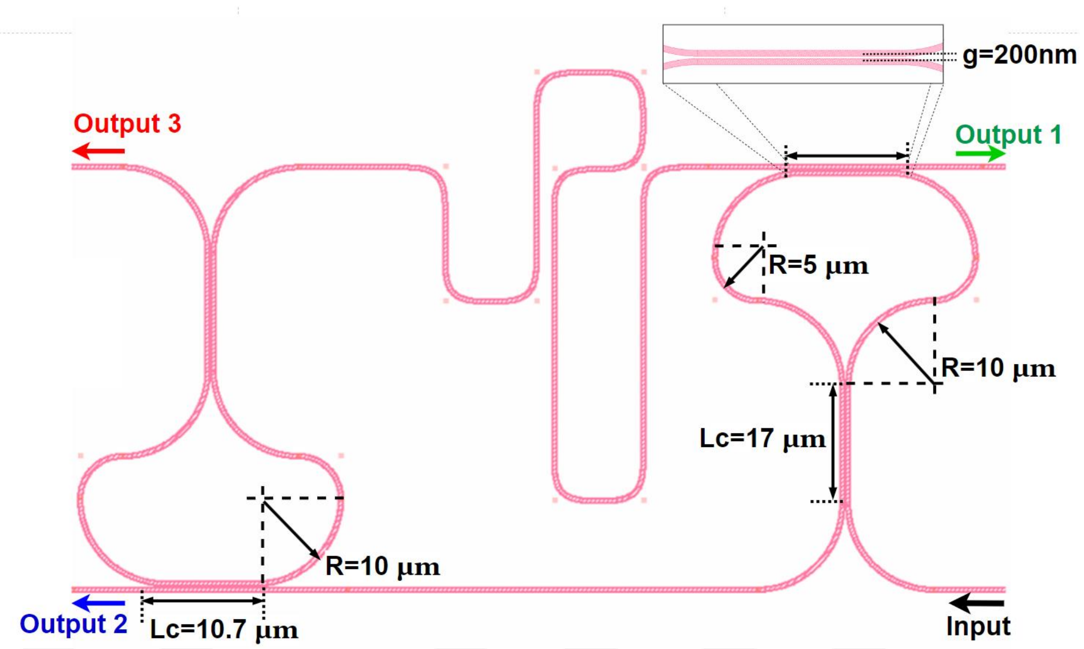

Figure 3.6-2: Representation of DC-SMR with output shown in black, output 1,2 and 3 is shown in green, blue, and red, respectively. The IC coupler has a coupling length of $L_{c=}$10.7 μm and the CC coupler has $L_{c=}$17 μm (specific to chosen design), waveguides have a bending radius of 5 μm while the couplers' bending radius is 10 μm, the gap between the bus waveguides in the couplers is g=200 nm

DC-RMR ADF with Lc_2=28 µm

Figure 3.6-3 shows the experimentally measured spectra of DC-SMR ADF from 1500 nm to 1580 nm with Lc_1=10.7 µm and Lc_2=28 µm. The output ports 1, 3 and 4 are shown in green, blue, and red, respectively. Figure 3.6-4 shows the experimentally measured DC-SMR ADF spectra from 1510 nm to 1520 nm with Lc_1=10.7 µm and Lc_2=28 µm. The output ports 1, 3 and 4 are shown in green, blue, and red, respectively. The FSR of the spectra is 3.43 nm. Figure 3.6-5 shows the experimentally measured DC-SMR ADF spectra of output 1 from 1516 nm to 1520 nm with Lc_1=10.7 µm and Lc_2=28 µm. The spectra have IL=15 dB, FSR=3.43 nm, best eff-Q=$4\cdot10^3$, ER=23 dB, SR=59 dB/nm. Figure 3.6-6 shows the experimentally measured DC-SMR ADF spectra of the output 3 from 1516 nm to 1520 nm with Lc_1=10.7 µm and Lc_2=28 µm. The spectra have IL=21 dB, FSR= 3.43 nm, best Q factor of $9.4\cdot10^3$, ER=9 dB and SR=68 dB/nm. Figure 3.6-7 shows the experimentally measured DC-SMR ADF spectra of the output 4 from 1516 nm to 1520 nm with coupling lengths of Lc_1=10.7 µm and Lc_2=28 µm. The spectra have IL=31 dB, FSR=3.43 nm, best eff-Q=$3\cdot10^3$, ER=7.7 dB, SR= 70 dB/nm.

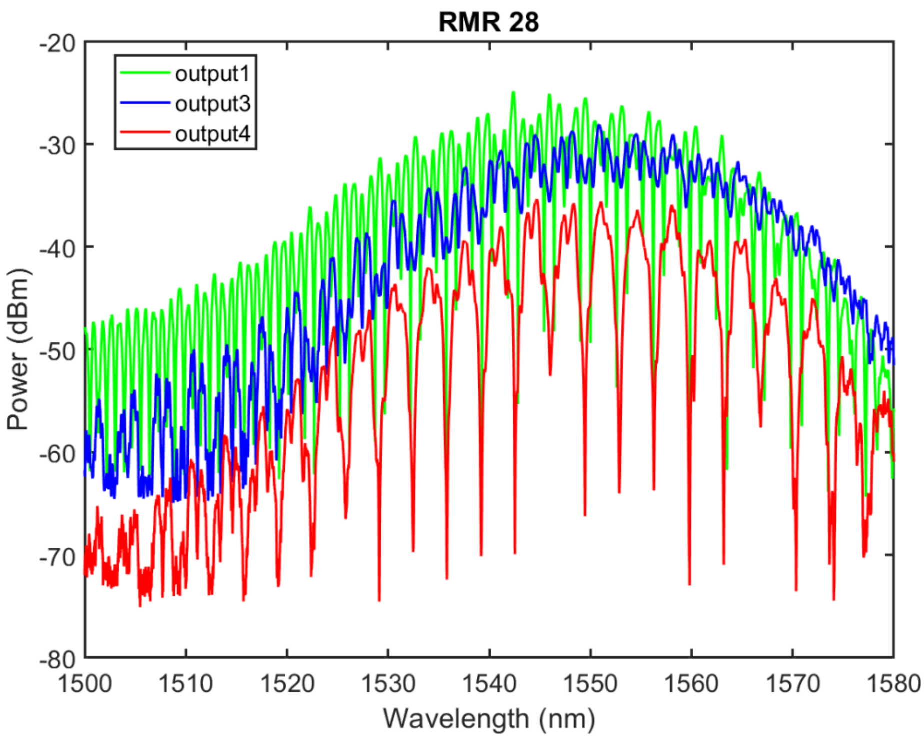

Figure 3.6-3: The experimentally measured spectra of DC-SMR ADF from 1500 nm to 1580 nm with Lc_1=10.7 µm and Lc_2=28 µm. The output ports 1, 3 and 4 are shown in green, blue, and red, respectively.

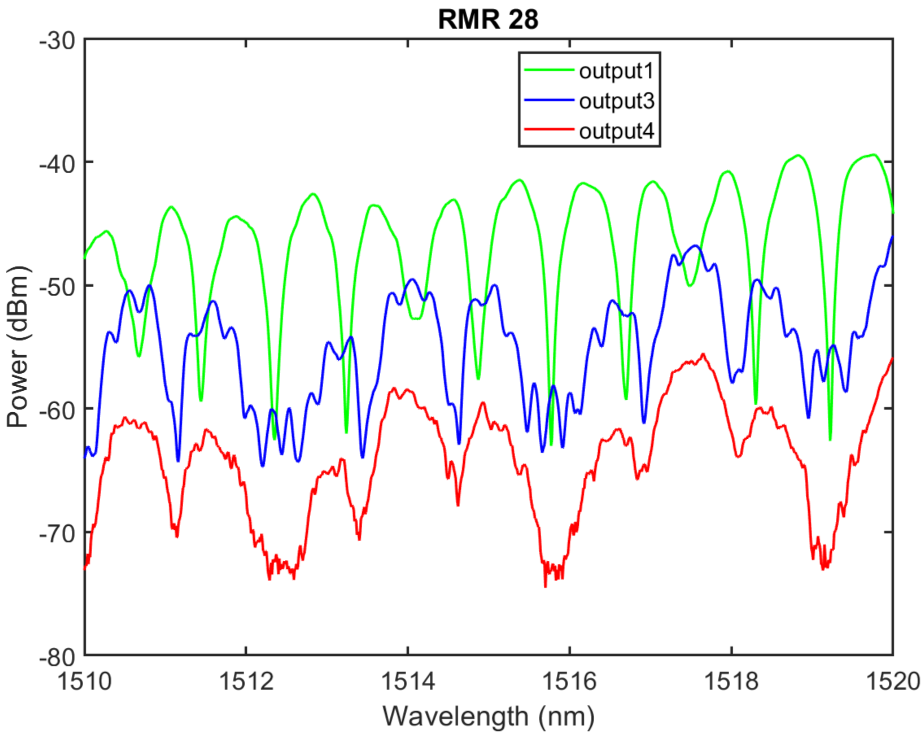

Figure 3.6-4: The experimentally measured DC-SMR ADF spectra from 1510 nm to 1520 nm with Lc_1=10.7 μm and Lc_2=28 μm. The output ports 1, 3 and 4 are shown in green, blue, and red, respectively. The FSR of the spectra is 3.43 nm.

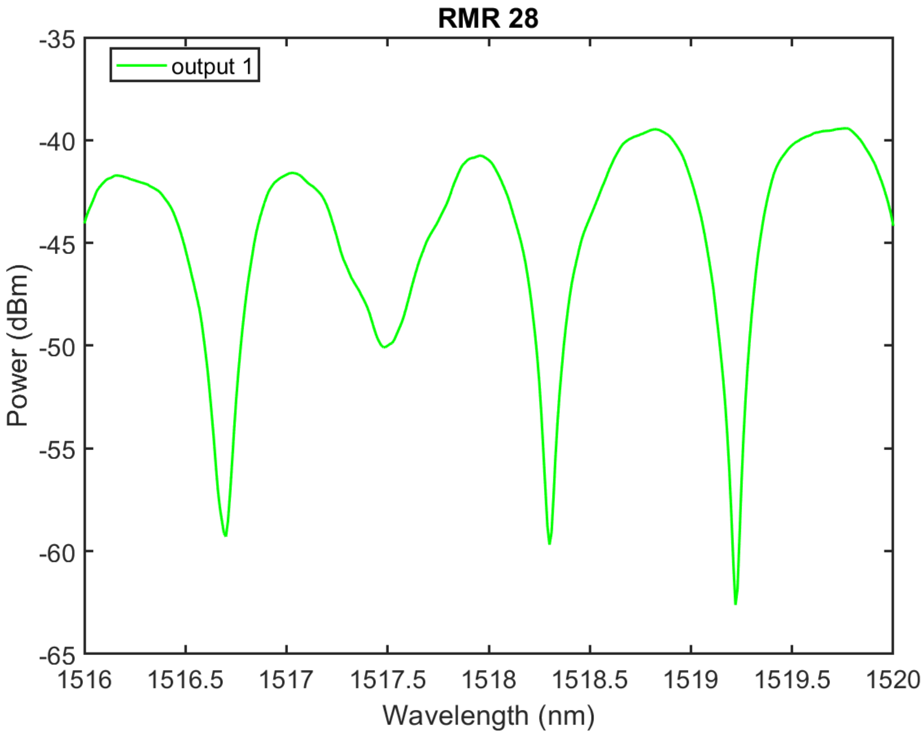

Figure 3.6-5: The experimentally measured DC-SMR ADF spectra of output 1 from 1516 nm to 1520 nm with Lc_1=10.7 μm and Lc_2=28 μm. The spectra have IL=15 dB, FSR=3.43 nm, best eff-Q=$4\cdot10^3$, ER=23 dB, SR=59 dB/nm.

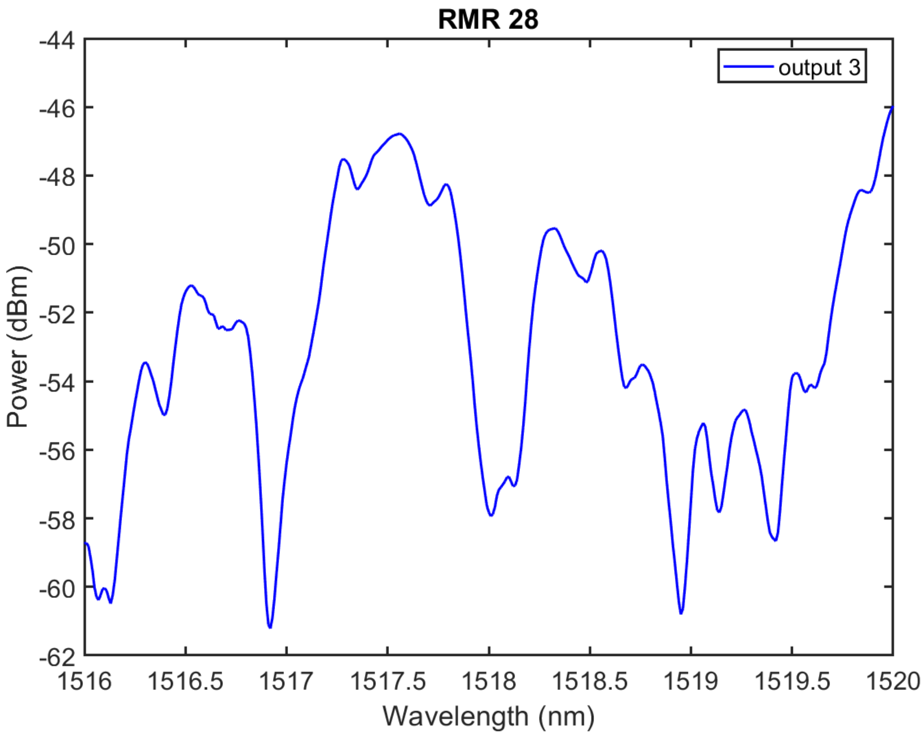

Figure 3.6-6: The experimentally measured DC-SMR ADF spectra of the output 3 from 1516 nm to 1520 nm with Lc_1=10.7 μm and Lc_2=28 μm. The spectra have IL=21 dB, FSR= 3.43 nm, best Q factor of $9.4 \cdot 10^3$, ER=9 dB and SR=68 dB/nm.

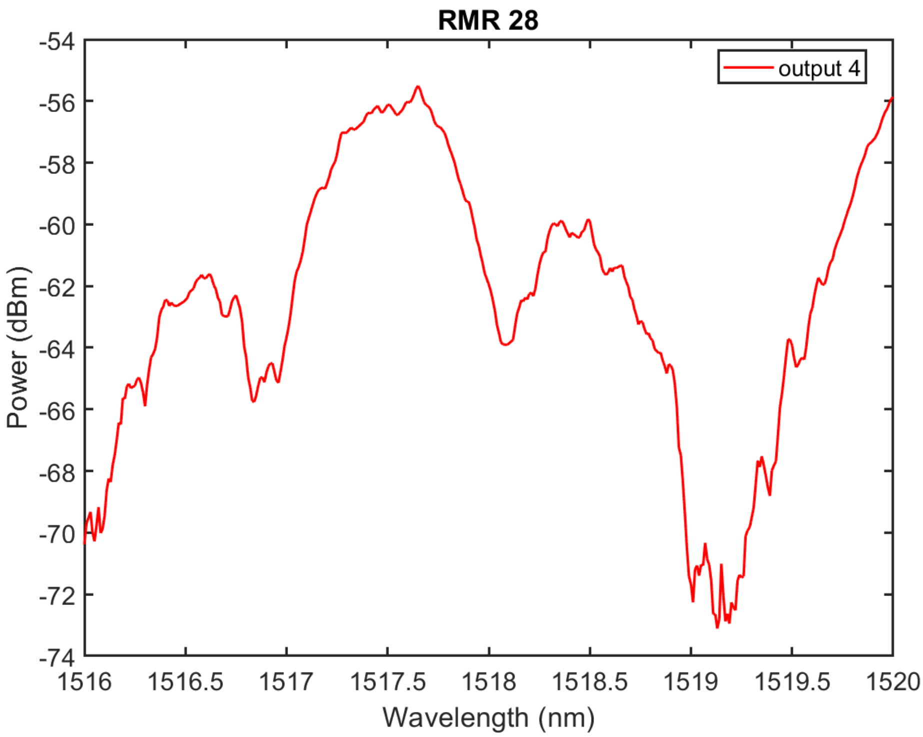

Figure 3.6-7: The experimentally measured DC-SMR ADF spectra of the output 4 from 1516 nm to 1520 nm with coupling lengths of Lc_1=10.7 μm and Lc_2=28 μm. The spectra have IL=31 dB, FSR=3.43 nm, best eff-Q=$3 \cdot 10^3$, ER=7.7 dB, SR= 70 dB/nm.

DC-RMR ADF with Lc_2=30 µm

Figure 3.6-8 shows the experimentally measured spectra of DC-SMR ADF from 1500 nm to 1580 nm with Lc_1=10.7 µm and Lc_2=30 µm. The output ports 1, 3 and 4 are shown in green, blue, and red, respectively. Figure 3.6-9 shows the experimentally measured DC-SMR ADF spectra from 1510 nm to 1520 nm with Lc_1=10.7 µm and Lc_2=30 µm. The output ports 1, 3 and 4 are shown in green, blue, and red, respectively. The FSR of the spectra is 3.38 nm. Figure 3.6-10 shows the experimentally measured DC-SMR ADF spectra of output 1 from 1516 nm to 1520 nm with Lc_1=10.7 µm and Lc_2=30 µm. The spectra have IL=15 dB, FSR=3.38 nm. Figure 3.6-11 shows the experimentally measured DC-SMR ADF spectra of the output 3 from 1516 nm to 1520 nm with Lc_1=10.7 µm and Lc_2=30 µm. The spectra have IL=19 dB, FSR= 3.38 nm. Figure 3.6-12 shows the experimentally measured DC-SMR ADF spectra of the output 4 from 1516 nm to 1520 nm with coupling lengths of Lc_1=10.7 µm and Lc_2=30 µm. The spectra have IL=27 dB, FSR=3.38 nm.

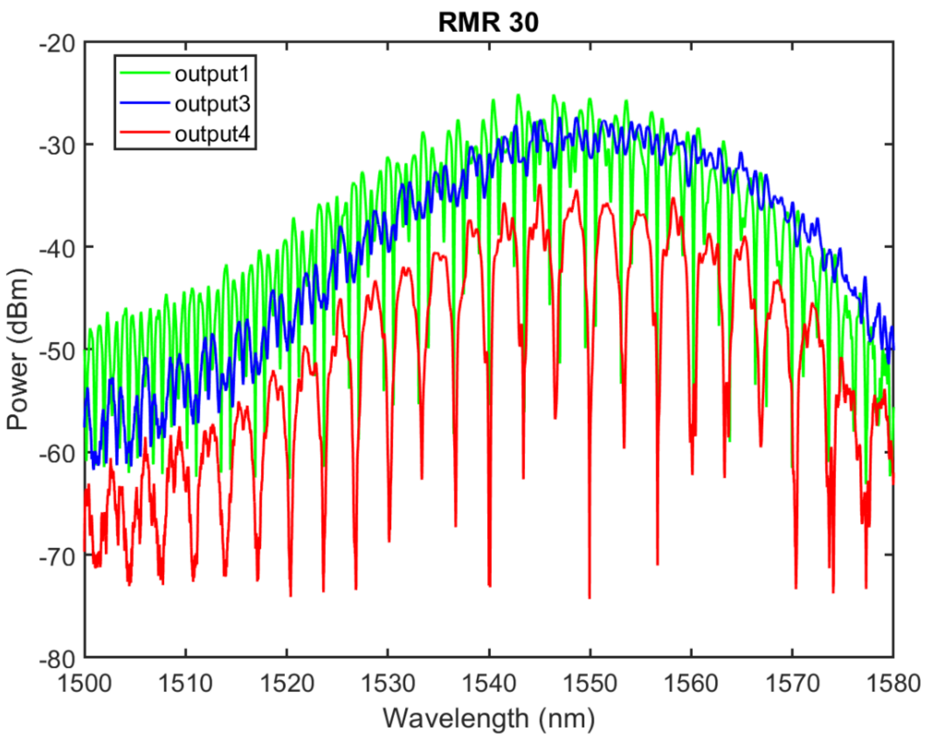

Figure 3.6-8: The experimentally measured spectra of DC-SMR ADF from 1500 nm to 1580 nm with Lc_1=10.7 µm and Lc_2=30 µm. The output ports 1, 3 and 4 are shown in green, blue, and red, respectively

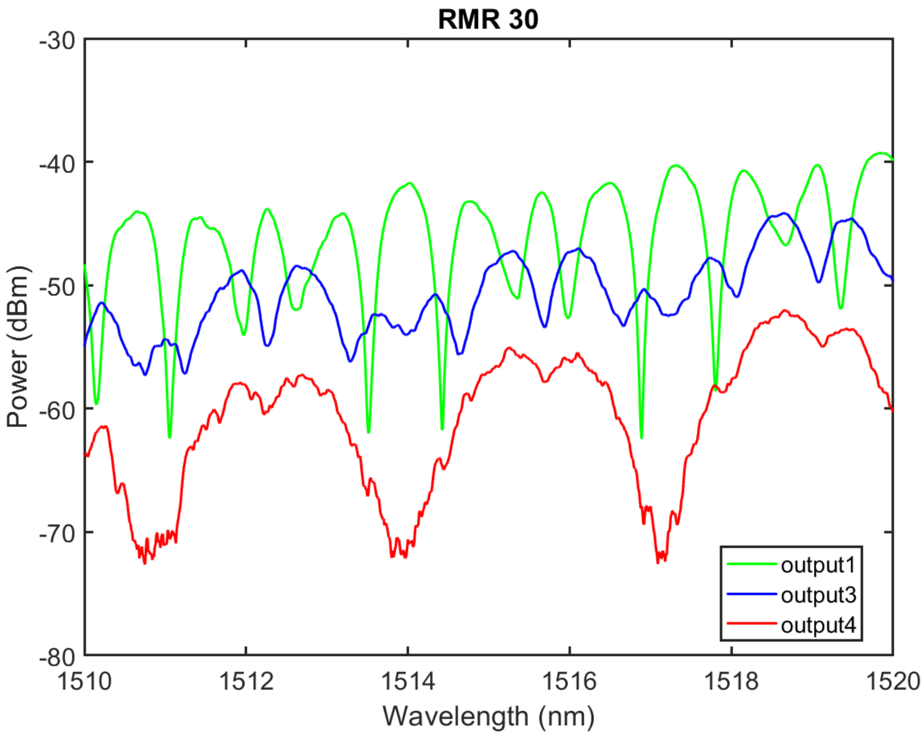

Figure 3.6-9: The experimentally measured DC-SMR ADF spectra from 1510 nm to 1520 nm with Lc_1=10.7 µm and Lc_2=30 µm. The output ports 1, 3 and 4 are shown in green, blue, and red, respectively. The FSR of the spectra is 3.38 nm.

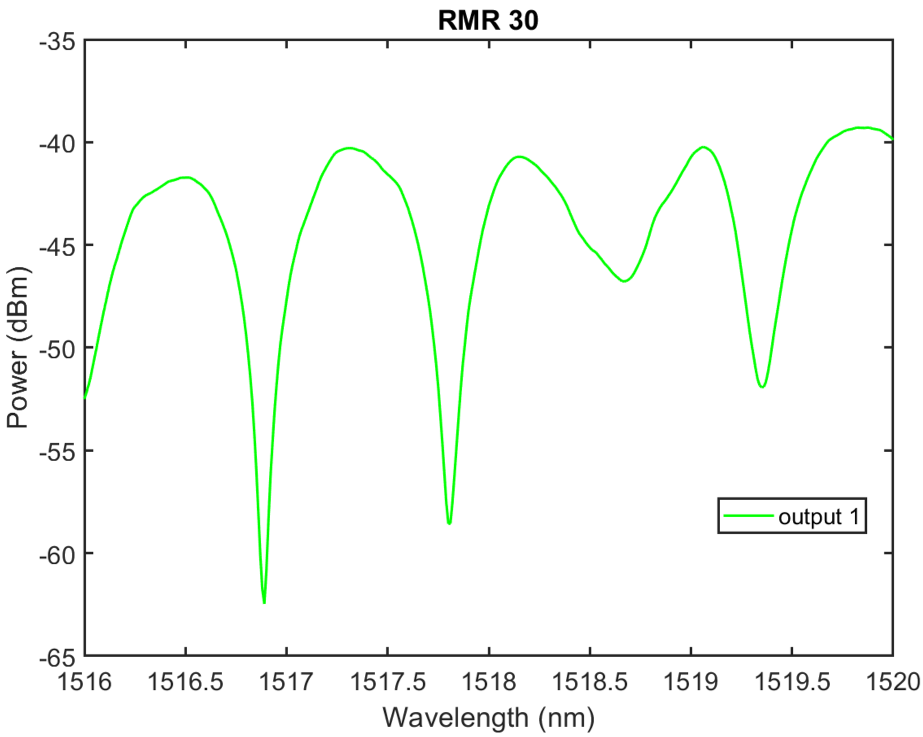

Figure 3.6-10: The experimentally measured DC-SMR ADF spectra of output 1 from 1516 nm to 1520 nm with Lc_1=10.7 µm and Lc_2=30 µm. The spectra have IL=15 dB, FSR=3.38 nm.

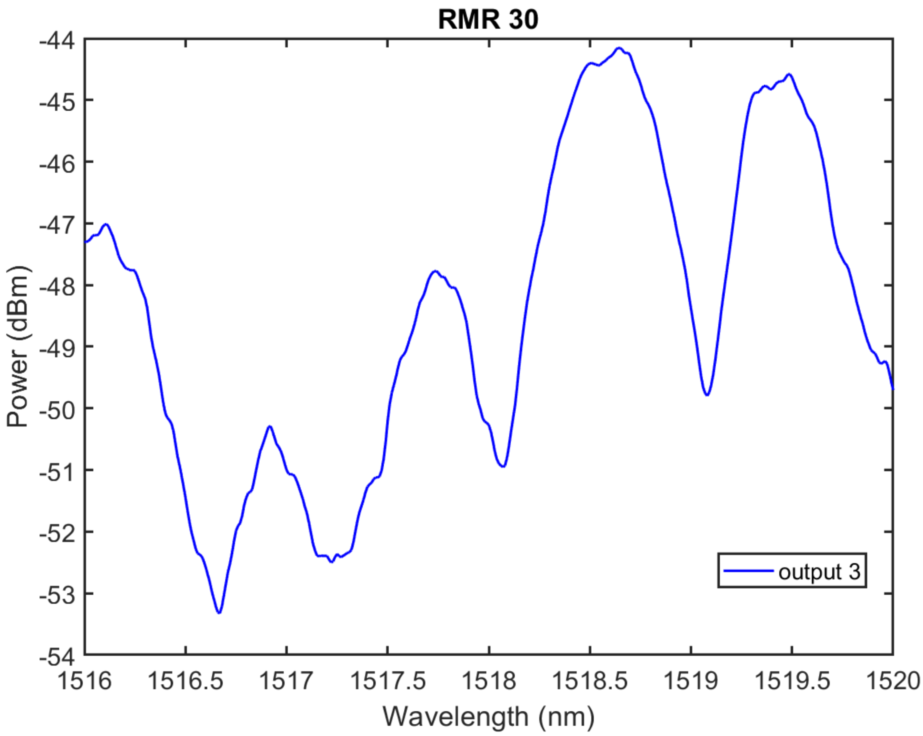

Figure 3.6-11: The experimentally measured DC-SMR ADF spectra of the output 3 from 1516 nm to 1520 nm with Lc_1=10.7 µm and Lc_2=30 µm. The spectra have IL=19 dB, FSR= 3.38 nm.

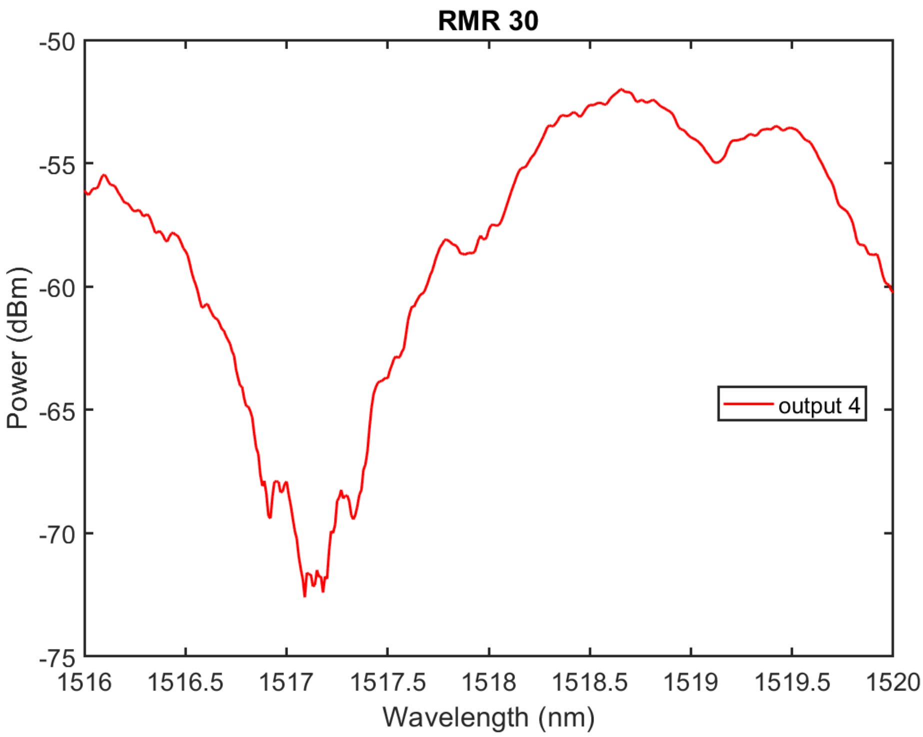

Figure 3.6-12: The experimentally measured DC-SMR ADF spectra of the output 4 from 1516 nm to 1520 nm with coupling lengths of Lc_1=10.7 µm and Lc_2=30 µm. The spectra have IL=27 dB, FSR=3.38 nm.

DC-RMR ADF with Lc_2=32 µm

Figure 3.6-13 shows the experimentally measured spectra of DC-SMR ADF from 1500 nm to 1580 nm with Lc_1=10.7 µm and Lc_2=32 µm. The output ports 1, 3 and 4 are shown in green, blue, and red, respectively. Figure 3.6-14 shows the experimentally measured DC-SMR ADF spectra from 1510 nm to 1520 nm with Lc_1=10.7 µm and Lc_2=32 µm. The output ports 1, 3 and 4 are shown in green, blue, and red, respectively. The FSR of the spectra is 3.33 nm. Figure 3.6-15 shows the experimentally measured DC-SMR ADF spectra of output 1 from 1516 nm to 1520 nm with Lc_1=10.7 µm and Lc_2=32 µm. The spectra have IL=13 dB, FSR=3.33 nm. Figure 3.6-16 shows the experimentally measured DC-SMR ADF spectra of the output 3 from 1516 nm to 1520 nm with Lc_1=10.7 µm and Lc_2=32 µm. The spectra have IL=17 dB, FSR= 3.33 nm. Figure 3.6-17 shows the experimentally measured DC-SMR ADF spectra of the output 4 from 1516 nm to 1520 nm with coupling lengths of Lc_1=10.7 µm and Lc_2=32 µm. The spectra have IL=28 dB, FSR=3.33 nm.

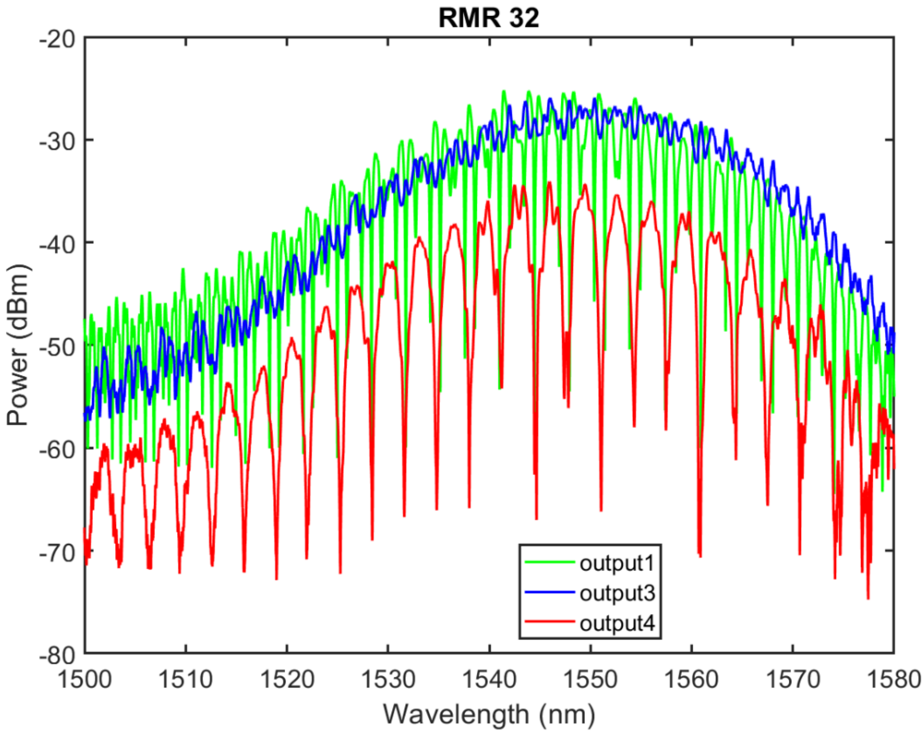

Figure 3.6-13: The experimentally measured spectra of DC-SMR ADF from 1500 nm to 1580 nm with Lc_1=10.7 µm and Lc_2=32 µm. The output ports 1, 3 and 4 are shown in green, blue, and red, respectively.

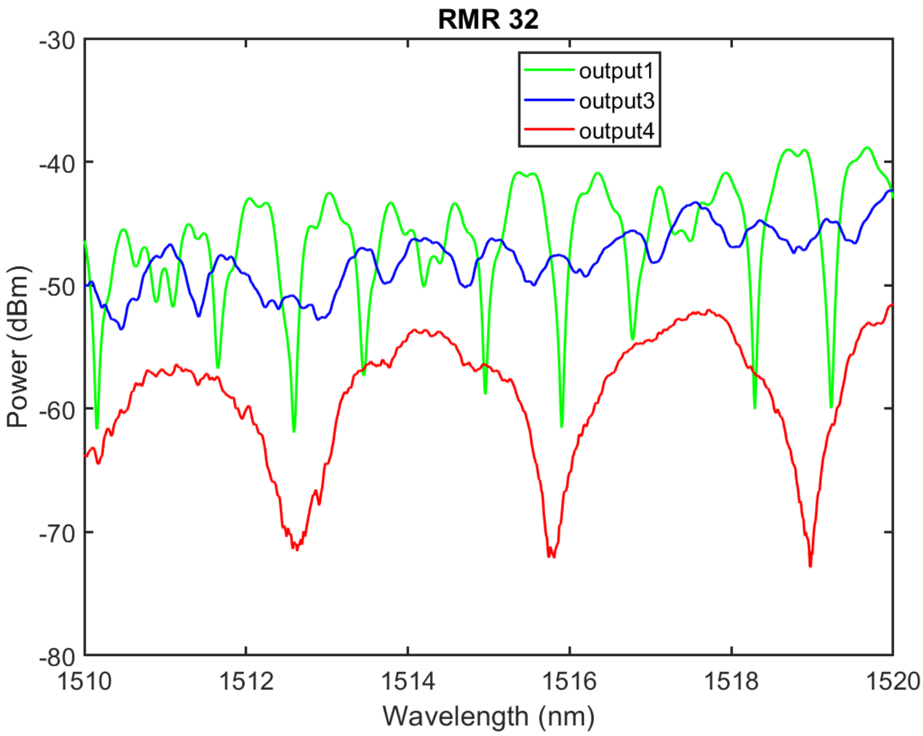

Figure 3.6-14: The experimentally measured DC-SMR ADF spectra from 1510 nm to 1520 nm with Lc_1=10.7 μm and Lc_2=32 μm. The output ports 1, 3 and 4 are shown in green, blue, and red, respectively. The FSR of the spectra is 3.33 nm.

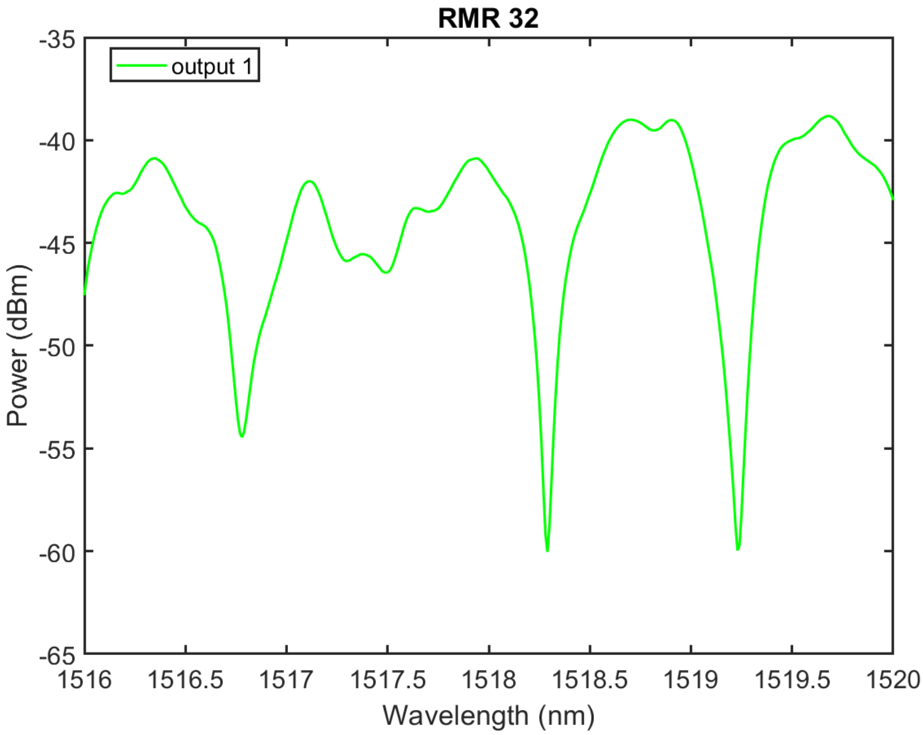

Figure 3.6-15: The experimentally measured DC-SMR ADF spectra of output 1 from 1516 nm to 1520 nm with Lc_1=10.7 μm and Lc_2=32 μm. The spectra have IL=13 dB, FSR=3.33 nm.

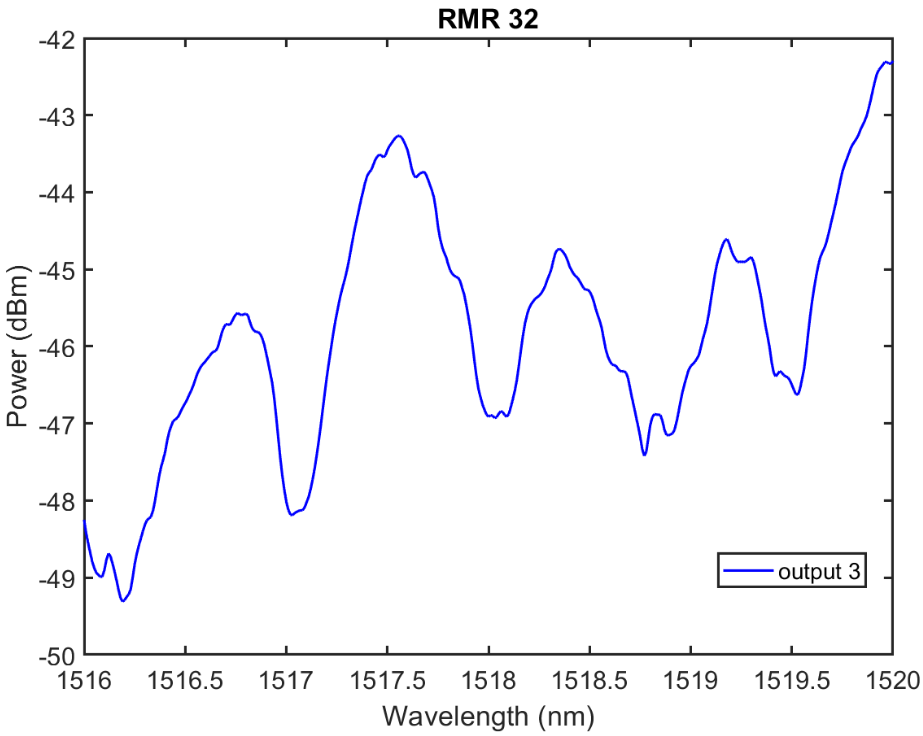

Figure 3.6-16: The experimentally measured DC-SMR ADF spectra of the output 3 from 1516 nm to 1520 nm with Lc_1=10.7 µm and Lc_2=32 µm. The spectra have IL=17 dB, FSR= 3.33 nm.

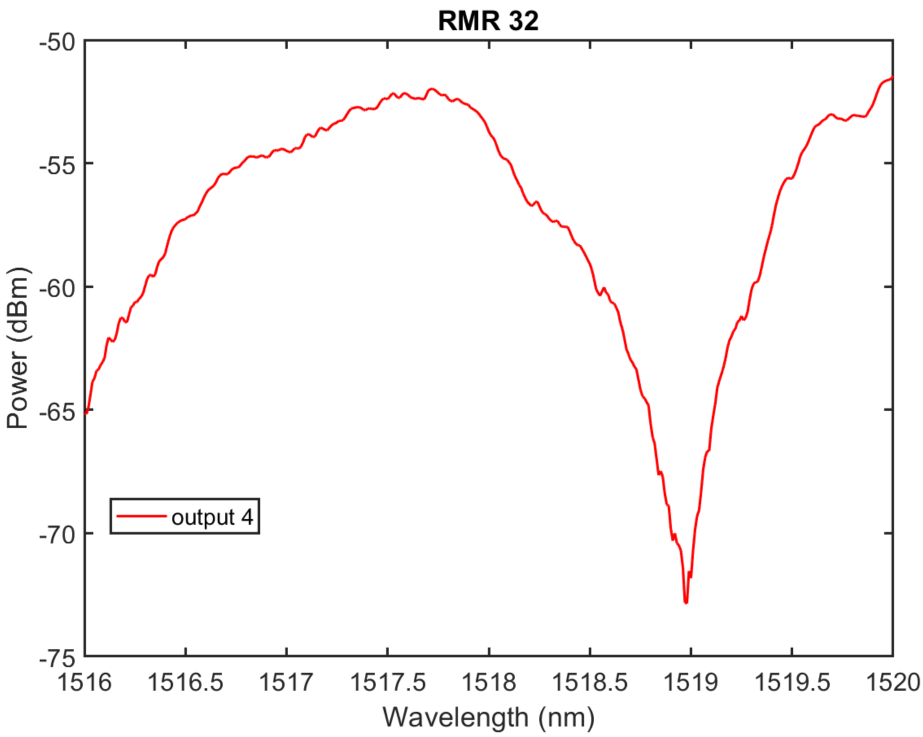

Figure 3.6-17: The experimentally measured DC-SMR ADF spectra of the output 4 from 1516 nm to 1520 nm with coupling lengths of Lc_1=10.7 µm and Lc_2=32 µm. The spectra have IL=28 dB, FSR=3.33 nm.

DC-RMR ADF with Lc_2=34 µm

Figure 3.6-18 shows the experimentally measured spectra of DC-SMR ADF from 1500 nm to 1580 nm with Lc_1=10.7 µm and Lc_2=34 µm. The output ports 1, 3 and 4 are shown in green, blue, and red, respectively. Figure 3.6-19 shows the experimentally measured DC-SMR ADF spectra from 1510 nm to 1520 nm with Lc_1=10.7 µm and Lc_2=34 µm. The output ports 1, 3 and 4 are shown in green, blue, and red, respectively. The FSR of the spectra is 3.28 nm. Figure 3.6-20 shows the experimentally measured DC-SMR ADF spectra of output 1 from 1516 nm to 1520 nm with Lc_1=10.7 µm and Lc_2=34 µm. The spectra have IL=12 dB, FSR=3.28 nm. Figure 3.6-21 shows the experimentally measured DC-SMR ADF spectra of the output 3 from 1516 nm to 1520 nm with Lc_1=10.7 µm and Lc_2=34 µm. The spectra have IL=16 dB, FSR= 3.28 nm. Figure 3.6-22 shows the experimentally measured DC-SMR ADF spectra of the output 4 from 1516 nm to 1520 nm with coupling lengths of Lc_1=10.7 µm and Lc_2=34 µm. The spectra have IL=24 dB, FSR=3.28 nm.

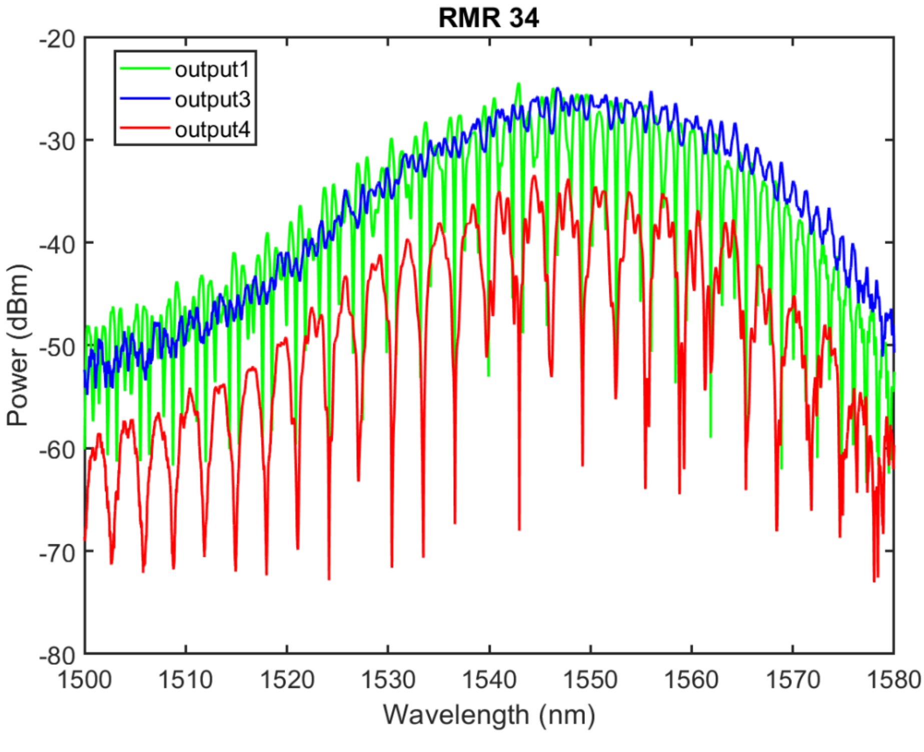

Figure 3.6-18: The experimentally measured spectra of DC-SMR ADF from 1500 nm to 1580 nm with Lc_1=10.7 µm and Lc_2=34 µm. The output ports 1, 3 and 4 are shown in green, blue, and red, respectively.

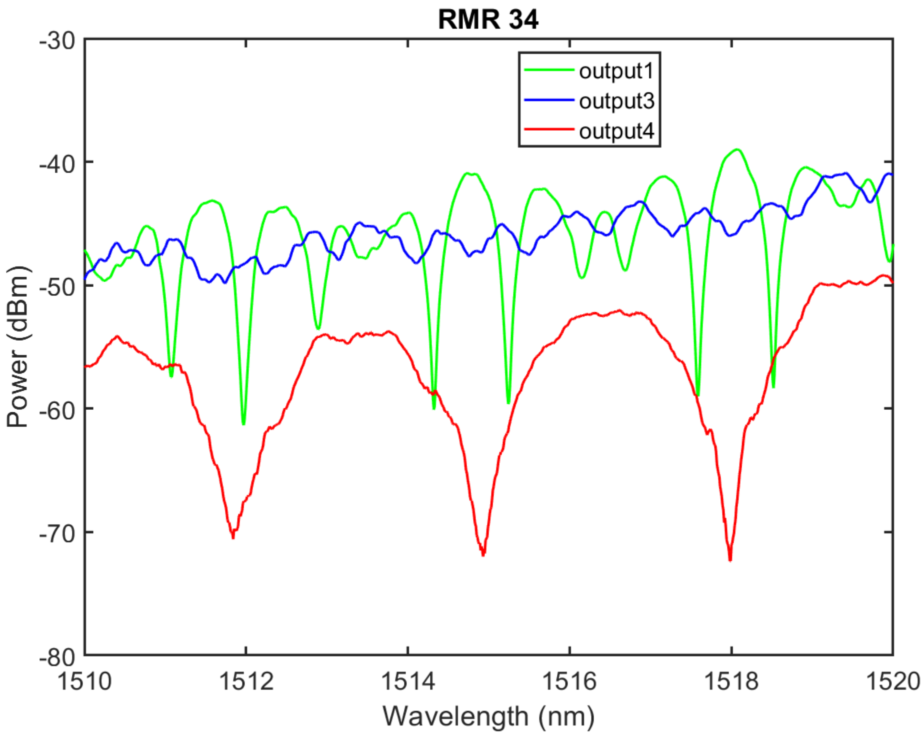

Figure 3.6-19: The experimentally measured DC-SMR ADF spectra from 1510 nm to 1520 nm with Lc_1=10.7 µm and Lc_2=34 µm. The output ports 1, 3 and 4 are shown in green, blue, and red, respectively. The FSR of the spectra is 3.28 nm.

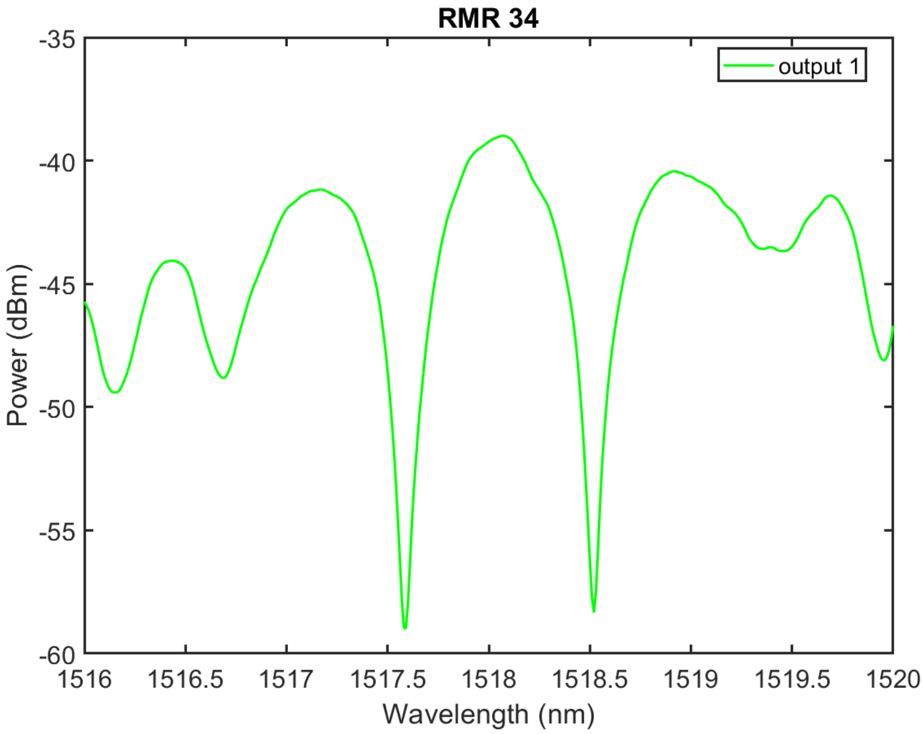

Figure 3.6-20: The experimentally measured DC-SMR ADF spectra of output 1 from 1516 nm to 1520 nm with Lc_1=10.7 µm and Lc_2=34 µm. The spectra have IL=12 dB, FSR=3.28 nm.

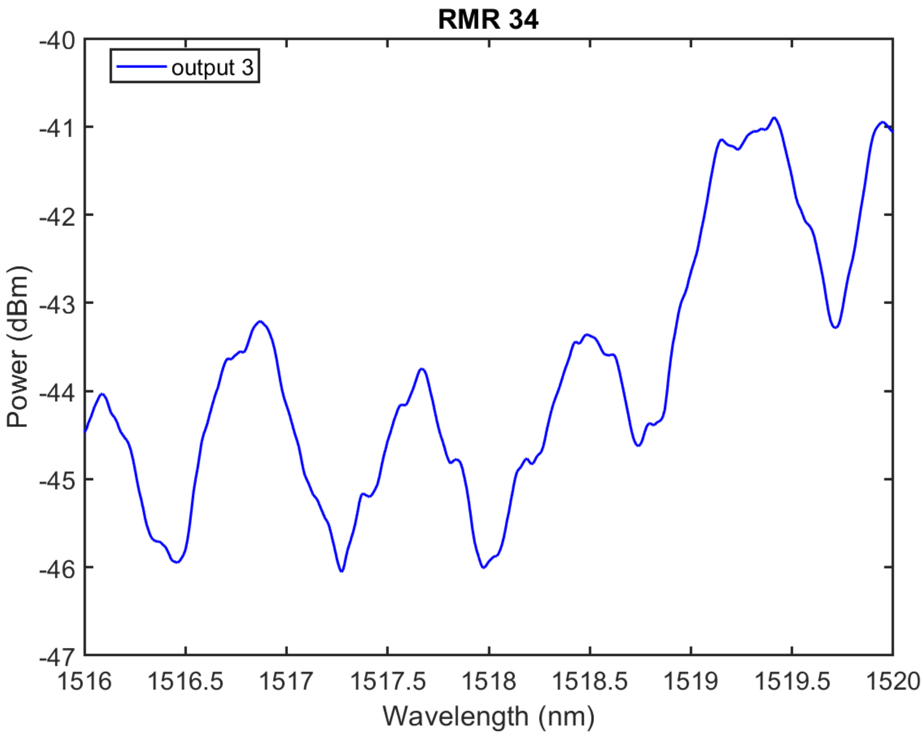

Figure 3.6-21: The experimentally measured DC-SMR ADF spectra of the output 3 from 1516 nm to 1520 nm with Lc_1=10.7 µm and Lc_2=34 µm. The spectra have IL=16 dB, FSR= 3.28 nm.

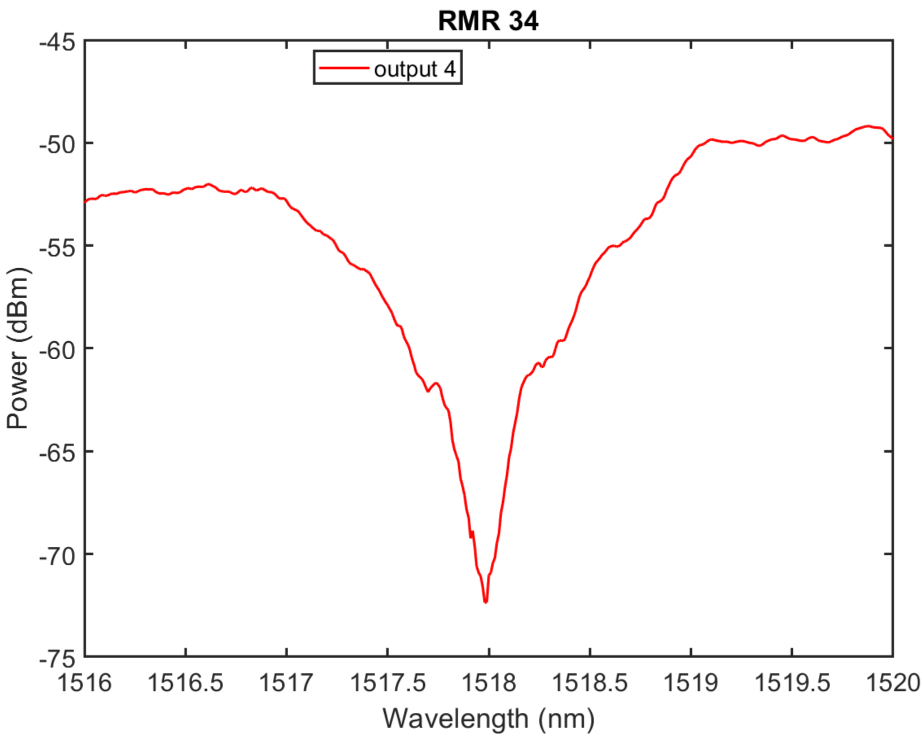

Figure 3.6-22: The experimentally measured DC-SMR ADF spectra of the output 4 from 1516 nm to 1520 nm with coupling lengths of Lc_1=10.7 µm and Lc_2=34 µm. The spectra have IL=24 dB, FSR=3.28 nm.

DC-RMR ADF with Lc_2=36 µm

Figure 3.6-23 shows the experimentally measured spectra of DC-SMR ADF from 1500 nm to 1580 nm with Lc_1=10.7 µm and Lc_2=34 µm. The output ports 1, 3 and 4 are shown in green, blue, and red, respectively. Figure 3.6-24 shows the experimentally measured DC-SMR ADF spectra from 1510 nm to 1520 nm with Lc_1=10.7 µm and Lc_2=34 µm. The output ports 1, 3 and 4 are shown in green, blue, and red, respectively. The FSR of the spectra is 3.24 nm. Figure 3.6-25 shows the experimentally measured DC-SMR ADF spectra of output 1 from 1516 nm to 1520 nm with Lc_1=10.7 µm and Lc_2=34 µm. The spectra have IL=12 dB, FSR=3.24 nm. Figure 3.6-26 shows the experimentally measured DC-SMR ADF spectra of the output 3 from 1516 nm to 1520 nm with Lc_1=10.7 µm and Lc_2=34 µm. The spectra have IL=16 dB, FSR= 3.24 nm. Figure 3.6-27 shows the experimentally measured DC-SMR ADF spectra of the output 4 from 1516 nm to 1520 nm with coupling lengths of Lc_1=10.7 µm and Lc_2=34 µm. The spectra have IL=24 dB, FSR=3.24 nm.

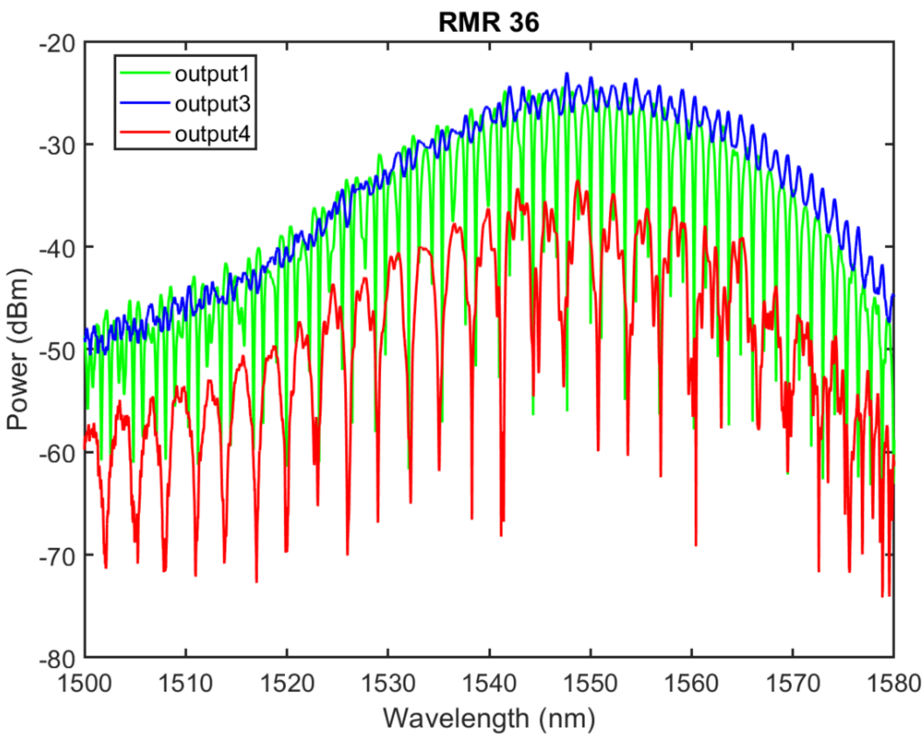

Figure 3.6-23: The experimentally measured spectra of DC-SMR ADF from 1500 nm to 1580 nm with Lc_1=10.7 µm and Lc_2=34 µm. The output ports 1, 3 and 4 are shown in green, blue, and red, respectively.

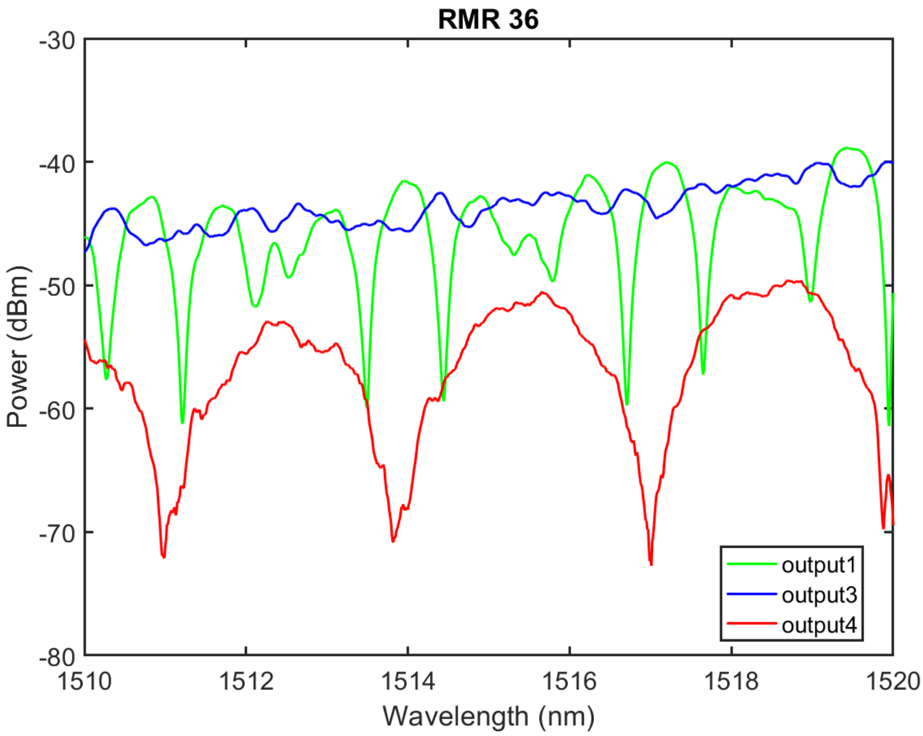

Figure 3.6-24: The experimentally measured DC-SMR ADF spectra from 1510 nm to 1520 nm with Lc_1=10.7 μm and Lc_2=34 μm. The output ports 1, 3 and 4 are shown in green, blue, and red, respectively. The FSR of the spectra is 3.24 nm.

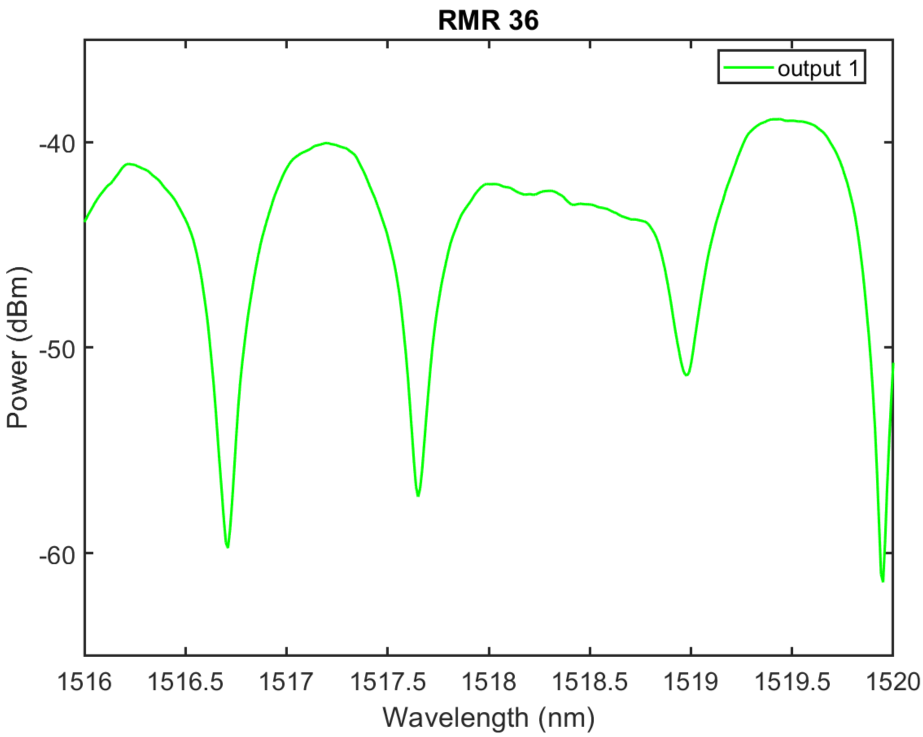

Figure 3.6-25: The experimentally measured DC-SMR ADF spectra of output 1 from 1516 nm to 1520 nm with Lc_1=10.7 μm and Lc_2=34 μm. The spectra have IL=12 dB, FSR=3.24 nm.

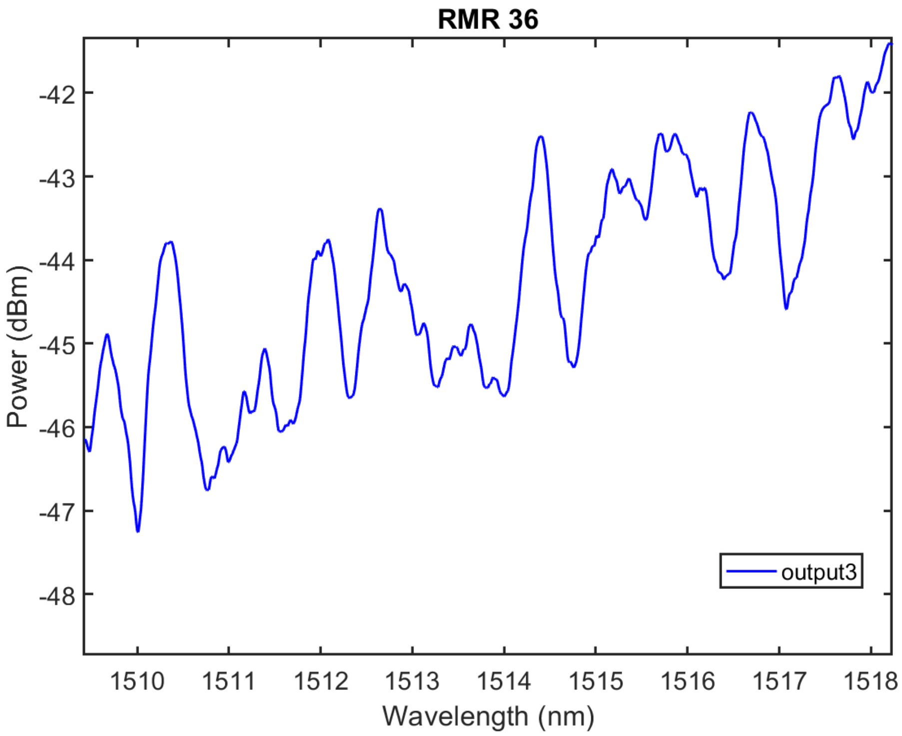

Figure 3.6-26: The experimentally measured DC-SMR ADF spectra of the output 3 from 1516 nm to 1520 nm with Lc_1=10.7 µm and Lc_2=34 µm. The spectra have IL=16 dB, FSR= 3.24 nm.

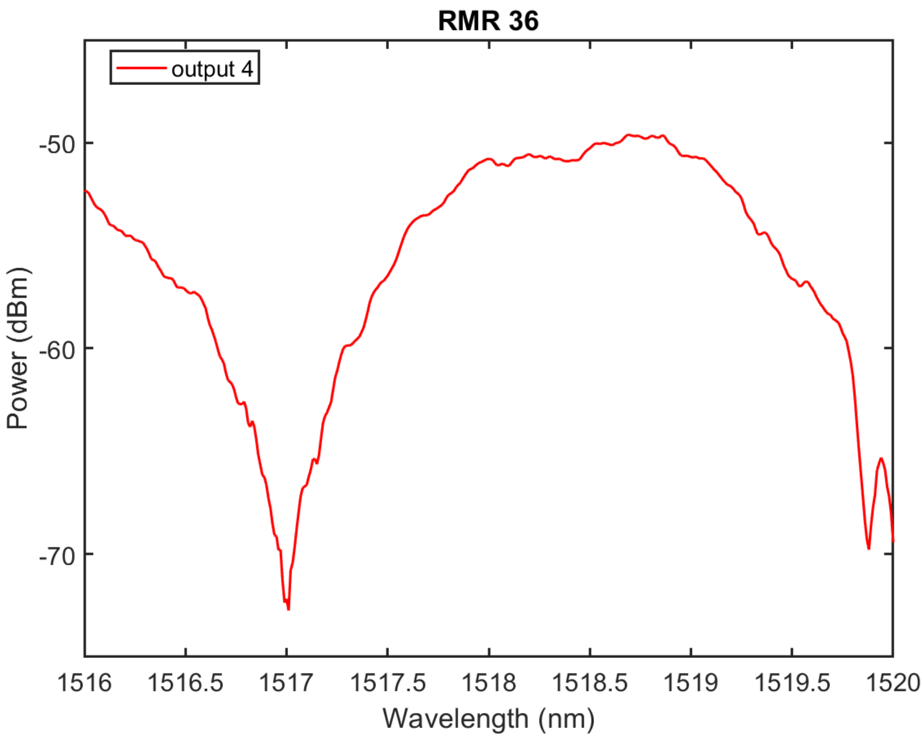

Figure 3.6-27: The experimentally measured DC-SMR ADF spectra of the output 4 from 1516 nm to 1520 nm with coupling lengths of Lc_1=10.7 µm and Lc_2=34 µm. The spectra have IL=24 dB, FSR=3.24 nm.

3.7. Summary

The figures of merits (FOMs) are given as the best result achieved for each design. The devices themselves have almost no insertion loss and the loss mechanism almost directly comes from the surface grating couplers -in and out- for all structures. SC-MR has an FSR of 1.6 nm with a best Q-factor of 19000, has an extinction ratio of 23 dB and a slope rate of 163 dB/nm. SC-MR has an FSR of 1.1 nm with a best Q-factor of 12000, has an extinction ratio of 30 dB and a slope rate of 307 dB/nm. DC-SMR has an FSR of 2.05 nm with a best Q-factor of 10000, a mode split of 1.1 nm, has an extinction ratio of 27 dB and a slope rate of 450 dB/nm. DC-AMR has an FSR of 1.83 nm with a best Q-factor of 40000, a mode split of 0.1 nm, has an extinction ratio of 33 dB and a slope rate of 872 dB/nm. DC-RMR has an FSR of 3.6 nm with a best Q-factor of 8000, a mode split of 1.1 nm, has an extinction ratio of 29 dB and a slope rate of 183 dB/nm.

In all of our designs we introduced a subsection of a waveguide with a specific length, if the round-trip optical path length is increased by increasing the length of the subsection, these devices can even be used for dense wavelength division multiplexing (DWDM) applications, which should have a spacing of 0.2 nm at 1550 nm. These results show that proposed devices, ADF-MLM, ADF resonators are good candidates for WDM applications, but still further modifications are required to be used as novel integrated photonic elements for optical communication, computation, and sensing.

Chapter 4

CONCLUSION

Add-drop filters (ADFs) based on Meandering Loop Mirrors (MLMs) and resonators based on MLMs are designed, fabricated, and analyzed using silicon integrated photonics technology for operation in the standard near-infrared (near-IR) telecommunication band. Optical waveguides, directional couplers (DCs), MLMs, single and double coupled meandering resonators (MRs), antisymmetric meandering resonators (AMRs), symmetric meandering resonators (SMRs), and reverse meandering resonators (RMRs) with symmetric and antisymmetric DCs were designed, fabricated, and analyzed as a function of the DC length to scan the desired near-infrared (near-IR) telecommunication band.

The reflection and transmission intensities are plotted in logarithmic (dB) scale. The free spectral range (FSR), quality factor (Q-factor), mode split, insertion loss (IL), extinction ratio (ER), and slope rate (SR) are deduced from experimentally measured spectra.

We analyzed the wavelength dependence of meandering loop mirrors (MLMs), MLMs the coup is one of the basic elements used in our designs. We looked at the coupled and the transmitted port intensities and compared them with the measurement results. These DCs were chosen for designing the meandering elements because the wavelength sweep would correspond to the tuning due to coupling of the devices. Then we studied the MLM spectral response, which incorporates a directional coupler. After developing the basic understanding of directional coupler and the MLM, we analyzed the spectral responses of more complex structures with ADF, e.g., MLM, DC-MR, DC-SMR, SC-MR, DC-AMR, and DC-RMR.

The general response of a tunable mirror was observed for the MLMs, where the dip corresponds to the maximum reflectivity of the mirror. The dip position shifted, when the coupling length of the DC was varied. The resonance observed in the spectrum of de-embedding structure is due to the FP effect created by the reflections from the input and the output grating couplers. The spectral behavior of the MR structures showed a Fabry-Pérot like behavior. At the maximum reflectance points of the MLM, the Q-factor was observed to be maximum. Maximum Q-factors of around $5x10^4$ was observed in MRs, Extinction ratios are sensitive to the reflectance of the MLMs and become worse at the high reflectance values of the mirror. The FSR is on the order of 1 nm for our fabricated MR devices.

We have designed and analyzed the DC-AMRs, and the structure showed a typical response which is similar to the coupled resonator induced transparency (CRIT), the analogue of the electromagnetically induced transparency (EIT), spectral response. The resonance peaks move towards higher quality factor values as the coupling is increased.

We plotted the intensities of AMR connected to the input and output grating couplers, for different coupling lengths, where Lc is varied from 20 to 36 μm. The FSR of the structure is on the order of 1-2 nm. The transmission spectra of DC-AMR can achieve different line shapes at different coupling values, these effects in the transmission spectra of AMR devices can be explored in sensing and communication applications to achieve bandwidths of operations which are not limited by the FSR value.

The DC-SMR has a richer spectrum with mode splitting of tunable Fano and Lorentzian lineshapes. These responses make the SMR an ideal candidate for designing optical filters.

The DC-RMR has resonator enhanced Mach-Zehnder interferometer (REMZI) behavior. The interference in DC-RMR creates a pattern with an FSR on the order of 3 nm.

The figures of merits (FOMs) are given as the best result achieved for each design. The devices themselves have almost no insertion loss and the loss mechanism almost directly comes from the surface grating couplers -in and out- for all structures. SC-MR has an FSR of 1.6 nm with a best Q-factor of 19000, has an extinction ratio of 23 dB and a slope rate of 163 dB/nm. SC-MR has an FSR of 1.1 nm with a best Q-factor of 12000, has an extinction ratio of 30 dB and a slope rate of 307 dB/nm. DC-SMR has an FSR of 2.05 nm with a best Q-factor of 10000, a mode split of 1.1 nm, has an extinction ratio of 27 dB and a slope rate of 450 dB/nm. DC-AMR has an FSR of 1.83 nm with a best Q-factor of 40000, a mode split of 0.1 nm, has an extinction ratio of 33 dB and a slope rate of 872 dB/nm. DC-RMR has an FSR of 3.6 nm with a best Q-factor of 8000, a mode split of 1.1 nm, has an extinction ratio of 29 dB and a slope rate of 183 dB/nm.

In all of our designs we introduced a subsection of a waveguide with a specific length, if the round-trip optical path length is increased by increasing the length of the subsection, these devices can even be used for dense wavelength division multiplexing (DWDM) applications, which should have a spacing of 0.2 nm at 1550 nm. These results show that proposed devices, ADF-MLM, ADF resonators are good candidates for WDM applications, but still further modifications are required to be used as novel integrated photonic elements for optical communication, computation, and sensing.

Curriculum Vitae

Suat Kurt has received B.S. in Electronics and Communication Engineering from İstanbul Technical University (ITU) in 2015. During his studies at ITU, he has contributed to the research regarding the piezoelectric driven optical fibers. Then he joined Koç University as a direct Ph.D. student. During his Ph.D. studies at Koç University, with Professor Ali Serpengüzel, he studied the observation of whispering gallery modes and the design of silicon integrated photonics structures. He has a conference paper, named "THz Region Elastic Scattering from a Silica Microsphere," presented in Frontiers in Optics / Laser Science, OSA Technical Digest (Optical Society of America, 2018), paper JW4A.43. Also, he is a co-author of poster named "Germania microspheres for near-infrared telecommunication" SPIE Optics and Opto-Electronics, Prague, Czech Republic, 2019, THz Region Elastic Scattering from a Silica Microsphere," 33rd Glass Symposium, Şişecam, İstanbul, Turkey, 2018, Observation of Whispering Gallery Modes in Microspheres," Laser Frontiers Summer School, São Paulo, Brazil, 2018. He also attended summer schools in Germany, Brazil and The Netherlands and presented his work regarding the whispering gallery mode microspheres. The following talks/poster are presented in these summer schools "Chalcogenide Glass based Photonic Structures," presented at: University of Twente, The Netherlands, 2017, Fraunhofer-Institut für Werkstoff- und Strahltechnik (IWS), Dresden, Germany, 2017 and presented at the 17th International Commission on Glass Annual Meeting & Şişecam Glass Symposium, İstanbul, Türkiye, 2017. Currently, he is working in Aselsan as a Systems Engineer.

REFERENCES

[1] B. P. Lathi and Z. Ding, *Modern digital and analog communication systems*, 4th ed. in Oxford series in electrical and computer engineering. New York: Oxford University Press, 2009.

[2] Mikiya Kamata and Toshihiko Baba, "OFDR analysis of Si photonics FMCW LiDAR chip," Opt. Express 31, 25245-25252 (2023).

[3] S. T. Naitik, J. V. Gorabal, S. Shetty, P. M. Srinivas, and S. Girish, “Photonic Communication Systems and Networks,” in Modeling and Optimization of Optical Communication Networks, 1st ed., C. Singh, R. R. Gatti, K. V. S. S. S. S. Sairam, and A. Singh, Eds., Wiley, 2023, pp. 303–330.

[4] H. O. Çirkinoğlu et al., “Silicon microsphere whispering gallery modes excited by femtosecond-laser-inscribed glass waveguides,” Appl. Opt., vol. 57, no. 14, p. 3687, May 2018.

[5] X. Li, L. Lu, Y. Zhou, W. Bao, J. Chen, and L. Zhou, “Low-Loss and Power-Efficient Polarization-Diversity 4 × 4 Microring Switch on a Multi-Layer Si3N4-on-SOI Platform,” J. Lightwave Technol., pp. 1–10, 2024.

[6] Q. Zhang, J. Wang, and A. W. Poon, “Silicon Carbide Microring Resonators for Integrated Nonlinear and Quantum Photonics Based on Optical Nonlinearities,” Photonics, vol. 11, no. 8, p. 701, Jul. 2024.

[7] E. Arslan et al., “Reconfigurable Intelligent Surface Enabled Over-the-Air Uplink NOMA,” IEEE Trans. on Green Commun. Netw., vol. 7, no. 2, pp. 814–826, Jun. 2023.

[8] K. C. Kao, and G. A. Hockham, “Dielectric-fibre surface waveguides for optical frequencies,” *Proceedings of the Institution of Electrical Engineers,* vol. 113, no. 7, pp. 1151-1158, 1966.

[9] C. Yeh, Applied Photonics (Academic Press, 1994). pp 1-2.

[10] N. Patle, A. B. Raj, C. Joseph, and N. Sharma, “Review of fibreless optical communication technology: history, evolution, and emerging trends,” *Journal of Optical* Communications, vol. 45, no. 3, pp. 679–702, Jul. 2024.

[11] Nakazawa, M., Kikuchi, K., & Miyazaki, T., "High spectral density optical communication technologies" Springer Science & Business Media (2010).

[12] C. Wang *et al.*, "10 kW tandem pumping fiber amplifier with good beam quality based on tapered ytterbium-doped fiber," *Opt. Express*, vol. 31, no. 24, p. 40980, Nov. 2023.

[13] R. Li *et al.*, "Design and optimization methods towards a 10 kW high beam quality fiber laser based on the counter tandem pumping scheme," *High Pow Laser Sci Eng*, vol. 12, p. e38, 2024.

[14] Optical Amplifiers - A Few Different Dimensions. Erscheinungsort nicht ermittelbar: IntechOpen, 2018.

[15] W. Xie et al., "Heterogeneous silicon photonics sensing for autonomous cars," Opt. Express, vol. 27, no. 3, p. 3642, Feb. 2019.

[16] C. Lam, Hong Liu, B. Koley, Xiaoxue Zhao, V. Kamalov, and V. Gill, "Fiber optic communication technologies: What's needed for datacenter network operations," *IEEE Commun. Mag.*, vol. 48, no. 7, pp. 32–39, Jul. 2010.

[17] M. Matsuura, H. Nomoto, H. Mamiya, T. Higuchi, D. Masson, and S. Fafard, "Over 40-W Electric Power and Optical Data Transmission Using an Optical Fiber," IEEE Trans. Power Electron., vol. 36, no. 4, pp. 4532–4539, Apr. 2021.

[18] Y. Huang, J. Song, X. Luo, T.-Y. Liow, and G.-Q. Lo, "CMOS compatible monolithic multi-layer Si_3N_4-on-SOI platform for low-loss high performance silicon photonics dense integration," Opt. Express, vol. 22, no. 18, p. 21859, Sep. 2014.

[19] M.-J. Li, "Optical Fiber Evolution Over the Past 5 Decades," in Frontiers in Optics / Laser Science, Washington, DC: Optica Publishing Group, 2020, p. FM4D.1.

[20] C. Gunn, "CMOS Photonics for High-Speed Interconnects," IEEE Micro **26**, 58-66 (2006).

[21] W. M. J. Green, M. J. Rooks, L. Sekaric, and Y. A. Vlasov, "Optical modulation using anti-crossing between paired amplitude and phase resonators," Opt. Express **15**, 17264 (2007).

[22] "Nanophotonic waveguides in silicon-on-insulator fabricated with CMOS technology," J. Lightwave Technol., vol. 23, no. 1, pp. 401–412, Jan. 2005.

[23] S. A. Miller et al., "Low-loss silicon platform for broadband mid-infrared photonics," Optica, vol. 4, no. 7, p. 707, Jul. 2017.

[24] A. Liu et al., “A high-speed silicon optical modulator based on a metal–oxide–semiconductor capacitor,” Nature, vol. 427, no. 6975, pp. 615–618, Feb. 2004.

[25] A. Liu et al., “High-speed optical modulation based on carrier depletion in a silicon waveguide,” Opt. Express, vol. 15, no. 2, p. 660, Jan. 2007.

[26] V. R. Almeida, C. A. Barrios, R. R. Panepucci, and M. Lipson, “All-optical control of light on a silicon chip,” Nature, vol. 431, no. 7012, pp. 1081–1084, Oct. 2004.

[27] Y. Shi et al., “Silicon photonics for high-capacity data communications,” Photon. Res., vol. 10, no. 9, p. A106, Sep. 2022.

[28] X. Shen, B. Chen, Y. Zhu, and W. Shi, “Silicon photonic integrated circuits and its application in data center,” in Seventh Symposium on Novel Photoelectronic Detection Technology and Applications, J. Chu, Q. Yu, H. Jiang, and J. Su, Eds., Kunming, China: SPIE, Mar. 2021, p. 369.

[29] M. R. Chaudhry, M. Zakwan, M. C. Onbasli, and A. Serpengüzel, “Symmetric Meandering Distributed Feedback Structures for Silicon Photonic Circuits,” IEEE J. Select. Topics Quantum Electron., vol. 26, no. 2, pp. 1–5, Mar. 2020.

[30] L. Chrostowski and M. Hochberg, Silicon Photonics Design: From Devices to Systems (Cambridge University Press, 2015).

[31] W. Bogaerts and L. Chrostowski, “Silicon Photonics Circuit Design: Methods, Tools and Challenges,” *Laser & Photonics Reviews*, vol. 12, no. 4, p. 1700237, Apr. 2018.

[32] T. Jiang, H. Zhou, and Y. Yang, “Research on photonic communication technology and its prospects for defense applications,” in Advanced Fiber Laser Conference (AFL2023), P. Zhou, Ed., Shenzhen, China: SPIE, Mar. 2024, p. 278.

[33] Soref, R. A. & Lorenzo, J. P. Single-crystal silicon: a new material for 1.3 and 1.6 μm integrated-optical components. *Electron. Lett.* **21**, 953–954 (1985).

[34] B. L. Weiss, G. T. Reed, S. K. Toh, R. A. Soref, and F. Namavar, “Optical waveguides in SIMOX structures,” IEEE Photon. Technol. Lett., vol. 3, no. 1, pp. 19–21, Jan. 1991.

[35] J. Schmidtchen, A. Splett, B. Schüppert, K. Petermann, and G. Burbach, “Low loss singlemode optical waveguides with large cross-section in silicon-on-insulator,” Electron. Lett., vol. 27, no. 16, p. 1486, 1991.

[36] S. Preble et al., “Passive silicon photonic devices,” in Integrated Photonics for Data Communication Applications, Elsevier, 2023, pp. 159–199.

[37] G. T. Reed and A. P. Knights, Silicon photonics: an introduction, Chichester: Wiley, 2005.

[38] M. Zhang, C. Wang, P. Kharel, D. Zhu, and M. Lončar, “Integrated lithium niobate electro-optic modulators: when performance meets scalability,” Optica, vol. 8, no. 5, p. 652, May 2021.

[39] L. Lu, L. Shen, W. Gao, L. Zhou, and J. Chen, “Reconfigurable Silicon Photonic Processor Based on SCOW Resonant Structures,” *IEEE Photonics J.*, vol. 11, no. 6, pp. 1–12, Dec. 2019.

[40] W. Luo et al., “Recent progress in quantum photonic chips for quantum communication and internet,” Light Sci Appl, vol. 12, no. 1, Jul. 2023.

[41] L. S. Madsen et al., “Quantum computational advantage with a programmable photonic processor,” Nature, vol. 606, no. 7912, pp. 75–81, Jun. 2022.

[42] G. Lihachev et al., “Low-noise frequency-agile photonic integrated lasers for coherent ranging,” Nat Commun, vol. 13, no. 1, Jun. 2022.

[43] A. Perez-Serrano, C. Quevedo-Galan, V. R. Aguilera-Sanchez, J. M. G. Tijero, and I. Esquivias, “Differential Absorption Lidar Transmitter Based on an Indium Phosphide Photonic Integrated Circuit for Carbon Dioxide Sensing,” IEEE J. Select. Topics Quantum Electron., vol. 28, no. 5: Lidars and Photonic Radars, pp. 1–8, Sep. 2022.

[44] H. Rong et al., “A continuous-wave Raman silicon laser,” Nature, vol. 433, no. 7027, pp. 725–728, Feb. 2005.

[45] B. Jalali and S. Fathpour, “Silicon Photonics,” J. Lightwave Technol., vol. 24, no. 12, pp. 4600–4615, Dec. 2006.

[46] R. Soref and J. Larenzo, “All-silicon active and passive guided-wave components for λ = 1.3 and 1.6 μm,” IEEE J. Quantum Electron., vol. 22, no. 6, pp. 873–879, Jun. 1986.

[47] A. E.-J. Lim et al., “Review of Silicon Photonics Foundry Efforts,” IEEE J. Select. Topics Quantum Electron., vol. 20, no. 4, pp. 405–416, Jul. 2014.

[48] W. Bogaerts, R. Baets, P. Dumon, V. Wiaux, S. Beckx, D. Taillaert, B. Luyssaert, J. Van Campenhout, P. Bienstman, and D. Van Thourhout, J. Lightwave Technol. 23(1), 401–412 (2005).

[49] S. Y. Siew et al., “Review of Silicon Photonics Technology and Platform Development,” J. Lightwave Technol., vol. 39, no. 13, pp. 4374–4389, Jul. 2021.

[50] J. S. Levy, A. Gondarenko, M. A. Foster, A. C. Turner-Foster, A. L. Gaeta, and M. Lipson, “CMOS-compatible multiple-wavelength oscillator for on-chip optical interconnects,” Nature Photon, vol. 4, no. 1, pp. 37–40, Jan. 2010.

[51] W. N. Ye and Y. Xiong, “Review of silicon photonics: history and recent advances,” Journal of Modern Optics, vol. 60, no. 16, pp. 1299–1320, Sep. 2013.

[52] Shekhar, S., Bogaerts, W., Chrostowski, L. *et al.* Roadmapping the next generation of silicon photonics. Nat Commun 15, 751 (2024).

[53] S. Zhang, R. Kraemer, X. Xue, N. Tessema, H. Freire Santana, E. Tangdiongga, and N. Calabretta, "Photonic integrated multicast switch-based optical wireless data center network," J. Opt. Commun. Netw. 15, pp C54-C62 (2023).

[54] N. Bavili, T. Balkan, B. Morova, M. Eryürek, Y. Uysallı, S. Kaya, and A. Kiraz, "Highly sensitive optical sensor for hydrogen gas based on a polymer microcylinder ring resonator," Sensors and Actuators B: Chemical 310, 127806 (2020).

[55] M. A. Butt, M. Shahbaz, Ł. Kozłowski, A. Kaźmierczak, and R. Piramidowicz, "Silica-Titania Integrated Photonics Platform-Based 1 × 2 Demultiplexer Utilizing Two Serially Cascaded Racetrack Microrings for 1310 nm and 1550 nm Telecommunication Wavelengths," Photonics 10, 208 (2023).

[56] X. Guo, X. Ji, B. Yao, T. Tan, A. Chu, O. Westreich, A. Dutt, C. Wong, and Y. Su, "Ultra-wideband integrated photonic devices on silicon platform: from visible to mid-IR," Nanophotonics 12, 167–196 (2023).

[57] M. Shahbaz, M. A. Butt, and R. Piramidowicz, "A Concise Review of the Progress in Photonic Sensing Devices," Photonics 10, 698 (2023).

[58] M. Asghari, and A. V. Krishnamoorthy, “Silicon photonics: Energy-efficient communication,” *Nature Photonics,* vol. 5, no. 5, pp. 268-270, 2011.

[59] B. Bai, H. Shu, X. Wang, and W. Zou, “Towards silicon photonic neural networks for artificial intelligence,” Sci. China Inf. Sci., vol. 63, no. 6, p. 160403, Jun. 2020.

[60] D. Thomson et al., “Roadmap on silicon photonics,” J. Opt., vol. 18, no. 7, p. 073003, Jul. 2016.

[61] J. Wang and Y. Long, “On-chip silicon photonic signaling and processing: a review,” Science Bulletin, vol. 63, no. 19, pp. 1267–1310, Oct. 2018.

[62] T. Komljenovic et al., “Heterogeneous Silicon Photonic Integrated Circuits,” J.

Lightwave Technol., vol. 34, no. 1, pp. 20–35, Jan. 2016.
[63] B. R. Koch et al., “Integrated Silicon Photonic Laser Sources for Telecom and Datacom,” in Optical Fiber Communication Conference/National Fiber Optic Engineers Conference 2013, Anaheim, California: OSA, 2013, p. PDP5C.8.
[64] A. Y. Liu et al., “High performance continuous wave 1.3 μ m quantum dot lasers on silicon,” Appl. Phys. Lett., vol. 104, no. 4, p. 041104, Jan. 2014.
[65] A. Lee, Q. Jiang, M. Tang, A. Seeds, and H. Liu, “Continuous-wave InAs/GaAs quantum-dot laser diodes monolithically grown on Si substrate with low threshold current densities,” Opt. Express, vol. 20, no. 20, p. 22181, Sep. 2012.
[66] R. Ho et al., “Silicon Photonic Interconnects for Large-Scale Computer Systems,” IEEE Micro, vol. 33, no. 1, pp. 68–78, Jan. 2013.
[67] Y. Ding, F. Ye, C. Peucheret, H. Ou, Y. Miyamoto, and T. Morioka, “On-chip grating coupler array on the SOI platform for fan-in/fan-out of MCFs with low insertion loss and crosstalk,” Opt. Express, vol. 23, no. 3, p. 3292, Feb. 2015.
[68] W. Shen, J. Du, J. Xiong, L. Ma, and Z. He, “Silicon-integrated dual-mode fiber-to-chip edge coupler for 2 × 100 Gbps/lambda MDM optical interconnection,” Opt. Express, vol. 28, no. 22, p. 33254, Oct. 2020.
[69] J. Witzens, “High-Speed Silicon Photonics Modulators,” Proc. IEEE, vol. 106, no. 12, pp. 2158–2182, Dec. 2018.
[70] Intel Silicon Photonics Pluggable Optical Transceivers (2024, September 21).
[71] S. Pitris et al., “400 Gb/s Silicon Photonic Transmitter and Routing WDM Technologies for Glueless 8-Socket Chip-to-Chip Interconnects,” J. Lightwave Technol., vol. 38, no. 13, pp. 3366–3375, Jul. 2020.
[72] H. Li, Z. Xuan, R. Kumar, M. Sakib, J. Sharma, C.-M. Hsu, C. Ma, H. Rong, G. Balamurugan, and J. Jaussi, “A 4 × 50 Gb/s all-silicon ring-based WDM transceiver with CMOS IC,” in European Conference on Optical Communication (ECOC) (2021), pp. 1–3.
[73] M. Sakib, P. Liao, C. Ma, R. Kumar, D. Huang, G.-L. Su, X. Wu, S. Fathololoumi, and H. Rong, “A high-speed micro-ring modulator for next generation energy-efficient optical networks beyond 100 Gbaud,” in Conference on Lasers and Electro-Optics (CLEO) (2021), paper SF1C.3.
[74] J. B. Driscoll et al., “A 60 Gb/s MDM-WDM Si photonic link with < 07 dB power

penalty per channel," Opt. Express, vol. 22, no. 15, p. 18543, Jul. 2014.

[75] H. Jia et al., "WDM-compatible multimode optical switching system-on-chip," Nanophotonics, vol. 8, no. 5, pp. 889–898, May 2019.

[76] W. Bogaerts, P. De Heyn, T. Van Vaerenbergh, K. De Vos, S. Kumar Selvaraja, T. Claes, P. Dumon, P. Bienstman, D. Van Thourhout, and R. Baets, "Silicon microring resonators," Laser and Photonics Reviews, vol. 6, no. 1, pp. 47-73, 2012.

[77] L. Zhang et al., "Ultralow-Loss Silicon Photonics beyond the Singlemode Regime," Laser & Amp; Photonics Reviews, vol. 16, no. 4, Apr. 2022.

[78] C. B. Dağ, M. A. Anıl, and A. Serpengüzel, "Novel Distributed Feedback Lightwave Circuit Elements." in Proceedings of the SPIE on Smart Photonic and Optoelectronic Integrated Circuits XVII, L. A. Eldada, E.-H. Lee, and S. He, Eds. 9366:93660A, (2015).

[79] C. B. Dağ, M. A. Anıl, and A. Serpengüzel, "Meandering Waveguide Distributed Feedback Lightwave Circuits," Journal of Lightwave Technology 33, 1691–1702 (2015).

[80] H. Arianfard, J. Wu, and D. J. Moss, "Integrated photonic coupled Sagnac loop reflectors for flat-top wavelength interleaving and switching," in 14th Pacific Rim Conference on Lasers and Electro-Optics (CLEO PR 2020), Sydney: OSA, 2020, p. C11H_4.

[81] H. Arianfard, J. Wu, S. Juodkazis, and D. J. Moss, "Spectral shaping based on optical waveguides with advanced Sagnac loop reflectors," in Integrated Optics: Devices, Materials, and Technologies XXVI, SPIE, Mar. 2022, pp. 117–123.

[82] M. Smit, J. Van Der Tol, and M. Hill, "Moore's law in photonics," Laser & Photonics Reviews, vol. 6, no. 1, pp. 1–13, Jan. 2012.

[83] R. Katsumi, Y. Ota, and M. Benyoucef, "Telecom-Band Quantum Dots Compatible with Silicon Photonics for Photonic Quantum Applications," Adv Quantum Tech, p. 2300423, Feb. 2024.

[84] D. Dai, J. Bauters, and J. E. Bowers, "Passive technologies for future large-scale photonic integrated circuits on silicon: polarization handling, light non-reciprocity and loss reduction," Light Sci Appl, vol. 1, no. 3, pp. e1–e1, Mar. 2012.

[85] D. J. Thomson et al., "50-Gb/s Silicon Optical Modulator," IEEE Photon. Technol. Lett., vol. 24, no. 4, pp. 234–236, Feb. 2012.

[86] L. Vivien et al., "Zero-bias 40Gbit/s germanium waveguide photodetector on silicon," Opt. Express, vol. 20, no. 2, p. 1096, Jan. 2012.

[87] Z. Zhou, B. Yin, and J. Michel, “On-chip light sources for silicon photonics,” Light Sci Appl, vol. 4, no. 11, pp. e358–e358, Nov. 2015.

[88] M. Tang et al., “Integration of III-V lasers on Si for Si photonics,” Progress in Quantum Electronics, vol. 66, pp. 1–18, Aug. 2019.

[89] D. Liang and J. E. Bowers, “Recent progress in lasers on silicon,” Nature Photon, vol. 4, no. 8, pp. 511–517, Aug. 2010.

[90] C. Guo and Y. Wan, “Light People: Prof. John Bowers spoke about silicon photonics,” Light Sci Appl, vol. 11, no. 1, p. 345, Dec. 2022.

[91] Z. Zhou, B. Yin, and J. Michel, “On-chip light sources for silicon photonics,” Light Sci Appl, vol. 4, no. 11, pp. e358–e358, Nov. 2015.

[92] W.-Q. Wei et al., “Monolithic integration of embedded III-V lasers on SOI,” Light Sci Appl, vol. 12, no. 1, p. 84, Apr. 2023.

[93] Z. Wang et al., “Room-temperature InP distributed feedback laser array directly grown on silicon,” Nature Photon, vol. 9, no. 12, pp. 837–842, Dec. 2015.

[94] Y. Wan et al., “Optically pumped 13 μm room-temperature InAs quantum-dot micro-disk lasers directly grown on (001) silicon,” Opt. Lett., vol. 41, no. 7, p. 1664, Apr. 2016.

[95] Z.-H. Wang, W.-Q. Wei, Q. Feng, T. Wang, and J.-J. Zhang, “InAs/GaAs quantum dot single-section mode-locked lasers on Si (001) with optical self-injection feedback,” Opt. Express, vol. 29, no. 2, p. 674, Jan. 2021.

[96] J. Liu et al., “Tensile-strained, n-type Ge as a gain medium for monolithic laser integration on Si,” Opt. Express, vol. 15, no. 18, p. 11272, 2007.

[97] J. A. Smith, D. Jevtics, B. Guilhabert, M. D. Dawson, and M. J. Strain, “Hybrid integration of chipscale photonic devices using accurate transfer printing methods,” Applied Physics Reviews, vol. 9, no. 4, p. 041317, Dec. 2022.

[98] D. J. Blumenthal, R. Heideman, D. Geuzebroek, A. Leinse, and C. Roeloffzen, “Silicon Nitride in Silicon Photonics,” Proc. IEEE, vol. 106, no. 12, pp. 2209–2231, Dec. 2018.

[99] C. Xiang et al., “High-performance lasers for fully integrated silicon nitride photonics,” Nat Commun, vol. 12, no. 1, p. 6650, Nov. 2021.

[100] D. J. Moss, R. Morandotti, A. L. Gaeta, and M. Lipson, “New CMOS-compatible platforms based on silicon nitride and Hydex for nonlinear optics,” Nature Photon, vol. 7, no. 8, pp. 597–607, Aug. 2013.

[101] D. Duchesne et al., “Efficient self-phase modulation in low loss, high index doped silica glass integrated waveguides,” Opt. Express, vol. 17, no. 3, p. 1865, Feb. 2009.

[102] J. S. Levy, A. Gondarenko, M. A. Foster, A. C. Turner-Foster, A. L. Gaeta, and M. Lipson, “CMOS-compatible multiple-wavelength oscillator for on-chip optical interconnects,” Nature Photon, vol. 4, no. 1, pp. 37–40, Jan. 2010.

[103] C. Xiang et al., “3D integration enables ultralow-noise isolator-free lasers in silicon photonics,” Nature, vol. 620, no. 7972, pp. 78–85, Aug. 2023.

[104] C. Xiang, W. Jin, and J. E. Bowers, “Silicon nitride passive and active photonic integrated circuits: trends and prospects,” *Photon. Res.*, vol. 10, no. 6, p. A82, Jun. 2022.

[105] D. Dai, J. Bauters, and J. E. Bowers, “Passive technologies for future large-scale photonic integrated circuits on silicon: polarization handling, light non-reciprocity and loss reduction,” *Light Sci Appl*, vol. 1, no. 3, pp. e1–e1, Mar. 2012.

[106] A. Rahim, E. Ryckeboer, A. Z. Subramanian, S. Clemmen, B. Kuyken, A. Dhakal, et al., "Expanding the silicon photonics portfolio with silicon nitride photonic integrated circuits", J. Lightw. Technol., vol. 35, no. 4, pp. 639-649, Feb. 2017.

[107] A. Hermans et al., “High-pulse-energy III-V-on-silicon-nitride mode-locked laser,” APL Photonics, vol. 6, no. 9, p. 096102, Sep. 2021.

[108] Gaeta, A. L., Lipson, M. & Kippenberg, T. J. Photonic-chip-based frequency combs. Nat. Photon. 13, 158–169 (2019).

[109] Y. Okawachi, K. Saha, J. S. Levy, Y. H. Wen, M. Lipson, and A. L. Gaeta, “Octave-spanning frequency comb generation in a silicon nitride chip,” Opt. Lett., vol. 36, no. 17, p. 3398, Sep. 2011.

[110] C. Xiang et al., “High-performance lasers for fully integrated silicon nitride photonics,” Nat Commun, vol. 12, no. 1, p. 6650, Nov. 2021.

[111] Applied Nanotools NanoSOI MPW: Available: https://www.appliednt.com/nanosoi-fabrication-service/

[112] F. B. Tarik, A. Famili, Y. Lao, and J. D. Ryckman, “Scalable and CMOS compatible silicon photonic physical unclonable functions for supply chain assurance,” Sci Rep, vol. 12, no. 1, p. 15653, Sep. 2022.

[113] Maple Leaf Photonics: Available: http://mapleleafphotonics.com

[114] SiEPIC github page: Avaiable: https://github.com/SiEPIC/SiEPIClab

[115] PLC connections: Available: https://www.plcconnections.com/